Cardiff University

Institute of Medical Engineering and Medical Physics

SCHOOL OF ENGINEERING

Verification of Stereotactic Radiotherapy

A dissertation presented to the Insitute of Medical Engineering and Medical Physics at Cardiff School of Engineering, Cardiff University in partial fulfillment of the requirements for the degree of Doctor of Philosophy

Anthony Millin

DECLARATION

This work has not previously been accepted in substance for any degree and is not concurrently submitted in candidature for any degree

Signed ..... (candidate) Date .....

STATEMENT 1

This thesis is being submitted in partial fulfilment of the requirements of the degree of Doctor of Philosophy

Signed ..... (candidate) Date .....

STATEMENT 2

This thesis is the result of my own independent work / investigation, except where otherwise stated. Other sources are acknowledged by explicit references

Signed ..... (candidate) Date .....

STATEMENT 3

I hereby give consent for my thesis, if accepted, to be made available for photocopying and for interlibrary loan, and for the title and summary to be made available to outside organisations

Signed ..... (candidate) Date .....

Verification of Stereotactic Radiotherapy

Abstract

Investigations have been made into the use of a computer based simulation technique (Monte Carlo (MC)) to ionising radiation transport in order to verify the doses delivered during linear accelerator based stereotactic radiotherapy and radiosurgery. Due to the complex nature of the micro multi-leaf collimators (μMLC) used in this these treatments, a bespoke model of the μMLC was developed and combined with standard component modules to represent the remainder of the linear accelerator.

Following validation of the above models, investigations were made into the dosimetry of small fields, defined by the μMLC and measured with a variety of detectors. Comparisons of relative output, profiles and depth doses were made against MC simulations, and a series of correction factors determined, to account for detector geometry and the non water equivalence of materials used in semiconductor detectors. An assessment was then made to determine the smallest fields that can be measured with each detector with confidence.

Systems were then developed to independently simulate stereotactic treatments and compare doses simulated with those calculated by the treatment planning system (TPS); excellent agreement between TPS calculations and MC simulations was observed.

The application of MC methods to determine the most appropriate treatment tactics and calculation algorithms for stereotactic body radiotherapy in the lung was then investigated with recommendations made on the most appropriate calculation algorithms and beam arrangements for the technique. The doses calculated using the type-b or collapsed cone algorithm agreed most closely with the MC simulation. There was little difference observed between plans using more than four beams in the treatment delivery. Treatment techniques using only three beams or less achieved poorer coverage of the tumour with dose, producing lower doses at the periphery of the tumour near the interface with the surrounding lung tissue, compared to using a greater number of beams.

Finally, methods of transit dosimetry using Electronic Portal Imaging Devices were investigated for use in cranial stereotactic radiotherapy. Three

methods were investigated based on a full MC simulation of the radiation transport through the patient and on to the imager, prediction of the dose based on a TPS calculation and an approximation of the radiological path length of the central axis of the beams to derive an expected dose at the imager plane. The MC method produced the best agreement at the expense of a longer time to acquire the comparison doses compared to the TPS calculation method. The equivalent path length method showed good agreement (within 3.5%) between delivered and predicted doses but at a single point.

Acknowledgements

I would like to thank Cancer Research Wales (CRW) for the generous financial support of this project and the manufacturers Varian UK Ltd and BrainLAB GmbH for their assistance in providing diagrams from which the Monte Carlo Models were developed. Without their help this work would not have been possible.

Within the university I would like to thank my supervisors Professors, Peter Wells and John Woodcock for their helpful comments throughout the length of this project.

Within Velindre Cancer Centre I owe particular thanks to Dr Geraint Lewis for providing many helpful comments on all aspects of the project from conception to proof reading this thesis.

Also within the hospital, I would like to thank Dr Cyril Smith for his useful advice at the beginning of the project, Dr Patrick Downes for interminable patience in sorting out problems, I induced on the RTGrid, Rebecca Cufflin for helpful discussions, especially associated with the EPID work, Jane Powell for acquiring some of the data used in the validation of the model and the *'stereotactic'* radiographers and physicists for humouring me by acquiring so many treatment field images when requested.

I would also like to thank Frank Verhaegen and Jason Belec for helpful discussions concerning MLC models and Iwan Kawrakow for finding a solution to some compilation issues during the project.

Contents

List of Figures

List of Tables

List of Acronyms

μMLC micro Multi Leaf Collimator.

AAPM Association of American Physicists in Medicine.

ABS Absolute.

BLMLC BrainLAB MLC, component module written to simulate the BrainLAB MLC.

CC Collapsed Cone superposition calculation algorithm.

CC01 Scanditronix 0.01 cubic centimetre volume ionisation chamber.

CC13 Scanditronix 0.13 cubic centimetre volume ionisation chamber.

CM Component Module.

CRW Cancer Research Wales.

CT Computed Tomography.

CTV Clinical Target Volume.

DBS Directional Bremsstrahlung Splitting.

Dmax Depth of maximum dose.

DRR Digitally Reconstructed Radiograph.

DTA Distance To Agreement.

DVH Dose Volume Histogram.

EFD Scanditronix Electron Field Detector diode.

EPID Electronic Portal Imaging Device.

EwwF Equivalent Window Width Field.

FSD Focus to Skin Distance.

GTC Gill-Thomas-Cosman relocatable stereotactic frame.

Gy Gray (unit of absorbed radiation dose).

HU Hounsfield Unit.

IMRS Intensity Modulated Radiosurgery.

IMRT Intensity Modulated Radiotherapy.

KERMA Kinetic Energy Released in Matter.

MC Monte Carlo1.

MLC Multi Leaf Collimator.

MRI Magnetic Resonance Imaging.

MU Monitor Unit.

NMR Nuclear Magnetic Resonance.

OAR Organ at Risk.

OMP Nucletron Oncentra MasterPlan treatment planning system.

PAG Poly-Acrylamide Gel.

PB Pencil Beam superposition calculation algorithm.

PDD Percentage Depth Dose.

PET Positron Emission Tomography.

PFD Scanditronix Photon Field Detector diode.

PTV Planning Target Volume.

RK Scanditronix RK ionisation chamber.

RKHZ Scanditronix RK Chamber oriented with long axis perpendicular to the radiation device central axis.

RKVRT Scanditronix RK Chamber oriented with long axis parallel to the radiation device isocentre.

SAR Scatter Air Ratio.

SBRT Stereotactic Body Radiotherapy.

SD Standard Deviation.

SFD Scanditronix Stereotactic Field Detector diode.

SFDHZ Scanditronix SFD diode oriented with long axis perpendicular to the radiation device central axis.

SFDVRT Scanditronix SFD diode oriented with long axis parallel to the radiation device central axis.

SRS Stereotactic Radiosurgery.

SRT Stereotactic Radiotherapy.

TAR Tissue Air Ratio.

TERMA Total Energy Released inn Matter.

TLD Thermoluminescent detector.

TMR Tissue Maximum Ratio.

TPR Tissue Phantom Ratio.

TPS Treatment Planning System.

VCC Velindre Cancer Centre.

VMAT Volumetric Modulated Arc Therapy.

VMC Voxel Monte Carlo.

WTe Water Equivalent Material.

Z Atomic Number.

Chapter 1

Introduction

Contents

1.1 Radiotherapy

Irradiating diseased cells with ionising radiation in order to achieve cell death has been used in the management of malignant and non-malignant disease since the end of the nineteenth century. This was initially achieved using kilovoltage X-ray sets and by the application of radium on or near the tumour. By the middle of the twentieth century, the science of radiotherapy had advanced to use

high energy beams obtained from high activity radiation sources, such as those found in ^{60}Co based teletherapy machines. These machines enabled treatment with high-energy radiation, allowing high, uniform doses to be applied to non-superficial tumours. The advantages of this approach were further developed with the invention of the medical linear accelerator, used to generate high-energy photon and electron radiation using radio-frequency waves to accelerate electrons along a wave-guide. These electrons are then used to generate photons as they interact within a high-density target to produce a high-energy photon beam or scattered using a scattering foil to produce an electron beam (more suited for superficial lesions).

The rationale of radiotherapy is to exploit the radiosensitivity of tumour cells by irradiating them to a lethal dose whilst irradiating healthy tissue to a dose that can be safely tolerated. This can be achieved by confining the radiation to the target volume using highly attenuating collimators, often accompanied by high density shielding blocks placed beneath the collimators, which further conform the radiation to the tumour shape, producing an optimally shaped radiation field for the particular patient and lesion. Multi Leaf Collimators (MLCs), consisting of thin fingers of a material with high-density and high average atomic number can be used to obtain the same effect by moving each leaf to the appropriate position prior to irradiation. The use of a high average atomic number materials increases the cross section for interactions occurring at these energies and therefore shields healthy tissue under the MLCs from receiving high radiation doses. Conforming the radiation field to the tumour has become known as 'conformal therapy' and is now widely used in routine radiotherapy practice (Khan, 2010).

1.2 Stereotactic Co-ordinate Systems

The use of conformal radiotherapy has developed in order to satisfy the oncologist's desire for a uniform high dose distribution in the tumour volume whilst sparing healthy tissue. However, uncertainties in the positioning of the patient during diagnostic scanning and subsequent treatment, together with movement of the tumour relative to the external patient outline, must be

accounted for when the oncologist draws clinical target volumes. This inevitably increases the size of the target volume and indeed the volume of healthy tissue that is irradiated to a significantly high dose. The purpose of Stereotactic Radiotherapy (SRT) and Stereotactic Radiosurgery (SRS) is to minimise the uncertainties in patient positioning during scanning and treatment in order to reduce the amount of healthy tissue irradiated and allow an increase in the tumour dose delivered in order to achieve a greater therapeutic effect.

Stereotactic techniques have been used in neurosurgery for many years in the treatment of malignant and non-malignant cranial disease. In the first decade of the 20th century, Horsley and Clarke (1908) published a paper in which they described an external device, illustrated in figure 1.1 used to study the cerebellar function of the monkey. This device was fitted externally to the monkey and used to define a three dimensional co-ordinate system using the fixation points of the device as reference positions. With this fixed frame of reference, it was possible to describe the function of the patient's brain to a high degree of positional accuracy.

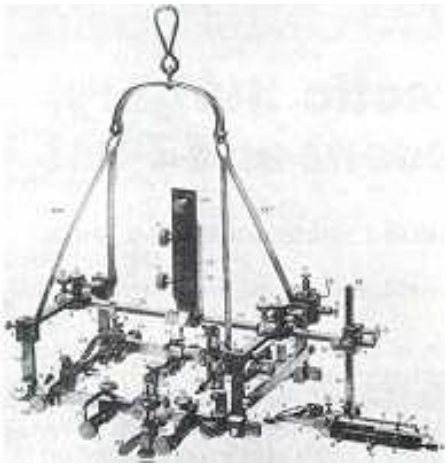

Figure 1.1: Horsley and Clarke's original stereotactic apparatus.

The first human application of this device did not take place until 1918, when Aubrey Mussen, a Canadian physiologist, commissioned the construction of a human stereotactic frame (Picard et al., 1983). This was similar to that of the original Horsley-Clarke apparatus and used ear bars fitting into the external auditory canal, and a clamp fixed to the infraorbital ridge to fix the device to

the cranium. As with the original device, it was used to produce stereotactic atlases of the human brain but despite his encouragements to the contrary, neurosurgeons were unwilling to use it for clinical neurosurgery.

However, some years later (in 1932) the apparatus was copied in Chicago, both at the North Western University and the University of Chicago where it was used to study the electrical activity of feline brains and subsequently by other institutions that extended its application to the production of atlases of human as well as animal brains. From these studies, it was found that despite the accuracy of the system being sufficient to localise sub-cortical structures with a fair degree of accuracy, anatomical differences between subjects introduced uncertainties that were considered too large for the system to be used in clinical practice.

At the same time that Horsley and Clarke were developing their stereotactic frame, an American neurosurgeon, Walter Dandy, was developing the imaging technique of ventriculography. However, it was not until some thirty years later in the mid 1940s, that it was used in conjunction with a stereotactic localisation system to locate lesions in the brain accurately during neurosurgery (Levy et al., 1998).

Dandy's paper of 1918 first describes the process of cranial ventriculography in which he was able to locate the ventricles of the brain by taking radiographs of the cranium following filling of the ventricles with gas pumped through holes drilled in the cranium (la Porte, 1993).

Using this technique to locate the ventricles, the external co-ordinate system could be accurately referenced to structures within the brain. This technique was pioneered by Spiegel et al. (1947), using a plaster cap, custom made for each patient, from which a head ring was suspended, which in turn supported an electrode carrier. Using this system, shown in figure 1.2 they were able to locate anatomical targets with reference to landmarks within the brain itself.

Inspired by the work of Spiegel and Wycis, Leksell (1949) developed his own stereotactic instrument utilizing the concept of the arc-quadrant. This device was fixed to the cranium, to which a movable arc-quadrant was attached. This arc quadrant could be moved so that the centre of the arc was positioned at the centre of the cranial target point. Developments to this apparatus resulted

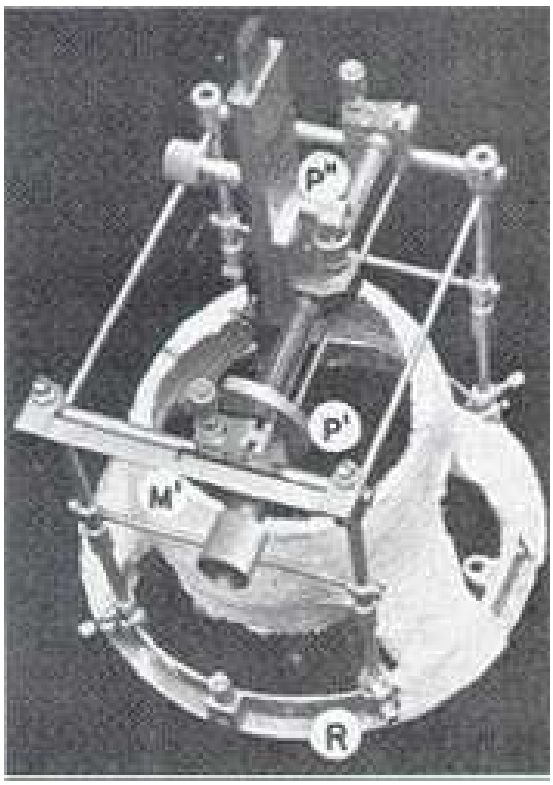

Figure 1.2: The original Spiegel and Wycis stereotactic instrument.

in the use of a cuboid frame of reference similar to the stereotactic co-ordinate systems used today. Other neurosurgeons, Talairach and Tournoux (1988) also developed a stereotactic system in Paris in the 1940s, in which a frame fixed to the patient's skull was used to support a double grid system through which radiographs were taken. From this grid projected onto the film, a co-ordinate system over the whole brain was defined relative to external markers, and the position of structures such as the ventricles could be determined if used in conjunction with a ventriculogram. A further feature of Talairach's system was that it was possible to remove the frame and reposition it in exactly the same position enabling subsequent procedures to be performed using the same frame of reference. By the beginning of the 1950s, the work of Spiegel and Wycis, Leksell and Talairach and Tournoux had convinced the neurological world of the value of stereotactic co-ordinate systems in accurately locating structures within the human brain.

Figure 1.3: CT scan of the BrainLAB stereotactic co-ordinate system attached to the head ring.

The subsequent development of advanced imaging techniques such as computed tomography (CT), magnetic resonance imaging (MRI) and positron emission tomography (PET) has increased the accuracy of the stereotactic system (Thomas et al., 1984) by enabling the reference of almost all visible neurological structures to the external stereotactic co-ordinate system. In a CT stereotactic system, a frame is fitted to the patient, which is worn during scanning. This frame, consisting of a number of diagonal bars, is used to define the external co-ordinate system independent of the movements of the scanning system. A typical system consists of a head ring attached to the patient to which a removable frame is fixed prior to scanning. Once the patient has been scanned, the co-ordinate defining bars can be seen on the CT slices from which absolute positions of structures relative to the external frame can be inferred. Figure 1.3 illustrates

the BrainLAB [1] localisation system attached to a patient head ring as the patient is about to be scanned. The high density diagonal bars, that can be seen on the side of the box appear as white dots outside the patient data on the resultant CT scan. These white dots are further illustrated in 1.4 in which a transverse CT section of a phantom used in the verification of stereotactic radiotherapy scanned within the localising frame can be seen. The localiser bars can be seen as white dots within blue circles.

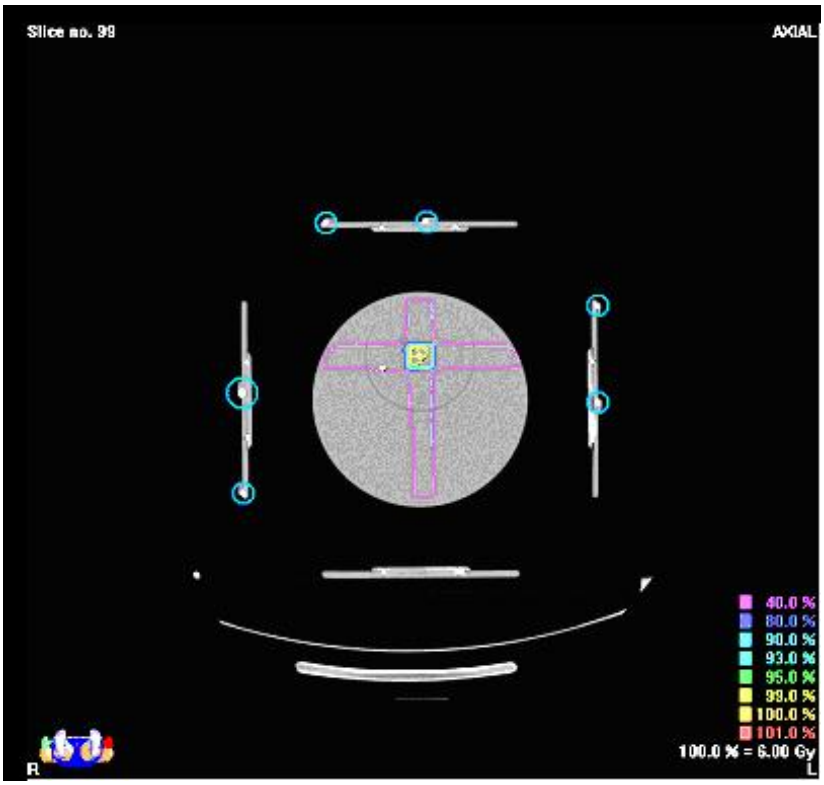

Figure 1.4: Stereotactic phantom scanned in the BrainLAB localiser box indicating position of localiser bars.

Further images of the patient, such as MRI, may be fused to the CT image to enable improved visualization of the patient anatomy, or with PET to indicate the function of tissues localised using the system. These images, by virtue of the fusion are transformed into the stereotactic co-ordinate systems and, as such, the positions of both lesions and healthy tissue can be referenced in terms of the

[1] BrainLAB Gmbh, Munich, Germany

stereotactic co-ordinate system, independent of any uncertainties associated with the system used to acquire the images or to deliver the clinical intervention. This may take the form of neurosurgical techniques or by the application of ionising radiation as in the case of stereotactic radiosurgery and radiotherapy.

1.3 Stereotactic Radiotherapy and Radiosurgery

Leksell (1951) proposed the use of radiation beams to replace surgical instruments in the treatment of neurological disorders using the stereotactic frame that he had developed. However, it was not until 1967 that the first prototype machine was built for this purpose, and the middle of the 1970s before the first purpose built machines were installed in clinical institutions. Leksell's machine consists of a number of radioactive sources that are collimated to produce narrow beams focused on a common isocentre. The dose from these beams when superimposed at the isocentre is sufficiently high to be lethal to the lesion. This outcome is achieved by first imaging the patient within a stereotactic frame and then using the same frame to position the patient such that the lesion lies at the isocentre of the system. In order to achieve the high degree of accuracy required, to within a spatial uncertainty of 1mm, an invasive frame is generally used which is attached to the patient's cranium using pins held at high pressure. Consequently, it is necessary to apply the radiation doses in a single treatment session or fraction, which is known as stereotactic radiosurgery (SRS).

Stereotactic radiotherapy (SRT) is analogous to conventional radiotherapy in that the treatment is delivered over several fractions (Warrington and Laing, 1994). This is used in preference to conventional radiotherapy techniques in circumstances where the advantage of the spatial accuracy of stereotactic techniques are clinically beneficial. Malignant and non-malignant lesions within the cranium, in which stable target volumes are situated near sensitive organs, were the first to benefit from such techniques but the technique has been implemented throughout the body. In these circumstances, it is necessary to fit the stereotactic frame to the patient on several occasions and, therefore, it is necessary to use a non invasive fixation device. Although there are no technical reasons why stereotactic radiotherapy may not be performed on a

Gamma Knife[2] (the commercial name of Leksell's machine), the majority of stereotactic radiotherapy treatments are performed using a linear accelerator based stereotactic system (Colombo et al., 1985).

1.4 The Medical Linear Accelerator

Linear accelerators, such as those shown in figure 1.5, have been used since the middle of the twentieth century to produce radiation for use in radiotherapy (Johns and Cunningham, 1969). In these machines, the momentum of electrons is increased by accelerating them through a wave-guide through which a radio-frequency signal propagates. The accelerated electrons are then directed towards a high density target, which as a consequence of bremsstrahlung interactions produce megavoltage radiation. These photons are then subsequently shaped

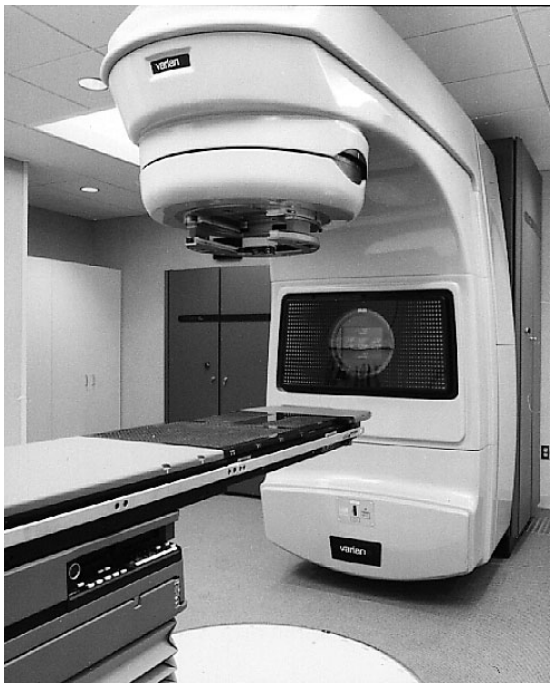

Figure 1.5: Varian 600c linear accelerator used at Velindre Cancer Centre.

by the use of collimating devices to deliver the most appropriate field size. In a typical modern linear accelerator the wave guide and collimator assembly are

[2]Elekta AB, Stockholm, Sweden

manufactured to rotate around a fixed point in space known as the machine isocentre, enabling efficient treatments to be delivered to the patient by ensuring that the lesion lies at this isocentre.

Collimation of the beam has conventionally been achieved using two pairs of fixed high density blocks positioned orthogonally to define the radiation field and limit dose delivery to a rectangle closest in geometry to the desired treatment volume. To further conform the field to the target volume, irregularly shaped shielding blocks, similarly made of high density material were often added to more closely match the area of high radiation dose. These have the advantage of reducing the volume of healthy tissue irradiated but each patient requires customised blocks made especially to match their particular anatomy, which has significant human resource implications due to the time required to make the blocks.

In order to reduce the workload but gain the advantages of the custom built shielding blocks, the multi-leaf collimator (MLC) was developed. As shown in figure 1.6, an MLC consists of a number of fingers or leaves made of high density materials that are moved under computer control to produce a field shape similar to that of a custom built block. This has enabled conformal radiotherapy fields to be offered routinely in many radiotherapy centres (LoSasso et al., 1993).

The invention of the MLC also heralded the implementation of Intensity Modulated Radiotherapy (IMRT) (Webb, 2003) on a routine basis. In the most widely used form of IMRT, the leaves of the MLC are moved during treatment in order to produce a radiation beam with a varying intensity determined by the movements of the leaves. By careful choice of the intensity profile of each beam, and the choice of optimal beam angles, healthy tissue can be avoided to a greater extent than conformal radiotherapy and the dose targeted at the tumour. A typical dose distribution produced by IMRT is shown in figure 1.7 in which concavities in the isodose lines can be seen that avoid the sensitive structures of the spinal cord and parotids. The possibility of delivering a higher dose to a partial volume of the target is also realised in this plan, which in the past would have required a two phase irradiation technique or a more complex plan.

With the widespread introduction of conformal radiotherapy and IMRT, improved imaging techniques have been introduced in order to verify that the

Figure 1.6: A Varian Millennium 120 Leaf MLC.

patient is correctly positioned. Initially, these were simply radiographic films placed opposing the treatment fields at the expected exit point of the radiation field. As these *portal images* required processing, it was difficult if not impossible to process the films quickly enough to determine if the patient position was correct prior to switching on the radiation. Therefore *offline* imaging techniques were applied where images taken over one or a number of radiotherapy fractions were examined retrospectively after treatment to determine a systematic error in patient position and the patient moved accordingly for the duration of treatment. This process clearly has the weakness of being unable to identify gross errors prior to treatment and has manpower implications associated with the requirement to process, calibrate and analyse the films. Consequently, electronic methods, using ionisation chamber arrays or fluorescent screens and semiconductor detector arrays were developed, allowing images to be acquired, processed quickly and windowed to display superior contrast than that of radiographic film. These

Electronic Portal Imaging Devices or EPIDs (Antonuk, 2002) have enabled *online* imaging to be performed on patients with high positional uncertainty or small margins for movement inherent in their treatment plan to be routinely achieved. EPIDs are also routinely used for offline imaging techniques also due to the speed of image processing, improved image quality, and their lack of a requirement for any chemical processing.

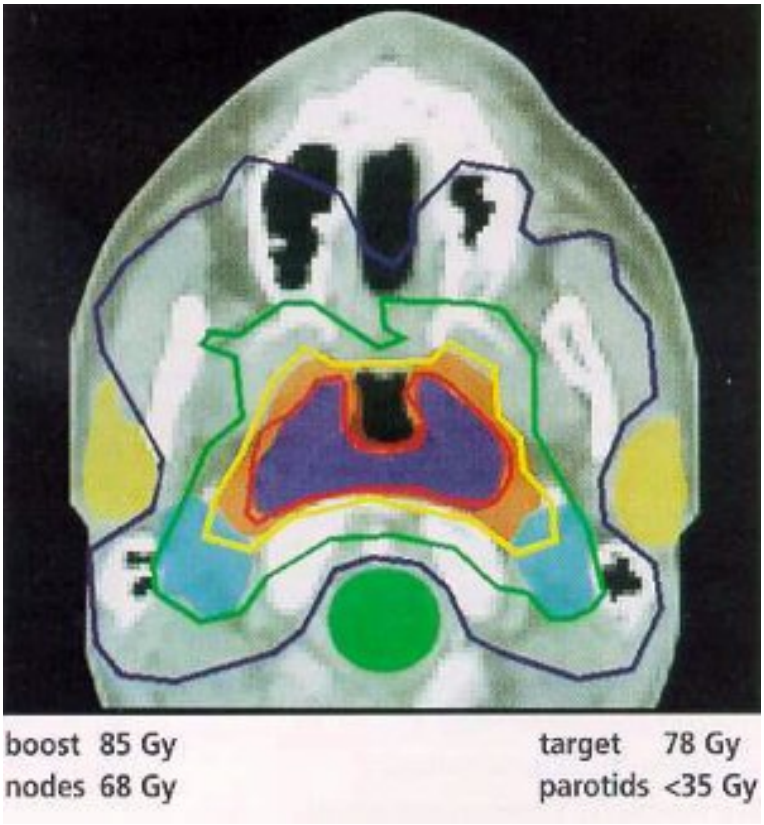

Figure 1.7: Typical isodoses produced by IMRT. The red lines indicate the boost isodose of 85Gy, the yellow the prescribed target dose of 78Gy and the blue isodose line the prophylactic nodal dose of 68Gy. The yellow and green shaded areas are the organ at risk (OAR) structures of the parotids and spinal cord respectively

1.5 Linear Accelerator Based Stereotactic Radiotherapy and Radiosurgery

In recent years, the medical linear accelerator has been widely used as the radiation source in stereotactic radiotherapy and radiosurgery (Colombo et al., 1985). The relatively small capital required to adapt a conventional accelerator for stereotaxy compared to the purchase cost of a dedicated Gamma Knife system has made stereotactic radiotherapy a more viable option for many treatment centres than was previously the case. Additionally, the increased freedom of movement in the linear accelerator gantry allows treatment for some lesions inaccessible to the Gamma Knife, which also suffers from the need to replace its radio-isotope sources every 5 to 10 years. Due to their number (over 200) and associated radiation hazards of these sources, there is a significant additional running cost of the machine, not incurred by a linear accelerator.

The evolution of linear accelerator based stereotaxy has largely followed that of conventional and conformal radiotherapy. Initial systems produced the small fields necessary for stereotactic treatment using standard conical collimators (Shrieve et al., 1998) that produced circular fields of varying sizes.

During treatment planning, the appropriate collimator size was chosen to cover the treatment volume whilst limiting the dose to healthy tissue. Analogous to custom shielding blocks in conventional radiotherapy, this system was developed to include custom cast inserts placed inside the collimator to tailor the radiation to match the shape of the tumour volume. Figure 1.8 illustrates a typical system installed on a conventional accelerator, with a custom block inserted into the conical collimator attached to the machine.

Similar to the issues associated with shielding blocks used in conformal therapy, there is a significant human resource requirement in the manufacture of customised collimators for each patient. In order to overcome these time consuming disadvantages, *micro* multi leaf collimators (μMLCs) have been developed in order to conform the radiation field to the shape of the target (Xia et al., 1999; Cosgrove et al., 1999). These are fitted to the end of the accelerator for a stereotactic treatment session and work in exactly the same way as conventional MLCs but consist of thinner leaves than those optimised for

Figure 1.8: Stereotactic collimator fitted to a conventional linear accelerator.

conventional conformal radiotherapy.

Typically, a conventional MLC leaf width projects a width of 1cm or 5mm at the isocentre whereas those used for stereotactic radiotherapy have widths of 4mm reducing down to 1.7mm at the isocentre. More recently, MLC leaves of 5mm aimed at conventional treatment have become commonplace and allow fields suitable for stereotactic radiotherapy to be produced with no modifications necessary to the linear accelerator prior to stereotactic treatment.

The principles of IMRT have also been applied to stereotactic radiotherapy in order to produce more complex isodose distributions. This is of particular importance as it is common for target volumes to exist close to sensitive structures within the brain such as the brain stem. An extension to this idea is dynamic arc treatment in which the gantry is moved during treatment around the tumour volume whilst the μMLC leaves are also moved to the optimal position to

irradiate the target and avoid any organs at risk. This may be further enhanced by modulating the dose rate and / or gantry speed. This technique is commonly known at Volumetric Modulated Arc Therapy (VMAT)(Cameron, 2005) and may be used to deliver a more complex dose distribution or to produce a more efficient IMRT style plan in terms of the number of monitor units used and treatment delivery time (Bortfeld and Webb, 2009).

1.6 Linear Accelerator Based Stereotaxy at Velindre Hospital

In 2004, the first patients were treated using stereotactically guided radiotherapy at Velindre Cancer Centre Cardiff (VCC). The system currently in use consists of a relocatable mask system, dedicated treatment planning system and μMLC; all of which are manufactured and supplied by BrainLAB[3]. A flow chart of the stereotactic radiotherapy process is shown in figure 1.9.

The mask system consists of a thermoplastic shell moulded for each individual patient. The patient is immobilised by the mask in a fixed position relative to a head ring, which is used to support the mask, and as the reference for the stereotactic co-ordinate system. During scanning, a localising frame is attached to the head ring as shown in figure 1.3, which is used as the basis on which the co-ordinate system is defined during treatment planning. Once scanned, images are transferred to the planning system, co-ordinates are defined and beam arrangements optimised to produce the required dose distribution. For treatment, a target-positioning device on which overlays of the projected beam arrangements are fixed and used to align the radiation beam to the desired direction, replaces the localising box. Beams are defined using a μMLC with a mixture of 3mm and 4.5mm wide leaves projected at the isocentre fitted to a conventional 6MV linear accelerator which is used in treatment delivery. For stereotactic radiosurgery, an invasive frame can be used in place of the mask system.

[3]BrainLAB GmbH, Munich Germany

1.7 Physical Issues in Practical Stereotaxy

In order to deliver stereotactically guided radiotherapy safely, account must be taken of the uncertainties of the treatment process. These are associated with

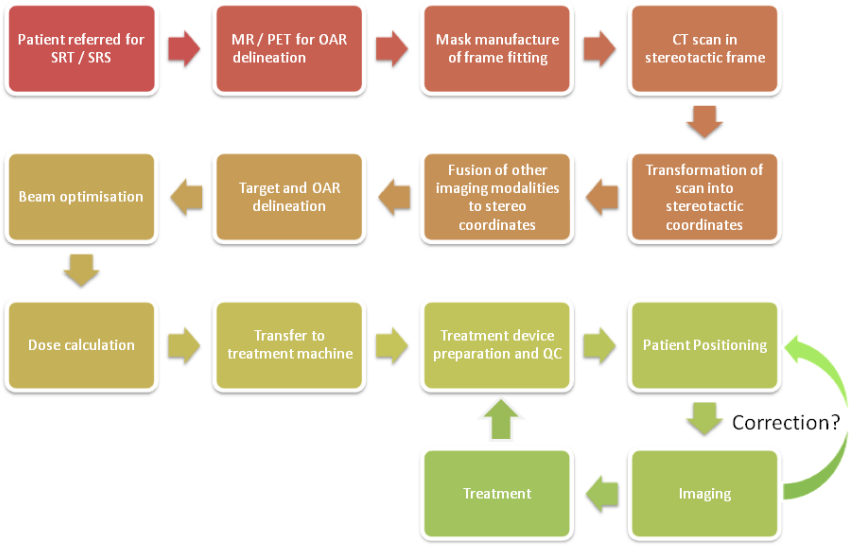

Figure 1.9: Flowchart of scanning, planning and delivery of stereotactic radiotherapy (SRT) and stereotactic radiosurgery (SRS).

the positioning of the patient during scanning and treatment, geometric accuracy of the treatment machine, the calculation accuracy of the treatment planning system dose calculation method and dosimetric uncertainties of data such as output factors used as the basis for any such dose calculation.

The geometric accuracy of the treatment unit itself, the patient immobilisation system and the treatment delivery facility have been considered by a few authors. Warrington and Laing (1994) summarised the quality assurance techniques applied at their centre at the time dividing the component parts into the relocatable frame, CT scanning, treatment planning and machine quality assurance checks made on a monthly basis. Their work concluded that using the *Gill-Thomas-Cosman (GTC)* relocatable frame (Gill et al., 1991),

patient positional accuracy of better than ±1mm could be achieved when setting up the frame using a phantom. With additional uncertainties associated with the rotation of the linear accelerator head and patient couch around the isocentre, and uncertainties due to the accuracy of patient positioning lasers, a maximum additive geometric uncertainty of ±3mm was observed. Adding these uncertainties in quadrature indicated that a 2mm set up margin could reasonably be applied to fractionated stereotactic radiotherapy. The geometric performance of the accuracy of the GTC frame was further examined by Kumar et al. (2005) from approximately one hundred and twenty anterior and lateral portal images of patients undergoing SRT with the GTC frame. For displacements, the total errors in the cranial/caudal direction were shown to have the largest SDs of 1.2 mm, while systematic and random errors reached SDs of 1.0 and 0.7 mm, respectively, in this direction. The corresponding data for rotational errors was 0.78°SD (total error), 0.58°(systematic) and 0.58°(random). The total 3D displacement was 1.8mm (mean), 0.8mm (SD) with a range of 0.3mm to 3.9mm.

The BrainLAB mask system (as used at Velindre Cancer Centre) was investigated in 2010 for repeatability of position accuracy throughout the treatment process (Minniti et al., 2010) by performing serial CT scans of the patient, before during and after treatment in combination with portal imaging of the patient during treatment. This returned further improved results than those reported with the GTC frame with a mean 3D difference of 0.5mm (SD 0.4mm) in patient positioning obtained from CT images of the patient in the treatment position over periods of up to four weeks post the initial scan. Using portal images, a similar magnitude of discrepancy between the isocentre position defined in the planning system and that observed by a subsequent imaging modality relative to patient anatomy was observed. This result is particularly impressive as the reference images were required to be generated outside of the stereotactic planning system, which did not have the capability to export digitally reconstructed radiographs.

The accuracy of stereotactic body frames was investigated by Wang et al. (2006a) in a work which summarised the commissioning and quality assurance of the entire stereotactic system supplied by Radionics[4]. Their investigation into the geometric accuracy of the system indicated that objects within a fixed phantom,

[4]Integra Radionics, Inc.,Burlington, MA 01803 USA

localised using the body frame, could be localised to an accuracy to a mean difference of around 0.6mm (standard deviation approx 0.5mm) in all directions. As with other phantom studies, this result does not include variation in the position of target structures due to changes in patient anatomy or movement of the patient with respect to the stereotactic frame which are more likely in areas outside the cranium.

Wang et al. (2006b) also considered the performance of the stereotactic micro μMLC used to collimate the fields to those required by the planning system including measurements of the leakage through the μMLC leaves, which was found to be similar in magnitude (1.4%) to that seen in conventional MLCs. As a test of the calculation performance of their system, Monte Carlo simulations were performed using the EGS-4 (Nelson et al., 1985) Monte Carlo system in combination with a number of sources describing the radiation incident on the μMLC. Despite not completely transporting the radiation through the μMLC, this study found good agreement between simulated and measured results. A similar study by Cosgrove et al. (1999), for the BrainLAB μMLC indicated leakage through and between the leaves similar to that reported by Wang et al. (2006b).

Dosimetric accuracy of cranial stereotactic systems has been considered by other authors such as Perks et al. (1999) who considered the dosimetric accuracy of a stereotactic system using the GTC frame to localise a water filled phantom containing a small ionisation chamber and concluded that a difference of 2% between doses calculated by the stereotactic planning system and those measured could be obtained. By its nature, this phantom was homogeneous and therefore these measurements were made in the most favourable of conditions. However, due to the composition of the interior of the cranium being also homogeneous, it is a good indicator of the calculation accuracy possible using a relatively simple calculation algorithm. These calculation situations may not apply elsewhere in the body, such as in the head and neck or lung where stereotactic techniques have been more recently employed. Traberg Hansen et al. (2005) present a comparison of two dose calculation methods of doses planned in extra-cranial stereotactic radiotherapy of the lung. Their study showed a difference of 20% in the doses calculated using the two calculation methods, indicating the problems in dose calculation in this group of patients. The study also looked at tumours within

the liver (a far more homogeneous region of the body), and found negligible differences between the two calculation regimes. These dosimetric difficulties are also likely to be present in the head and neck region where there are similar conditions of tissue heterogeneity to the lung.

Even in the case of homogeneous tissue regions, the dose calculation accuracy of the treatment planning system is dependent on the data input to it. A series of papers by McKerracher and Thwaites illustrate these difficulties. In their first paper, (McKerracher and Thwaites, 2007a) the importance of phantom design was considered. From measurement, they propose that the use of a small plastic top equal in height to the depth of maximum dose can be applied to a small radiation field detector without the need to preserve lateral electronic equilibrium or to measure collimator scatter factors at a depth beyond the range of electron contamination. Although this finding is in contrast to the work of other authors, (Dutreix et al., 1997; Netherlands Commission on Radiation Dosimetry, 1998) their results comparing output factors at the depth of maximum dose (d_{max})to that at 5cm deep show minimal differences of less than 0.2%. Their second paper, (McKerracher and Thwaites, 2007b) dealt with the dependence of detector type and focal source on the measurement of collimator and phantom scatter factors. Using a technique of measuring 'in air' profiles to eliminate volume averaging effects of each detector, several detectors were examined for suitability with the conclusion that several of them can be used for measurement of factors down to fields with dimensions of 1cm. They also investigated the effect of source size on these measurements and showed a large dependence on output factor with the amount of the opening of the primary collimator 'seen' by the detector which can be considered as the equivalent of source size. This is, of course, also dependent on the model of linear accelerator.

A third paper (McKerracher and Thwaites, 2008) discussed the measurement of phantom scatter factors using data obtained from a previous work (McKerracher and Thwaites, 1999a) to show that phantom scatter factors are independent of the linear accelerator design and collimation system even for small fields if a correct measurement methodology is used. A fuller description of the dosimetric issues associated with small fields as used in stereotactic radiotherapy is considered in Chapter 5.

In the case of extra cranial stereotaxy, there are further problems associated with motion of the tumour during treatment, in which case it is common practice to reduce the amplitude of breathing using abdominal compression and breath hold techniques. This can have significant dosimetric effects as shown by Kontrisova et al. (2006) who described how the volumes of healthy lung receiving 18Gy, 15Gy and 12Gy (in a 3x12.5Gy regime) were reduced by at least 20% by restricting beam on time to occur only when the patient was performing a deep inspiration breath hold.

1.8 Study Structure, Aims and Objectives

The aim of this study is to investigate the application of Monte Carlo (MC) methods to stereotactically guided radiotherapy and radiosurgery. The objectives of the study are :

1. To develop and validate an accurate model of the stereotactic delivery equipment
2. To apply Monte Carlo methods to the measurement of doses delivered by small radiation fields
3. To investigate and develop a system of independent calculation methods of treatment planning system dose calculations for stereotactic applications
4. To use the Monte Carlo model to determine the most appropriate treatment tactics and calculation algorithms for extra-cranial stereotactic radiotherapy
5. To investigate and develop a system for the use of electronic portal imaging devices for transit dosimetry in stereotactic radiotherapy

The first objective of the project requires an accurate model of the BrainLAB μMLC used in treatment delivery; once this is complete the model will be validated in areas of low experimental uncertainty and then used in situations where precise experimental measurements are difficult. Following validation of the model, the remaining objectives will be completed by the use of the model within a distributed computing environment.

1.9 Thesis Outline

The structure of this thesis is as follows

- Chapter 1: Introduction.
- Chapter 2: A review of dosimetric methods and a description of the Monte Carlo method, superposition calculation algorithms and the problems associated with small field dosimetry.
- Chapter 3: A description of the distributed computing system used in the investigations and of the variance reduction techniques employed.
- Chapter 4: A description of the development of the Monte Carlo model used throughout the investigation and the measurements made to validate the model in large fields ($>$ 5cm x 5cm) and small field situations.
- Chapter 5: Deals with the application of the above model to small field dosimetry and the particular case of small fields produced using the μMLC and the use of such measurements as an input to stereotactic treatment planning systems and the verification of doses calculated using such systems.
- Chapter 6: Describes the implementation of the μMLC model on an individual patient verification system for cranial and extra-cranial work and discusses the relevance of such techniques to these situations.
- Chapter 7: Investigates the performance of the planning system in calculating doses in areas of high tissue heterogeneity and therefore investigates appropriate treatment techniques such as rotational therapy versus fixed field conformal radiotherapy and the choice of interactive treatment planning calculation algorithm used.
- Chapter 8: Describes a system or routine patient verification systems using electronic portal imaging devices using a Monte Carlo model of the accelerator and imaging device to determine parameters used in generating expected doses from treatment plans.

- Chapter 9: Discussion and Conclusions.
- Chapter 10: Presentations and publications where parts of this work have previously been presented.
- Appendix 1 : Source code of the BLMLC component module.

Chapter 2

Dosimetric Methods

Contents

2.1 Introduction

The purpose of radiotherapy is to deliver a lethal dose of radiation to a tumour whilst sparing healthy tissue. Due to the sensitivity of both tumours and healthy tissue it is essential that the amount of radiation delivered by the treatment can be measured to a high degree of accuracy. Similarly, the algorithms used to calculate doses in radiotherapy treatment planning systems must also have dose calculation uncertainties lower than the magnitude of clinically significant dose increments to tissue.

2.2 Experimental Dosimetry

Radiation, consisting of a beam of photons may be described by determining the number of photons that cross a given area; this is known as the photon fluence. However, for non mono-energetic beams it is more appropriate to look at the amount of photon energy crossing a given area. If a time factor is added to these quantities then the energy (fluence) rate can be determined by calculating the photon energy passing through the material per unit area per unit time. Although it is intuitively simple to describe these quantities, their measurement is almost impossible. Therefore, it is more convenient to describe a radiation beam in terms of the amount of energy it deposits in a medium per unit mass. This is known as absorbed dose.

Direct measurement of absorbed dose is only possible using a technique such as calorimetry. In this method, the temperature rise in a medium such as water or graphite due to interactions of the radiation within the medium is detected. Thus, from a knowledge of the mass of the medium the energy deposited per unit mass, i.e. the absorbed dose, can be determined. However, due to the small amounts of energy imparted to the medium (a typical therapeutic radiation fraction of 2 Gray or 2 Jkg^{-1} would produce a temperature rise of $5x10^{-4}$ degrees centigrade in a kilogramme of water), practical calorimeters are only of use in highly controlled environments such as national standard laboratories. Therefore, other measurement techniques have been developed to accurately measure radiation. Those used within this study are discussed below.

2.2.1 Ionization Chambers

Ionisation chambers are the most commonly used ionising radiation detectors currently in clinical use. These consist of a gas filled cavity surrounding a collecting electrode, held at a different potential to a chamber wall, usually made of graphite or similar material. This is used to contain the cavity within the medium. Photons traversing the chamber produce electrons in the chamber wall, which in turn ionise the gas within the cavity. The movement of these ions, collected by the electrode, produces a current, the magnitude of which is proportional to the amount of ionisation occurring within the cavity. The Bragg-Gray theory (Ma and Nahum, 1991) states that the ionisation produced within a gas-filled cavity (such as this) inside a medium is related to the energy deposited in the surrounding medium and therefore the absorbed dose.

If the thickness of the chamber wall is greater than the range of the electrons produced in the medium, then it can be assumed that the charge collected is a direct result of interactions within the chamber wall. The charge collected can therefore be related to the dose to the chamber wall and, by the application of an experimentally derived correction factor the dose to the medium can be determined. Further correction factors are required to account for the perturbation in the dose due to the presence of the cavity, the volume of gas in the cavity as a result of pressure and temperature variations, recombination of ions within the cavity and the polarity of the electric field applied between the electrode and chamber wall. A system of cross calibrations between local field chambers and dosimetry systems held at national laboratories enables an accurate ($<2\%$) dose to be measured.

2.2.2 Semiconductor and Diamond Detectors

Diode detectors have been used in radiotherapy for some years to measure relative dose distributions such as radiation field intensity profiles, and for 'in-vivo' patient dose measurements. Diodes have the advantage over ionisation chambers in that their higher effective atomic number, and therefore increased absorption allow the use of smaller detecting volumes resulting in a greater spatial resolution than can generally be achieved using ionisation chambers.

Radiation incident on the depletion layer of a p-n junction produces electron - hole pairs which separate due to an electric field applied across the diode, giving rise to a current proportional to the energy deposited within the depletion region. A typical diode consists of a silicon p-n junction held within packing material for ease of handling. Although the active collecting volume (of the order of $0.3mm^3$) is much smaller than that of an ionisation chamber, the current produced within the diode is an order of magnitude higher, making the diode very suitable for routine use due to the much lower energy required to produce an ion pair in silicon (3.5eV) compared to air (34eV) and the far greater effective density of silicon over air.

However, diodes have some disadvantages. Their construction generally requires the use of high atomic number materials in their electrodes and protective housing giving energy and directional dependencies, which must be taken into account when using a particular diode for a particular application (Saini and Zhu, 2007). The energy dependence may introduce errors in polyenergetic beams, particularly in areas outside of the open field where, the deposition of energy occurs from scatter in the head of the machine and from within the patient and phantom. In these positions there are significant differences in the spectrum of radiation at these positions compared to the open part of the beam, which may produce spurious readings as a consequence of the energy dependence of the detector. Gager et al. (1977) described a method to avoid this effect using filtration, but this technique is not able to completely remove the phenomenon. Diodes also have a directional dependence (Jursinic, 2009) that must also be accounted for in measurements. The magnitude of this effect may be as much as 12% but with careful design may be reduced to less than 2% (Jursinic, 2009). Similarly, their small temperature dependence and effects due to changes in sensitivity due to radiation damage must also be considered.

2.2.3 Film Dosimeters

Increases in the optical density of radio-sensitive film (radiographic film) as a result of exposure to ionising radiation can be used in radiation dosimetry with the application of careful data acquisition, scanning using a photo-densitometer and calibration techniques (Pai et al., 2007). The active element of radiographic

film, has a significant content of silver (Z = 45). As the interaction cross section of the photoelectric effect is proportional the between the fourth or fifth power of the atomic number, standard radiographic film is more sensitive to lower energy radiation (where the photoelectric effect dominates) than higher energies where Compton scattering or pair production are the dominant processes. Consequently, if films are calibrated at megavoltage energies using the open part of the field, an over-estimate of the dose may be returned in areas of lower beam energy beyond the beam edges of a radiation field. Furthermore, due to the density of the film, there are directional dependencies inherent in the system, especially when the plane of the film is parallel to the direction of the primary beam. These issues can lead to significant dosimetric errors but film has the advantage over other dosimetric methods of having a very high spatial resolution, down to fractions of a millimetre. This is due to the continuous nature of the film substance and is limited primarily by the resolution of the scanning system used to analyse the data.

Despite the dosimetric difficulties, film can been used to measure isodose distribution to an accuracy of 3% of local dose with a high degree of geometric accuracy. Dosimetry using radiographic film has become less prevalent in recent years, partially due to energy and directional dependencies but mainly due to the transfer of many departments to film-less radiography, in which digital images are captured and used as the basis for diagnosis in place of conventional film. This has left many departments without the facility to process film at all, or with excessive costs and difficulty in ensuring film processors are available and maintained with fresh chemicals, which are a necessity to ensure adequate calibration of the films. Increasingly, departments that have adopted film dosimetry have used radiochromic film (Niroomand-Rad et al., 1998) as an adequate, and in some respects superior alternative.

Radiochromic film is an almost tissue equivalent substance which exhibits a change in colour proportional to exposure to ionising radiation. Consequently, it would appear to have the advantage over standard radiographic film of near energy and positional independence. It also benefits from a high dose range, (10^{-1} Gray to 10^{3} Gray), is relatively insensitive to visible light and requires no chemical processing. Its status as a film dosimeter of choice would appear, therefore, to be well founded. Indeed, the film has been used for several

applications within radiotherapy, Meigooni et al. (1996) showed a uniform dose response across the film to within 4% across the film in one direction but a deviation of up to 15% in the other, due to non uniformity of the light source in the scanner. He also found a variation in the energy response of less than 5% in the megavoltage range. This effect is thought to be due to a combination of the polarisation of the light used to read the films and the polymer structure of the radiation sensitive parts of the film, which may give the film a preferred orientation (Niroomand-Rad et al., 1998). However this experiment was replicated by Zhu et al. (1997) who found no dependence on the direction of the film but proposed methods of applying correction factors to obtain a linear response across the film. The American Association of Physicists in Medicine (AAPM), report on the use of radiochromic film, (Niroomand-Rad et al., 1998) made recommendations concerning the type of scanner used, recommending that:

- red light should be used as this is the wavelength at which peak absorption occurs.
- the orientation of the film should be considered carefully to avoid any polarisation effects such as those described by Meigooni or a double exposure technique described by Zhu should be employed.

Several authors have reported successful implementation of these principles in measurement of doses using this type of film. Bjarngard et al. (1990) measured central axis depth doses of narrow photon beams using the film and found good agreement between doses measured with the film and those simulated using Monte Carlo techniques for large fields but found the agreement diminished as the fields became smaller. Consequently, it was postulated that the difference may be associated with the beam spectra used in the Monte Carlo simulation. It is questionable, however whether this disagreement may be associated with the energy response of the film or set up uncertainties. McLaughlin et al. (1994) used the film in a study of the absolute and relative dosimetry of the Elekta Gamma Knife[1] and found excellent agreement between the data measured using the film and that calculated by the treatment planning system.

[1]Elekta AB, Stockholm, Sweden

A more modern implementation of this type of film technology, known as Gafchromic-EBT film has also been the subject of investigations. Fiandra et al. (2006) found that the new film has a 10x improved sensitivity than that of previous film stock while maintaining the tissue equivalence and energy independence of its predecessor. However, it was also found that a correction for the lateral heterogeneity was still required, but achieved this without the need for a double exposure by employing a light scattering correction factor to each film during processing. Using this method they enabled a dosimetric uncertainty of 3.6% for doses greater than 0.3Gy. Chiu-Tsao et al. (2005) investigated solely the energy response of EBT and other new generation radiochromic films and found that for megavoltage energies the film has no energy dependence within the range of experimental uncertainties.

2.2.4 Gel and Chemical Dosimeters

Energy deposited in a chemical by radiation may produce a chemical change, which may be observed and related to the quantity of energy deposited in the medium. Thermoluminescent dosimeters (TLDs) (Khan, 2010) have been used for many years in routine dosimetry. In this approach, energy stored in the crystal lattice of a thermoluminescent material can be released (by heating) in the form of light, which may be detected and related to the amount of incident radiation. TLDs have the advantage of a relatively high spatial resolution, (depending on packaging) and a high degree of stability. Uncertainties in TLD measurements are of the order of 5% but have, with individual labelling or careful calibration techniques, reduced experimental uncertainties down to 2%.

Fricke gels or fluids are also used, using the phenomenon of radiation-induced oxidation of the Fe^{2+} ions in the ferrous sulphate solution to Fe^{3+} ions. These Fe^{3+} may be observed using spectrophotometry of the dosimeter solution, which detects changes in the absorption of ultraviolet light as a result of the oxidation. The major disadvantage of Fricke gels is the large amount of radiation (>10Gy) required to cause a detectable change.

Poly-Acrylamide (PAG) and BANG (Baldock et al., 2010) [2] gels utilise the radiation-induced polymerisation of the acrylic monomers to determine dose

[2]BANG stands for Bis (N, N'-methylene-bisacrylamide, a monomer used in the gel),

distributions. This works as the polymer chains produced by the radiation, form micro particles by becoming entangled with the gel matrix, which produce a visible change which can be used to quantify the dose distribution. Additionally, this influences the mobility of water molecules within the gel, which consequently changes the nuclear magnetic resonance (NMR) transverse relaxation time (T2) of the water's hydrogen nuclei allowing MRI to be used as the dose read out mechanism.

A recent review (Baldock et al., 2010) listed the advantages of gel dosimeters over other dosimetric methods. The advantages are primarily associated with the fact that the gels produce a 3D dose distribution that can be used to determine the dose delivered by a single or multiple treatment beams, which can be analysed after the measurement has been made.The gels are almost tissue equivalent, suffer from little energy dependence and exhibit no directional dependence. These polymers do, however, suffer from atmospheric oxygen entering them, inhibiting polymerisation and subsequently adversely affecting the sensitivity of the gel.

A significant development in the use of gels was reported by Fong et al. (2001) who manufactured a gel containing ascorbic acid and copper sulphate (amongst other substances) which act together to bind atmospheric oxygen limiting its inhibiting effects.

The main disadvantage of gel dosimetry, however, is the requirement of manufacture by the measuring centre, as few, if any, commercial solutions exist to allow purchase of ready made gels, and the requirement to scan the gels using a MR scanner, although some success has been achieved using an optical scanner as the readout mechanism (Baldock et al., 2010). Despite the advantages of energy and directional independence of a 3D measurement, the use of gel dosimetry throughout radiotherapy has not been widespread, probably as a consequence of the difficulties associated with manufacture and data acquisition.

2.2.5 Dosimetry using Electronic Portal Imaging Devices

Electronic Portal Imaging Devices (EPIDs) have been used for some years in the verification of patient positioning during treatment (Kirby and Glendinning,

acrylamide (another monomer used in the gel), Nitrogen (in which the gel is produced) and gelatine

2006). Fundamentally, they consist of a radiation sensitive flat panel to detect radiation transporting through the patient. The resulting signal or image is related to the radiation fluence incident on the detector. Initially, these systems were based on a fluorescent screen and video camera which have been shown to be suitable for quality assurance dosimetric measurements and patient specific exit dosimetry (Kirby and Williams, 1995; Symonds-Tayler et al., 1997). These authors report an agreement to within 3% when comparing measured doses using the portal imager against those measured using silicon diodes when considering exit dosimetry. Agreement of flatness measurements used in routine quality assurance using the EPID against those taken with a farmer ionisation chamber agreed to within 1.5%.

In recent years these video based EPID devices have been replaced with liquid filled ionisation chamber based devices and those using amorphous silicon as the radiation detector. Ionisation chamber based devices have been shown to have a response to incident dose of approximately $\sqrt{Dose}$, which is almost independent of field size (Zhu et al., 1995). Variations in pixel-by-pixel sensitivity were observed by the same author and, due to the liquid filled nature of the device a gantry angle dependency has also been observed (Chin et al., 2004). Louwe et al. (2004) also investigated the long term stability of such devices, finding that by applying a rigorous quality control procedure a high degree of reproducibility can be achieved.

Amorphous silicon has become the detective basis for the majority of modern portal imaging devices. Use of this technology has improved image quality of the device and eliminated the gantry angle response of the detector. However, the phosphor screen used to generate photons detected by the silicon which creates the image has been reported (Sabet et al., 2010) to introduce dosimetric errors into the device due to the non tissue equivalence of the phosphor screen and scattering of the visible light. Sabet et al. (2010) investigated removing the phosphor layer to avoid these effects and used layers of copper and solid water as build up material. Using this method, they showed that agreement between doses measured using the EPID, and doses measured using conventional devices could be achieved to within 1%. However, due to the requirement to remove the phosphor screen, the practical application of this technique is likely to be limited.

The GLAaS algorithm (Nicolini et al., 2006) for absolute dosimetry successfully applies a calibration algorithm based on the depth of patient or phantom through which the radiation beam propagates, and the field size of the incident radiation. Although relatively complex, the algorithm shows good agreement between doses measured using the EPID and expected results. The position of the retractable arm on Varian EPIDs has also been shown to be an important effect on the dosimetric performance of the imager (Siebers et al., 2004). Siebers et al solved this problem by introducing a uniform layer of lead into the imager to filter much of the back scatter coming from the support arm. The application of this technique produced an agreement between doses measured and expected of less than 1% in the open part of the field. Similar results have been achieved by approximating the geometry of the support arm in Monte Carlo simulations to obtain information which can be later used for dosimetric purposes (Cufflin et al., 2010).

2.3 Application of Dosimetric Methods to Stereotactic Radiotherapy and Radiosurgery

The majority of the above dosimetric techniques have been applied to stereotactic radiation therapy. Ionisation chambers are the basis of all absolute calibration regimes due to the traceability of the dosimetry chain to primary standards so that individual treatment machines can deliver doses to an agreed national or international standard. Even if other dosimeters are used for the calibration of the machine, this would still require a cross comparison at some point to an ionisation chamber to achieve comparison to a national standard. Indeed, due to the large amount of experience of the use of ionisation chambers within radiotherapy physics, it is unlikely that any department with a stereotactic radiotherapy or radiosurgery service will not use ionisation chambers for at least part of their dosimetric commissioning or validation. The calibration chain is well known and the correction factors applied to make an absolute dosimetric measurement are well understood as are the weaknesses of such devices.

Primarily, these weaknesses are associated with the physical dimensions of such devices which tend to be large compared to some of the fields employed

in stereotactic techniques. Measurements in small fields are problematic due to the volume averaging effects of a detector, often large in volume compared to the field size under investigation which may lead to an underestimate of the measured dose. This effect can be overcome somewhat by the use of micro-ionisation or pin point chambers for fields generally down to 1.5cm x 1.5cm (Crop et al., 2009) but these may suffer from noise introduced to the measurement system by the very low output from such a low active volume. Despite uneven fluences across the detector, not invalidating Bragg-Gray theory (Ma and Nahum, 1991), and that stopping powers for small fields have been shown to be the same as for larger fields (Verhaegen et al., 1998; Sanchez-Doblado et al., 2003), it has been shown that the use of reference field stopping powers and perturbation factors may be insufficient in the dosimetry of small fields (Seuntjens and Verhaegen, 2003). Consequently, several authors have investigated the use of ionisation chambers within small fields, using either experimental (Stasi et al., 2004) or Monte Carlo methods (Scott et al., 2008), either arriving at a total correction factor, for the ionisation chamber in the conditions under investigation, or the derivation of a series of adjusted correction factors (Crop et al., 2009).

Perhaps, due to the complexity of the corrections necessary for ionisation chambers, alternatives have been sought. The high degree of spatial resolution, (near) energy independence and possibly angular independence of a silicon diode is an attractive choice for dosimetry in such conditions. The Scanditronix stereotactic field detector (SFD)[3], for instance, offers a very small active volume making it suitable for use in the measurement of beam profiles with high spatial precision and in output factor measurements (McKerracher and Thwaites, 1999a). Solid state detectors have a dependence on temperature and on energy due to the photoelectric cross section being much greater for silicon than tissue equivalent material but correction factors for these may be easily applied and diodes such as the SFD have been widely used in stereotactic radiotherapy and radiosurgery.

Diamond detectors (Heydarian et al., 1996) offer similar advantages in terms of spatial resolution (although not as small as some diode detectors), with energy and directional independence, although there is a dependency on dose rate. Dose rate correction factors are more problematic outside the beam edges during profile

[3]IBA Dosimetry GmbH, Schwarzenbruck, Germany

measurement and, due to the difficulties associated with manufacture, diamond detectors are more expensive. They have however been successfully applied to stereotactic radiation therapy techniques (Pappas et al., 2008; Verhaegen et al., 1998).

Other more novel semiconductor devices such as MOSFETs may also be used, which have excellent responses, independent of dose rate, energy and direction but require frequent calibration (Das et al., 2008). Semiconductor arrays were considered by Pappas et al. (2008) and Manolopoulos et al. (2009) who found that their use solved some of the spatial effects associated with ionisation chambers when measuring relative dose profiles of stereotactic cones.

Film may be used in output factor determination, particularly for small fields but its use is generally limited to the measurement of relative dose distributions in the validation of treatment planning systems either on a systemic or patient by patient basis.

In recent years, there has been a national recommendation within the UK to perform patient specific in-vivo dosimetry on all patients (Royal College of Radiologists, 2008) which is likely to include stereotactic techniques. Conventional techniques such as diodes, which are considerably larger than the SFD may have problems associated with their positioning at the entrance of a small field and their uneven perturbation to the intended dose, which is likely to be made up of one or a small number of fractions. TLDs may suffer from similar positional uncertainties and also the fact that they do not provide a real time measurement of the dose, so that any dosimetric error discovered by such a measurement may only be determined after the treatment has been delivered, which in the case of stereotactic radiosurgery is too late for any correction to be made. Transit dosimetry using EPIDs may be of use in that the large planar detector measuring dose at the exit of the patient does not suffer from positioning errors or perturb the beam incident on the patient. There are however no reports of this being utilised in stereotactic radiotherapy and this will be a focus of one of the investigations considered in this work.

2.4 Dose Calculation Methods

2.4.1 Point Dose and Accelerator Calibration

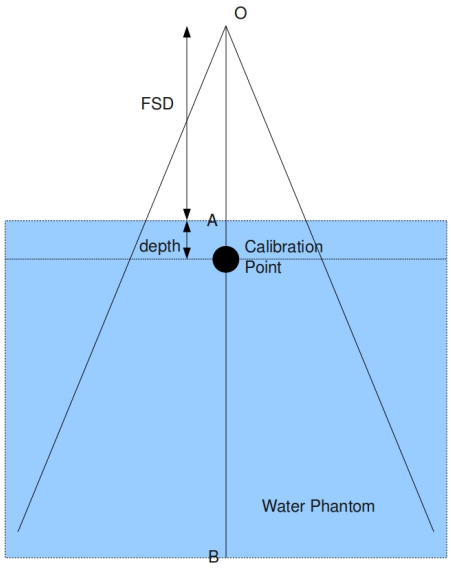

Figure 2.1: Standard calibration conditions.

In general, medical linear accelerators are calibrated to produce a known dose, typically 1cGy, per treatment machine monitor unit at a standard depth in a water or tissue equivalent phantom at the centre of a standard field size, typically 10cm x 10cm at the isocentre. Figure 2.1 illustrates these conditions. Typically, a focus to surface (FSD) of 90cm is used with the ionisation chamber placed at the isocentre, a depth of 10cm within the phantom is used. Other possibilities such as FSD of 95cm with the measurement point at 5cm deep within the phantom, or setting the calibration point to the depth of maximum dose with the surface of the phantom at 100cm FSD can also be used. At this point the

dose delivered to the calibration point can be determined by the relation:

$$Dose = MU \times f_{cal} \tag{2.1}$$

where

- MU is the number of monitor units delivered
- f_{cal} is the calibration factor, defined as the dose per monitor unit, which is generally set as part of a local departmental protocol to be a figure of typically 1cGy/MU. The treatment device is calibrated to deliver this dose during initial calibration of the machine.

At positions away from the calibration point, doses can be determined by the application of other factors, accounting for reductions or increases in dose as a result of a change in field size, a change in depth within the phantom or distance from the radiation source. There are several methods of calculating dose using factors describing changes in dose as a result of changes in the geometry of the radiation. It is usual to calculate the number of monitor units required to deliver a prescribed dose to a point in question using one of the methods described in the following sections.

2.4.1.1 Percentage Depth Dose Method

$$MU = \frac{TD \times 100}{f_{cal} \times \frac{\%DD(r_s)}{100} \times F_{fac}(d, FSD) \times S_c(r_c) \times S_p(r_d) \times F_{ISL}(FSD)} \tag{2.2}$$

where

- TD, is the prescribed target dose in Gray
- f_{cal}, the calibration factor defining the dose per monitor unit, usually in this formalism at the depth of maximum dose, for a 10cm x 10cm field in a phantom placed 100cm from the radiation source.
- $\%DD(r_s)$, the depth dose normalised to the calibration point for the field size r_s defined at the patient surface

- $F_{fac}(d, FSD)$, the divergence factor to account for changes at depth d in the inverse square law characteristics of depth doses at differing $FSDs$
- $S_c(r_c)$, the collimator scatter factor for field size r_c defined by the collimators (i.e at the isocentre depth)
- $S_p(r_d)$, the phantom scatter factor for the field size r_d defined at the measurement depth
- $F_{ISL}(FSD)$, the inverse square law factor to account for changes in radiation intensity with changes in FSD

This was the most commonly used dose calculation technique adopted when the majority of radiotherapy treatment plans were delivered at fixed FSD although the quantities of S_c and S_p were often combined to form a field size factor.

2.4.1.2 Tissue Maximum Ratio / Tissue Phantom Ratio Methods

As isocentric treatments were widely introduced, the above definition of monitor unit calculations was replaced by systems using tissue maximum ratios (TMRs) or Tissue Phantom Ratios (TPRs) in which the depth doses of 2.2 are replaced by either TMRs or TPRs. These are similar functions describing the variation of dose as a a function of depth within the patient or phantom. Whereas depth doses are measured with a fixed source to phantom distance, and therefore contain information concerning both attenuation and inverse square law effects TMRs and TPRs are measured with a fixed source to detector distance with the depth of water or attenuating material between the detector and the source of radiation varied. Consequently, only a reduction in dose due to attenuation with depth is contained within the TPR or TMR curve. This is analogous to an isocentric treatment and therefore produces calculations based on data acquired closer to the treatment conditions and simplifies the calculation expression. TMR curves are normalised to the depth of maximum dose whereas TPRs are normalised to a defined depth such as 5cm or 10cm deep. For the case of TPRs, the expression describing a calculation of monitor units can be defined as

$$MU = \frac{TD \times 100}{f_{cal} \times TPR(r_d) \times S_c(r_c) \times S_p(r_d) \times F_{ISL}} \tag{2.3}$$

where

- TD, is the prescribed target dose in Gray
- f_{cal}, the calibration factor defining the dose per monitor unit often at a depth of 10cm at the isocentre (i.e. the focus to phantom surface distance is 90cm)
- $TPR(r_d)$, the Tissue Phantom Ratio normalised to the calibration point for the field size r_d defined at the calculation depth
- $S_c(r_c)$, the collimator scatter factor for field size r_c defined by the collimators (i.e at the isocentre depth)
- $S_p(r_d)$, the phantom scatter factor for the field size r_d defined at the measurement depth
- $F_{ISL}(FSD)$, the inverse square law factor to account for changes in radiation intensity if the calculation point is not at the isocentre

Very good agreement between doses calculated using these methods and those measured can be achieved with careful measurement of the factors for regularly shaped fields due to the slowly varying nature of each of these factors with field size. For small fields, however, the quantities such as S_p , S_c and TPR are difficult to measure as their variation with field size is quite rapid when the geometric dimensions of the measurement device are similar to that of the field under investigation. Consequently, even for point calculations in small fields, there are large uncertainties, which may prevent their implementation clinically.

For two dimensional or three dimensional planning techniques, dose calculation at several points is required to enable optimum dose distributions to be delivered. In recent years *beam library* methods have been superseded by convolution techniques and, more recently, Monte Carlo techniques have become a more realistic solution in areas of calculation uncertainty. The evolution of these methods is described below.

2.4.2 Beam Library and Clarkson Methods

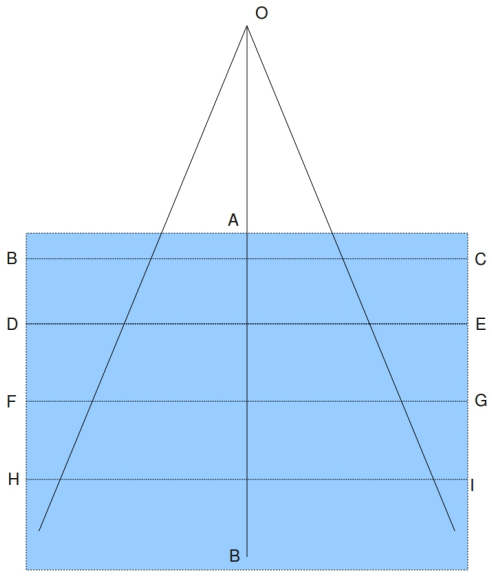

Figure 2.2: Geometry of measurement positions of beam library planning system.

Beam library planning systems were originally described by Bentley and Milan (1971) using a calculation algorithm based on the interpolation of measured data, illustrated in 2.2. In this illustration, a beam produced at the radiation source O is incident on a water phantom. Depth doses are measured along AB, normalised to the dose calibration point at intervals of a few millimetres depending on storage facilities available at the time. In order to calculate dose off axis, beam profiles describing the variation of the beam intensity with lateral distance are used. These vary more slowly with depth than depth doses but may vary rapidly laterally particularly within the penumbral area of the beam. Consequently these are measured along a relatively small number of depths such as BC, DE, FG, but with a high concentration of points in the penumbral region. Each of these profiles is normalised to the central axis of the beam. The dose at any point in the 2D plane can therefore be evaluated

using the following equation:

$$Dose_{beam,d,x} = D_{cal} \times Fout_{fs} \times MU \times \frac{DD_{fs,d}}{100} \times PRF_{fs,d,x} \qquad (2.4)$$

where

- $Dose_{beam,d,x,y}$ is the dose delivered at a depth, d and a radial distance, x from the central axis from a beam.
- D_{cal} is the dose per monitor unit at the calibration point
- $Fout_{fs}$ is the output factor describing the dose variation at the calibration point as a result of the change in field size
- MU is the number of monitor units delivered.
- $DD_{fs,d}$ is the depth dose for a field size, fs at a depth, d normalised to the calibration point
- $PRF_{fs,d,x}$ is the relative intensity a distance x from the central axis at a depth, d for a field size fs normalised to the central axis at the depth, d

At points where data do not exist due to restrictions in data storage capabilities, the quantities $PRF_{fs,d,r}$ and $DD_{fs,d}$ can be obtained by linear interpolation by careful selection of the measurement resolution to avoid any significant dosimetric errors.

By repeating this technique at all points in the patient data matrix, a dose distribution can easily be built up. For a plan involving several beam this process can be completed for all beams and the total dose determined by a superposition of the dose contributions from each beam such that:

$$Dose_{x,y} = \sum_{i=1}^{nbeams} Dose_{i,x,y} \qquad (2.5)$$

following which isodose lines can be plotted for subsequent plan evaluation.

2.4.2.1 Limitations of Beam Library Calculations

The calculations discussed above can be easily understood and implemented using regular field shapes (squares, rectangle and circles) incident on simple phantoms. In practice, tumours are rarely simple in shape and reside in patients with heterogeneous tissue and complex surface geometry. Therefore, corrections are required to the beam library data to ensure an accurate calculation to allow for dose variation caused by these phenomena. These have been described by many authors. Clarkson (1941) proposed a method of dose calculation in which the scattered component of a depth dose may be considered separately from the primary component. To facilitate this the Tissue Air Ratio (TAR) is defined as the ratio of dose at a point within the phantom, D_d to the same point in free space, D_{fs} , hence:

$$TAR_{d,r_d} = \frac{D_d}{D_{fs}} \tag{2.6}$$

where TAR_{d,r_d} is the tissue air ratio of a field of size r_d at a depth d.

Similarly, the concept of Scatter Air Ratio (SAR) may be used to describe the amount of scattered radiation within a field, defined as the ratio of scattered dose within a phantom to the dose in free space. This is commonly obtained by extrapolating TAR measurements to obtain a zero area TAR and subtracting this value from the TAR of the field size in question, which represents the primary dose from the TAR of this field, to obtained the scattered component, hence:

$$SAR_{d,r_d} = TAR_{d,r_d} - TAR_{d,0} \tag{2.7}$$

Using these quantities, the dose may be calculated at points in situations such as that illustrated in 2.3 of an irregular field centred at O with a collimating block. By drawing radii from point O, which may or may not be at the central axis, the field may be divided into elementary sectors, each of which can be characterised by the radius drawn. Therefore, if the shape is divided into 10 radii, for example, then the scattered radiation will be equal to $\frac{1}{10}$ of the SAR for a field of that radius centred at O. By looking up the SAR of each of these radii, an average SAR may be generated, which can be used to generate an average TAR using the relation:

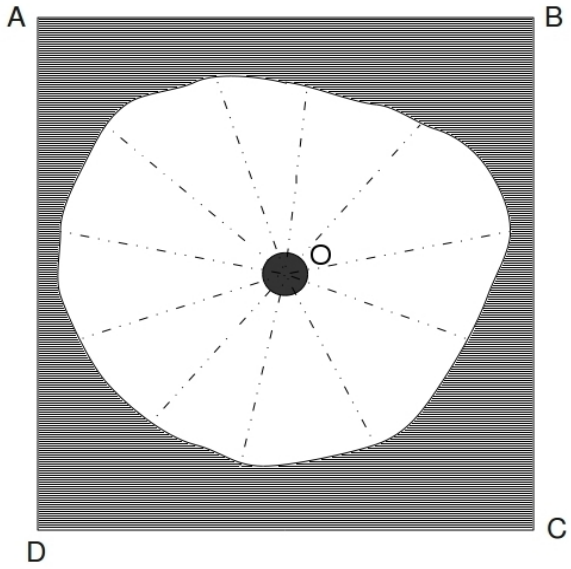

Figure 2.3: Beam's eye view of a typical irregular field.

$$\overline{TAR} = TAR_{d,0} + \overline{SAR} \tag{2.8}$$

This can then be used in subsequent dose calculations using formalisms similar to that described in equation 2.3; the accuracy of which can be increased by increasing the number of radii used in the $\overline{SAR}$ calculation.

Day (1950) proposed a similar method based around defining the fields into constituent rectangles with similarly good results in a range of circumstances. For treating within the human body, corrections for changes in density are required, especially in areas of large heterogeneity such as in the lung or head and neck. Corrections to the depth dose or similar quantity used in the dose calculation method can be applied, such as those proposed by Batho (1964) utilising ray tracing methods to arrive at average attenuation coefficients subsequently developed by other authors (Siddon, 1984; Cassell et al., 1981) to arrive at more general solutions. Further corrections to the raw beam data are required for the presence of missing tissue compensators (Gray and Smith, 1994), asymmetric fields (Millin and Smith, 1994) and other beam modifying devices. To extend the flexibilities of such systems, methods of generating beam profiles and depth doses have been considered (Chui and Mohan, 1986) but due to the introduction

of uncertainties with each correction and the large amount of data required to obtain the data to generate profiles, depth doses and correction factors, these dose calculation techniques have generally been abandoned in favour of other techniques described below.

2.4.3 Convolution-Superposition Dose Algorithms

The transfer of energy from a photon beam to a medium takes place in two stages. The first stage consists of an incident photon interacting with an atom, resulting in one or more electrons gaining kinetic energy from the photon and moving through the material. The second stage consists of this energy being transferred to further particles in the medium and deposited as absorbed dose to the patient's tissue, or it may escape the patient altogether. A quantity KERMA (kinetic energy released in matter) has been assigned to the energy released in the first stage which can be defined as:

$$K = \Phi \times \left(\frac{\mu}{\rho}\right) \times \overline{E_{tr}} \tag{2.9}$$

where

- K is the KERMA
- Φ the photon fluence
- $\left(\frac{\mu}{\rho}\right)$ the mass attenuation coefficient for the medium and
- $\overline{E_{tr}}$ is the average amount of energy transferred to the electrons by these interactions

In radiotherapy, absorbed dose is the quantity of most interest as this is the quantity that describes the amount of energy deposited to a phantom or patient at a point in the medium. As electrons are released in the medium due to the first stage of the process, they lose their energy as a result of ionisation and excitation which takes place at various points along the particles' track and may irradiate some energy as a result of bremsstrahlung. Consequently KERMA and

absorbed dose do not necessarily occur at the same place. The International Commission on Radiation Units has defined absorbed dose to be:

$$D = \frac{\overline{dE_{ab}}}{dm} \tag{2.10}$$

where

- D is the absorbed dose
- $\overline{dE_{ab}}$ is the mean energy imparted by the radiation to a mass, dm of matter.

In conditions of *charged particle equilibrium* in a medium in which there is no attenuation of the primary beam and there are no radiative losses of energy, the absorbed dose and kerma are equal. It is therefore possible to write:

$$K = \Phi \times \left(\frac{\mu}{\rho}\right) \times \overline{E_{tr}} = \frac{\overline{dE_{ab}}}{dm} \tag{2.11}$$

Therefore, it can be seen that there is a direct relationship between photon fluence and absorbed dose in this unrealistic situation. However, even in a realistic situation, a similar relationship holds; if charged particle equilibrium exists at a point and attenuation is considered, it can be shown that absorbed dose is proportional to KERMA. This relation is in practice almost constant since, in high energy photon beams, the average energy of the generated electrons and hence their range does not change appreciably with depth in the medium. This is illustrated in figure 2.4 in which it can be seen that at any depth beyond the point where electronic equilibrium is reached, the absorbed dose delivered exceeds KERMA due to the interactions causing the deposition of dose occurring further upstream in the beam direction. Building upon this concept of dose deposition occurring in a two phase process, algorithms convolving the primary energy incident on the patient or phantom with a *'kernel'*, describing the energy spread of these secondary particles have been developed. These produce a more general solution to dose calculation and are able to calculate dose distributions in as wide a variety of beam modifying devices, tissue inhomogeneity and field irregularities as currently used in external radiotherapy.

This can be a achieved using a quantity $TERMA$, which, is similar to $KERMA$ but describes the total energy released to the matter per unit mass

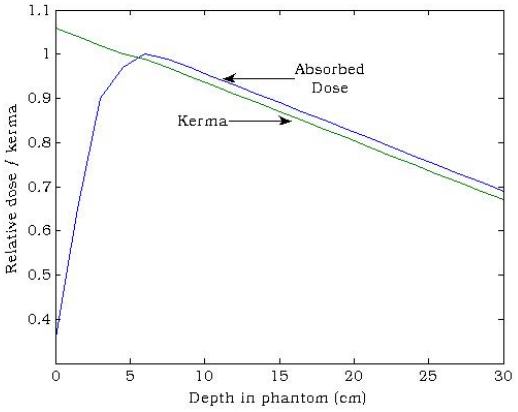

Figure 2.4: Representation of the variation of absorbed dose and $KERMA$ with depth.

and can be described as:

$$T_E = \Phi E \left(\frac{\mu}{\rho}\right) \tag{2.12}$$

where E is the energy at a the point of calculation.

This quantity can be used to determine the dose deposition resulting from scattered particles transporting energy away from the initial interaction site. Consider the situation of figure 2.5 in which a photon enters the patient, interacts at x' and transports dose to x. For a primary photon fluence of Φ with an energy spread function of G_T, the dose $D(r)$ in a volume v can be described as

$$D(r) = \int_v \Phi(x') G_T\left(x - x'\right) d^3x' \tag{2.13}$$

The energy spread function, G_T, includes energy from charged particles (positrons and electrons) produced from primary, secondary and multiple scatter photon interactions and as written $(G_T\left(x - x'\right))$ relates to the dose deposited at x due to a unit fluence at x' including factors converting photon fluence to energy per unit mass by the inclusion of the mass attenuation coefficient $\left(\frac{\mu}{\rho}\right)_0$ multiplied by the beam energy. Therefore, for a mononenergetic beam of energy E_0:

$$G_T\left(x - x'\right) = \left(\frac{\mu}{\rho}\right)_0 E_0 H_T\left(x - x'\right) \tag{2.14}$$

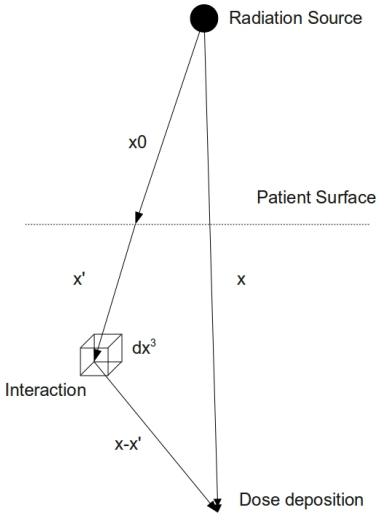

Figure 2.5: Representation of the principle of a photon interacting at x' and transporting dose to x.

where $H_T(x - x')$ is a point spread function representing the fraction of energy released at x' deposited at x. Equation 2.13 can then be written as

$$D(r) = \int_v \Phi(x') \left(\frac{\mu}{\rho}\right)_0 E_0 H_T(x - x')\, d^3x' \tag{2.15}$$

which by combining equation 2.12, becomes

$$D(r) = \int_v T(x')\, H_T(x - x')\, d^3x' \tag{2.16}$$

This, however, is for a monoenergetic beam, but by adding energy components to the fluence or TERMA and dose spread quantities of equation 2.16, and integrating over both energy and volume we have a double integral describing

the dose D at x hence

$$D(x) = \int_E \int_v T_E\left(x', E\right) H\left(x - x'\right) d^3x' dE \tag{2.17}$$

The practical implementation of such a technique, therefore, relies on accurately describing the primary fluence and spread functions. The primary fluence can be readily obtained from a knowledge of the primary beam intensity and functions describing the collimation and beam direction of the incident radiation. Additionally modulation functions describing the perturbations of the beam as a consequence of the presence of a wedge, or other beam altering device may also be included in the calculation. There have been several approaches to the implementation of spread functions, which can be considered as two main types

1. point kernels, commonly known as collapsed cone or type-b algorithms
2. pencil kernels commonly known as pencil beam or type-a algorithms

Collapsed cone algorithms, as described by Ahnesjo (1989) approximate the point spread function by dividing the area over which it irradiates secondary particles into a number of cones covering the full volume of tissue surrounding each point. The dose components over each cone are then *collapsed* to the axis of the cone, as illustrated in figure 2.6. Using this technique, the dose over the whole volume of the patient can be built up and, due to the nature of the algorithm revolving around points within the patient, dose can be tracked across boundaries of materials and doses in the periphery of high density structures surrounded by low density structures, which may be calculated with a high degree of accuracy.

Pencil beam algorithms (Ahnesjo et al., 1992) have the advantage over point kernel methods in that the calculation time is much lower. These work by dividing the beam into a number of pencils as illustrated in 2.7. In this function, the spread function is modelled by the profile of each pencil and the dose at a point calculated by summing the doses deposited from each pencil. The dose from each pencil is scaled according to the relative electron density of the line along the axis of the pencil obtained from the CT data of the patient to obtain the radiological depth to the calculation point. Using this method doses from

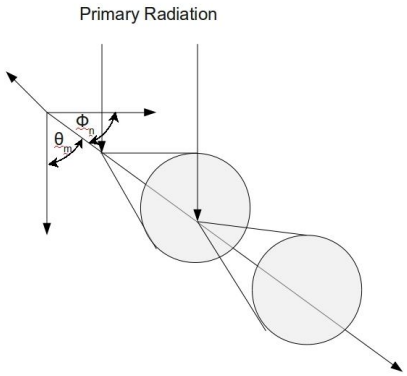

Figure 2.6: Diagrammatic representation of collapsed cone algorithm.

irregular fields can be calculated in areas of tissue homogeneity. However, due to the nature of each pencil having only a bulk density correction being made to the depth scaling, no account can be made of the build up effects in tissue inhomogeneities.

Both of these convolution techniques may be used to model primary radiation and head scatter within the linear accelerator collimator head which may be considered separately and then subsequently added together.

2.4.4 The Monte Carlo Method

In recent years, there has been a significant rise in the use of Monte Carlo methods in radiotherapy physics. This is the result of the implementation of advanced treatment techniques becoming available, such as CT based conformal therapy, Intensity Modulated Radiotherapy and stereotactically guided radiotherapy; all

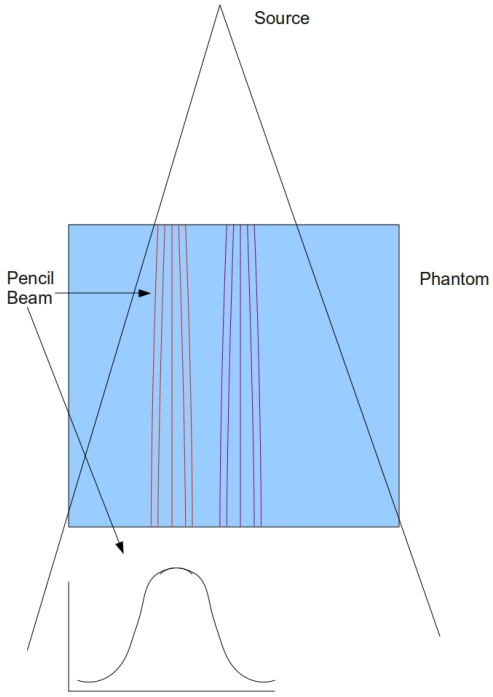

Figure 2.7: Diagrammatic representation of pencil beam algorithm.

of which present situations in which accurate dose calculations using conventional methods are difficult, together with the reduced cost of high performance computers. Verhaegen and Seuntjens (2003) have published a review of the topic describing the evolution of the Monte Carlo technique in radiotherapy from early studies in the 1940s on atomic weapons to its implementation in radiotherapy physics, as has Rogers (2006)

Fundamentally these techniques involve tracking individual particles through the accelerator geometry and patient and by applying a series of random numbers to probabilities of interactions occurring obtained from an understanding of the physics, a simulated dose distribution can be built up.

If the geometric model of the treatment delivery device, the composition of the patient and the physical interactions are represented sufficiently well, and enough particles are simulated to reduce statistical errors to an acceptable level,

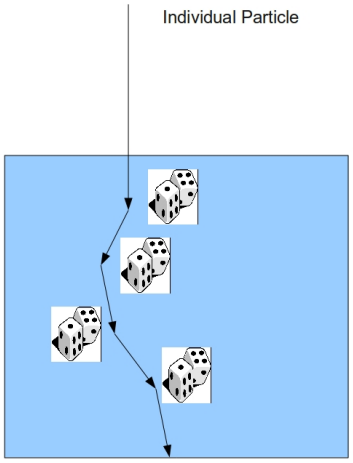

Figure 2.8: Diagrammatic representation of a Monte Carlo simulation.

then doses may be modelled accurately in all dosimetric situations to a degree not possible by analytical techniques. Monte Carlo techniques, therefore, offer many benefits over conventional methods in terms of calculation performance but have the disadvantage of long simulation times and a requirement to know the exact geometry of the treatment delivery machine, which may not always be readily available. The issues of speed have been somewhat overcome using the implementation of variance reduction techniques, which are summarised by Verhaegen and Seuntjens (2003) and discussed briefly in Chapter 3 and by the use of distributed computing techniques (Downes et al., 2009). All of these have contributed to the widespread implementation of Monte Carlo techniques to patient by patient plan verification (Leal et al., 2003), investigations into the efficacy of existing radiotherapy treatment systems (Spezi et al., 2001) and implementation of new radiotherapy and dosimetric techniques (Siebers et al., 2004). Prudent approximations in the physical interactions simulated within

human tissue at therapeutic energies using systems such as the Voxel Monte Carlo (VMC) model (Kawrakow et al., 1996) have reduced simulation times further and made the possibility of interactive treatment planning with Monte Carlo methods a possibility.

The flexibility of the Monte Carlo method therefore makes it of great interest in the verification of stereotactically guided radiotherapy, for various applications such as treatment plan verification, small field dosimetry and portal dosimetry which will be discussed in the following chapters.

Chapter 3

Monte Carlo Codes and Infrastructure

Contents

3.1 The EGSnrc Monte Carlo Code

The EGSnrc Monte Carlo code system was developed out of the EGS4 code incorporating many of the additions developed by several authors following the initial release of the software. The history of EGS4 has been described by Bielajew et al. (1994) and the functions of EGSnrc by Kawrakow (2010).

The key features of EGSnrc are that it allows photons, positrons and electrons to be simulated in any element, compound or mixture using the data preparation package PEGS4, which is used to create data for use by the EGSnrc system using a series of cross section tables for each element. The geometry of the space through which the radiation is transported is defined by user written subroutines which can make use of a series of predefined subroutines to describe planes, spheres and other simple geometry. Within this geometry, tracked particles are transported in steps of random length, the length of which is adjusted near boundaries to ensure accurate modelling of boundary effects. Interactions including Bremsstrahlung, pair production, Compton scattering and photoelectric effect are simulated as well as a wide range of other processes such as positron annihilation, Coulomb scattering etc., enabling accurate dose simulation for the purposes of radiotherapy physics.

3.2 The BEAMnrc and DOSXYZnrc Monte Carlo Codes

The BEAMnrc and DOSXYZnrc codes are based on the EGSnrc codes and provide the user with a set of predefined tools to assemble codes necessary to simulate linear accelerators and other treatment delivery devices for the case of BEAMnrc or by using a voxelised geometry a more general model can be constructed such as that of a patient etc.

Simulation time can be improved using these systems using the built in options such as Russian Roulette and Bremsstrahlung splitting which are discussed briefly in this chapter and described in the relevant user manuals (Rogers et al., 2009) (Kawrakow, 2010)

3.3 Distributed Computing

The Monte Carlo technique relying on a large number of sequential events can be considered as an 'embarrassingly parallel' problem in that the same result can be obtained by sequentially simulating a million particles on a single computer

process or simultaneously simulating a single particle on a million processors and combining the results at the end of all the simulations. In both situations a unique random number is required as the starting point for each particle's transport through the accelerator and patient geometry. The splitting of these jobs requires no communication between jobs and can therefore rely on either accessing a shared memory for input data as in the case of a parallel computing system or in communication between processors over a computer network or similar as is the case in a distributed computing solution (Andrews, 2000).

3.3.1 Local Condor Grid

Within Velindre Cancer Centre, as with most if not all similar institutions an array of personal computers (PCs) used for general office work is installed which, when powered up and not performing any tasks may have redundant processor cycles available for tasks such as distributed computing.

The Condor system (Thain, 2005), is an open-source software package designed to distribute computing jobs amongst a dedicated cluster of computers or amongst idle computers on an existing office or other network. It is therefore suitable for use as the basis for a distributed network at our centre.

Condor was initially installed on approximately 50 computers, situated primarily within the Medical Physics Department which gave approximately 80 cores at an average processor speed of 1 - 1.5 GHz. These computers were generally powered on overnight and therefore gave an almost uninterrupted resource of 16 hours per day as well as any idle time that may occur during the standard working day. Therefore outside of normal working hours there are 1280 hours of computing time available each day. During office hours the available time is difficult to estimate and depends on the settings used in a particular installation. These may be set such that submitted jobs may be run with a similar priority to the machine user's tasks or to suspend execution as soon as the user begins any task. In order to interfere as little as possible with the routine running of the department the latter option was chosen.

Jobs were submitted to the system using the methodology shown in figure 3.1 with 'Perl' scripts used to produce a unique input file describing the input

geometry of the simulation. Each of these input files is identical with the

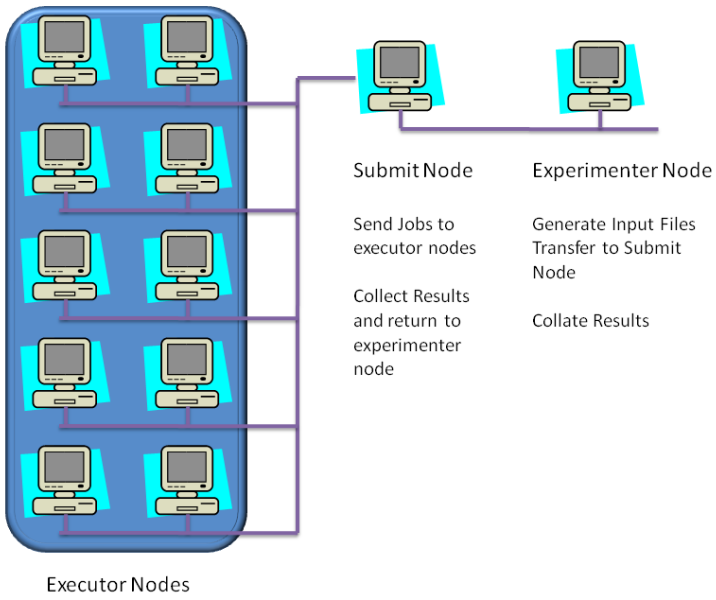

Figure 3.1: Representation of the local Condor grid at Velindre Cancer Centre.

exception of the random number seeds used to begin each simulation. These are then submitted as separate jobs by the 'experimenter' node to the 'submit' node which distributes each job throughout the Condor network, copying the relevant files to each node, collecting any output from each job and returning these outputs to the submit node.

In this system, it is up to the user to generate the input files and to ensure that the correct executables are available and are presented to each executor node. The correct files are transferred by the use of a batch file that is run as each job is submitted.

3.3.1.1 Validation

In order to validate the system depth doses, profiles and output factor measurements were simulated on the system and compared to those simulated on a single machine for the same number of particles and also for the same

amount of time to compare the gain in simulation precision as a consequence of the increased computing power.

Typical results of relative dose and output factors are shown in figure 3.2, which illustrates the agreement between simulations using the local Condor grid and the local machine. In all of the simulations examined there were no differences observed between the running of the simulation using the Condor grid or on a local machine.

A drawback of such a system however is the requirement of the users to generate all of the input files themselves. Although potentially straightforward it was fairly common for errors to be introduced into the system due to the large number of files required. Consequently it was determined to investigate a system for doing this more transparently to the user such as the 'RTGrid' system as described below.

3.3.2 The RTGrid; A Radiotherapy Monte Carlo Portal

The RTGrid (Downes et al., 2009) is a layer sitting above a Condor server that allows the user to present a single input file to the system via a web browser based interface illustrated in figure 3.3, leaving the RTGrid to manage the submission of the correct input files to each of the executor nodes. The system therefore, acts to the user in exactly the same way as a single machine.

Particular tasks can be described by the use of profiles which can be used to determine the particular Monte Carlo executables to use, based on Monte Carlo code or the hardware on which the simulation is desired to run. This can include customised executables as is the case with simulations using the bespoke model of the BrainLAB μMLC described in the next chapter.

The RTGrid can run using Condor or other high performance computing job managers and interface to a number of computing operating systems such as Linux and OSX as well as Windows. During the early stages of this project the RTGrid portal sitting on top of the Cardiff University Condor network became available and was used as the basis for the majority of simulations described in the following chapters.

The Cardiff University Condor network consists of several thousand PCs allowing far more jobs to be run in parallel, compared to the local grid. The use of a web portal also allows access to the grid from anywhere with internet access, enabling easy submission, control and return of the simulations from within the hospital environment.

An instance of the RTGrid was also installed on a local server and attached to the local Condor grid, enabling the benefits of a single point of entry onto the resource to be realised. Although the number of processes controlled by the RTGrid is somewhat limited compared to the Cardiff University Condor pool, the local installation benefits from a much smaller demand on the Condor network compared to that of the university network and allows the possibility to run simulations on phantoms derived from patient anatomy, avoiding data protection issues that may be present even with anonymised data on a more public network.

3.3.2.1 Validation

The system was validated using the same method described in section 3.3.1.1, the output of which is shown in figure 3.4 illustrating the outputs of relative and absolute dosimetric investigations.

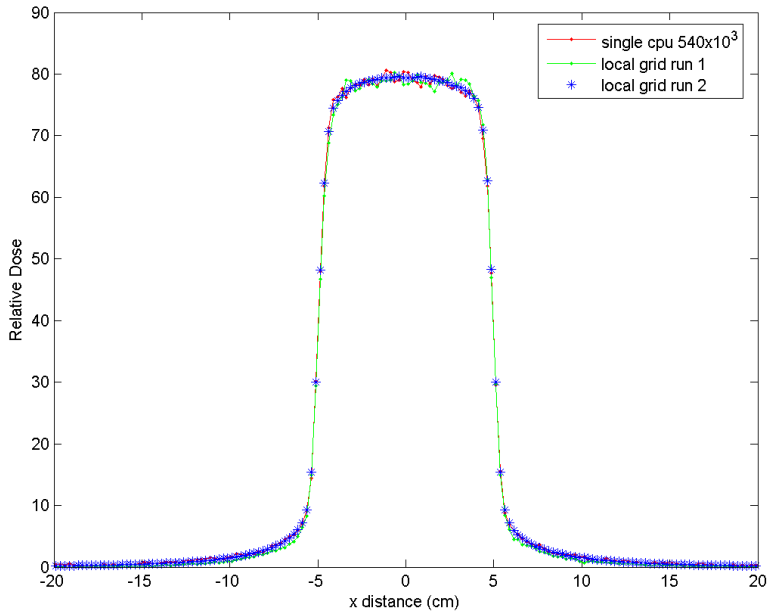

(a) Profiles

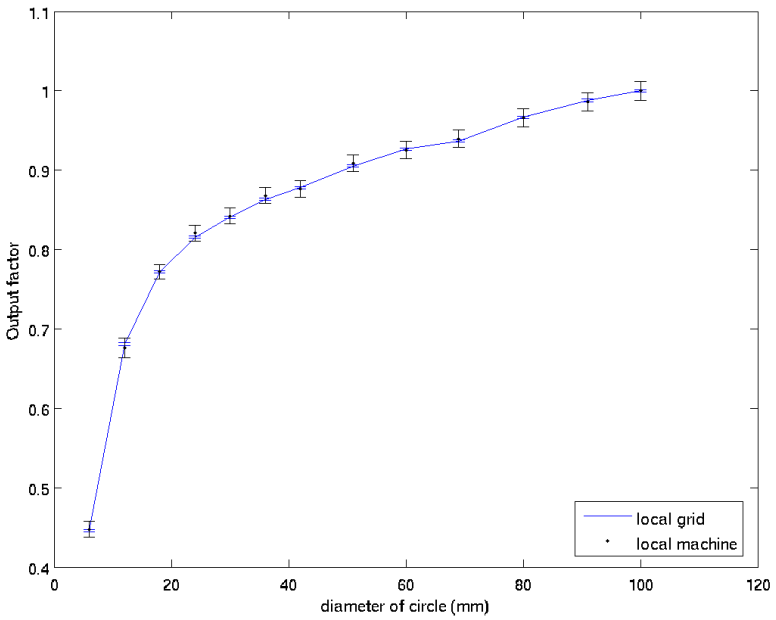

(b) Output Factors

Figure 3.2: Comparison of results of simulation running on a local machine and the local Condor grid.

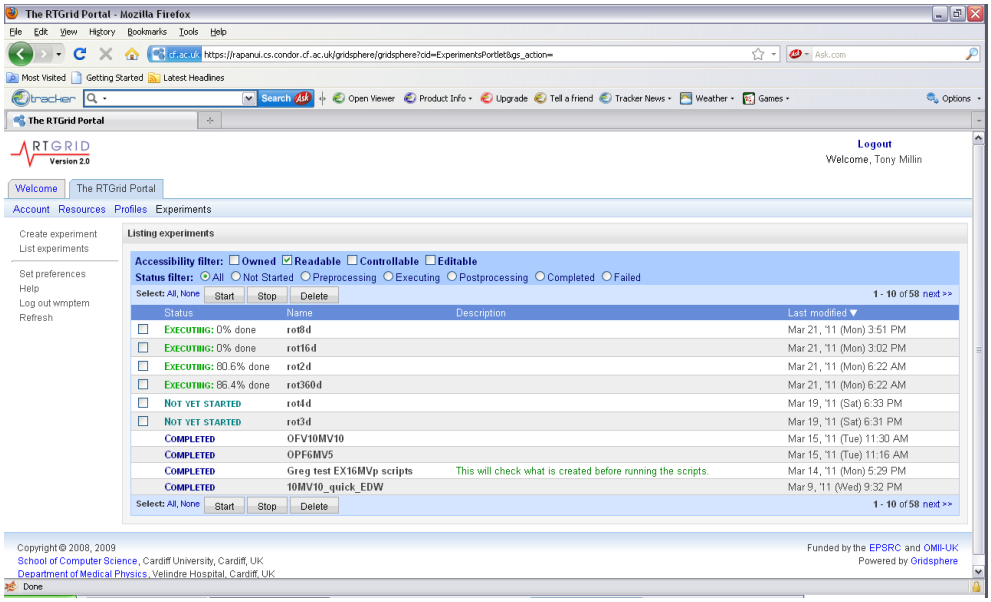

Figure 3.3: Web portal of the RTGrid showing the progress of four running jobs, two to start and four completed.

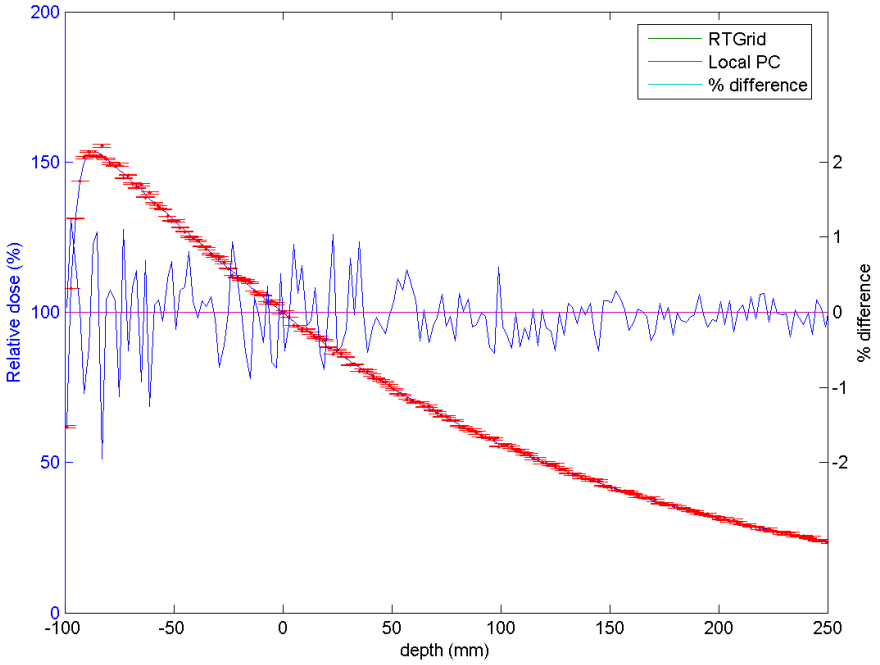

(a) Depth Dose Curve

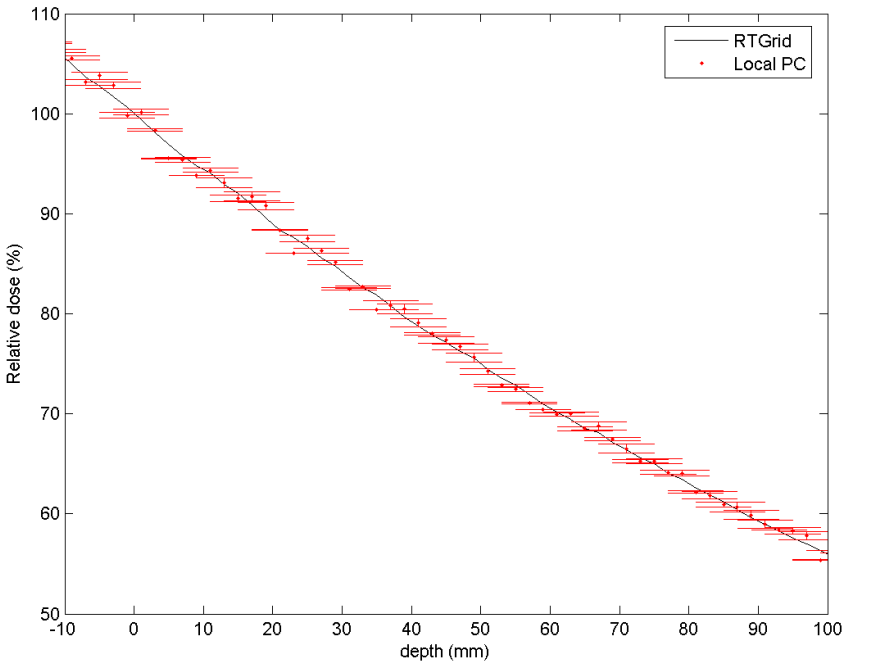

(b) Magnified Depth Dose Curve

Figure 3.4: Comparison of results of simulation running on a local machine and the local Condor grid. Phantom placed such that the isocentre (depth = 0mm on the horizontal scale) is positioned at 10cm deep at an FSD of 100cm

3.3.2.2 Speed and Efficiency

The efficiency of the RTGrid has been discussed by Downes et al. (2009) who showed that significant efficiencies can be obtained by the use of the system with simulation times reduced by thirty times or more. Following the principles described in the paper jobs were divided into approximately 2 hour runs per processor and divided into an appropriate number to obtain the desired statistical uncertainty.

A feature of the system utilising standard desktop PCs is that their specification is likely to vary significantly from machine to machine and therefore run times on one particular calculation node may be significantly longer than those of another. The consequence of this, is that the time to assemble all of the results may be unacceptably long as the last few jobs are awaited by the server. Consequently the RTGrid has a feature allowing jobs to be reassembled after a certain percentage has been completed, as chosen by the user. It was found that setting this figure to 90% returned jobs in an acceptable amount of time. To achieve this with suitable statistical uncertainties required increasing the number of particles in the input file by the appropriate proportion. Another limiting factor of the grid is the storage space available on the server, which with other users utilising it was often only tens of gigabytes in size. For a typical patient simulation, such as those described in Chapter 6, a phantom of 100Mb in size may be produced and therefore a '.3ddose' file (the standard output file of the DOSXYZnrc) of similar magnitude produced. For a plan containing 5 beams and each beam divided into 100 jobs this relates to a storage requirement of 50Gb for all of the jobs when returned. This figure can be reduced by ensuring only relevant parts of the patient are included in the phantom, and by forcing DOSXYZnrc to produce compressed output files (.pardose files) used in parallel processing which can reduce the storage space requirements by around 50%.

3.4 Variance Reduction Techniques

Variance reduction methods can be used to increase the precision of Monte Carlo simulations that can be obtained for a given number of iterations. Within

EGSnrc and BEAMnrc several methods are available such as photon forcing and bremsstrahlung splitting.

Bremsstrahlung splitting improves the statistics of photons produced by bremsstrahlung events within the simulation by splitting each electron a given number, $NMBRSPL$ times with directions and energies determined by an appropriate probability distribution, and given a weight equal to $\frac{1}{NMBRSPL}$. Directional Bremsstrahlung Splitting (DBS) develops this idea by separately considering photons that are *directed* at a region of interest, for example a radiotherapy treatment field and those that are not. As photons are split $NMBRSPL$ times following a bremsstrahlung event, they are each assigned a weight of $\frac{1}{NMBRSPL}$. Each split photon is then individually considered, if it is directed at the region of interest it is tracked with its new weight as in a conventional simulation. Those directed outside the region of interest have their survival determined by comparing a random number to a survival threshold ($\frac{1}{NMBRSPL}$). If the number is greater than this then the particle is eliminated but if not its weight is multiplied by $NMBRSPL$ and is considered to be a *fat* photon. Photons produced from other interactions involving a fat photon, a Compton scattering event for example, will also be split $NMBRSPL$ times and transported or eliminated following the survival mechanism, Russian Roulette.

Russian Roulette survival is also required for *non-fat* photons to undergo a photoelectric, Compton or pair production event and is additionally applied to all electrons liberated as a result of a split Compton interaction. Consequently the number of charged particles within the simulated beam is reduced considerably as a consequence of the application of this technique increasing the efficiency of the simulation of photon dose and fluence but may introduce errors if the charged particle contribution of any simulated doses is of most interest.

3.4.1 Validation

Due to the potential efficiency gains of DBS investigations were made into the calculation efficiency of performing simulations with this technique. Using settings of $NMBRSPL$, splitting radius etc. as recommended by the writers of the code (Rogers et al., 2009) simulations were run with and without DBS for a number of profile and depth dose measurements. Typical results are shown in

figure 3.5. No significant difference was observed between the simulations with the variance reduction techniques applied and with these techniques removed other than could be attributed to statistical uncertainty.

The parameters used in this study for all Monte Carlo simulations unless otherwise stated are listed in table 3.1.

3.5 Discussion and Conclusion

The RTGrid, combined with variance reduction techniques such as directional bremsstrahlung splitting allow for fast simulations of the doses delivered by radiotherapy treatment machines with no reduction in simulation accuracy as a consequence of introducing them into the simulation system.

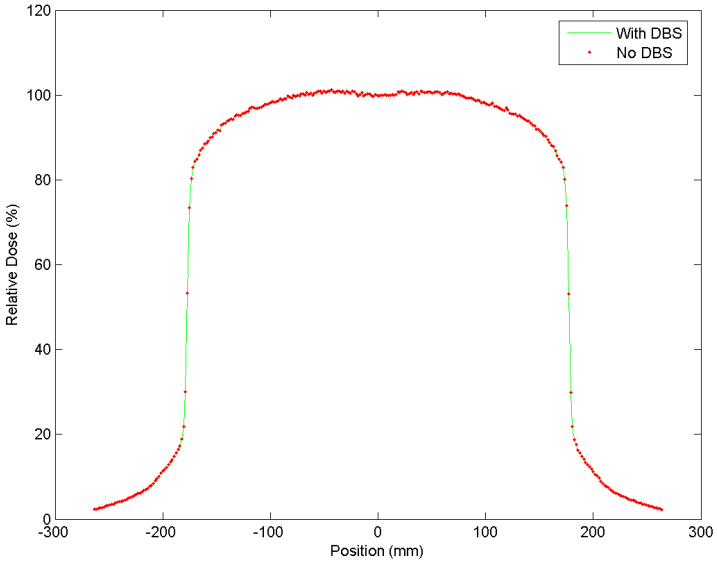

(a) Profiles

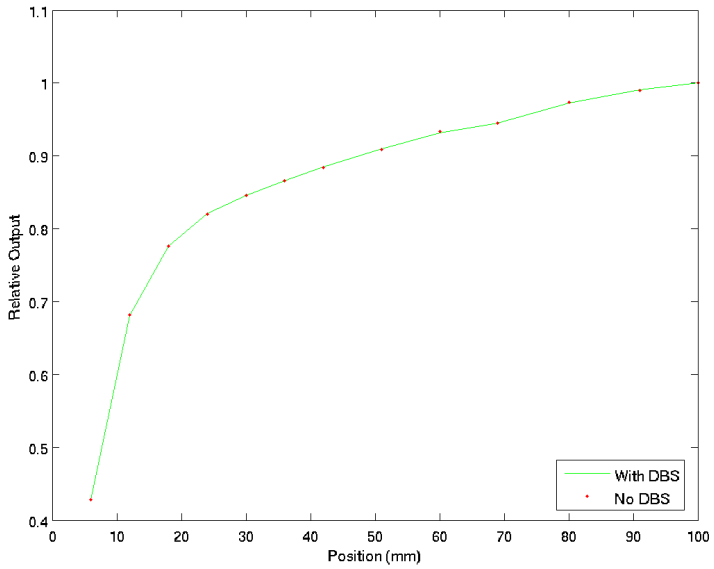

(b) Relative Output

Figure 3.5: Comparison of results of simulation with and without the variance technique DBS, in which electrons undergoing a bremsstrahlung event are split a number of times and then transported with individual energies and directions of each particle assigned according to a probability distribution. therefore reducing the proportion of the number of *wasted* electrons that are transported and never produce *useful* photons in the therapeutic beam. The number of incident particles were adjusted so that similar uncertainties in each case were observed in the DOSXYZnrc phantom

BEAMnrc	
Item	Value
ECUT	0.521MeV
PCUT	0.01MeV
Bremsstrahlung splitting	Directional
DBS splitting field radius	20cm
Source to surface distance	100cm
Brem splitting number	1000
Use rejection plane	60.0cm
CM for e-/e+ splitting	2 (flatfilt)
e- / e+ splitting plane no.	13 (Z=11.1856cm)
Z of Russian Roulette plane	11.14cm
Redistribute of split e-/e+	None
Augmented range rejection	OFF
Brems cross-section enhancement	OFF
Split electrons or photons at CM	none
Electron range rejection	OFF
DOSXYZnrc	
Item	Value
ECUT	0.521MeV
PCUT	0.1MeV
Exclude fat photons from DBS	YES
Range Rejection	OFF
photon splitting number	200
HOWFARLESS	OFF
Global SMAX	5
XIMAX	0.5
Boundary crossing algorithm	PRESTA-I
Skin depth for BCA	0
Electron-step algorithm	PRESTA-II
Spin effects	On
Brems angular sampling	Simple
Brems cross sections	BH
Bound Compton scattering	Off
Compton cross sections	default
Pair angular sampling	Simple
Pair cross sections	BH
Photoelectron angular sampling	Off
Rayleigh scattering	Off
Atomic relaxations	Off
Electron impact ionization	Off
Photon cross-sections output	Off

Table 3.1: Parameters used in the Monte Carlo Simulations of patient plans.

Chapter 4

Monte Carlo Model of The Stereotactic MLC and Linear Accelerator

Contents

4.1 Overview

The machine used for stereotactic treatments at Velindre Cancer Centre was modelled using the BEAMnrc / DOSXYZnrc (Rogers et al., 1995) suite of software. These are Monte Carlo codes based on the EGSnrc (Kawrakow et al., 2010) general codes, optimised for use in radiotherapy. The BEAMnrc code is used to model the geometry of medical linear accelerators, the output of which is commonly used as a source to its sister code DOSXYZnrc (Walters et al., 2005), which enables a voxelised geometry to be used to model patient and other geometry in a manner analogous to the calculation matrices produced by a computerised treatment planning system. In each case, the EGSnrc code is used to simulate the transport of particles within the accelerator and patient or phantom geometry. Many authors have shown good agreement in the modelling of medical linear accelerators using these codes, for example Mukumoto et al. (2009) and Spezi et al. (2001). The system was modelled in the following stages:

1. Modelling of the linear accelerator without the μMLC using standard BEAMnrc component modules

2. Modelling of the μMLC requiring the writing of a bespoke model of the beam geometry

This approach was chosen so that, in considering the model of the accelerator without the μMLC, any errors in the model upstream of the μMLC could be identified prior to the addition of the μMLC components. For reasons described later in this chapter, the μMLC geometry, being more complex than a standard MLC used in radiotherapy, was difficult to model using the BEAMnrc code exactly. Belec et al. (2005), and latterly Kairn et al. (2010), made approximations of the μMLC design and, in the case of the former used small adjustments to the standard BEAMnrc geometry to include the μMLC in their simulations. As an intention of this work was to examine the dosimetry in small fields and other areas where an inexact geometric model of the μMLC may introduce errors into the system, it was decided to produce a new component module which modelled the geometry of the BrainLAB device more exactly. A further advantage of this approach was the ability to optimise the code to increase simulation speed.

4.2 Modelling of the Linear Accelerator

The linear accelerator used, a 6MV Varian 600c, is schematically illustrated in figure 4.1. As is the standard case for a medical linear accelerator the major components used to produce the clinical radiation field are as follows:

- An electron gun, used to produce electrons
- A waveguide (in this case an inline guide) used to accelerate the electrons
- A target used to generate photons primarily from bremsstrahlung interactions between the accelerated electrons and the target
- A flattening filter used to generate a beam of uniform intensity
- A primary collimator to limit the dose to the maximum usable field size
- A monitor chamber used to quantify the amount of radiation produced by the accelerator
- A light field mirror used to project a visual indication of the field area on the patient
- Conventional Collimator
- Reticle

In the case of the machine modelled, there was no conventional MLC attached. As a result of this relatively standard geometry the accelerator could be modelled using standard BEAMnrc components.

4.2.1 Determination of Source Size and Energy

The methodology used to model the linear accelerator is diagrammatically shown in figure 4.2. Although not identical to the procedures suggested by Pena et al. (2007) and Sheikh-Bagheri and Rogers (2002), this approach is similar, relying on a significant quantity of measurements to determine the energy and width of the incident electron beam. By analysing the performance of the model for

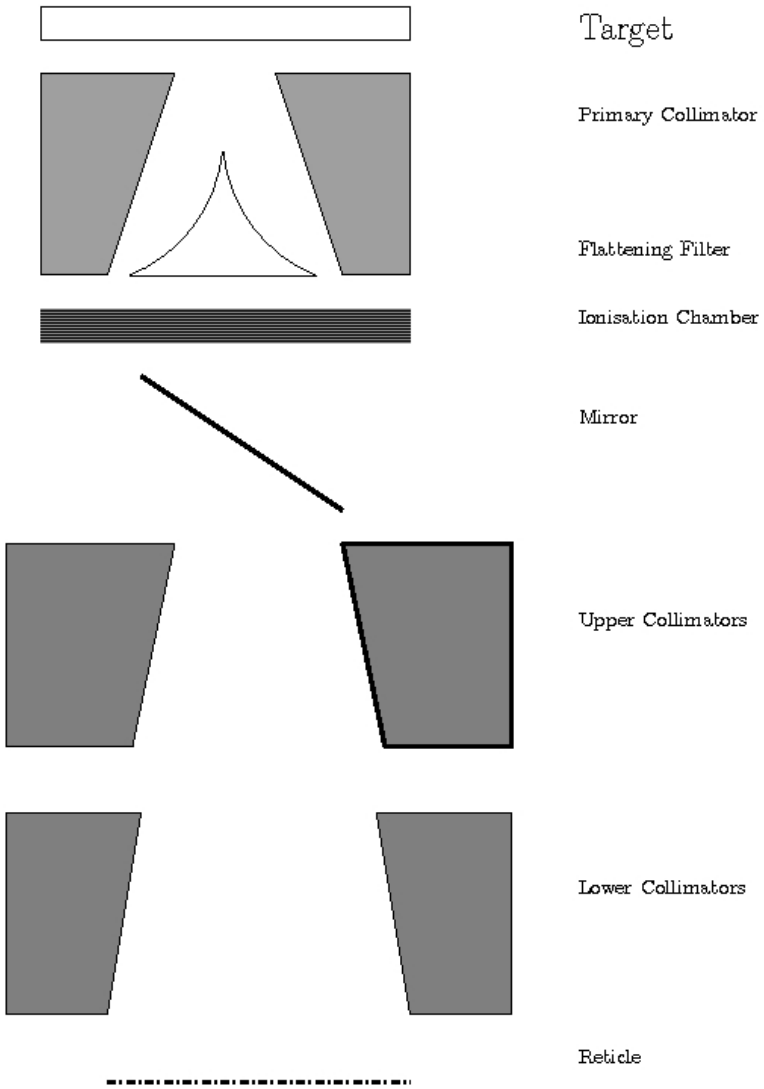

Figure 4.1: Schematic diagram of the components of the Varian 600c linear accelerator. The lower jaws are shown rotated by 90 degrees for clarity.

both large and small fields, it was hoped that an accurate determination of the incident electron beam width and energy could be obtained. This is particularly important when considering the dosimetry of small fields, which are sensitive to changes in these quantities.

A nominal energy of 6MeV and a source width of 1.0mm was chosen as a starting position. Shallow profiles, measured at the nominal depth of maximum

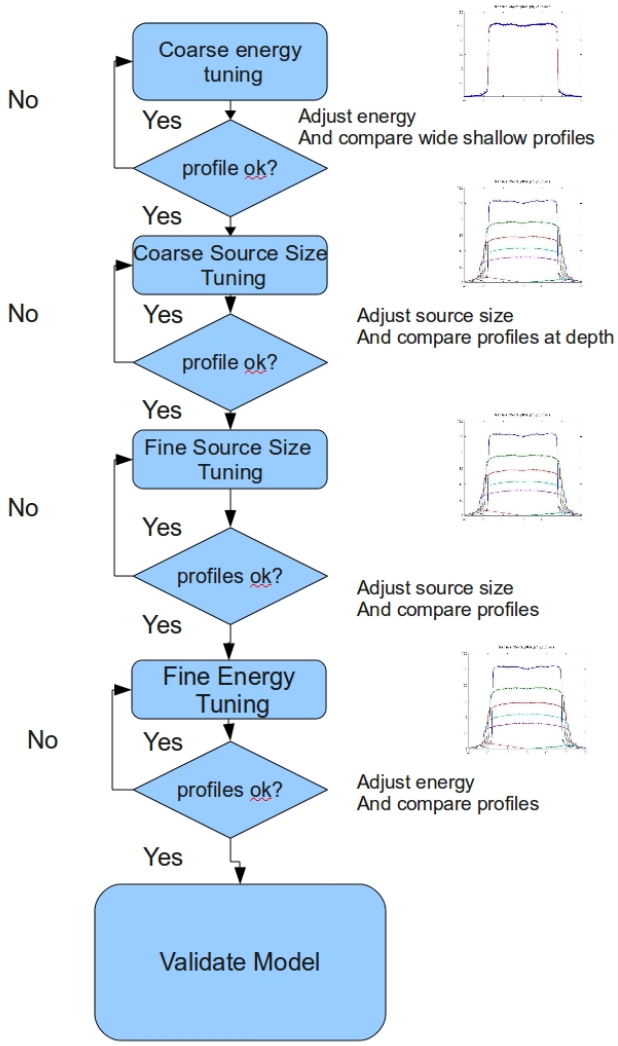

Figure 4.2: Flowchart of process used to determine incident energy and source size of electrons hitting the target used in Monte Carlo simulations of the Varian 600c linear accelerator.

dose (1.5cm) were simulated for a 35cm by 35cm wide field and compared against those measured in a water tank using a Scanditronix [1] photon field diode (pfd). This diode is an energy compensated device with an active area of approximately 2.5mm square, mounted on a higher density backing of tungsten epoxy, used as

[1]IBA Dosimetry GmbH, Schwarzenbruck, Germany

the energy compensation device (McKerracher and Thwaites, 2006). A 35cm wide profile was chosen as this comfortably fitted within the water phantom used for measurements and was wide enough to enable differences in the profile shape caused by incorrect energies and source widths to be seen.

Monte Carlo simulations were performed using a BEAMnrc input file describing the configuration of the accelerator without the μMLC as a source to a DOSXYZnrc simulation using a water phantom. Doses were collected in 2mm x 5mm x 5mm voxels, where the smallest dimension was in the plane of the central axis along the line of the profile under inspection. Simulations using 200 million particles were run, giving typical average uncertainties of 1% in the voxels of interest.

Typical profiles are shown in figure 4.3, which illustrates the comparison of a measured 35cm x 35cm profile and simulated profiles using incident electron energies of 5.20MeV and 6.0MeV, with a full width half maximum source size of 1.0mm.

Each of the curves was normalised to the central axis and, as can be seen from the magnified image in figure 4.3(b) there is a large discrepancy between measured and simulated profiles at the lower energy but good agreement as the simulated energy is increased to 6.0MeV. This process was repeated for a range of energies from 5.0MeV to 7.0MeV in 0.1MeV steps which, indicated by inspection that the closest agreement between measurement and simulation was at a nominal energy of 6.0MeV.

Further comparisons were performed by comparing measured and simulated profiles at a greater range of depths, with each data set normalised to a point 1.5cm deep on the central axis, the results of which are illustrated in figure 4.4 illustrating measured and simulated profiles at depths of maximum dose (1.5cm), 6cm, 14cm, 21cm and 27cm deep. It can be seen that there is good agreement between measured and simulated profiles at the central axis for all profiles, illustrating the insensitivity of depth dose data as the comparator for energy and source size derivation, but there is a deviation between the two at lower and higher energies than the nominal 6MeV incident electron energy, which, although more apparent at the depth of maximum is consistent with depth. Figure 4.4(l) illustrates the average absolute differences between the measured

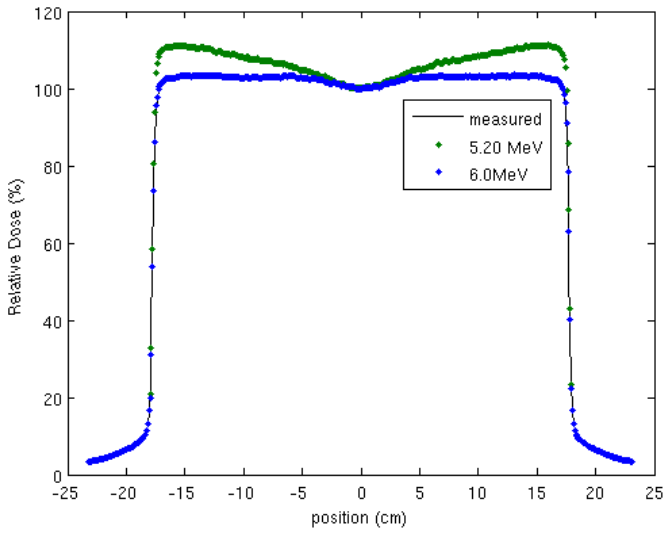

(a) full plot

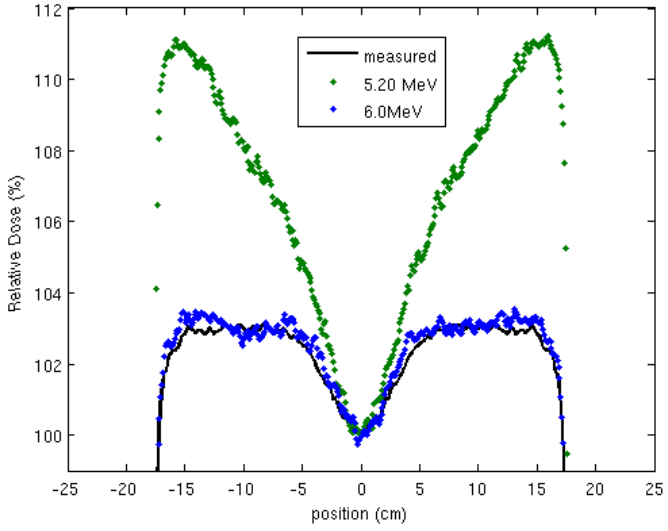

(b) zoomed plot

Figure 4.3: Typical wide shallow profiles for 35cm x 35cm field with varying incident energies (points Monte Carlo simulations, lines measurement.

and simulated curves over the central 90% of the profiles. From this figure it can again be seen that the best match between measurement and simulation of the energies simulated is at 6.00MeV.

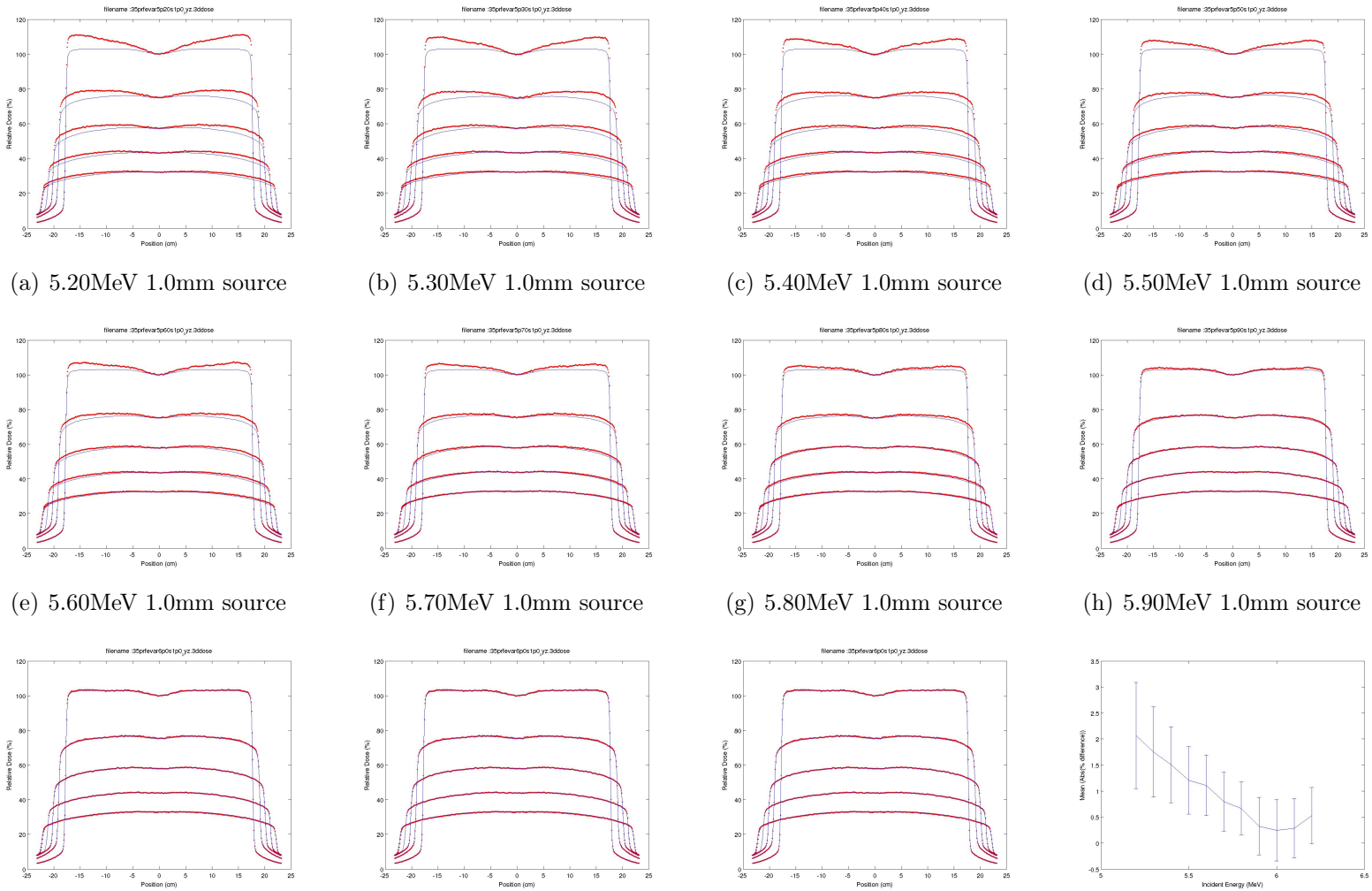

(a) 5.20MeV 1.0mm source

(b) 5.30MeV 1.0mm source

(c) 5.40MeV 1.0mm source

(d) 5.50MeV 1.0mm source

(e) 5.60MeV 1.0mm source

(f) 5.70MeV 1.0mm source

(g) 5.80MeV 1.0mm source

(h) 5.90MeV 1.0mm source

(i) 6.00MeV 1.0mm source

(j) 6.10MeV 1.0mm source

(k) 6.20MeV 1.0mm source

(l) Mean ABS(%differences) v Incident Energy (Error bars are 1 standard deviation)

Figure 4.4: Profiles used in the coarse tuning of incident electron energy (Lines measurements, symbols MC simulations).

An assessment of the source size was made by doing a similar comparison between measured and simulated profiles. Several authors have stated that the source is most accurately modelled using a Gaussian shape distribution (Huang et al., 2005), (Wang and Leszczynski, 2007), which may also be elliptical in nature (Kim, 2009b), having different widths in dimensions orthogonal to the electron beam direction. This was assumed to be correct and, consequently, Gaussian source sizes were investigated independently along both axes of the accelerator.

Beams were initially simulated with a symmetric 0.5mm full width half maximum (FWHM) source and increased in 0.5mm steps to a FWHM of 3.5mm, which is at the top end of source sizes reported by Verhaegen and Seuntjens (2003). The output of these experiments is illustrated in figure 4.5 in which the energy is fixed at the previously determined value of 6.0MeV and the source size varied. There is good agreement in the relative output of each source size along the central axis on each of the profiles.

Despite the relatively 'noisy' profiles it can be observed that an increasingly favourable agreement between measurement and simulation as the source size increases to a FWHM of 1.5mm, which then becomes worse at larger FWHM values. From the plot of differences shown in 4.5(h), showing the mean absolute differences between the measured and simulated profiles over the central 90% of the beam, it can be seen that the appropriate source size is between FWHMs of 1.0mm and 1.5mm.

The experiment was then repeated, increasing the source size in 0.1mm steps until an optimum agreement was achieved. Results of this are shown in figure 4.6 for profiles measured and simulated in the inline (gantry target direction). Although as can be seen from figure 4.6(l) the agreement of measured to simulated profile is fairly insensitive to source width, optimal agreement between measured and simulated results were obtained with a source width of 1.4mm in the inline direction. Setting the source size at 1.4mm in the inline direction the source size in the orthogonal direction was then adjusted and the experiment repeated, increasing the source width from 1.0mm to 2.0mm in 0.1mm steps. In this direction, an optimal source width of 1.3mm was derived.

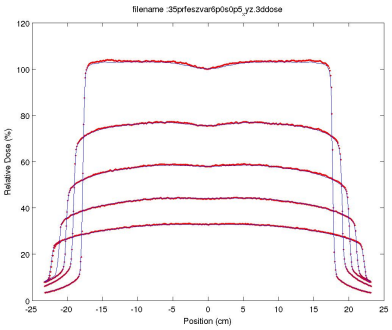

(a) 6.00MeV 0.5mm source

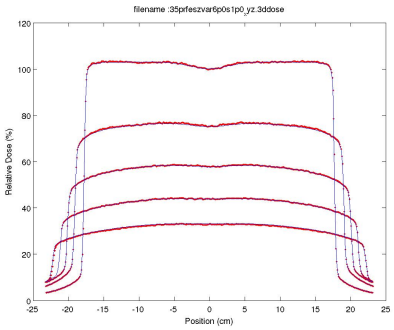

(b) 6.00MeV 1.0mm source

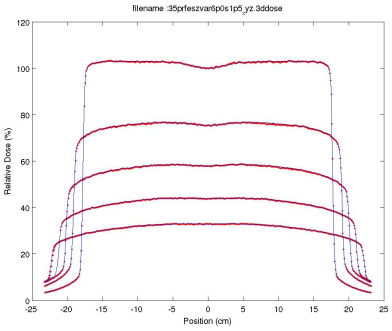

(c) 6.00MeV 1.5mm source

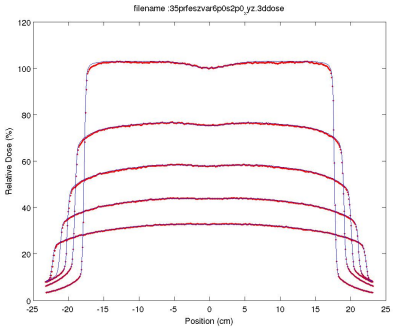

(d) 6.00MeV 2.0mm source

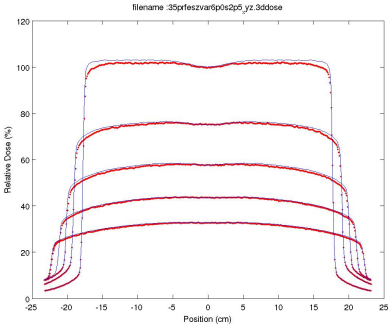

(e) 6.00MeV 2.5mm source

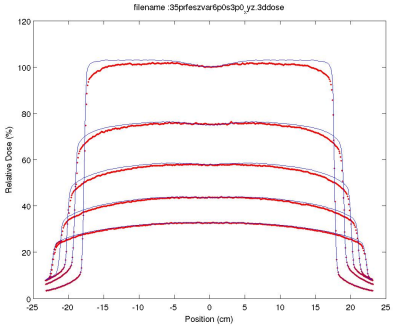

(f) 6.00MeV 3.0mm source

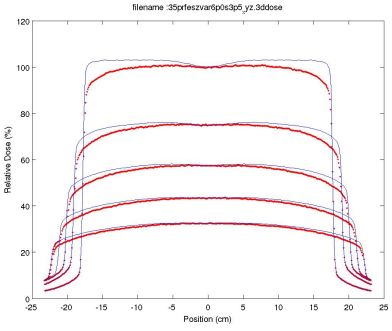

(g) 6.00MeV 3.5mm source

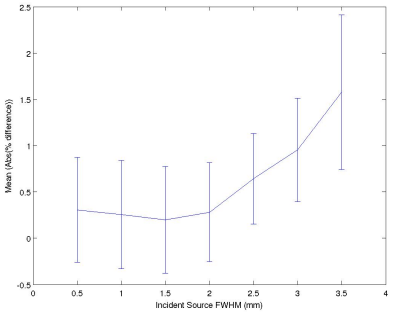

(h) Mean ABS(%differences) v Incident Energy (Error bars are 1 standard deviation)

Figure 4.5: Profiles used in the coarse tuning of source size in inline direction

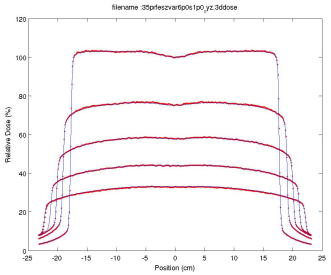

(a) 6.00MeV 1.0mm source

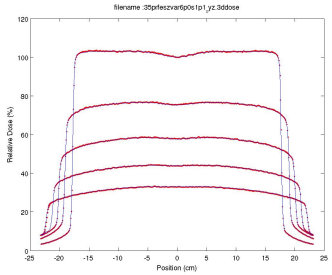

(b) 6.00MeV 1.1mm source

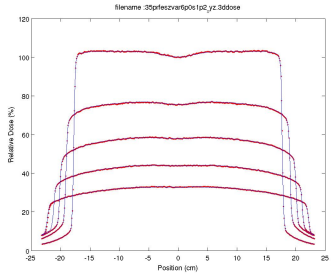

(c) 6.00MeV 1.2mm source

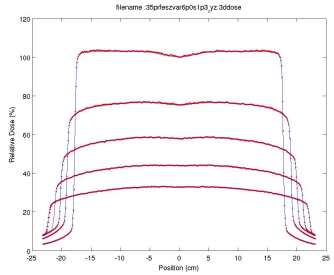

(d) 6.00MeV 1.3mm source

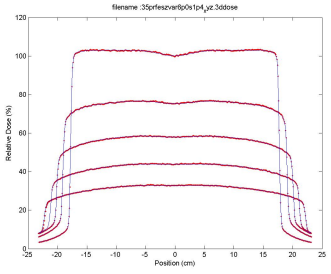

(e) 6.00MeV 1.4mm source

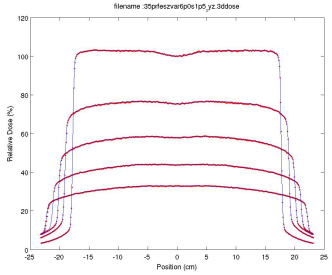

(f) 6.00MeV 1.5mm source

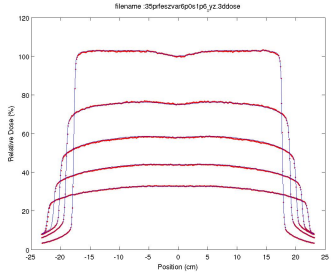

(g) 6.00MeV 1.6mm source

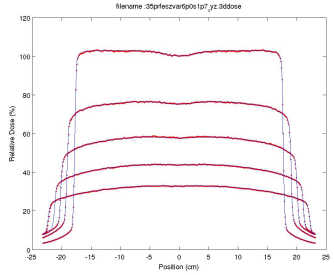

(h) 6.00MeV 1.7mm source

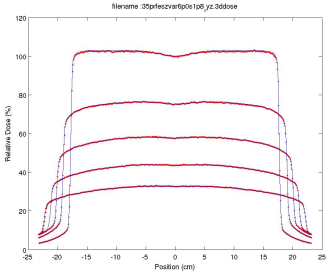

(i) 6.00MeV 1.8mm source

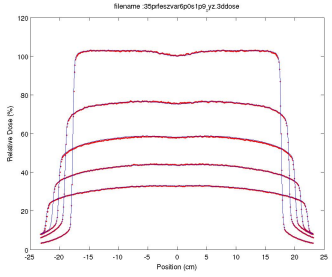

(j) 6.00MeV 1.9mm source

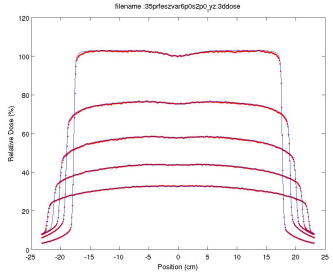

(k) 6.00MeV 2.0mm source

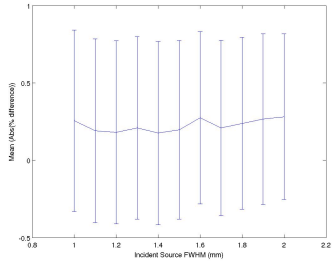

(l) Mean ABS(%differences) v Incident Energy (Error bars are 1 standard deviation)

Figure 4.6: Profiles used in the fine tuning of incident electron source width in inline direction (Lines measurements, symbols MC simulations).

Subsequently, as a significant change in the source size had been made the same test comparing simulated and measured profiles was performed but the incident energy was varied from 5.95MeV to 6.05MeV, in 0.01MeV steps until the best fit between measured and calculated profiles was obtained. These results are shown in figure 4.7 indicating an optimum energy of 5.99MeV. Although only a small change had been made to the incident energy, the source width experiment was repeated in both cross line and inline directions to ensure that changes to the incident energy had not unduly affected the influence of the source size. As may be expected, there were no observable changes in the performance of the model in correctly simulating doses. It was therefore determined that the optimum parameters had been derived, giving the closest fit to measured and simulated data. These were an incident energy of 5.99MeV and a source width of 1.4mm inline and 1.3mm crossline.

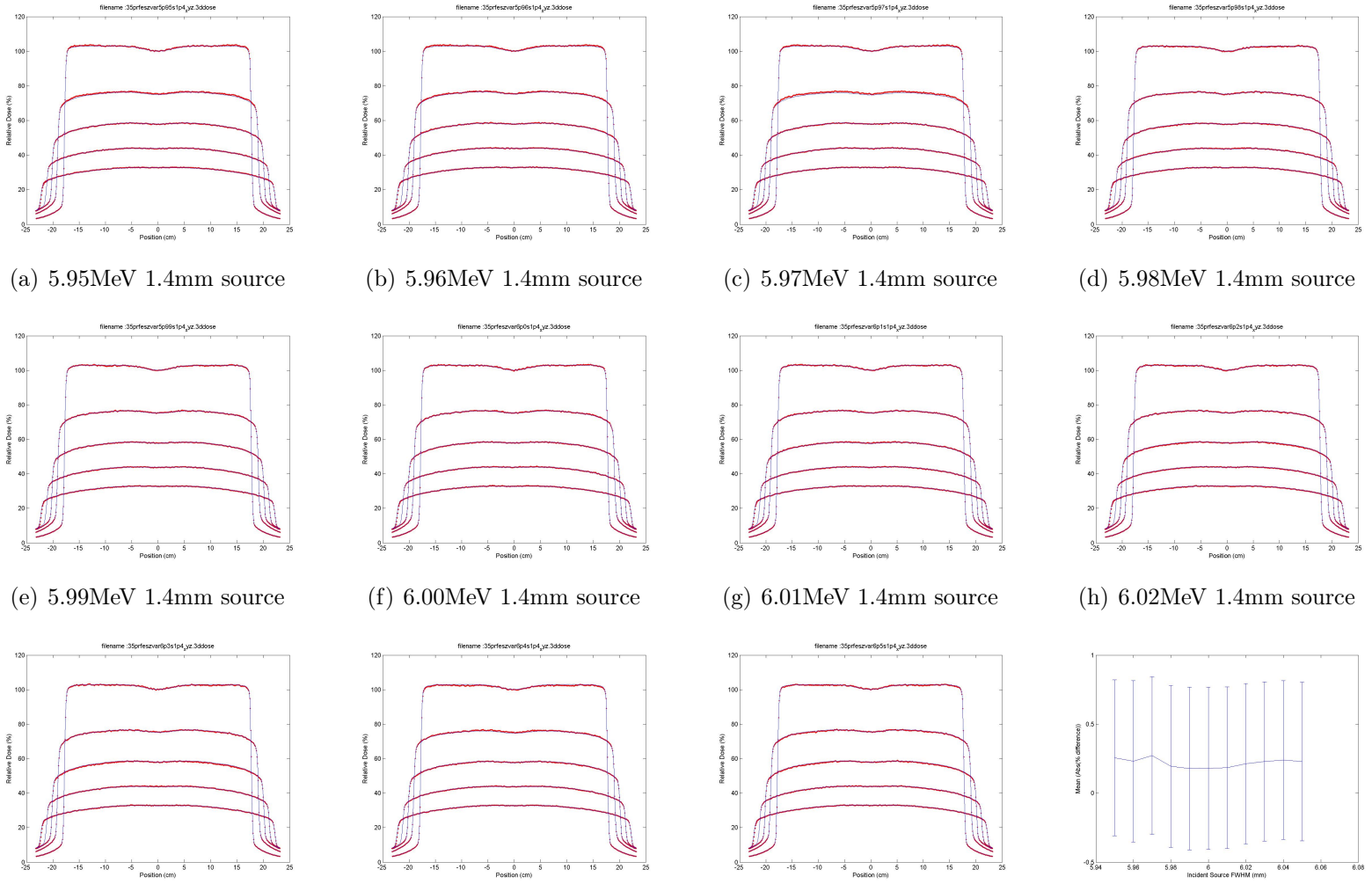

(a) 5.95MeV 1.4mm source (b) 5.96MeV 1.4mm source (c) 5.97MeV 1.4mm source (d) 5.98MeV 1.4mm source

(e) 5.99MeV 1.4mm source (f) 6.00MeV 1.4mm source (g) 6.01MeV 1.4mm source (h) 6.02MeV 1.4mm source

(i) 6.03MeV 1.4mm source (j) 6.04MeV 1.4mm source (k) 6.05MeV 1.4mm source

(l) Mean ABS(%differences) v Incident Energy (Error bars are 1 standard deviation)

Figure 4.7: Profiles used in the coarse tuning of incident electron energy (Lines measurments, symbols MC simulations).

4.2.2 Validation of Model

In order to further validate the determined source and incident energy parameters, profiles were measured and simulated for a variety of field sizes in both directions along the central axis which are illustrated in figure 4.8.

These illustrate profiles of 5cm, 10cm, 15cm and 20cm width square fields within a water phantom placed at 90cm fsd from the source. Profiles at the nominal depth of maximum dose (1.5cm), 5cm, 10cm and 20cm deep were measured using the SFD diode and compared against simulations of the accelerator under similar conditions. As can be seen, there is excellent agreement, between the two data sets, similar to that observed when considering wider profiles for the accelerator without the μMLC attached. This would indicate that doses delivered by the accelerator can be modelled using standard component modules for the conventional parts of the accelerator with accuracies well within the range of experimental uncertainty.

Further validation was achieved by comparing depth doses, measured along the central axis of the accelerator using a RK chamber in a water phantom placed at 90cm FSD. Results of measurements versus simulated doses of the accelerator in this configuration are illustrated in figure 4.9. Again it can be seen that there is excellent agreement between measurement and simulation for the range of field sizes considered.

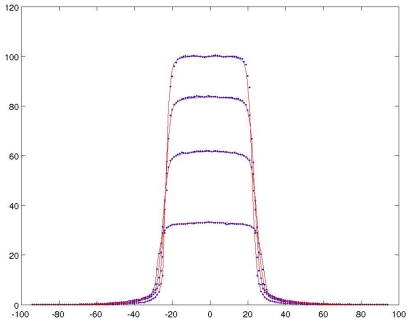

(a) 5cm x 5cm profile in 'x' direction

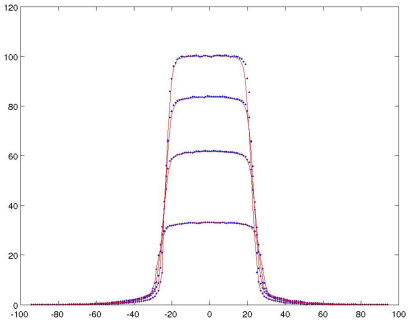

(b) 5cm x 5cm profile in 'y' direction

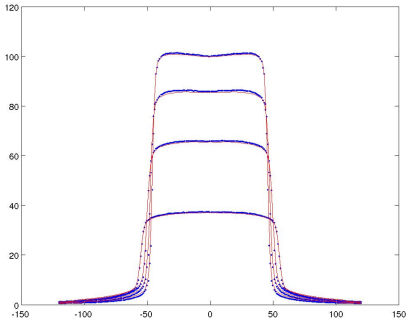

(c) 10cm x 10cm profile in 'x' direction

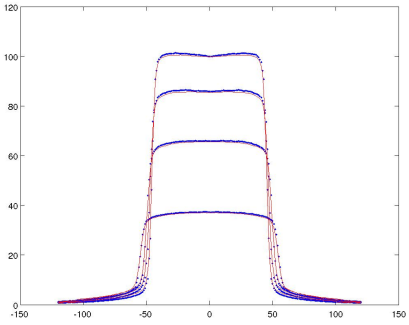

(d) 10cm x 10cm profile in 'y' direction

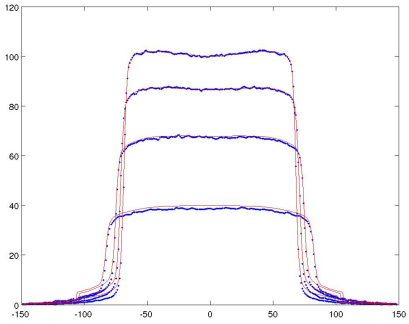

(e) 15cm x 15cm profile in 'x' direction

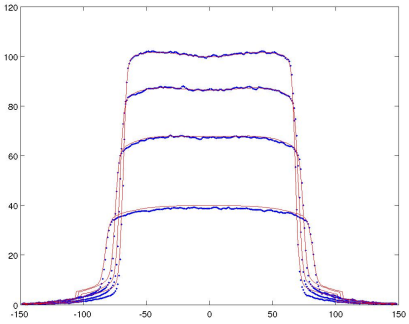

(f) 15cm x 15cm profile in 'y' direction

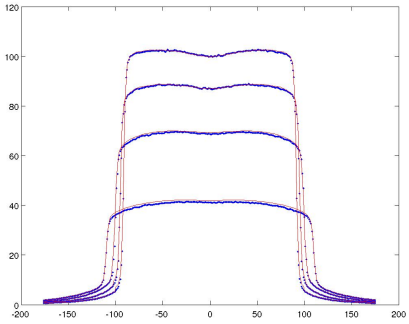

(g) 20cm x 20cm profile in 'x' direction

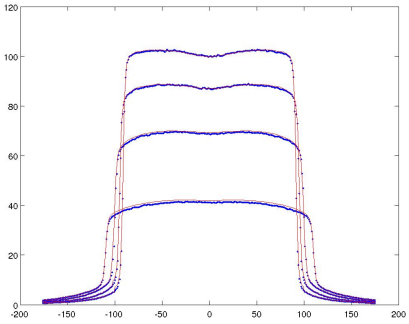

(h) 20cm x 20cm profile in 'y' direction

Figure 4.8: Comparison of varying size profiles at 1.5cm, 5cm, 10cm and 20cm deep at 90cm FSD (lines measured, points simulations).

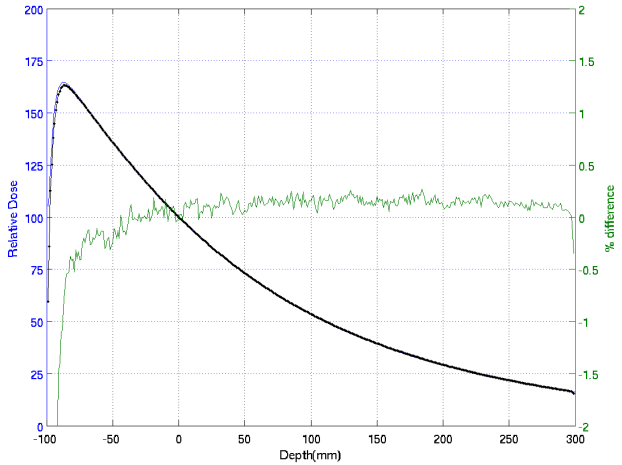

(a) 5cm x 5cm depth dose

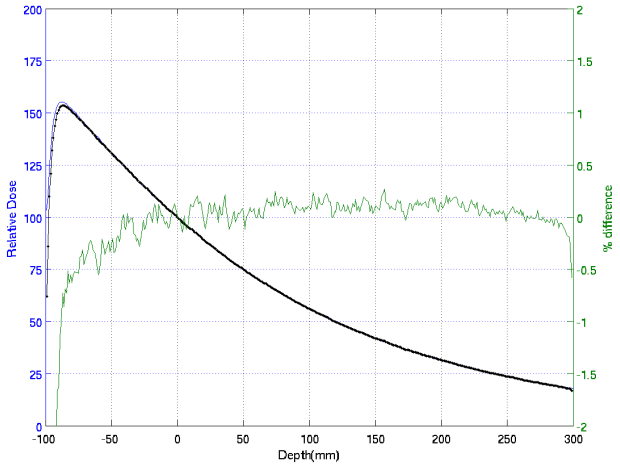

(b) 10cm x 10cm depth dose

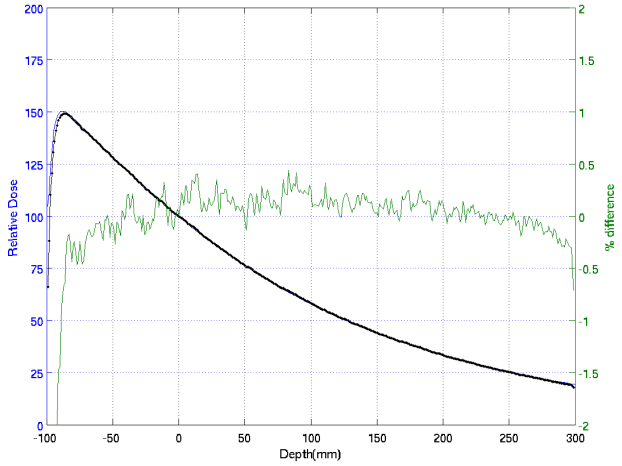

(c) 15cm x 15cm depth dose

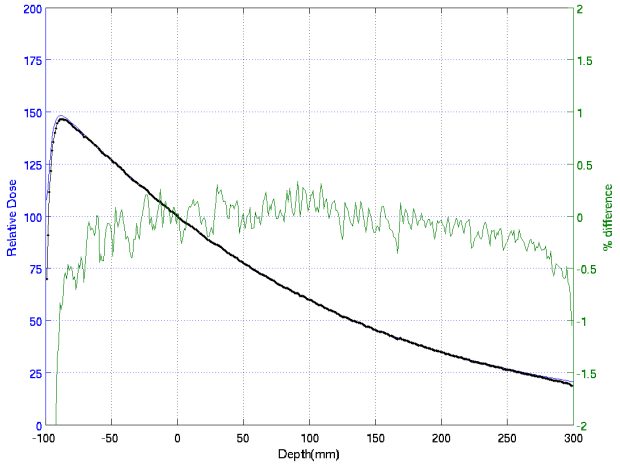

(d) 20cm x 20cm depth dose

Figure 4.9: Comparison of depth doses for various field sizes at 90cm FSD normalised at 10cm deep (lines measured, points simulations).

Relative output factors were then considered by calculating the relative output for a number of standard field sizes (5cm x 5cm, 10cm x 10cm, 15cm x 15cm and 20cm x 20cm). These were derived from simulations of the appropriate field size and compared to measurements made using a standard Farmer chamber within a water phantom made. All measurements and simulations were made at 10cm deep within a phantom placed at 90cm FSD. Excellent agreement between measurement and simulated results can be observed with a maximum deviation between calculated and simulated results well within the simulation uncertainties of around 0.75%.

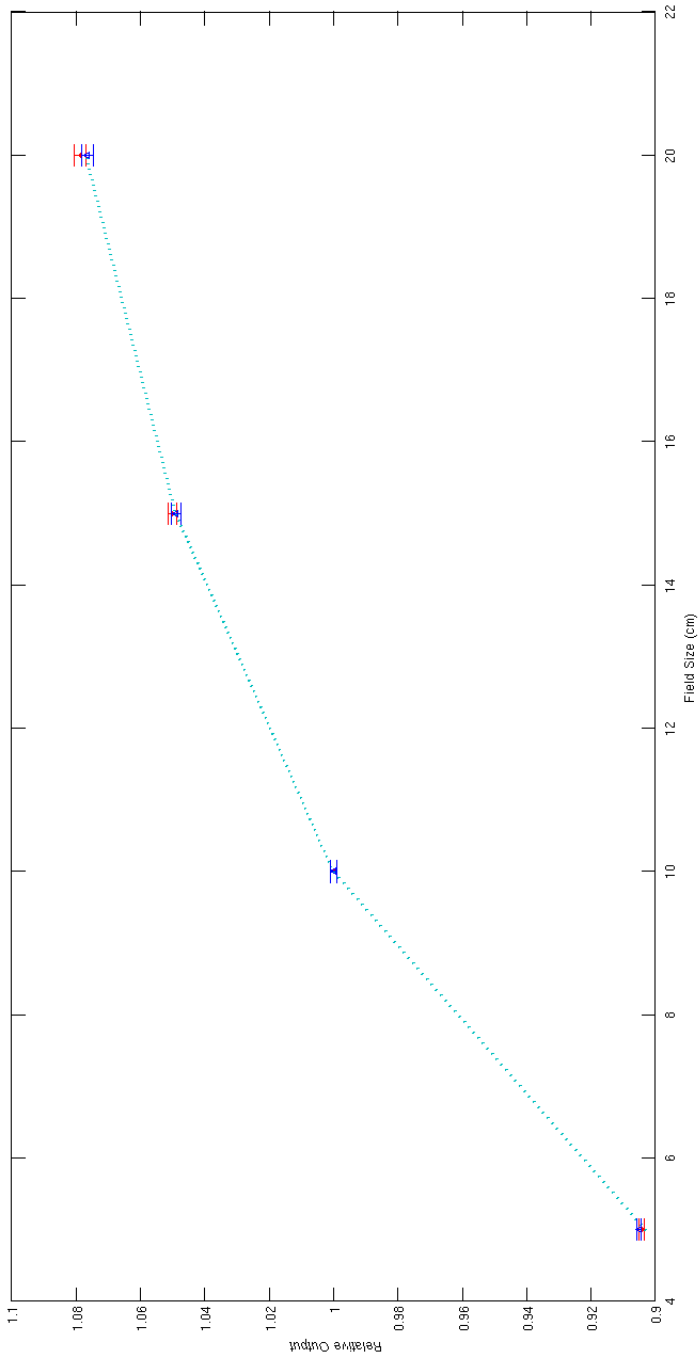

Figure 4.10: Comparison of measured and simulated output factors measured at 10cm deep within a water phantom at 90cm FSD from the beam focus. The line displays the measured values, the circles those obtained by simulation and the triangles those adjusted for back scatter into the monitor chamber as discussed in 4.2.3.2.

4.2.3 Absolute Dosimetric Modelling

The above discussion has concentrated on the derivation of source parameters in order to simulate beams correctly, from which profiles and depth doses were obtained and used in subsequent analysis. Whereas there is clearly a place for these relative dose distributions in verification of treatment planning methods or investigations into new methods, it is also necessary to be able to simulate absolute doses correctly. For standard fixed fields, the requirement to do this may be less important as it is possible, with the application of standard tables, to calculate with some degree of accuracy the output at the centre of a field and normalise measured and simulated results to this point. However, for more complex treatments, such as IMRT, or its analogue in radiosurgery 'Intensity Modulated Radiosurgery' (IMRS), or rotational techniques, this may not be possible due to the extended complexity of these treatment modalities requiring a more sophisticated calculation. In these situations, Monte Carlo modelling comes into its own as the majority of parameters affecting the change in absolute output with changes in beam geometry can be accurately modelled.

However, Liu et al. (2000) have shown that the change in output as a result of beam geometry occurs as a consequence of the following:

- scattered radiation from the head of the machine
- scatter from within the patient or phantom
- backscattered radiation from the collimator jaws into the monitor chamber

The first two of these effects are inherently modelled during a Monte Carlo simulation but the latter, due to the difficulties of analysing both the radiation transporting through the linear accelerator head and scattering back into the chamber is not explicitly accounted for in a simulation. Liu et al. (1997) have shown that radiation backscattered into the monitor chamber increased the absolute output of the accelerator by up to an additional 3% when comparing the output of a 3cm by 3cm field and a 40cm by 40cm field, when the effects of head and phantom scatter are eliminated. Although this is still a small effect compared to other factors, the effect of backscattered radiation into the monitor chamber must be considered for a correct estimation of the absolute dose delivered.

4.2.3.1 Initial Calibration

The initial calibration of the machine was performed by running a simulation of a 10cm x 10cm field using the model described previously with 1×10^9 particles incident on a DOSXYZnrc phantom at 90cm FSD. Nine measurement points of 2.5mm x 2.5mm x 5mm were positioned around the central axis in a 3 x 3 grid and the dose from each voxel combined using equation 4.1. This describes the combination of each dose D sampled m times at position ijk with an uncertainty $\Delta\tilde{D}$. The lth sample can be written as $\tilde{D}_{ijk}^{(l)}$ with uncertainties $\Delta\tilde{D}_{ijk}^{(l)}$ which can be combined to produce a single quantity of $\tilde{D}_{ijk}$ and uncertainty $\Delta\tilde{D}_{ijk}$ as described by Kawrakow (2002), in which samples with the lowest uncertainty have the highest weighting in the combination.

Assuming that the nine voxels under investigation are equivalent a dose per incident particle of $9.637 \times 10^{-17} Gy$ was extracted from the dose matrix produced by the simulation, with an uncertainty of $3.5443 \times 10^{-4}\%$ which was used in the subsequent analysis.

$$\tilde{D} = \Delta\tilde{D}_{ijk}^2 \sum_{l=1}^{m} \tilde{D}_{ijk}^{(l)} \left(\frac{1}{\Delta D_{ijk}^{(l)}} \right)^2 \tag{4.1}$$

where

$$\frac{1}{\Delta\tilde{D}_{ijk}^2} = \sum_{l=1}^{m} \left(\frac{1}{\Delta\tilde{D}_{ijk}^{(l)}} \right)^2 \tag{4.2}$$

The accelerator was initially calibrated to give a dose of 1cGy per monitor unit at the depth of maximum at the centre of a 10cm by 10cm field using a phantom placed at 100cm FSD. This equates to a dose of 0.796cGy at 10cm deep within a water phantom at 90cm FSD from a 10cm by 10cm field (derived from standard output factor tables and depth doses). The conversion factor from Monte Carlo dose per incident particle to dose delivered per monitor unit can then be calculated by

$$f_{cal} = \frac{D_{cal\_point}}{D_{mc}} mu^{-1} \tag{4.3}$$

where

- F_{cal} is the calibration factor
- D_{cal_point} is the dose delivered by the accelerator at the calibration point per monitor unit
- D_{mc} is the Monte Carlo simulated dose per incident particle at the calibration point

In this case this relates to:

$$f_{cal} = \frac{0.796}{9.637 \times 10^{-17}} = 8.2598 \times 10^{15} mu^{-1} \tag{4.4}$$

4.2.3.2 Back Scattered Radiation Into The Monitor Chamber

Any radiation backscattered into the monitor chamber clearly has an effect on the output of the machine and will not be modelled by a Monte Carlo simulation as the code will simply transport radiation through the machine and take no account of any dose back scattering into the chamber causing the machine to switch off prematurely. A correction for this in the absolute calibration is therefore required. This was done using a procedure similar to that described by Liu et al. (2000).

A two phase technique was adopted, the first stage of which was to simulate an accelerator consisting of only a target, flattening filter and primary collimator to generate a phase space file beyond the primary collimator and before the monitor chamber. The absence of any subsequent components ensured that no particles, backscattered from the collimators or other parts of the accelerator, were present in the phase space file, which may have an effect on subsequent analysis. Using the phase space file generated from the first stage of this experiment as an input, the machine was modelled in various configurations of collimator position and the dose scored in the MU1 channel of the monitor chamber, which is used to terminate beam delivery. Using the latch option of BEAMnrc, it was possible to determine the origin of each particle in the chamber. Particles were labelled as being resultant from primary forward radiation, back scattered from the Y collimators (closest to the radiation focus) or back scattered from the X collimators.

The machine was simulated by opening the jaws not under investigation to their widest position and then simulating the accelerator with the jaws moved from their widest position to the smallest, while keeping the opposing jaw at its widest position. From these measurements, it was possible to determine the amount of back scattered radiation transporting to the chamber as a function of collimator position.

Results of this are shown in figure 4.11, from which it can be seen that the effect is largest for the Y collimators (closest to the chamber) compared to that from the lower X collimators. The maximum proportion of the radiation depositing dose in the chamber is approximately 0.7% which is significantly lower than the almost 3% observed by Liu et al. (2000). Their measurements, however, were performed on a Varian 2100c accelerator in which the flattening filter is positioned beneath the primary collimator and, therefore, acts as an uncollimated source of scatter onto the collimators which may account for this. A least squares linear fit was fitted to this data to produce a curve of back scatter factor as a function of collimator position for both X and Y collimators; these are shown on the graphs of figures 4.11(a) and 4.11(b) for subsequent incorporation into methods for determining the dosimetric output of the accelerator.

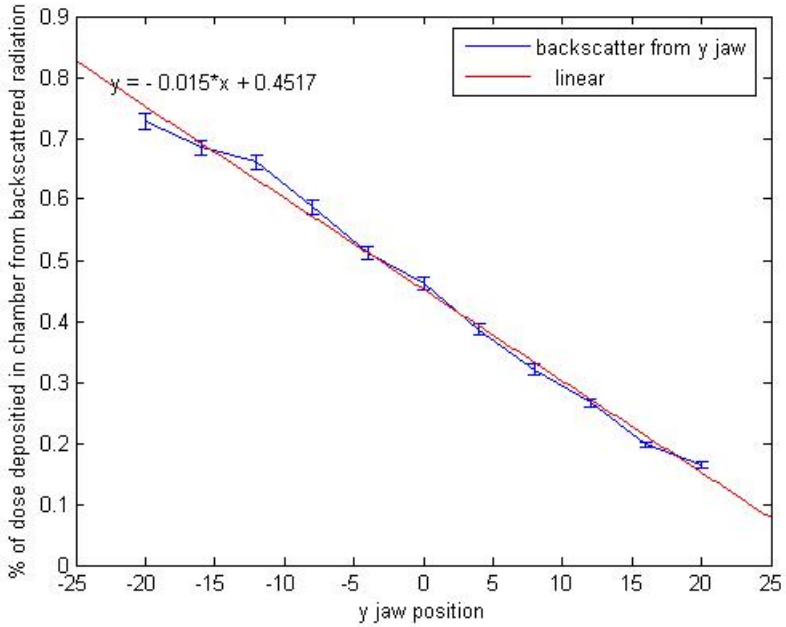

(a) Y Collimators

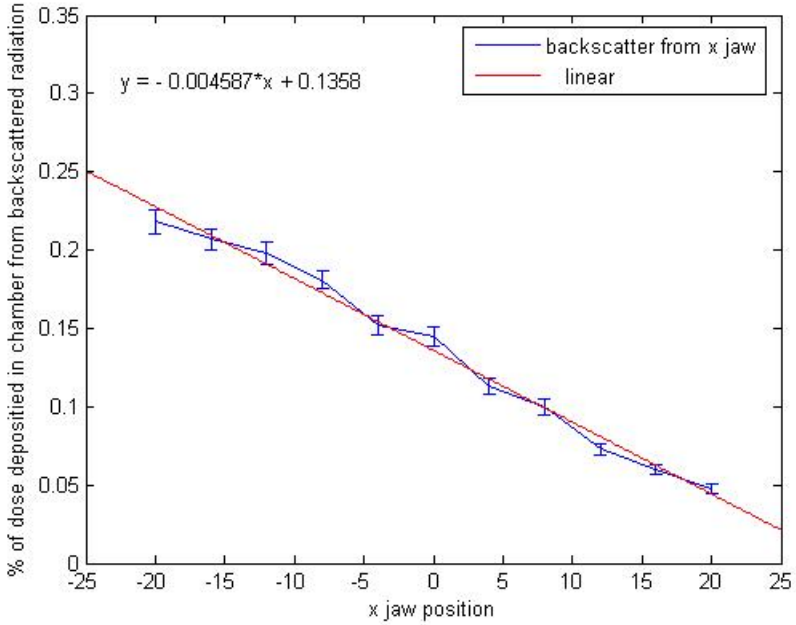

(b) X Collimators

Figure 4.11: Proportion of radiation back scattered into the chamber as a function of collimator position for Y and X collimators.

4.3 Modelling the μMLC

4.3.1 μMLC geometry

Several authors have modelled linear accelerators used in stereotactic radiotherapy. A model of the *cyberknife* stereotactic system has been produced (Deng et al., 2004), as has a dedicated stereotactic linear accelerator (Verhaegen et al., 1998), based on a standard Varian linear accelerator with its collimator jaws replaced by stereotactic cones. Both of these authors report good success in accurately modelling the characteristics of each device compared to measurements. Similarly, conventional MLCs have been modelled by many authors using exact models of the MLC geometry (Heath and Seuntjens, 2003), and approximations (Keall et al., 2001). Belec et al. (2005) reported their work modelling the BrainLAB M3 μMLC, which used an adaptation to the DYNVMLC (Heath and Seuntjens, 2003) used to model Varian MLCs to approximate the more complex geometry of the BrainLAB device.

Unlike conventional MLCs, which generally use a single tongue and groove, the BrainLAB μMLC consists of a large number of tongues and grooves introduced into the device to reduce inter-leaf leakage. Although this could be achieved by a more simple design, its added complexity is required to allow for the small dimensions of the MLC whilst allowing full inter-digitation of the leaves. The design of the leaves is illustrated in 4.12. The multiple tongues and grooves can be seen in figure 4.12(b), which is the main difference between the BrainLAB device and conventional MLCs. Figure 4.12(a), however, also shows that the leaf ends are shaped in a linear fashion with three facets rather than a singularly angled or rounded design more commonly used on other devices.

As a consequence of this complex design, it is not possible to exactly model the μMLC using existing BEAMnrc component modules. The approximation of Belec et al. (2005), based on DYNVMLC component module (Heath and Seuntjens, 2003) allowed the ends of the leaves to be sloped at any angle. A model of μMLC was then constructed using three layers of this module, and were thus it was possible to model the leaf ends exactly. The tongues and grooves of the μMLC could not, however, be modelled exactly and these were approximated by combining the tongues and grooves into a single structure.

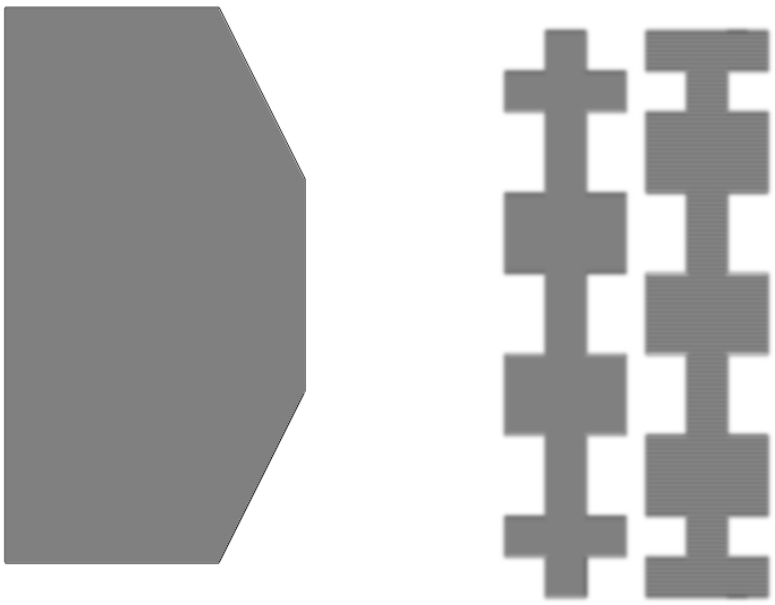

(a) Cross Section Through Leaf (b) End on view of leaves (separated for clarity)

Figure 4.12: Representation of Leaf Geometry of the BrainLAB μMLC.

Using this technique, good agreement between simulated and measured doses was achieved for a number of situations.

Due to the intention in this study to investigate some aspects of small field dosimetry, there is a concern that approximations of the tongue and groove design of the leaves may unduly influence the dose delivered at the centre of particularly small fields. Furthermore, the three layer approach is likely to have a negative impact on simulation time due to the requirement to track particles across unnecessary boundaries, which would be removed by a bespoke model of the μMLC. Consequently, it was decided that a component module would be written to model the leaf design more faithfully than previously, which would remove the uncertainties of doses simulated in the penumbra and in the centre of small fields, with the added advantage of increasing the simulation speed.

4.3.2 BLMLC (BrainLab MLC) - a bespoke model of the BrainLAB μMLC

Component modules for the BEAMnrc code are used to describe the physical components of the linear accelerator such that the EGSnrc code can be used to simulate interactions therein. Component modules are, therefore, required to communicate with other parts of the system in predefined ways and provided sufficient information to enable the simulation to be performed. A new component module must consist of at least five subroutines to satisfy these requirements. These are described in the BEAMnrc user manual (Rogers et al., 2009) and can be briefly be summarised as

- INPUT_$CMNAME a routine to prompt the use for the input variables for the module from either the command line or input file
- HOWFAR_$CMNAME defines the geometry boundaries
- HOWNEAR_$CMNAME calculates the perpendicular distance to the nearest boundary
- WHERE_AM_I_$CMNAME determines the region of the particle on entry into the the component module
- ISUMRY_$CMNAME writes a summary of input parameters for the component module to the output listing prior to running of the simulation

Additionally, a series of macros is required to define variables and call these subroutines at the appropriate time. The bespoke component module, therefore, required writing of a new version of these to input, describe the geometry and summarise the data pertaining to the μMLC. The resulting code written in MORTRAN (as is the rest of the BEAMnrc code) is included in Appendix 1 and conceptually described below.

Using the approach used in other BEAMnrc component modules, the leaf area is divided into several regions describing the major characteristics of each leaf bank (illustrated in figure 4.13), in which the leaf bank is divided into several regions describing the particular part of it where a particle may interact. For

consistency with other component modules such as DYNVMLC (Heath and Seuntjens, 2003) the variable IR is used which is set to a value described in table 4.1.

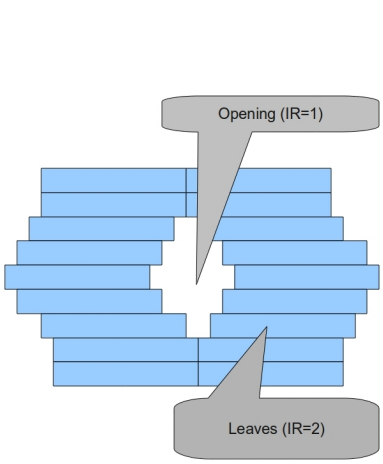

(a) Beams eye view of leaves in component module

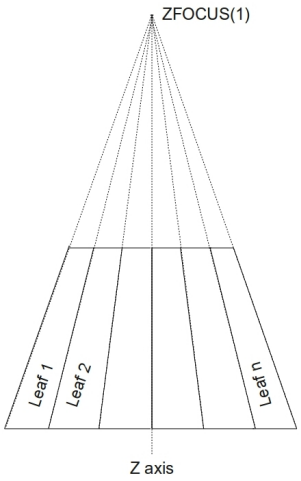

(b) Cross section through leaves perpendicular to leaves

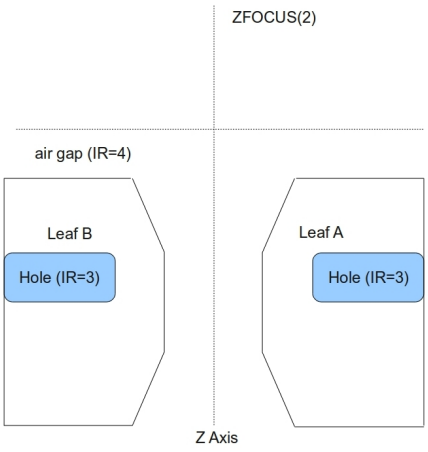

(c) Cross section through leaves parallel to leaves

Figure 4.13: Schematic diagrams of μMLC geometry.

Once a particle enters the component module, the region number is determined by applying simple geometric checks for its exact position in the leaf bank. For particles in regions of IR greater than 1 (i.e not in the open

Value of IR	Description
1	Open Part of the field
2	Main part of a leaf
3	The lead screw used to transport the leaf
4	The air gap between the start of the component module and leaves

Table 4.1: Table of values of IR used in the BLMLC component module.

part of the field), the voxel within the leaf is determined. The material through which the particle is transporting is returned to the main BEAMnrc code as is the distance to the next voxel. This is in order to ensure interactions are tracked across boundaries correctly, as the step length of each particle is shortened near boundaries to assume boundary effects are modelled correctly.

For particles interacting within the leaves themselves, the situation is more complex. As has been discussed earlier, the μMLC consists of relatively complex geometry incorporating several tongues and grooves which are modelled by dividing each leaf into a *lattice* of voxels, which may or may not be filled with the collimator material as illustrated in 4.14.

Using this technique, by choosing appropriate dimensions of each voxel, any shape leaf can be described, limited only by the resolution of the voxels used to *build up* the leaf geometry, which, if this is within acceptable limits can be used to model any geometry within any accelerator. Such a component module would therefore have a high degree of flexibility associated with it and consequently was the first approach used in modelling the μMLC.

In reality, the leaf geometry differs slightly from that shown in figure 4.14, in that the width of the radiation penumbra is limited by adding divergent edges to the leaves such that they are focused at the radiation source. In order to incorporate this design into the component module, the lattice distances were defined at the top of the beam geometry and adjusted at distances further from the radiation source using similar triangles to obtain the voxel boundaries. In this way, the divergent shape of the leaves could be modelled as is illustrated in figures 4.15(a) and 4.15(b) showing *even* and *odd* leaves mapped onto the divergent matrix.

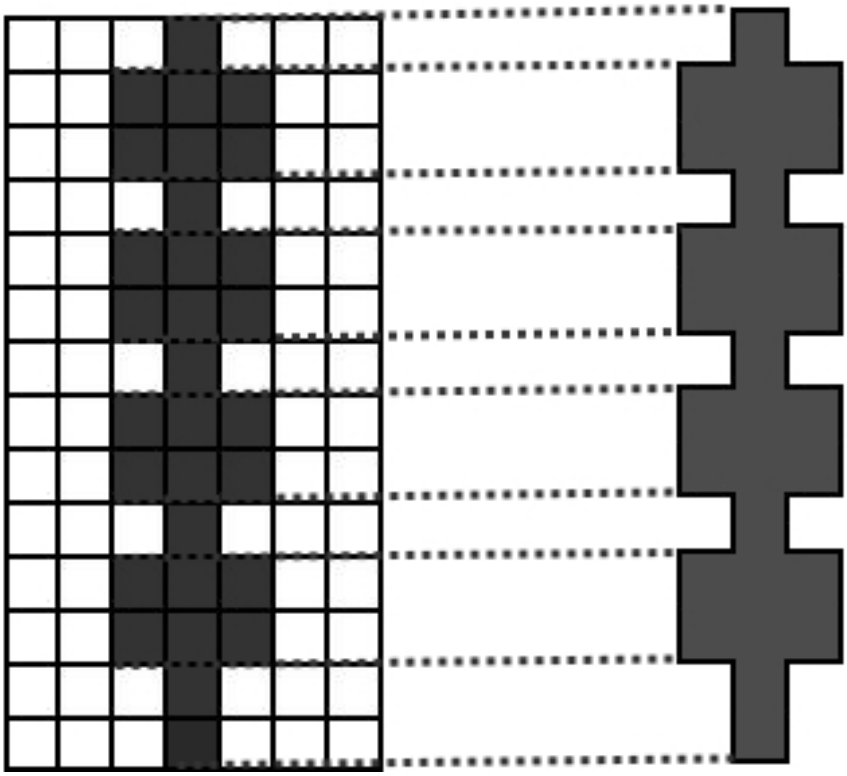

Figure 4.14: Schematic diagram of a single leaf geometry being mapped onto a lattice as used in the component module.

For debugging and illustrative purposes, a feature was built into the module to output the co-ordinates of each particle transporting through the component module to a text file for later plotting. An example of such a plot can be seen in figure 4.16. For clarity, adjacent leaves are shown in contrasting colours and it can clearly be seen that the model is correctly simulating the divergent nature and geometry of the μMLC. Once the model had been completed and debugged, several simulations were run to validate the model indicating good agreement between simulated and measured doses. However, the input file consisting of a number of lattice positions in x and y directions for 26 unique leaves became overly complex and consequently comprised many hundreds of lines, compared to a few tens of lines for a conventional MLC component module.

More significantly, however, was the computing overhead taken up by needlessly reducing each particle's step size near the boundary of voxels of the same material. This effect can be seen in 4.16. In this diagram, near the voxel

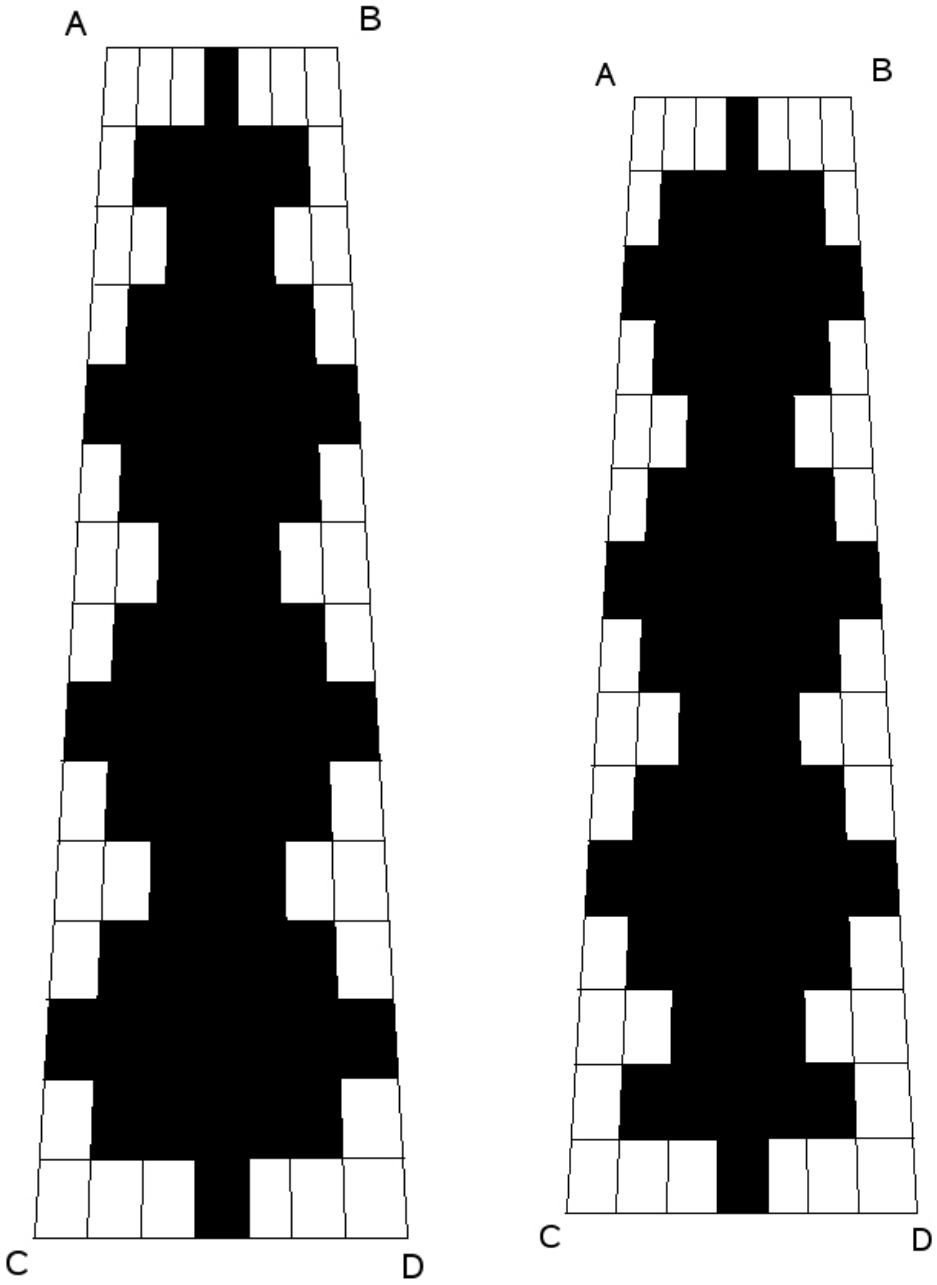

(a) Even leaf (b) Odd leaf

Figure 4.15: Illustration of odd and even leaves on a divergent matrix.

boundaries, the particles are bunched up causing almost constant areas of colour as particle interactions are tracked across the boundaries, whilst in the middle of the larger voxels, clear areas can be seen where few interactions take place.

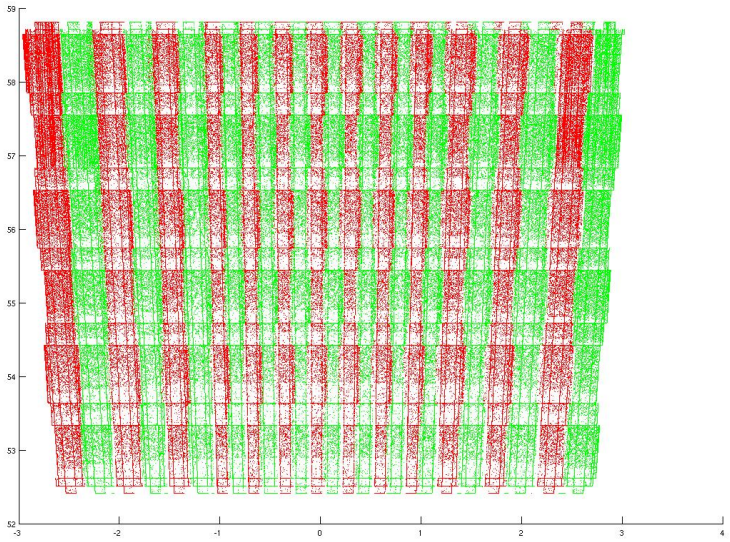

Figure 4.16: Points of interaction within the generic module.

It was therefore considered prudent to explore a more bespoke model of the MLC in which the input file required would be much smaller and easier to understand, consisting of a simple position for each leaf, and to return distances to the main line of the program between a point of interaction and the nearest real boundary between materials. These correct distances are illustrated in 4.17, which illustrates the much greater distances (in the case shown) to the leaf boundaries compared to those of the voxel boundaries.

This method, however, clearly has the disadvantage of losing almost all of the flexibility of the component module to model other MLC designs but which, together with some minor optimisation of the code to improve speed returned a 40% decrease in simulation times, which for the purposes of this study was considered the optimal option. An output of the debug mode points of interaction can be seen in 4.18 in which a similar number of points of interaction to that in 4.16 can be seen.

In this case, the appearance is of a uniform distribution of particles within the model indicating the expected behaviour of the module in giving a more realistic representation of the points of interaction.

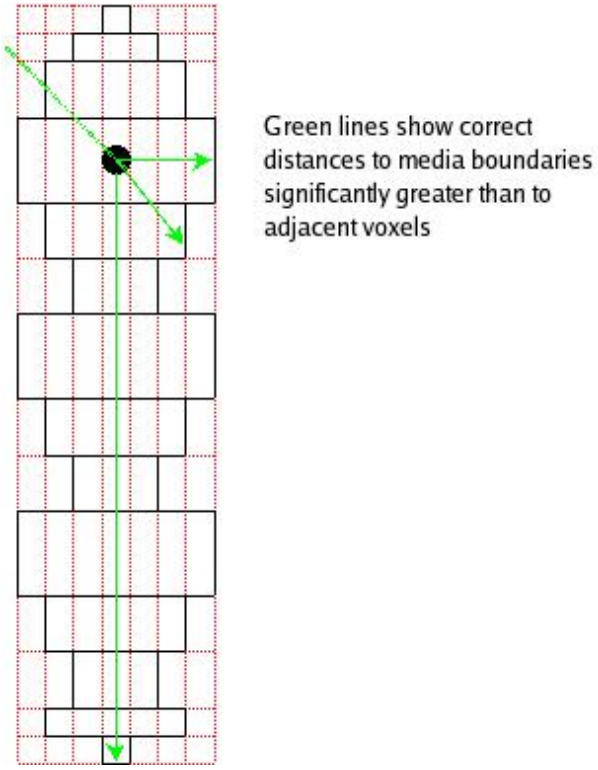

Figure 4.17: Illustration of distances to closest boundary calculation in BLMLC.

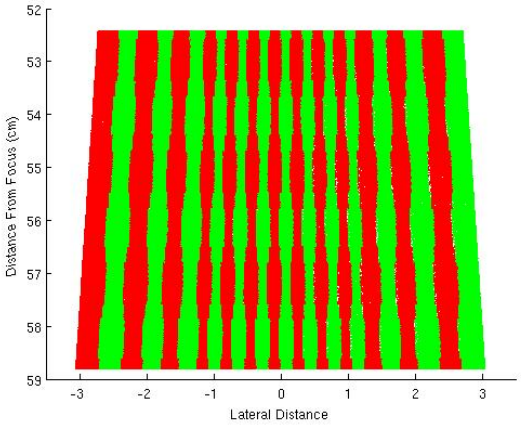

Figure 4.18: Plot of points of interaction in final module.

4.3.3 BLMLC subroutines and input files

Despite being simplified compared to the previous version of the CM, the resultant component module still requires input from the user to describe the geometry of the collimating device. An extract of a typical input file is shown in 4.19. The quantities required to be entered by the user are:

- The distance of the CM from the radiation source
- The thickness of the leaves and start position of the first leaf
- The orientation and number of leaves
- The interleaf air gap
- The choice of leaf end design (rounded or angled)
- Angle or radius of leaf ends
- Leaf positions
- Media, energy cut off and latch parameters for the CM simulation as are standard for BEAMnrc CMs

The majority of the parameters are self explanatory and are typical of other MLC CMs such as DYNVLMLC and MLCE. The exception to this is the angular items required to define the leaf end geometry. These are entered as two angles describing the shape of the upper and lower sections of each leaf. These are illustrated in 4.20.

The leaf thicknesses are not required as these are built into the code to simplify the input values required by the user. This information is listed in a relatively user friendly manner at the beginning of the component module code so as to allow easy editing should future users desire to adjust the model to suit their particular design of the μMLC. This would be the case if it was purchased to fit on an accelerator with a different configuration with a likely different distance from the machine focus (The BrainLAB M3 device is custom built depending on machine design to minimise the widths of penumbrae and to

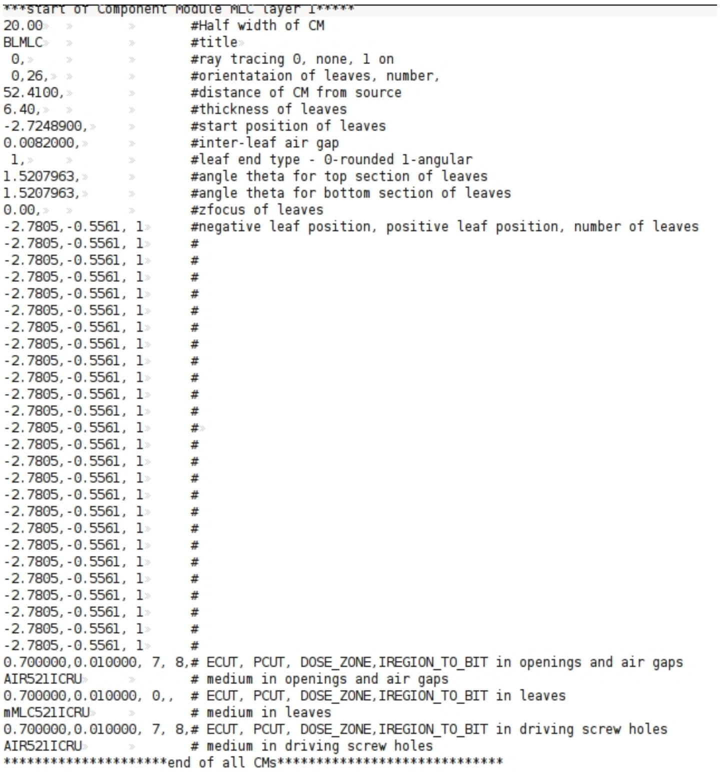

```
***start of Component Module MLC layer 1*****
20.00                   #Half width of CM
BLMLC                   #title
 0,                     #ray tracing 0, none, 1 on
 0,26,                  #orientataion of leaves, number,
52.4100,                #distance of CM from source
6.40,                   #thickness of leaves
-2.7248900,             #start position of leaves
0.0082000,              #inter-leaf air gap
 1,                     #leaf end type - 0-rounded 1-angular
1.5207963,              #angle theta for top section of leaves
1.5207963,              #angle theta for bottom section of leaves
0.00,                   #zfocus of leaves
-2.7805,-0.5561, 1      #negative leaf position, positive leaf position, number of leaves
-2.7805,-0.5561, 1      #
-2.7805,-0.5561, 1      #
-2.7805,-0.5561, 1      #
-2.7805,-0.5561, 1      #
-2.7805,-0.5561, 1      #
-2.7805,-0.5561, 1      #
-2.7805,-0.5561, 1      #
-2.7805,-0.5561, 1      #
-2.7805,-0.5561, 1      #
-2.7805,-0.5561, 1      #
-2.7805,-0.5561, 1      #
-2.7805,-0.5561, 1      #
-2.7805,-0.5561, 1      #
-2.7805,-0.5561, 1      #
-2.7805,-0.5561, 1      #
-2.7805,-0.5561, 1      #
-2.7805,-0.5561, 1      #
-2.7805,-0.5561, 1      #
-2.7805,-0.5561, 1      #
-2.7805,-0.5561, 1      #
-2.7805,-0.5561, 1      #
-2.7805,-0.5561, 1      #
-2.7805,-0.5561, 1      #
-2.7805,-0.5561, 1      #
-2.7805,-0.5561, 1      #
0.700000,0.010000, 7, 8,# ECUT, PCUT, DOSE_ZONE,IREGION_TO_BIT in openings and air gaps
AIR521ICRU              # medium in openings and air gaps
0.700000,0.010000, 0,,  # ECUT, PCUT, DOSE_ZONE,IREGION_TO_BIT in leaves
mMLC521ICRU             # medium in leaves
0.700000,0.010000, 7, 8,# ECUT, PCUT, DOSE_ZONE,IREGION_TO_BIT in driving screw holes
AIR521ICRU              # medium in driving screw holes
********************end of all CMs****************************
```

Figure 4.19: A typical input file for the BLMLC component module.

maintain consistency of field sizes across different machines). The code requiring adjustment for these quantities is illustrated in 4.21.

Although this may require 250 lines of editing per μMLC it is a 'one-off' task that, once completed, has the benefit of greatly simplified input files. For similar reasons, all parameters, such as the distance of the μMLC from the radiation source, the leaf thickness, inter-leaf air gaps and leaf end design, could have been included into the CM code itself and the user simply asked to enter the leaf co-ordinates. However, as some iterations may be required to obtain the correct inter-leaf air gap and adjustment of the leaf end, parameters may be useful in validating the model. These were therefore left as a user input.

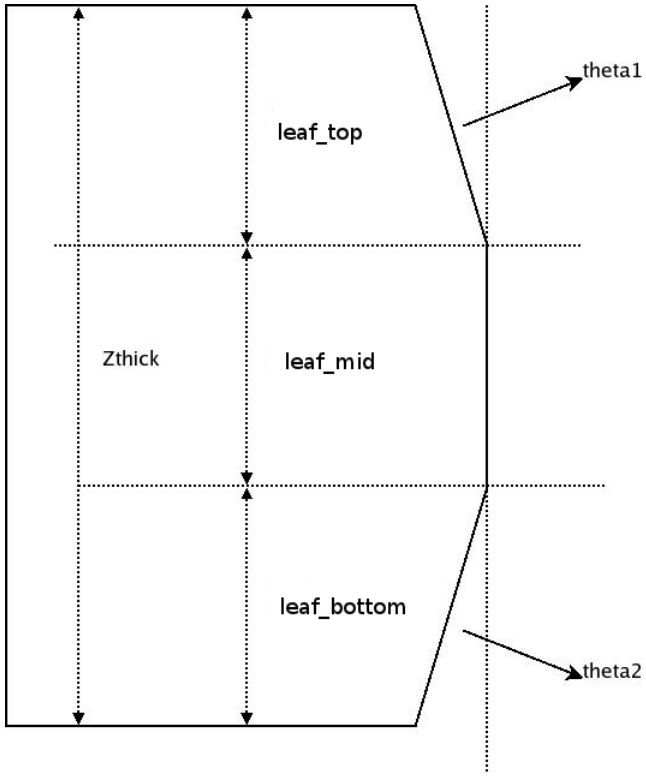

Figure 4.20: Description of parameters entered by the user for the BLMLC component module.

```
'Y Positions of leaves"
'======================"
'LEAF 1 -18-04"
    YREG_$BLMLC(1,1)=START_$BLMLC;
    YREG_$BLMLC(1,2)=YREG_$BLMLC(1,1)+0.023386;
    YREG_$BLMLC(1,3)=YREG_$BLMLC(1,1)+0.047224;
    YREG_$BLMLC(1,4)=YREG_$BLMLC(1,1)+0.116995;
    YREG_$BLMLC(1,5)=YREG_$BLMLC(1,1)+0.211534;
    YREG_$BLMLC(1,6)=YREG_$BLMLC(1,1)+0.281305;
    YREG_$BLMLC(1,7)=YREG_$BLMLC(1,1)+0.305143;
    YREG_$BLMLC(1,8)=YREG_$BLMLC(1,1)+0.328529;
    LEAFTYPE_$BLMLC(1)=2;
```

(a) Mortran code for Y co-ordinates

```
" LEAF 1 18-04
    ZREG_$BLMLC(1,1)=ZMIN_$BLMLC;
    ZREG_$BLMLC(1,2)=ZREG_$BLMLC(1,1)+0.1;
    ZREG_$BLMLC(1,3)=ZREG_$BLMLC(1,1)+0.1675;
    ZREG_$BLMLC(1,4)=ZREG_$BLMLC(1,1)+0.9575;
    ZREG_$BLMLC(1,5)=ZREG_$BLMLC(1,1)+1.2575;
    ZREG_$BLMLC(1,6)=ZREG_$BLMLC(1,1)+1.9775;
    ZREG_$BLMLC(1,7)=ZREG_$BLMLC(1,1)+2.2775;
    ZREG_$BLMLC(1,8)=ZREG_$BLMLC(1,1)+3.0675;
    ZREG_$BLMLC(1,9)=ZREG_$BLMLC(1,1)+3.3675;
    ZREG_$BLMLC(1,10)=ZREG_$BLMLC(1,1)+4.0875;
    ZREG_$BLMLC(1,11)=ZREG_$BLMLC(1,1)+4.3875;
    ZREG_$BLMLC(1,12)=ZREG_$BLMLC(1,1)+5.1775;
    ZREG_$BLMLC(1,13)=ZREG_$BLMLC(1,1)+5.4475;
    ZREG_$BLMLC(1,14)=ZREG_$BLMLC(1,1)+6.1975;
    ZREG_$BLMLC(1,15)=ZREG_$BLMLC(1,1)+6.3000;
    ZREG_$BLMLC(1,16)=ZREG_$BLMLC(1,1)+ZTHICK_$BLMLC;
```

(b) Mortran code for Z co-ordinates

Figure 4.21: Code requiring editing for customisation of the μMLC for different accelerator designs.

4.3.4 Validation of BLMLC

Clearly, following the writing of the code, validation of the model is necessary to ensure that simulations performed with it and any conclusions can be relied upon. Initially, a scaled diagram of the MLC debug output similar to that of figure 4.18 was printed out and measurements made and compared with that of the manufacturer supplied information. These were found to be well within the estimated uncertainty of 0.2mm associated with the printing and hand measurement process. Results of this analysis are not included due to this information being the subject of a non-disclosure agreement between Velindre Cancer Centre and BrainLAB. This was done for all leaves, and in all possible planes. Additionally, the BEAMnrc documentation includes a report on the quality assurance of component modules (Walters and Rogers, 1999), which suggest tests to be performed for quality assurance purposes of new component modules. On examination of this documentation, relevant tests were done to determine if the component module was working in the expected manner.

4.3.4.1 'p1a' test

The p1a test, shown in figure 4.22, is designed to test that the structures within the collimator are attenuating the incident beam correctly. In order to achieve a significantly large number of particles in the resulting phase space file, the tests in the manual suggest using a square electron beam as an incident radiation source and 'air leaves' within a 'lead space' as the component module. As it was possible to run an entire linear accelerator simulation using photons in an acceptable time for this, it was determined to run tests using both lead leaves in an air space and air leaves in a lead space. Initially, the results were analysed from a short run (approximately 30 minutes), using the phase space file scored at the exit of the μMLC, the results of which can be seen in 4.23. Four runs were performed, the first of which, shown in 4.23(a), is a scatter plot of the position of each particle in the phase space file for the standard configuration of tungsten alloy leaves existing in an air space with estimated inter-leaf gaps of 0.1mm between each leaf. The shapes of regions with a higher concentration of particles correspond to that of the test shape shown in 4.22, and it can be seen that the component module is transporting particles through the inter-leaf

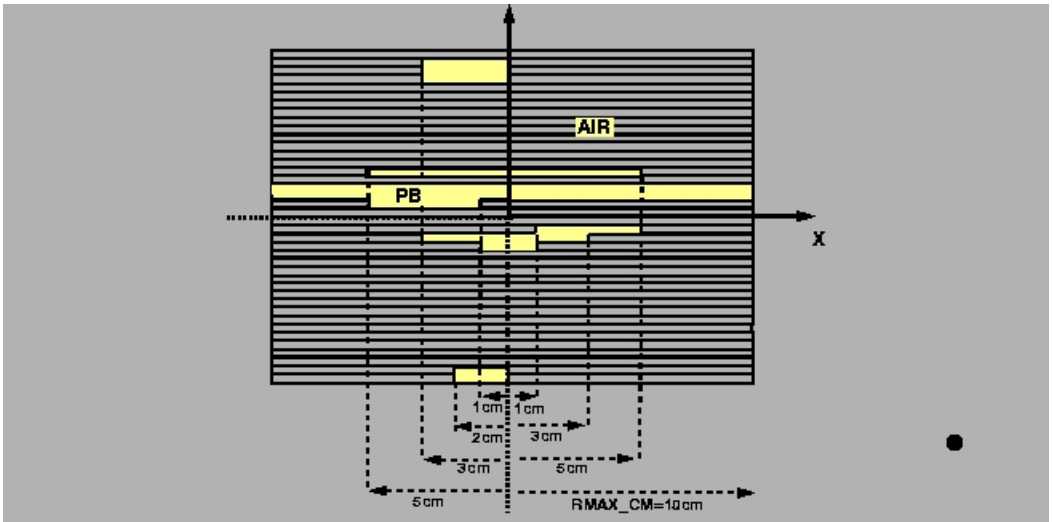

Figure 4.22: Description of p1a test (from BEAMnrc QA document (Walters and Rogers, 1999)).

gaps in an expected manner. When scaled and measured, the widths of these gaps corresponded and the widths of the leaves themselves agreed to within the estimated measurement uncertainty of 0.2mm.

Figure 4.23(b) illustrates a similar case but with the μMLC constructed from air existing in 'metallic alloy space'. The effects of the converse of inter-leaf leakage can be seen along each leaf, and in this case, the effect of the leaf end geometry can be seen at the abutting edge shown by a region of a decreased concentration of particles along the central axis orthogonal to the leaf direction.

Figures 4.23(c) and 4.23(d) illustrate similar situations of lead leaves in an air space and air leaves in a lead space respectively, but with the inter-leaf gaps set to zero. These show the expected result of no transmission occurring between the leaves. An additional transmission can be seen along the right hand edge of figure 4.23(c), which corresponds to the total width of the leaves being reduced

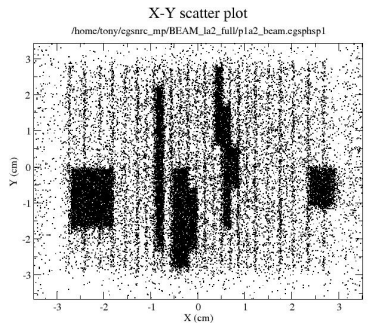

(a) 'Lead' leaves in 'air' space with with interleaf gaps

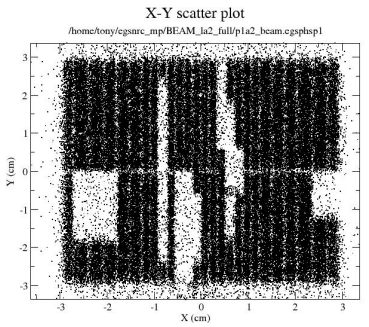

(b) 'Air' leaves in 'lead' space with interleaf gaps

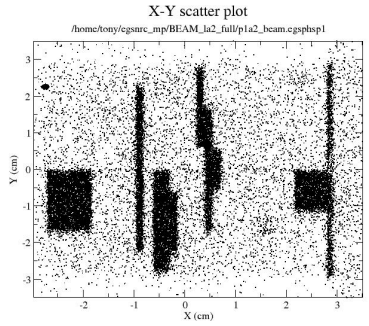

(c) 'Lead' leaves in 'air' space without interleafgaps

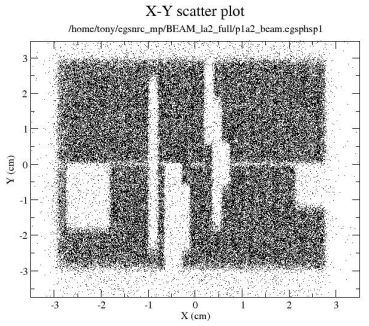

(d) 'Air' leaves in 'lead' space without interleaf gaps

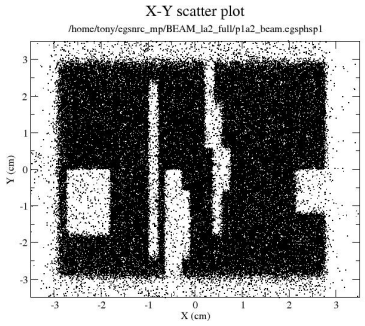

(e) 'Air' leaves in 'lead' space without interleaf gaps

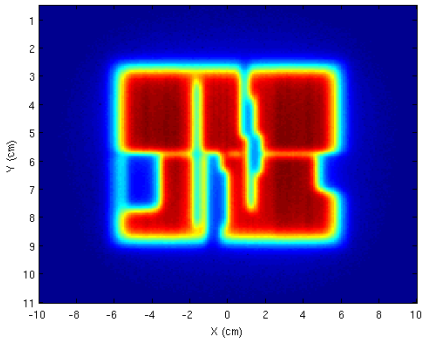

(f) DOSXYZnrc Simulation of p1a2 shapes

Figure 4.23: Outputs of phase space analysis of p1a test.

due to the removal of the inter-leaf gaps, resulting in radiation leaking through this newly induced air gap.

Figure 4.23(e) illustrates the case with the leaf ends set to be straight. As, in this case, the leaves abut perfectly across the central axis, no additional transmission through the abutting region, compared to that through the leaves themselves would be expected, which is indeed the case in the illustration.

These figures indicate that the component module was behaving in the expected manner for these tests. Due to the difficulty in scaling these measurements, a scaling test was performed by running the simulation using this configuration as an input to a DOSXYZnrc simulation. The results of this are shown in figure 4.23(f). For this experiment, the BEAMnrc simulation was incident upon a water phantom consisting of 1mm x 1mm x 5mm voxels placed at 98.5cm FSD. The plane shown is a relative dose distribution of doses deposited in voxels centred around the nominal depth of maximum dose (1.5cm). This image was then scaled and printed out at 4× actual size and the openings measured by hand and compared against those expected. All differences between measured and simulated distances were within the estimated uncertainty of 0.2mm.

4.3.4.2 Inter-leaf Leakage and Leaf Transmission

A simulation of radiation transport between the leaves of the μMLC was used to determine both the magnitude of the transported radiation and as a check of the geometric positioning of the leaves. Simulation of radiation transport through a closed set of leaves has been performed by several authors (Heath and Seuntjens, 2003; Belec et al., 2005) and generally compared against measurements made using radiographic film (Belec et al., 2005; Cosgrove et al., 1999; Heath and Seuntjens, 2003). The difficulties associated in the use of radiographic film in a modern radiotherapy centre without film processing facilities are described in section 2.2.3. Velindre Cancer Centre, in common with many others no longer has film processing facilities, so an approach using the Electronic Portal Imaging Device (EPID) was used. The EPID present on the Varian 600C accelerator is discussed in greater detail in Chapter 8, but consists of 512 by 384 semiconductor detectors used to read out the visible light emitted from a radiation sensitive screen. This has shown to be a reliable tool in dosimetric tests (McCurdy et al., 2001; Nicolini et al., 2006; Siebers et al., 2004; Cufflin et al., 2010) and was consequently used to investigate the transmission through and between the

μMLC leaves. The imager has a spatial resolution of 0.784mm and was placed at 140cm from the source which relates to a spatial resolution of 0.56mm at the isocentre. To calibrate the imager, the maximum available field size of 9.8cm by 9.8cm, defined by the machine collimators and μMLC, was used to irradiate different doses from 0.5cGy to 80cGy (MU calculated using standard tables). The resultant calibration curve is shown in figure 4.24.

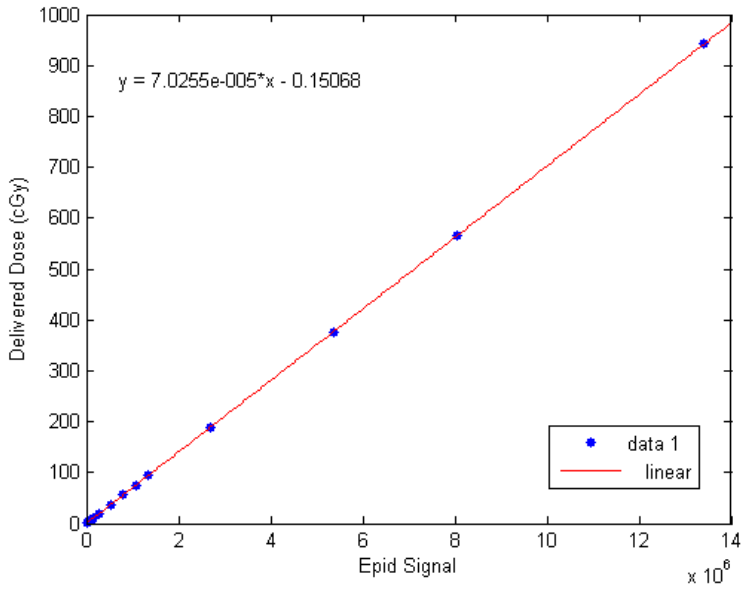

Figure 4.24: Calibration curve used to convert EPID signal to dose for inter-leaf leakage measurement.

A transmission of 2.5% of the open field dose was measured through the closed leaf banks during initial acceptance of the device, this figure was then used to calculate the monitor units required to deliver approximately 50cGy to the EPID using standard tables. Following irradiation, the calibration curve was then applied to the measured data to acquire a data set against which subsequent simulations were compared. To account for any uncertainties in the positioning of the imaging device, a 9.8cm x 9.8cm field was irradiated. The width of the profile obtained was then compared to that expected to derive a scaling factor to determine the exact positioning of the sensitive volume of the imaging device. This revealed an accuracy of better than 1mm in the position of the device at 140cm.

Monte Carlo simulations were performed with identical leaf positions to those used in the irradiation, and a model of the EPID used derived from measurements obtained from the manufacturer and previously validated (Cufflin et al., 2010). In the Monte Carlo simulations an inter-leaf gap of 0.14mm was initially chosen as derived by Belec et al. (2005).

A DOSXYZnrc phantom, with the sensitive volume of the imaging device placed at the position calculated from the scaling measurements calculated above, was created with voxels identical in size to that of the sensitive region of the imager. The co-ordinates of the centre of the calibration field were then compared to that of an identical field simulated. Using these calculated values of the centre of the fields, the co-ordinates of the phantom were then adjusted so that phantom and imager co-ordinates were in identical positions. The simulation was then run and a plot similar to that shown in figure 4.25 produced. Both measurement and simulations were normalised to the values at the centre of a 9.8cm by 9.8cm open field with the μMLC leaves retracted.

Following a comparison of measurement and simulation, the width of the inter-leaf air gap was then adjusted, with the start position of the leaves moved for each simulation by an appropriate amount to ensure the leaf banks maintained symmetry about the central axis, the simulation re-run and the comparison re-performed. This iterative process was repeated several times until the optimum comparison between measured and simulated results were observed. An inter-leaf gap of 0.08mm was determined to be the optimum distance. The optimum case is shown in figure 4.25 from which excellent agreement is shown between measurements and simulations in terms of a spatial comparison and in magnitude.

The magnitude of interleaf leakage can be seen to be of the order of 2.4% which compares closely to that of Cosgrove et al. (1999) who reported 2.8% and Belec et al. (2005), 2.4%. The average transmission through the leaves of 1.5% (sd 0.4 %) also compares well with the 1.4% reported by Belec et al. (2005). In this experiment, a lower transmission under the thicker leaves was observed both by simulation and measurement, which may be due to the experimental procedure undertaken, using an EPID with a significantly lower spatial resolution than the gap being investigated. This averaging effect is somewhat cancelled out in

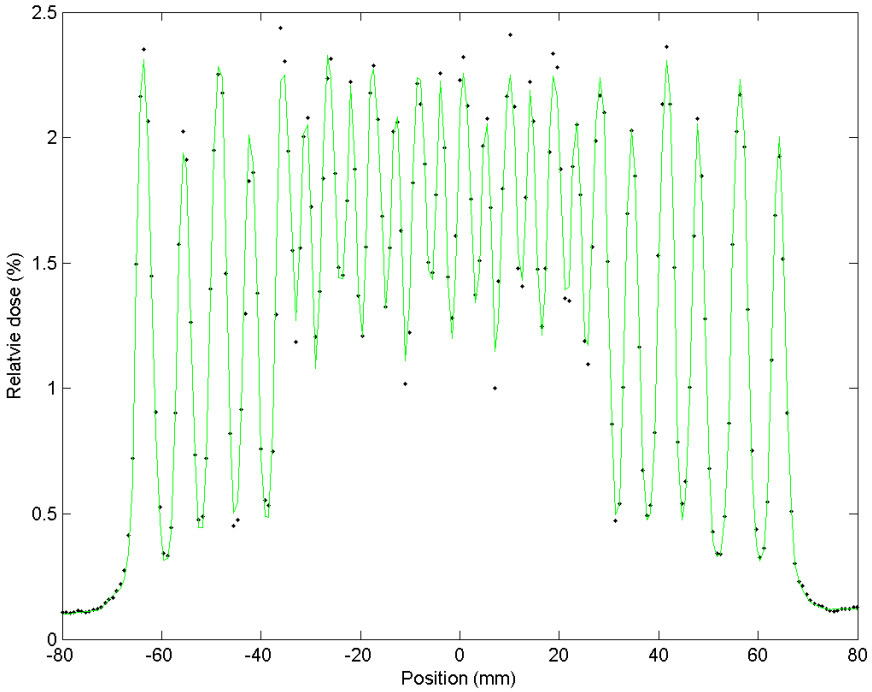

Figure 4.25: Plot of Interleaf leakage test (points simulations, lines measured).

the comparison by positioning the simulated voxels in exactly the same position as the pixels of the sensitive volume of the measurement device and, thereby, simulating exactly the measurement position.

Therefore, it can be concluded that the component module is correctly modelling the position of the μMLC leaves, the air-gap between them and the magnitude of the radiation intensity transporting through them.

4.3.4.3 Positional Tests - Lattice

Using the leaf gap calculated in the previous section, a lattice shape consisting of alternating open and closed leaves as illustrated in figure 4.26(a) was used, in a simulation to determine if the magnitude and position of dose transporting through the leaf air gaps was modelled correctly by the CM.

Measurements were made using the portal imager placed at 140cm FSD

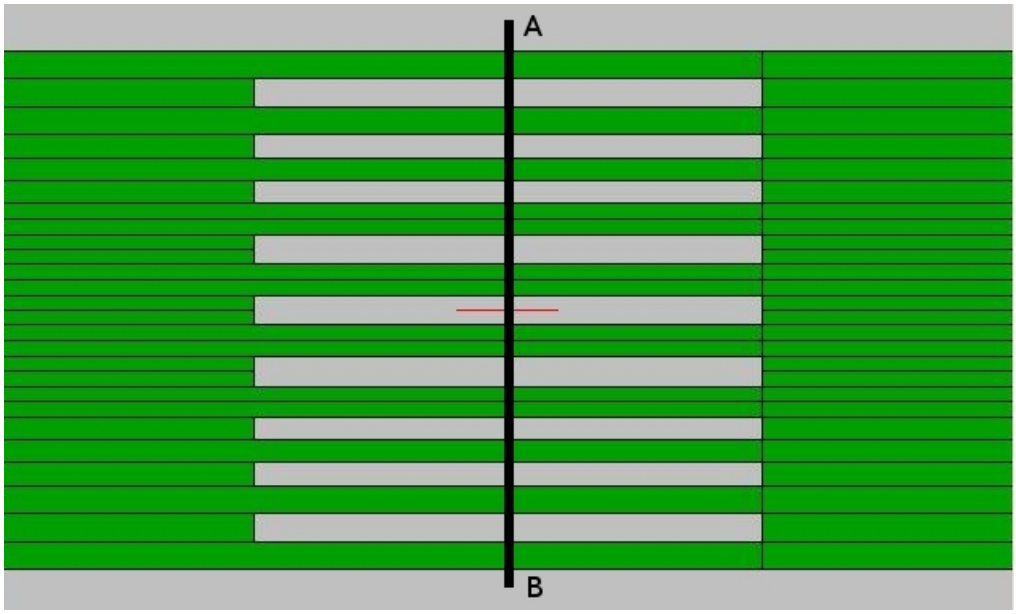

(a) lattice shape used in test - simulations along line AB

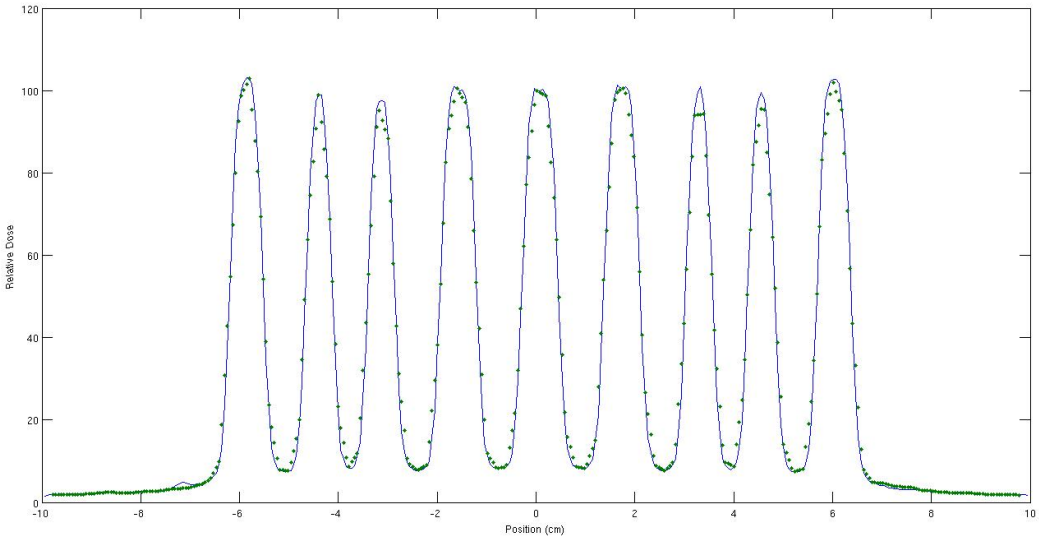

(b) plot of lattice test (points simulations, lines measured)

Figure 4.26: Illustration of shape and result of lattice test.

from the radiation focus with a 5cm block of solid water placed on the top surface of the imager panel. The same calibration was used, as described in the previous section, to convert the portal image signal into a dose. The relative dose

measured by the imager was extracted along the line AB and normalised to the point at the central axis. The model of the EPID was adjusted to increase the width of the voxels parallel to the leaf direction to 2cm to reduce the experimental uncertainty at each measurement point. A simulation of 250×10^6 particles was then run and the doses normalised to the point at the central axis.

As can be seen in figure 4.26(b), there is excellent geometric agreement between calculated and simulated results indicating that the model is correctly positioning the leaves in the simulation. There are some slight discrepancies between the data sets, particularly in the openings around +3cm and +4cm but generally there is good agreement in both position and magnitude between the doses measured and simulated.

4.3.4.4 Relative Dosimetric Tests

Relative dosimetric tests were performed using measurements performed in a water tank using a Scanditronix SFD[2] stereotactic diode for the profiles shown in 4.28 and a Scanditronix RK Chamber for the depth doses of figure 4.27(b). The SFD has a very small active volume of $0.17\text{x}10^{-4}\text{cm}^3$, giving good spatial resolution. The device has the disadvantage of a small output current, requiring many samples at each measurement point, resulting in larger uncertainties compared to other larger volume diodes and most ionisation chambers. The RK chamber was used due to its small volume and, in common with other ionisation chambers, a low energy dependence. A 9.8cm diameter circle shape illustrated in figure 4.27(a) was used to define the field with the collimator jaws defining a 10cm square field. The diode and chamber were both first centred by plotting a profile along the central axes of a 10cm by 10cm field and the detector moved to the geometric centre of the field as defined by the points at 50% of the central axis dose. The origin was set by subsequently setting the active region of the detector device at the surface. The surface of the water was set to 90cm FSD so that profiles measured at 10cm deep were at the isocentre distance.

In order to eliminate discrepancies between measured and simulated data as a consequence of uncertainties in detector and collimator positioning, each profile was moved so that the 50% position of the profile were symmetric about

[2]IBA Dosimetry, Schwarzenbruck, Germany

the central axis. This required a maximum movement of 0.3mm for the set of profiles illustrated in figures 4.28 which illustrate measured and simulated profiles taken at lines on and off the central axis.

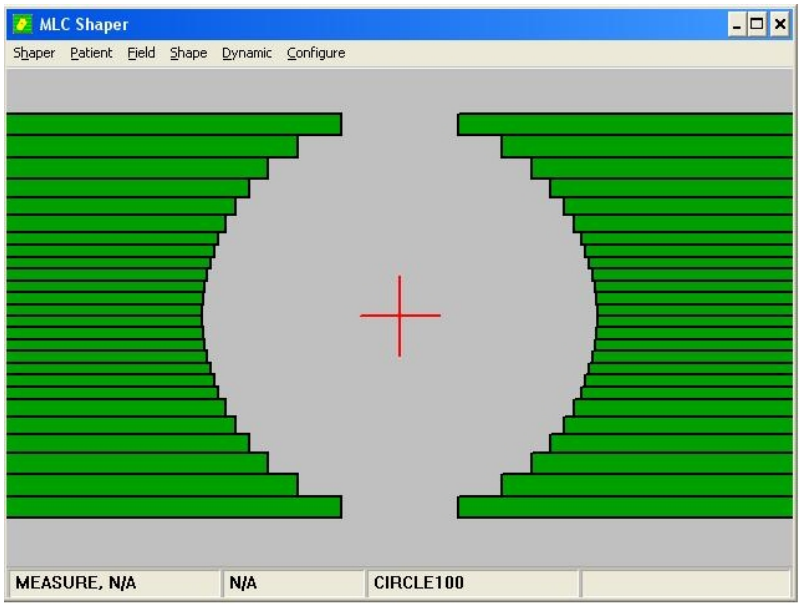

(a) Shape used in test

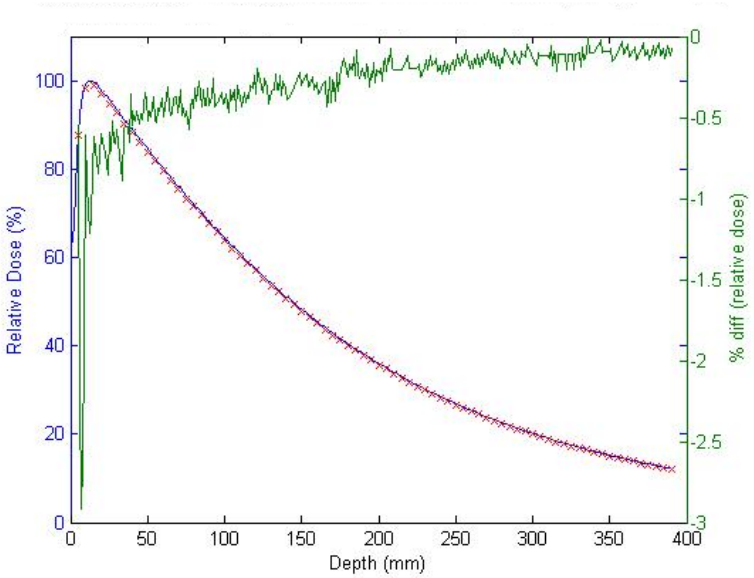

(b) Central Axis Depth Dose

Figure 4.27: Outputs of relative dosimetry tests using a 98mm diameter circle shape - shape and central axis depth dose.

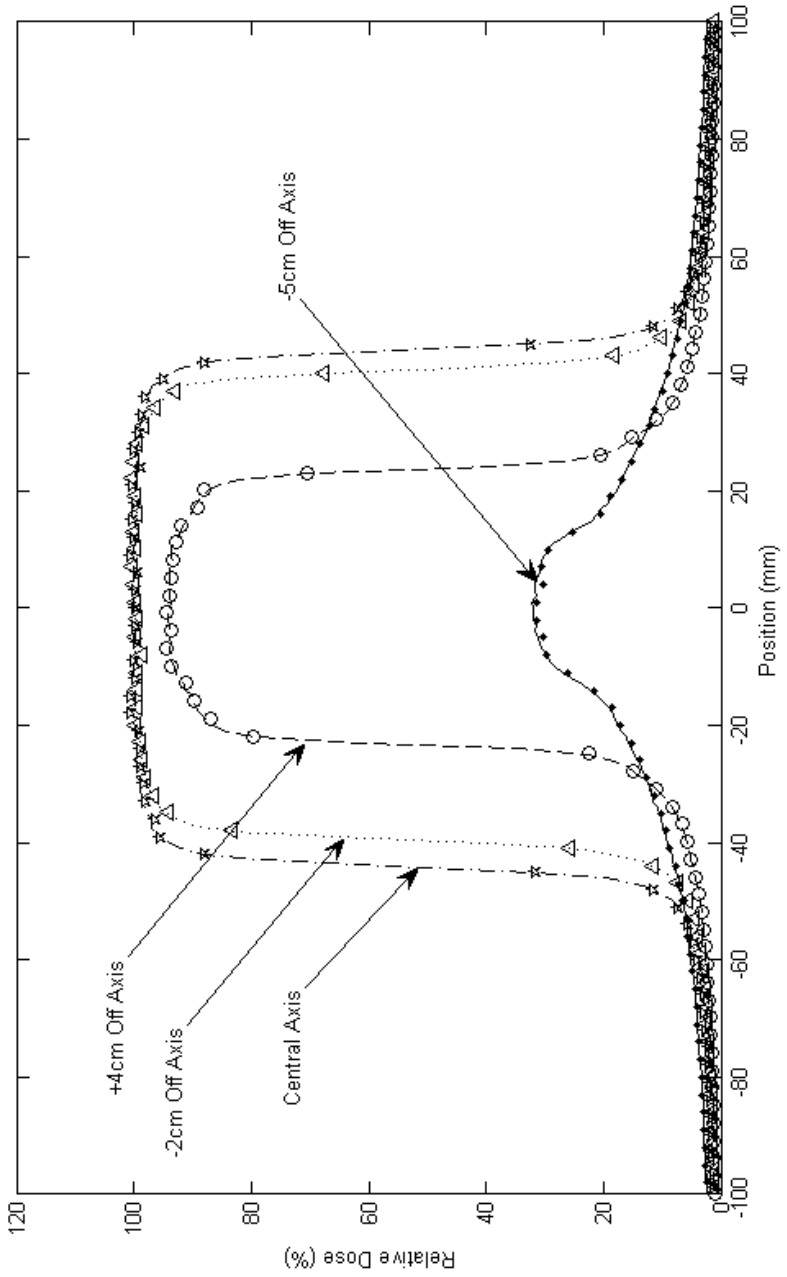

Figure 4.28: Relative profiles on and off axis measured and simulated using the 98mm circular field shape.

Simulations were performed using a BEAMnrc model of the accelerator plus μMLC as an input to a DOSXYZnrc simulation configured to model a simple square water phantom with 2mm x 5mm x 5mm voxels at a depth of 10cm where the profiles were measured. 250×10^6 particles were simulated for the experiment with uncertainties around 1.0% in the open part of the fields.

Results of the comparison between measurement and simulation in which both data sets were normalised to the dose at the isocentre are shown in figure 4.28. As can be seen there is excellent agreement in both position, magnitude and shape of the profiles even with the profiles measured at 5cm off axis which is in the penumbra region of the beam.

Simulations of the depth dose measurement, acquired using 10mm x 10mm x 1mm voxels show similarly good agreement with those measured with differences beyond the build-up region generally less than 0.5% of d_{max} dose.

4.3.4.5 Absolute Calibration

.

An absolute calibration factor was found by using the same method described in section 4.2.3.1. In this case the dose simulated and measured was that at the centre of a 9.8cm by 9.8cm square field defined by the μMLC to derive a new calibration factor of similar magnitude to that calculated in equation 4.4 ($8.513 \times 10^{15} mu^{-1}$).

4.3.4.6 Back Scatter Into The Monitor Chamber

Radiation back scattered into the monitor chamber from the collimator jaws has been considered in section 4.2.3.2, in which up to 0.7% of radiation transporting through the ionisation chamber originated from back scatter from the upper collimators and 0.25% from the lower collimators. It may be assumed that the amount of radiation back scattered into the monitor chamber from the μMLC, which is further downstream than the lower collimators would be further reduced compared to that of the lower collimators. In practice, the collimator jaws will cover the μMLC leaves in order to restrict transmission through the leaves to a minimum.

In order to verify this assumption, an experiment almost identical in nature to that described in section 4.2.3.2 was repeated for the μMLC. In this case, both sets of jaws were opened to their widest position and all the leaves on one leaf bank also moved to their widest position (4.9cm). A series of simulations were then run using a phase space file, previously created just before the chamber, as input source to each simulation. For each simulation, the opposing leaf bank to that held in its widest position were moved progressively across the field and using the latch feature of BEAMnrc, the amount of radiation backscattered into the monitor chamber obtained. The results are plotted in figure 4.29(a).

As can be seen, with the jaws fully open at 40cm by 40cm, and the leaves plotted from the maximum available field size for the μMLC of 10cm x 10cm square there is a change in the back scatter of 0.11% for the lowest proportion of dose into the monitor chamber to 0.13% for the most. In practice this is greater than would be the case in a realistic situation as the jaws would be positioned no greater than equivalent to a 10cm by 10cm field. The output of the experiment repeated in this situation is illustrated in figure 4.29(b). It can be seen that in this case, the radiation back scattered into the monitor chamber is of the order of 0.03% and can therefore be considered to be of little significance to the dosimetric modelling of the device.

In a typical clinical configuration, the collimator jaws are positioned to back up the collimation of the μMLC leaves as much as possible to reduce the magnitude of radiation propagating through and between the leaves. This makes modelling of the situation difficult to generalise.

Consequently a typical shape illustrated in figure 4.29(c), in which approximately half of the open field was shielded by the collimators was modelled and the back scatter into the monitor chamber found to be 0.032%. Therefore the effect of back scatter into the monitor chamber was neglected in the dose calibration of the model.

4.4 Conclusions

Detailed commissioning tests have shown that the use of standard BEAMnrc components and a bespoke model of the BrainLAB M3 μMLC can be used to

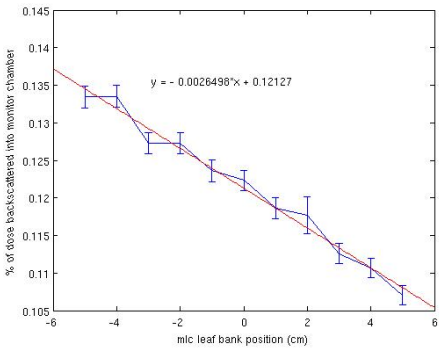

(a) 40cm by 40cm jaws

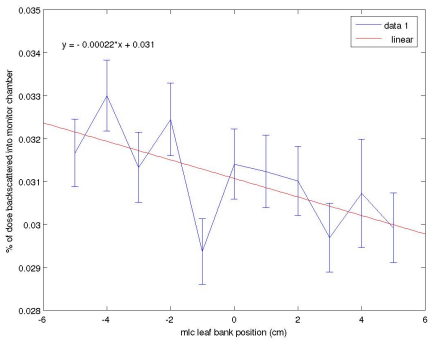

(b) 10cm by 10cm jaws

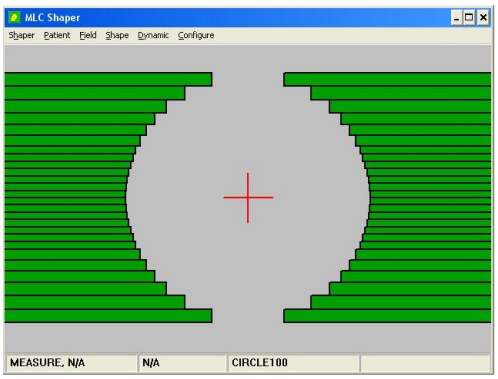

(c) Typical Clinical Shape

Figure 4.29: MLC shape used for, and results of back scatter test.

model doses delivered by such equipment to a high degree of accuracy (<0.5%) if sufficient particles are simulated to reduce the experimental uncertainties to a similar level.

Chapter 5

Applications of BLMLC I : Small field dosimetry

Contents

5.1 Small field dosimetry

The dosimetry of small fields is of particular importance in stereotactic radiation therapy, as fields are generally smaller than those used in conventional therapy. Small fields are usually defined as fields of less than 4cm in any direction and may have dimensions as narrow as a few millimetres. They can be problematic as, due to their size, there may be a lack of lateral electronic equilibrium in the field, making measurements highly susceptible to variations in the positioning

and design of the measurement device. Furthermore, volume averaging may take place if a large detector (relative to the size of the field) is used. These effects may result in a significant error in the determination of the dose delivered by such a field. Additionally, in this situation, positional uncertainties may cause significant variations in the output measured by the device both on the central axis and off axis where the influence in collimator design is of particular significance. In order to determine the limitations of our measurement techniques and develop solutions to some these problems, the dosimetry of small fields was investigated applying Monte Carlo techniques using the model described in chapter 4.

5.2 Methods and Materials

Depth doses were measured for an array of field sizes and a series of detectors; these are listed below and shown in figure 5.1:

- Scanditronix RK chamber (RK)
- Scanditronix Stereotactic field diode (SFD)
- Scanditronix Photon field detector (PFD)
- Scanditronix Electron field detector (EFD)
- Scanditronix-Wellhofer CC13 ionisation chamber (CC13)
- Scanditronix CC01 micro ionisation chamber (CC01)
- Farmer style ionisation chamber (Farmer)

To improve spatial resolution, the RK chamber and SFD detectors were positioned with their long axes vertically (parallel to the central axis of the beam) and horizontally (orthogonal to the beam central axis) where appropriate. In the discussion below these are labelled, RKHZ, RKVRT,SFDHZ and SFDVRT. A summary of the dimensions of each of the detectors is shown in table 5.1.

A Scanditronix RFA-300 water tank was used as the phantom for these measurements with the detector moved from the deepest position towards the

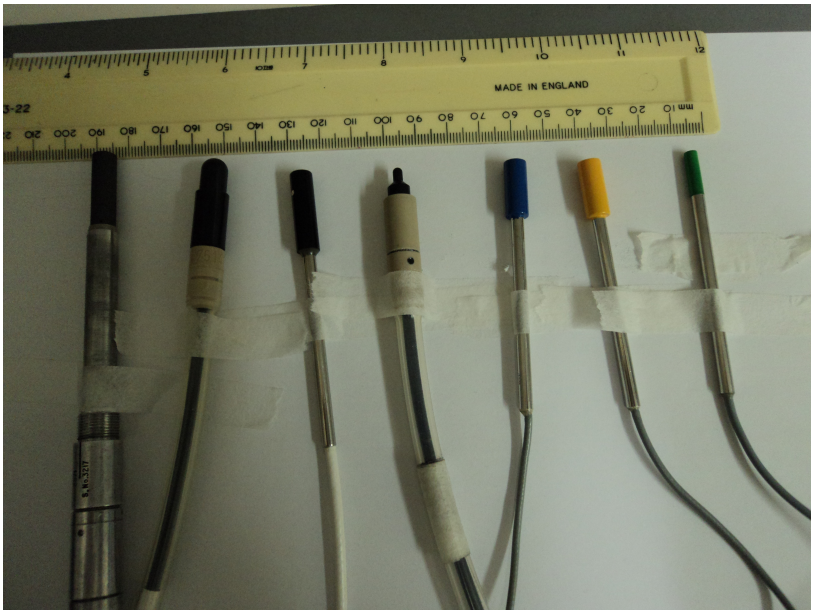

Figure 5.1: Photograph of detectors used in small field investigations. From left to right, Farmer, CC13, RK, CC01, EFD, PFD, SFD.

surface to prevent uncertainties due to disturbance of the water being introduced. The number of sampling points (i.e. the number of times the relative dose was acquired and averaged at the measurement point) for each detector was adjusted until a smooth depth dose curve was observed. This number was considerably more for the SFD (50) compared to that of the RK, PFD or EFD devices (10). Approximately circular fields of diameters (ϕ) of 100mm down to 6mm were used for this comparison. The detectors were centred on the radiation field under investigation prior to the measurement of the depth dose curve and the origin found by positioning the effective measurement point of the device at the surface of the phantom. A depth dose of a large (10cm by 10cm) field was then measured and the position of maximum dose found. All detectors located a depth of maximum dose to within 1mm of that expected for a 6MV beam (15mm). A signal obtained from the accelerator dosimetry system was used to account for variations in machine output during measurement in lieu of a reference detector which would have produced significant perturbations in beam intensity for the smaller fields.

Profiles were measured using the same field sizes and detectors as described above, along the central axes of each field at a depth of 10cm with the phantom positioned with its surface at 90cm from the radiation focus. Measurements were made at 1mm intervals throughout the beam using a similar number of samples at each point as that used in the acquisition of depth doses described above.

Total scatter factor measurements, defined as the ratio of dose measured at the centre of a field under investigation to that of a standard field were measured using the detectors described above in a water tank placed at 90cm FSD from the radiation focus. For these measurements, the standard field used was a 100mm ϕ circle rather than a more standard 100mm square field due to the requirement to remove the μMLC to perform these measurements, which would introduce additional positional uncertainties. In addition a standard Farmer chamber was also used to measure these output factors within a standard water calibration phantom.

Monte Carlo simulations were performed using an accelerator modelling the μMLC as a source to a DOSXYZnrc phantom, which was used to collect data in 3mm by 3mm by 1mm voxels for depth doses and 1mm by 1mm by 3mm for profile measurements. Output factors were simulated by adding doses collected in a 2 x 2 grid of 1mm by 1mm x 3mm voxels for the 6mm, 12mm and 18mm circles and a 4 by 4 grid of 1mm by 1mm by 3mm voxels for all other field sizes. Doses were combined using equation 4.1.

5.3 Results and Discussion

5.3.1 Relative Dosimetry

5.3.1.1 Profile Measurement

Figures 5.2 and 5.3 show the output of simulations and measurements for the 100mm and 6mm ϕ fields. As can be seen, there is generally good agreement between the measurements using each of the detectors in the open part of the 100mm field but the data sets deviate in the penumbra which is illustrated more clearly in figure 5.4(a). The 6mm ϕ profiles consist almost entirely of penumbral

doses. Again, as illustrated more clearly in figure 5.4(b), deviations between the detectors, calculations and simulations are evident. For both field sizes, it can be seen that the detectors with the smallest active area are closest to the Monte Carlo simulations as one might expect. The calculations of the treatment planning system show a reasonable agreement with the Monte Carlo simulations for the 100mm circle but a relatively poorer agreement for the 6mm circle. For the case of the 6mm circle, artefacts of the 1mm x 1mm calculation matrix can be seen in the shape of the curve

Field widths are defined as the distance between the positions of 50% of the dose at the isocentre position. These are tabulated in table 5.2 for both field sizes. For the 6mm field, using the detector with the poorest spatial resolution (CC13), an apparent field width of 7.7mm and 8.1mm in the x and y directions was measured and with the finest (SFD) a field width of 5.6mm and 6.0mm has been returned. For a spherical tumour defined by such collimators, a 6mm wide field corresponds to a volume of 84.8mm^3. If profiles measured with the CC13 detector were used as the basis for dose calculations (as would be the case in a beam library based planning system), a collimator position of approximately 4mm would be set to apparently encompass the tumour which would irradiate a volume of 25.1mm^3, irradiating only 30% of the target to the prescribed dose.

The high dependency of field size on the measurement device would indicate that at least a careful selection of detector be made before measuring and subsequently entering the data into a treatment planning system or that certain fields should be disallowed for such algorithms. Currently, most commercially available systems do not rely on such measurements as the fundamental basis for dose calculation but this experiment would indicate that care should be taken in the use of such fields. The iPLAN system, whose data has been validated against measurements with the SFD diode, returns field widths in the X and Y directions of 4.94mm and 4.81mm, which using an average radius of 4.88mm relates to a volume of 45.5mm^3. Taking the MC profile (average width 5.8mm, spherical volume 76.2mm^3) as most accurate this relates to a 40% reduction in the volume of tissue irradiated, confirming the choice to disallow treatments of such small fields using the iPLAN software at Velindre Cancer Centre. Prior to this study, fields with their smallest dimension less than 25mm were not allowed.

5.3.1.2 Depth Dose Measurement

Figure 5.5 illustrates measurements and simulations for depth doses acquired along the central axis of a 100mm ϕ circle; each curve is normalised to a point at 10cm deep. As can be seen from the magnified figure of 5.5(b), there is close agreement between the simulated curve and the depth doses measured by each of the measurement devices. Some discrepancies can be seen at the surface. These effects may be explained by physical dimensions of the detector introducing artefacts as the parts of it closer to the radiation source than the effective point of measurement clear the surface of the phantom, causing an over estimate of the dose. The SFDHZ diode which has the smallest dimension upstream of the effective measurement point has a smaller discontinuity in the curve near the surface of the phantom and measures the lowest surface dose.

Figure 5.6 illustrates the equivalent case for the 6mm circle field. As with the case of the larger field depth doses, the curves are normalised to a depth of 100mm. For this case there are significant differences between the detectors, particularly near the surface, where at the depth of maximum there is a difference of approximately 20% between the smallest (SFDHZ) and the largest (CC13) detectors.

The Monte Carlo simulations, using 2mm x 2mm x 1mm voxels agree very well with the SFDHZ detector indicating that this detector may be most appropriate detector for measuring such small fields. The advantage of MC simulation over conventional measurement is that it is possible to simulate dose deposition in situations where it is difficult, or indeed impossible, to measure doses accurately. Although the measurement of a depth dose is a routine procedure in radiotherapy physics, it may be argued that the Monte Carlo simulation is a significantly superior technique to that of physical measurement in situations of such small fields. The difficulty is of course in knowing that the MC model is correct. The validation described in chapter 4 has shown that the model agrees very well with measured doses in areas of low experimental uncertainty and can, therefore, be used with some confidence in such cases. However, for these very small fields where there is little secure data to validate the model against one may need to be circumspect. However, it can be seen from figure 5.6(b) that the behaviour of the detectors is as expected with those with the smallest active volume agreeing

closest with the MC simulation. There is a small difference ($\sim$ 3%) between the cc01 and the MC simulation near the depth of maximum dose where the difference is greatest confirming the choice of the cc01 as the detector of choice in such fields with the EFD and SFD also agreeing fairly well. The iPLAN depth dose shows a significant deviation at this field size, confirming the decision to disallow such fields for clinical use prior to this study.

detector	type	Volume	active dimension	Note
CC13	Ionisation Chamber	$0.13cm^3$	5.8mm x 6.0mm	Constructed of shonka ($1.76g/cm^3$)
RKHZ	Ionisation Chamber	$0.12cm^3$	10.0mm x 4.0mm	Epoxy Resin / Perspex
RKVRT	Ionisation Chamber	$0.12cm^3$	4mm ϕ x 10.0mm	Epoxy Resin / Perspex
CC01	Ionisation Chamber	$0.01cm^3$	3.6mm x 2.0mm	Shonka
PFD	Diode	$2.9x10^{-4}cm^3$	2.0mm diam x 0.06mm thick	Shielded Diode
EFD	Diode	$2.9x10^{-4}cm^3$	2.0mm ϕ x 0.06mm thick	Unshielded Diode
SFDVRT	Diode	$0.17x10^{-4}cm^3$	0.6mm ϕ x 0.06mm thick	Unshielded Diode
SFDHZ	Diode	$0.17x10^{-4}cm^3$	0.06mm x 0.6mm	Shielded Diode
Farmer	Ionisation Chamber	$0.6cm^3$	21.8mm x 5.5mm	Standard Reference Chamber

Table 5.1: Summary of detector dimensions and volumes.

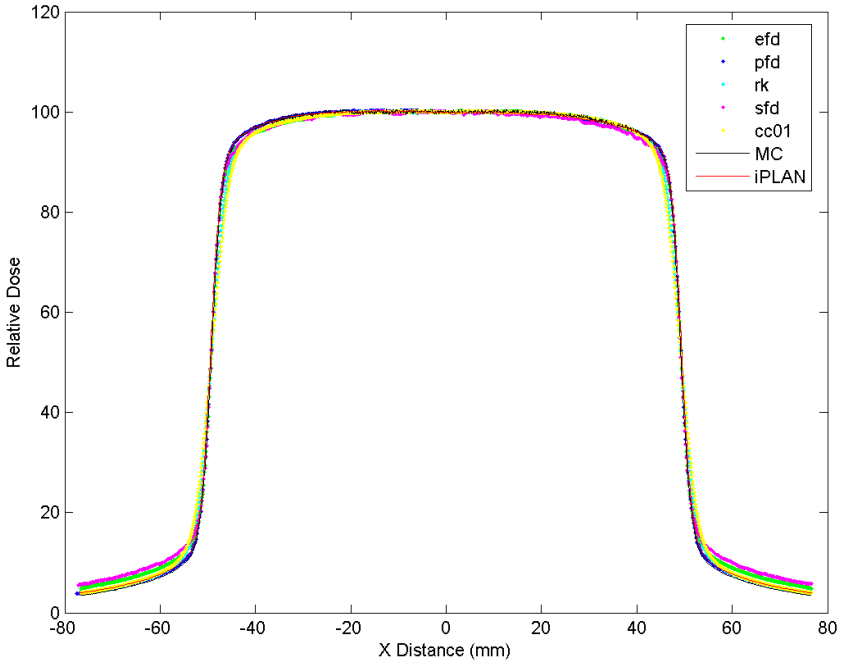

(a) 'X' Direction

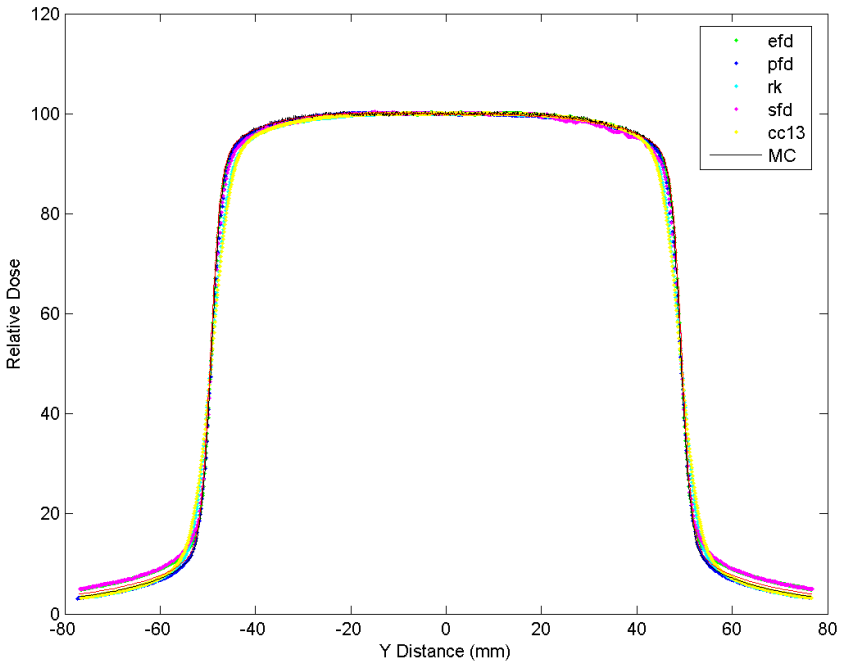

(b) 'Y' Direction

Figure 5.2: 100mm ϕ circle profiles.

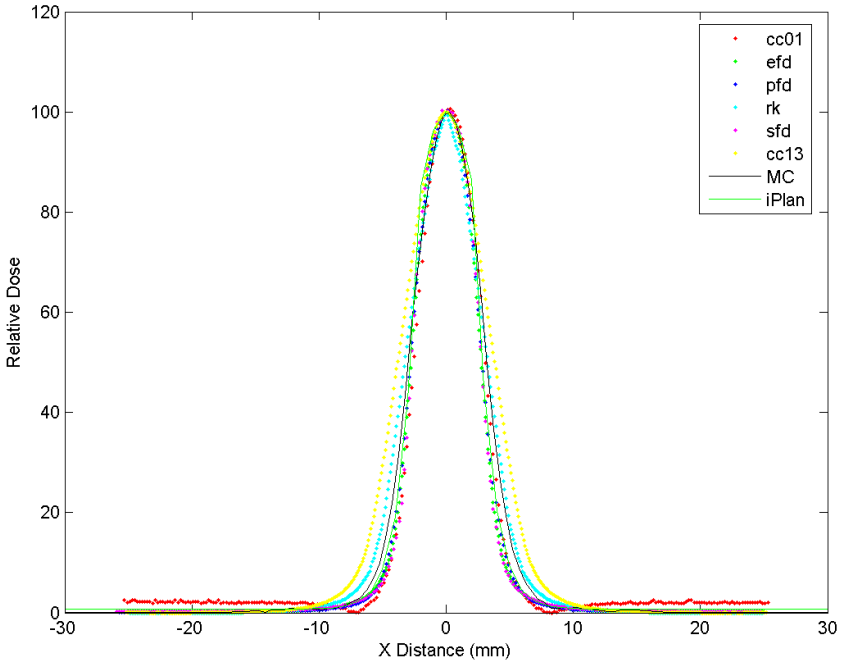

(a) 'X' Direction

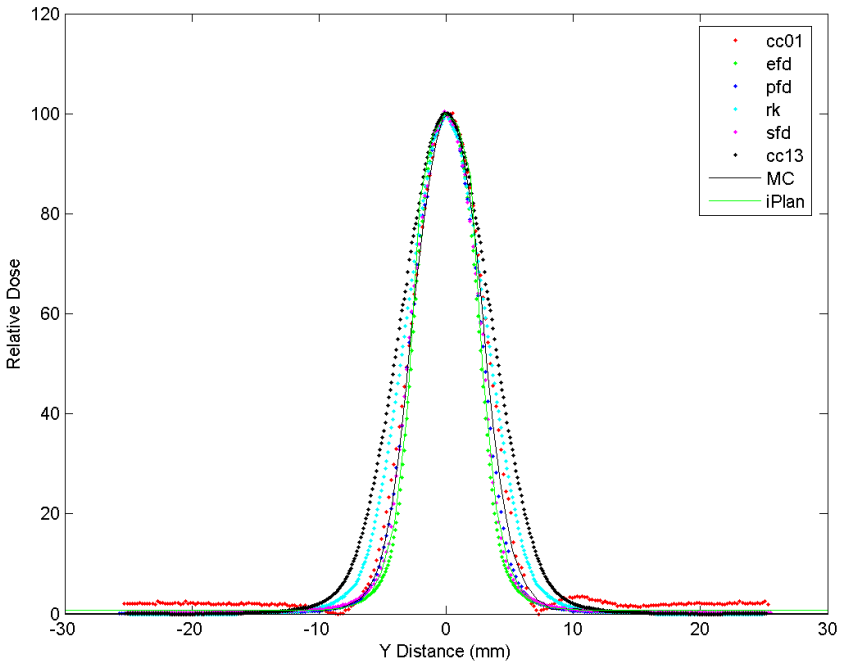

(b) 'Y' Direction

Figure 5.3: 6mm ϕ circle profiles.

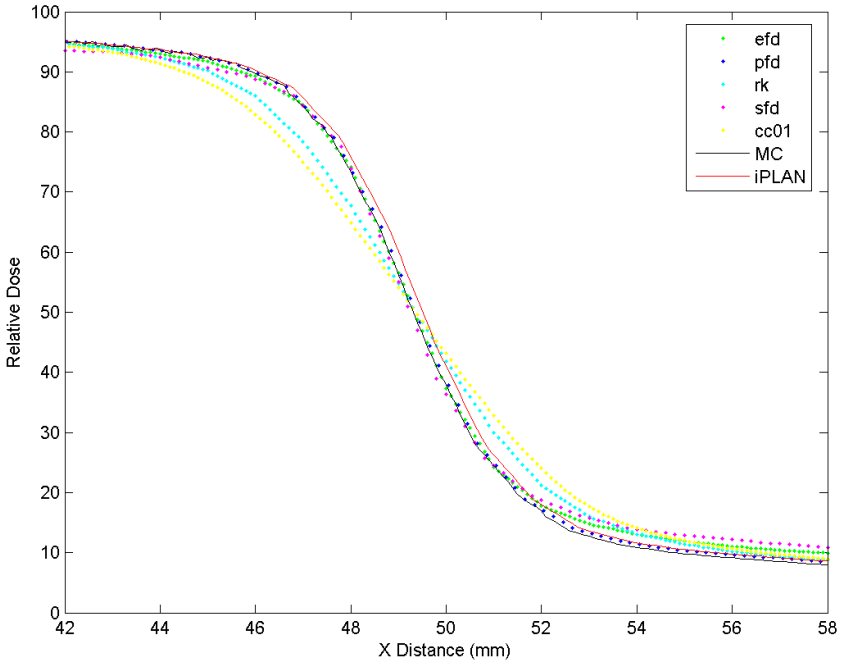

(a) 100mm circle

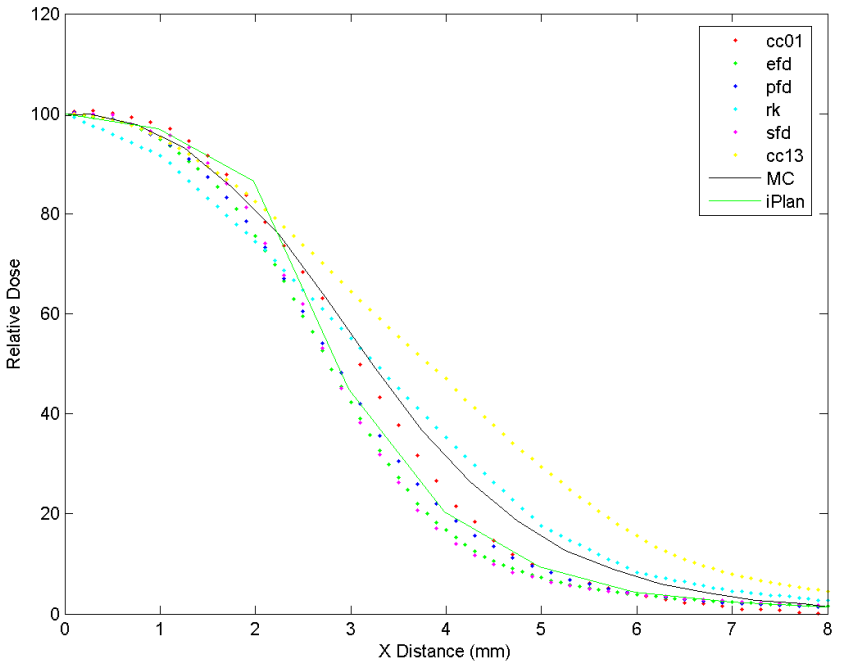

(b) 6mm circle

Figure 5.4: Penumbral region of 100mm and 6mm circular field profiles in 'x' direction.

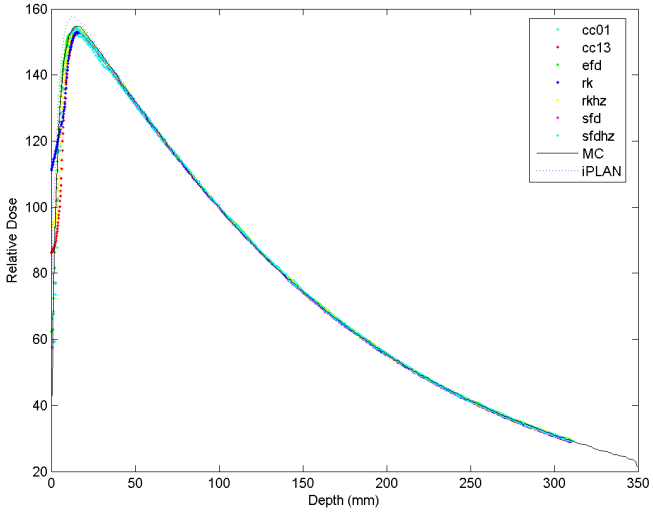

(a) Depth Doses for 100mm ϕ circle using a variety of detectors

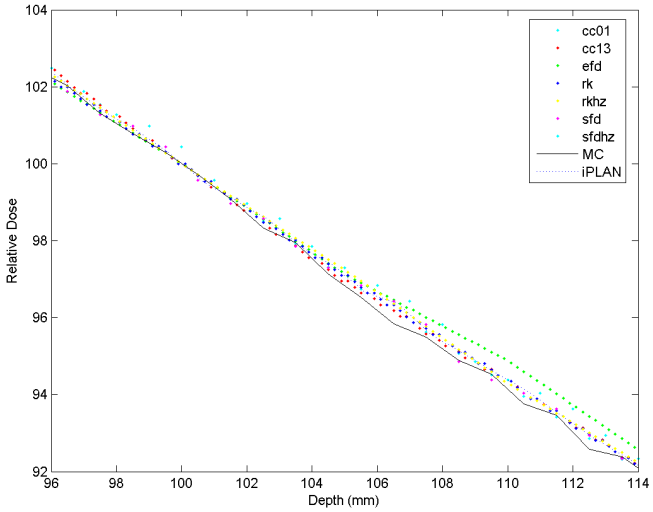

(b) Magnified depth dose curves for 100mm ϕ circle using a variety of detectors around 100mm depth

Figure 5.5: 100mm ϕ circle depth doses.

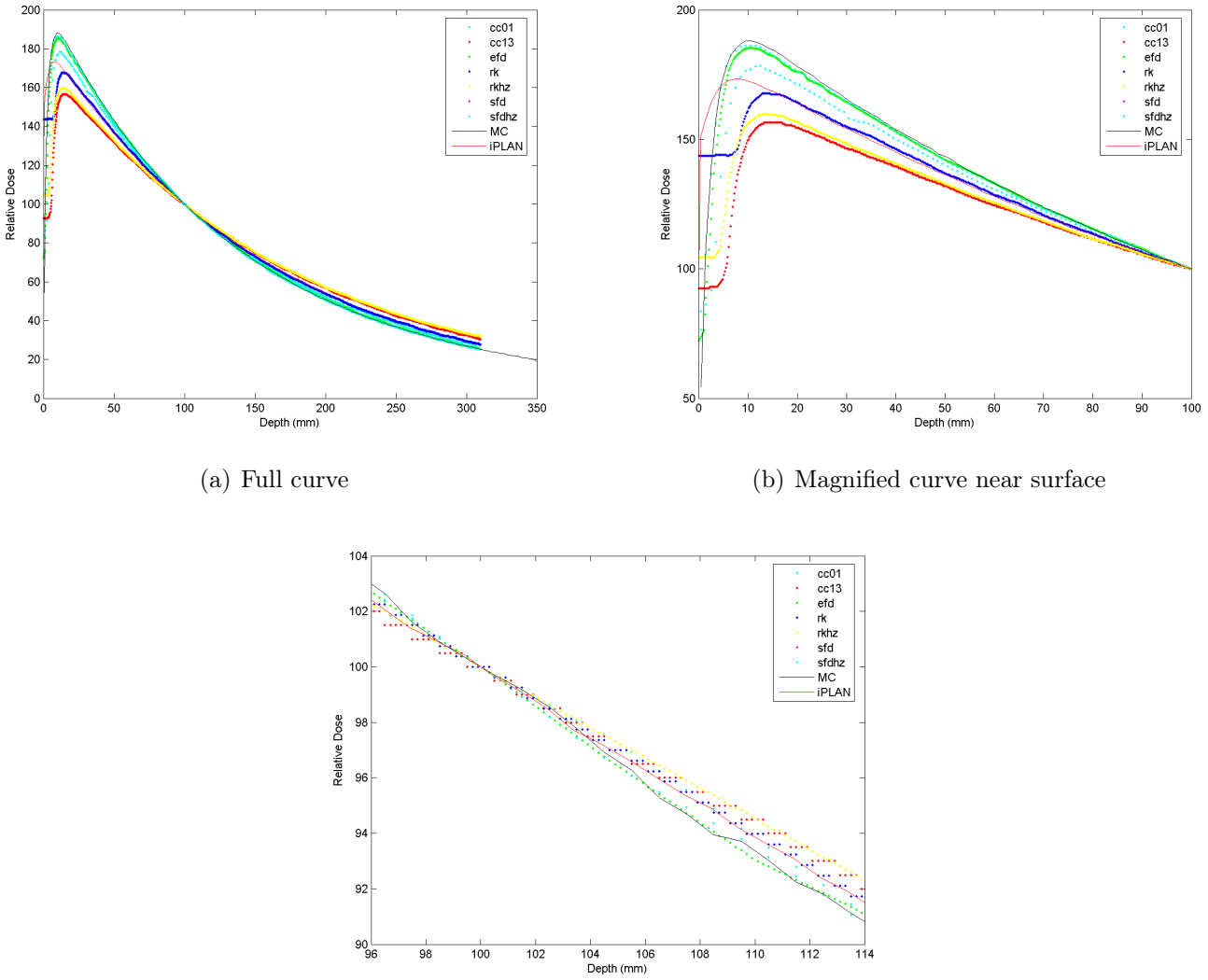

(a) Full curve

(b) Magnified curve near surface

(c) Magnified curve around 100mm depth

Figure 5.6: 6mm ϕ circle depth doses. The stepped effect of some of the measured data in 5.6(c) is due to re-sampling of the data to a 0.1mm step size to match the data of other curves.

5.3.2 Relative Output Factors

Output factors measured with each of the detectors under investigation were normalised to the output of the 100mm ϕ circle, as this was the largest circular field possible with the μMLC. This could therefore be related back to the standard calibration field of 10cm by 10cm using a standard Farmer ionisation chamber. MC simulations were performed by averaging the dose deposited to a 4 x 4 array of 1mm x 1mm x 1mm voxels distributed about the central axis of a phantom simulating the measurement conditions. As these voxels covered a significant amount of the open field and encroached close to the collimators, a single 1mm x 1mm x 1mm voxel was used for the 18mm circle field size and smaller. Figure 5.7 illustrates a comparison of outputs simulated for all field sizes using this method. Good agreement is observed between the simulations at all sizes. Although this may indicate that the use of the array may be appropriate for all field sizes a single point was used for the smallest field sizes to avoid any collimator effects influencing the simulated output factors.

A plot of the relative output factors for each of the detectors and Monte Carlo simulations is shown in figure 5.8 and tabulated in table 5.3.

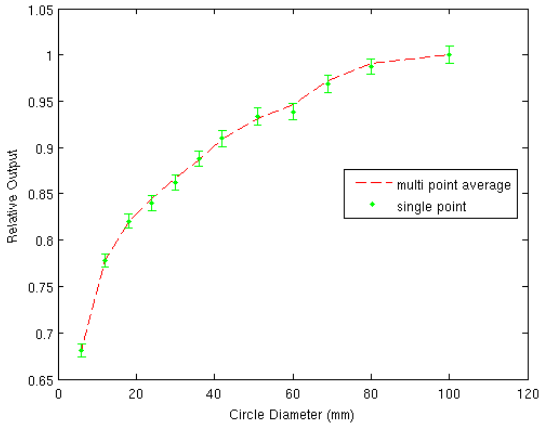

Figure 5.7: Comparison of simulated output factors measured at 10cm deep within a water phantom at 90cm FSD from the beam focus using an array of measurement points or a single point

	Detector							
Profile	cc01	efd	pfd	rk	sfd	cc13	MC	iPLAN
6mm x-profile	5.44	5.50	5.63	6.50	5.57	7.70	5.77	4.94
6mm y-profile	6.37	6.30	6.03	7.10	6.04	8.10	5.81	4.81
100mm x-profile	98.70	98.62	98.70	98.52	98.70	99.20	98.71	99.02
100mm y-profile	98.70	98.57	98.70	98.78	98.50	99.10	98.71	99.01

Table 5.2: Field widths in x and y directions measured and simulated using a variety of detectors.

Circle ϕ (mm)	pfd	sfd	cc13	rk	cc01	efd	rk hz	sfd hz	Farmer
100	1.0000	1.0000	1.0000	1.0000	1.0000	1.0000	1.0000	1.0000	1.0000
91	0.9888	0.9848	0.9880	0.9880	0.9880	0.9868	0.9880	0.9864	0.9868
80	0.9702	0.9609	0.9693	0.9695	0.9702	0.9643	0.9705	0.9657	0.9669
69	0.9492	0.9437	0.9485	0.9488	0.9467	0.9395	0.9485	0.9425	0.9446
60	0.9302	0.9123	0.9284	0.9277	0.9263	0.9188	0.9290	0.9206	0.9237
51	0.9087	0.8880	0.9060	0.9059	0.9014	0.8949	0.9063	0.8976	0.9006
42	0.8852	0.8613	0.8809	0.8815	0.8761	0.8685	0.8814	0.8714	0.8733
36	0.8680	0.8413	0.8623	0.8622	0.8556	0.8495	0.8624	0.8523	0.8509
30	0.8488	0.8198	0.8414	0.8428	0.8339	0.8280	0.8410	0.8324	0.8128
24	0.8270	0.7964	0.8146	0.8171	0.8068	0.8044	0.8116	0.8096	0.7135
18	0.8009	0.7673	0.7713	0.7808	0.7752	0.7751	0.7614	0.7801	0.5355
12	0.7510	0.7113	0.6532	0.6949	0.7032	0.7188	0.6015	0.7262	0.3064
6	0.5568	0.5466	0.3084	0.4063	0.4691	0.5393	0.2592	0.5565	0.0988

Table 5.3: Uncorrected output factors of circular fields defined by μMLC collimators measured with different detectors

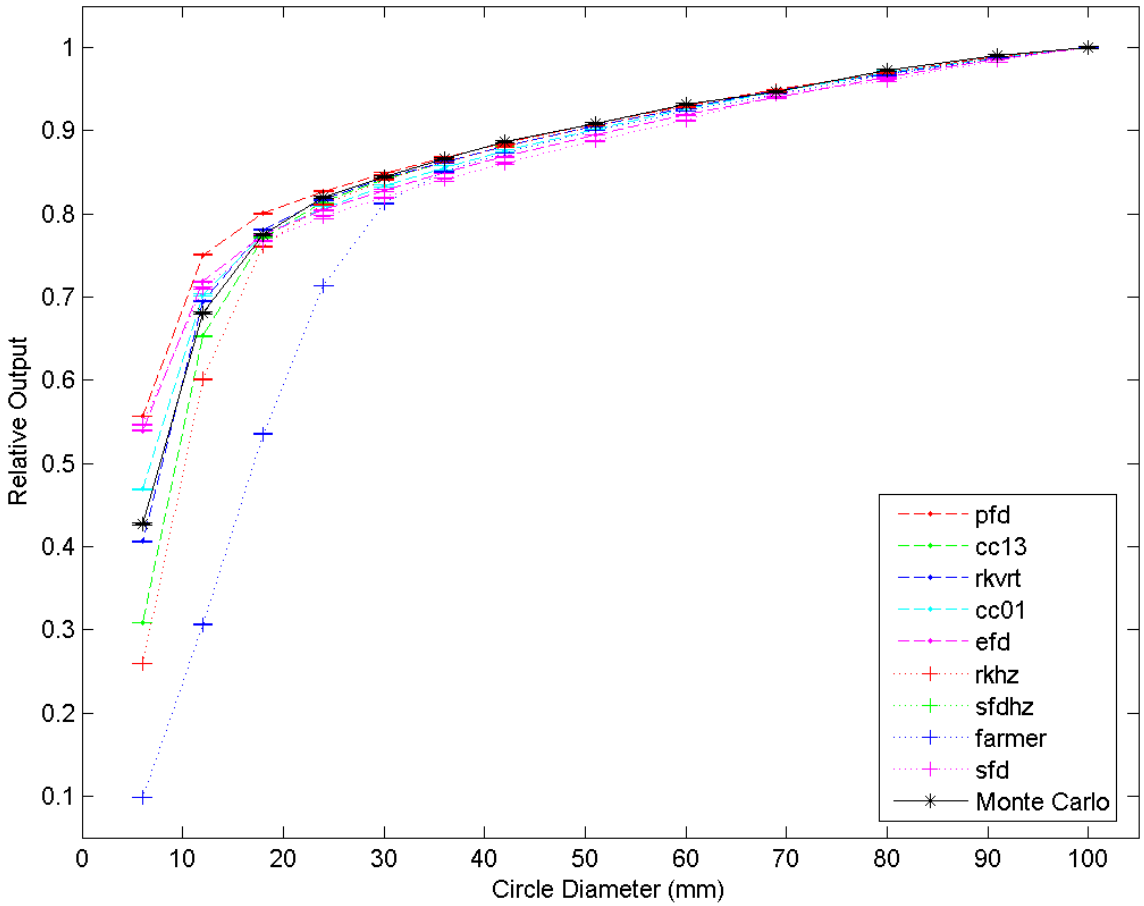

Figure 5.8: Comparison of measured and simulated output factors measured at 10cm deep within a water phantom at 90cm FSD from the beam focus using a variety of different detectors.

There is a spread in the calculated output factors measured and simulated of around 0.5% for field sizes greater than 42mm. This spread increases rapidly as the field size is decreased with the greatest variation occurring, unsurprisingly, at the smallest field size in which uncertainties associated with the detector size are largest. This is exemplified in the output factor for the 6mm circle which varies from less than 0.1 for the Farmer detector to greater than 0.5 for the diode detectors.

The cause of this effect is volume averaging, which occurs when the dimensions of the detector are greater than those of the radiation field under investigation. This is clearly the case for a Farmer chamber in a 6mm field and, compared with a reference 100mm field, the result is a much lower signal and hence a lower output factor.

5.3.2.1 Volume Averaging Effects

In order to investigate the effects of volume averaging, simulations were performed for each of the fields using a water phantom having 0.1mm x 0.1mm x 3mm voxels over the central 2.0cm x 2.0cm of the phantom to derive a high resolution description of the dose variation across the detector. Using the RTGrid Portal on the Cardiff University Condor pool as described in chapter 3, it was possible to obtain average uncertainties over the open part of the field of less than 0.50% within 12 hours of submitting to the pool for each field. A surface plot of this simulation for the 6mm circle field is shown in figure 5.9 illustrating the non-uniform dose distribution across the likely area of the detector at the central axis.

The doses from each field were then normalised to unity at the isocentre. For each detector, its extent was determined and the volume under this area was calculated to derive a volume averaging factor to be applied to each measurement. A separate simulation using 0.25mm x 0.25mm x 3mm voxels was run for the case of the Farmer chamber over the central 25mm x 6mm of the phantom. These factors are listed in table 5.4 and plotted in 5.11.

As can be seen, the factors are very close to unity in the case of larger fields for all of the detectors but deviate from this as the field size decreases. For the biggest detector, the Farmer chamber this occurs around the 30mm circle field

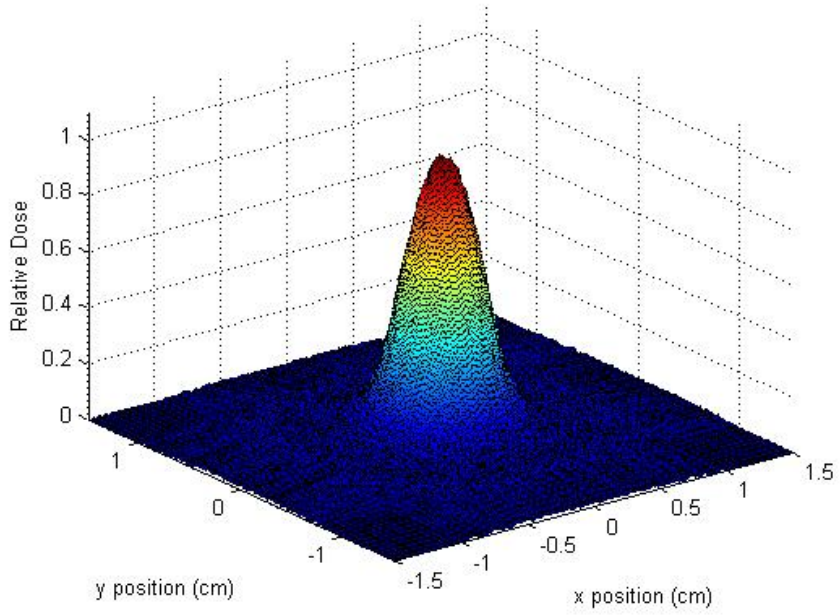

Figure 5.9: Surface plot of 6mm circle field, simulated using 0.1mm x 0.1mm x 0.5mm voxels, 10cm deep within a water phantom placed 90cm from the beam focus.

size, whereas for the smallest detector (SFDHZ) the factor remains more or less constant at unity throughout the field sizes examined, as indeed does the factor applied to the Monte Carlo simulations.

These volume averaging factors were then used to adjust the measured and simulated output factors according to equation 5.1. These adjusted factors are plotted in figure 5.10 and tabulated in table 5.5.

$$F_{scat} = \frac{\frac{R_{raw}(det,size)}{f_{volave}(det,size)}}{\frac{R_{raw}(det,ref)}{f_{volave}(det,ref)}} \tag{5.1}$$

where

- F_{scat} is the total scatter factor
- $R_{raw}(det, size)$ is the raw reading for the detector (det) and field size
- $f_{volave}(det, size)$ is the volume averaging factor for the detector and field

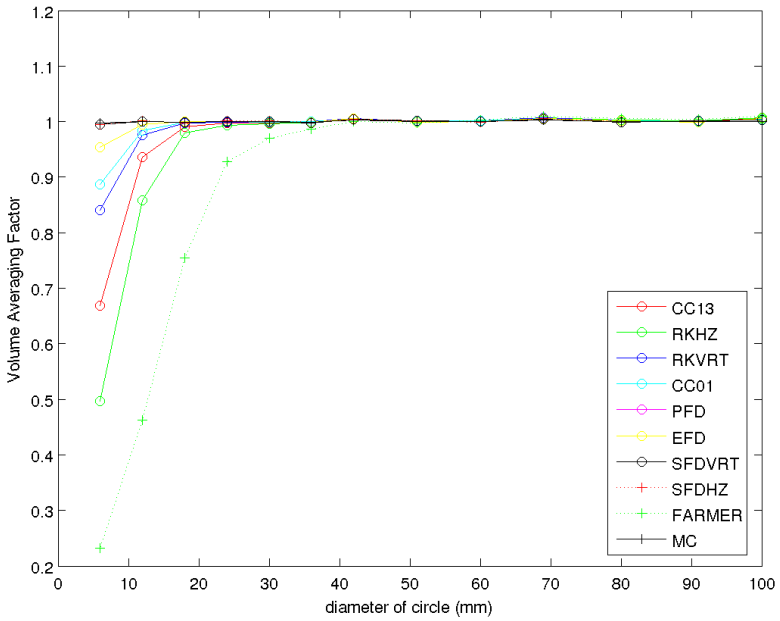

Figure 5.10: Plot of volume averaging factors for each of the investigated detectors.

size

- $R_{raw}(det, ref)$ is the raw reading of the reference field size
- $f_{volave}(det, ref)$ is the volume averaging factor for the reference field size using the detector

As can be seen, there is a convergence of some of the data indicating, unsurprisingly, that the volume averaging effect is the dominant effect in the deviation of these output factor measurements between detector types, with the EFD performing the best of the diodes and the CC01, being an ionisation chamber with the smallest detector volume showing the best agreement against the Monte Carlo simulations.

Circle ϕ(mm)	CC13	RKHZ	RKVRT	CC01	PFD	EFD	SFDVRT	SFDHZ	Farmer	MC
100	1.0056	1.0068	1.0048	1.0048	1.0061	1.0061	1.0023	1.0008	1.0103	1.0005
91	1.0003	1.0013	1.0007	1.0002	0.9982	0.9982	1.0016	1.0004	1.0046	1.0005
80	1.0018	1.0029	1.0016	1.0019	1.0008	1.0008	0.9992	0.9997	1.0061	1.0003
69	1.0072	1.0070	1.0066	1.0058	1.0060	1.0060	1.0047	1.0053	1.0093	1.0026
60	1.0013	1.0014	1.0011	1.0009	1.0003	1.0003	1.0005	0.9991	1.0031	1.0002
51	1.0001	0.9996	1.0002	1.0002	0.9993	0.9993	1.0011	1.0013	0.9980	1.0003
42	1.0055	1.0053	1.0052	1.0047	1.0050	1.0050	1.0036	1.0036	0.9997	1.0022
36	0.9992	0.9986	1.0002	0.9998	0.9991	0.9991	0.9979	0.9990	0.9871	0.9988
30	0.9979	0.9961	0.9985	0.9982	1.0000	1.0000	1.0002	1.0018	0.9707	0.9995
24	0.9970	0.9936	0.9989	0.9995	1.0005	1.0005	0.9998	1.0018	0.9276	1.0000
18	0.9901	0.9791	0.9970	0.9988	0.9998	0.9998	0.9984	0.9967	0.7546	0.9994
12	0.9357	0.8587	0.9761	0.9841	0.9948	0.9948	0.9996	1.0012	0.4626	0.9997
6	0.6681	0.4963	0.8410	0.8873	0.9537	0.9537	0.9943	0.9950	0.2322	0.9980

Table 5.4: Volume averaging factors for each of the detectors.

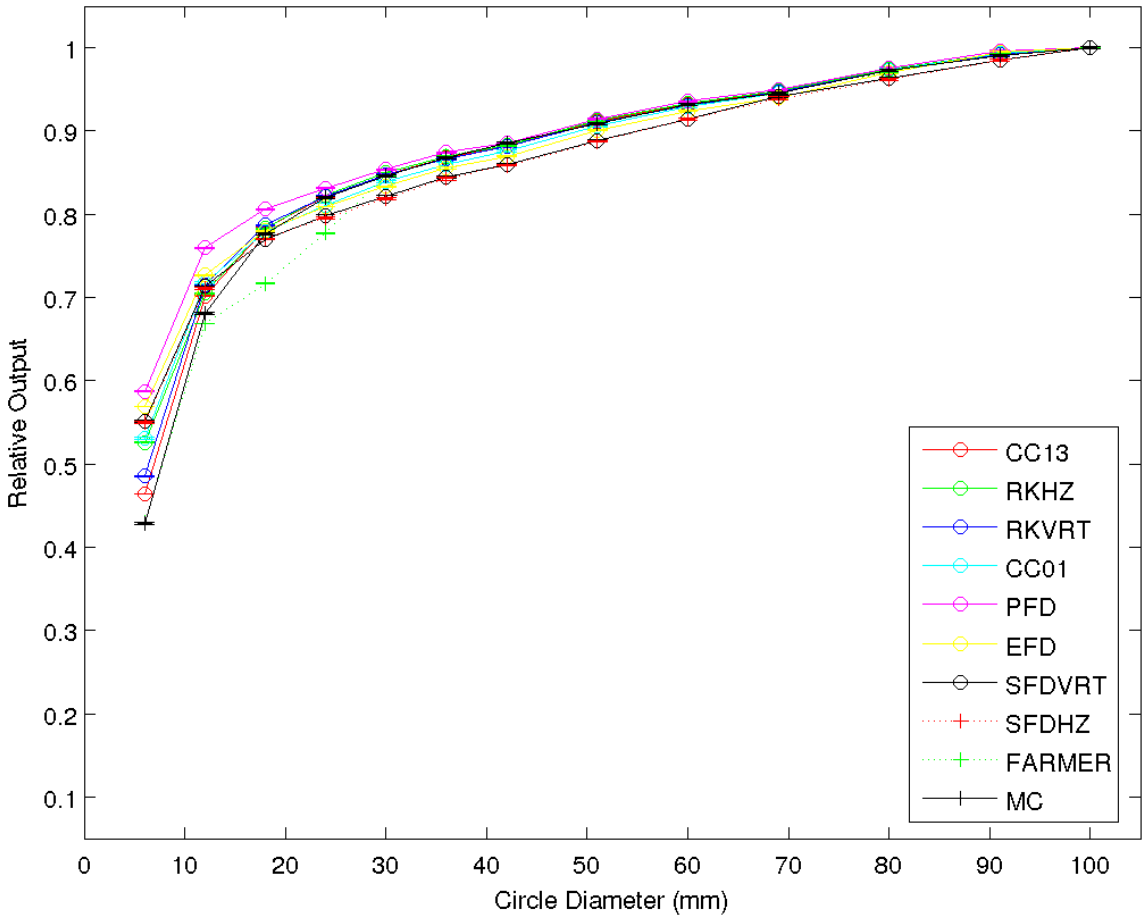

Figure 5.11: Comparison of measured and simulated output factors measured at 10cm deep within a water phantom at 90cm FSD from the beam focus using a variety of different detectors with volume averaging factors applied

5.3.2.2 Detector Material Compensation

As can be seen in figure 5.11, the PFD (photon diode) shows a more significant deviation from the Monte Carlo derived factors (and those measured by other detectors), particularly at the smaller field sizes. This detector contains what the manufacturer calls an 'integrated energy filter' (IBA Dosimetry GmbH, 2010; McKerracher and Thwaites, 2006), which appears to be a tungsten sheet placed within the diode construction to reduce the number of low energy photons traversing into the active region of the diode. Figure 5.12 illustrates the results of an investigation of the spectral components of the radiation transported to the central 4mm of the 6mm and 100mm ϕ fields. This was obtained by running the simulation of the accelerator with the appropriate field sizes using the BEAMnrc code alone with additional slabs of air and water appended to the accelerator model to simulate the phantom arrangement used in the simulation of total scatter factors. Although a fairly coarse series of bins were used, which may mask some effects such as an expected pair production peak at 511KeV it can be seen that there is a greater lower energy component in the 100mm circle, compared to that of the 6mm circle. Due to the differing stopping power ratios of water and higher Z components of silicon and tungsten, this could account for the difference in output of devices containing these elements compared to the Monte Carlo simulations and small ionisation chamber measurements.

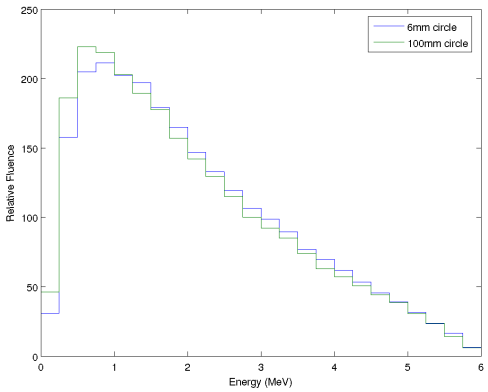

Figure 5.12: Spectral components of radiation over central 4mm of 6mm and 100mm ϕ circular fields.

In order to investigate potential composition effects, the simulation was repeated and the array of voxels used in the Monte Carlo derivation of output factor that had previously been set to a material of water were replaced with silicon voxels. A comparison of the output factors determined with this technique is shown in figure 5.13(a) and a plot of the relative outputs defined as the ratio of simulated dose in silicon to simulated dose in water is shown in 5.13(b). For the small fields in particular, there is a significant difference between the relative outputs simulated in water and silicon.

These factors were then applied to the measurements made with the diode detectors and again compared to those simulated by the Monte Carlo code. These are illustrated in figure 5.14, from which the further convergence of the measurement towards the Monte Carlo simulation can be seen.

Following the application of the volume averaging, and (where appropriate) silicon output factors the data sets shown in table 5.6 and figure 5.15 were obtained.

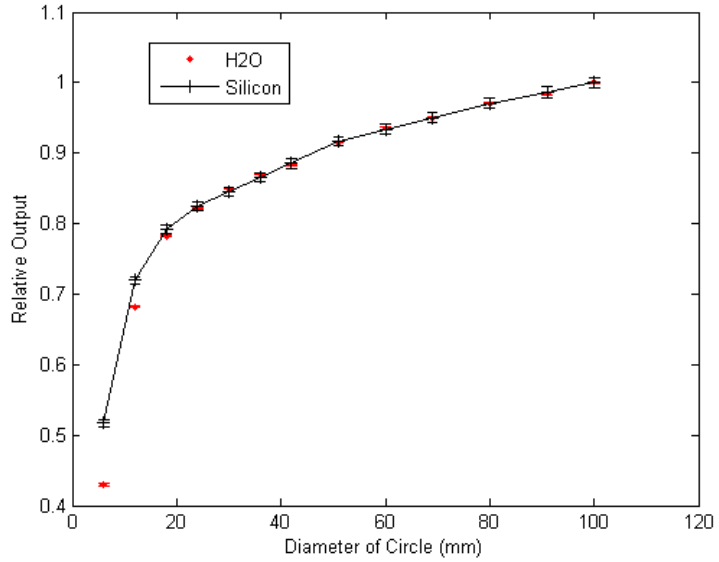

(a) Relative output factors simulated in Water and Silicon

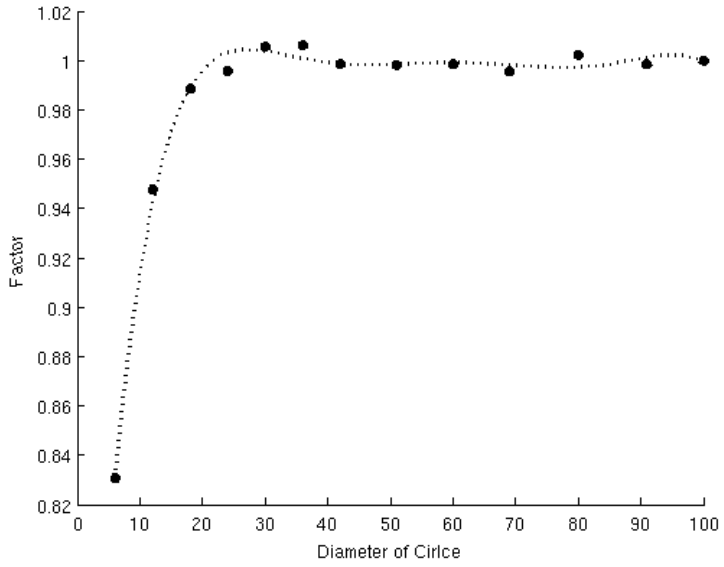

(b) Ratio of Water to Silicon Simulated Outputs

Figure 5.13: Graphical output of simulations using voxels of Water and Silicon

Circle ϕ(mm)	CC13	RKHZ	RKVRT	CC01	PFD	EFD	SFDVRT	SFDHZ	Farmer	MC
100	1.0000	1.0000	1.0000	1.0000	1.0000	1.0000	1.0000	1.0000	1.0000	1.0000
91	0.9932	0.9933	0.9921	0.9928	0.9966	0.9949	0.9855	0.9852	0.9924	0.9912
80	0.9730	0.9742	0.9726	0.9729	0.9753	0.9696	0.9638	0.9619	0.9710	0.9728
69	0.9469	0.9482	0.9471	0.9457	0.9493	0.9399	0.9414	0.9394	0.9456	0.9450
60	0.9324	0.9340	0.9312	0.9298	0.9356	0.9244	0.9139	0.9138	0.9304	0.9320
51	0.9109	0.9128	0.9102	0.9057	0.9149	0.9013	0.8890	0.8875	0.9117	0.9093
42	0.8810	0.8826	0.8813	0.8761	0.8862	0.8697	0.8601	0.8589	0.8826	0.8852
36	0.8679	0.8694	0.8663	0.8599	0.8741	0.8557	0.8449	0.8428	0.8709	0.8684
30	0.8479	0.8499	0.8481	0.8392	0.8540	0.8333	0.8215	0.8189	0.8460	0.8459
24	0.8216	0.8223	0.8219	0.8112	0.8317	0.8092	0.7983	0.7956	0.7772	0.8206
18	0.7833	0.7829	0.7869	0.7797	0.8059	0.7802	0.7702	0.7704	0.7170	0.7764
12	0.7020	0.7052	0.7153	0.7178	0.7595	0.7272	0.7132	0.7109	0.6691	0.6813
6	0.4642	0.5259	0.4855	0.5311	0.5875	0.5692	0.5511	0.5498	0.4300	0.4284

Table 5.5: Relative output factors following the application of volume averaging factors

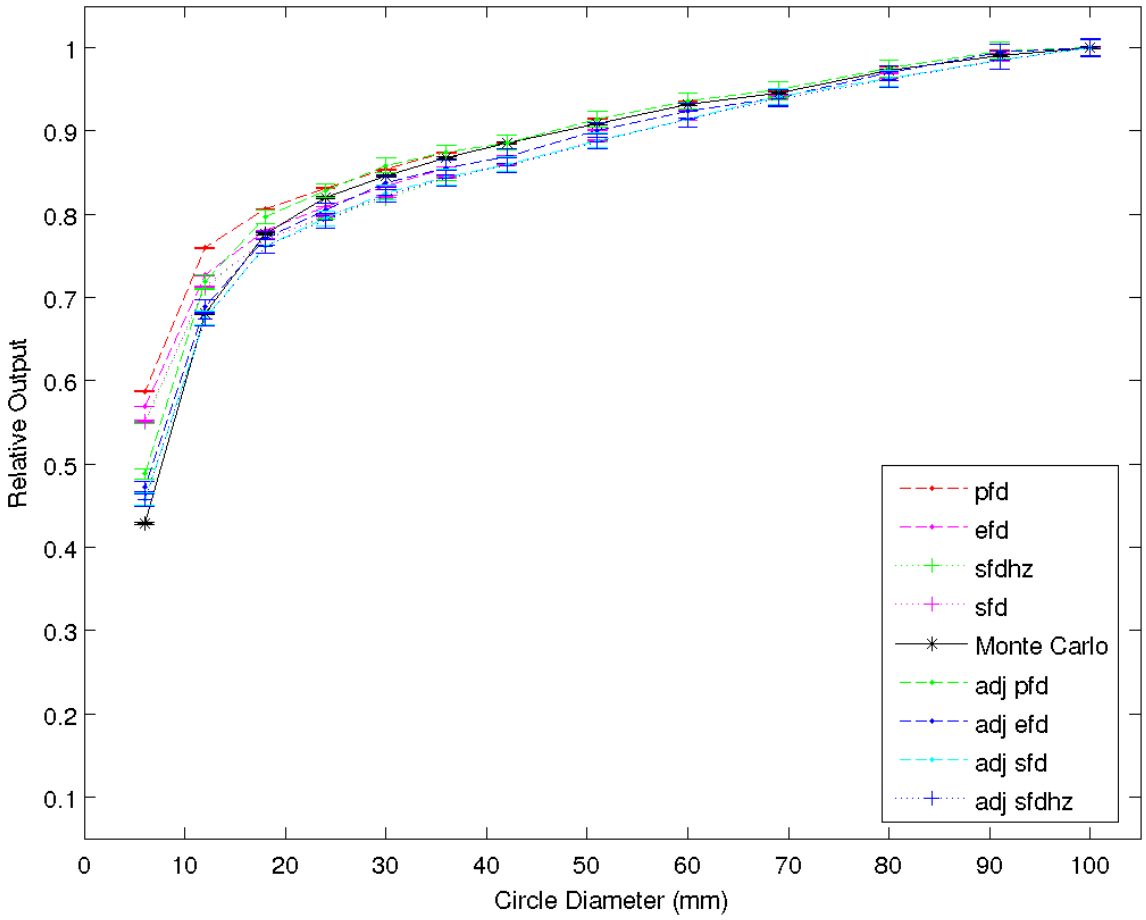

Figure 5.14: Measured Output factors of diode detectors with volume averaging factors applied and with and without silicon correction factors applied; 'adj pfd' etc. is the factor obtained with the application of the silicon correction factor.

Circle ϕ(mm)	CC13	RKHZ	RKVRT	CC01	PFD	EFD	SFDVRT	SFDHZ	Farmer	MC
100	1.0000	1.0000	1.0000	1.0000	1.0000	1.0000	1.0000	1.0000	1.0000	1.0000
91	0.9932	0.9933	0.9921	0.9928	0.9966	0.9949	0.9855	0.9852	0.9924	0.9912
80	0.9730	0.9742	0.9726	0.9729	0.9753	0.9696	0.9638	0.9619	0.9710	0.9728
69	0.9469	0.9482	0.9471	0.9457	0.9493	0.9399	0.9414	0.9394	0.9456	0.9450
60	0.9324	0.9340	0.9312	0.9298	0.9356	0.9244	0.9139	0.9138	0.9304	0.9320
51	0.9109	0.9128	0.9102	0.9057	0.9149	0.9013	0.8890	0.8875	0.9117	0.9093
42	0.8810	0.8826	0.8813	0.8761	0.8862	0.8697	0.8601	0.8589	0.8826	0.8852
36	0.8679	0.8694	0.8663	0.8599	0.8741	0.8557	0.8449	0.8428	0.8709	0.8684
30	0.8479	0.8499	0.8481	0.8392	0.8586	0.8378	0.8259	0.8233	0.8460	0.8459
24	0.8216	0.8223	0.8219	0.8112	0.8282	0.8057	0.7950	0.7922	0.7772	0.8206
18	0.7833	0.7829	0.7869	0.7797	0.7967	0.7712	0.7614	0.7615	0.7170	0.7764
12	0.7020	0.7052	0.7153	0.7178	0.7197	0.6891	0.6759	0.6737	0.6691	0.6813
6	0.4642	0.5259	0.4855	0.5311	0.4880	0.4728	0.4577	0.4567	0.4300	0.4284

Table 5.6: Final output factors following application of volume averaging and silicon correction factors.

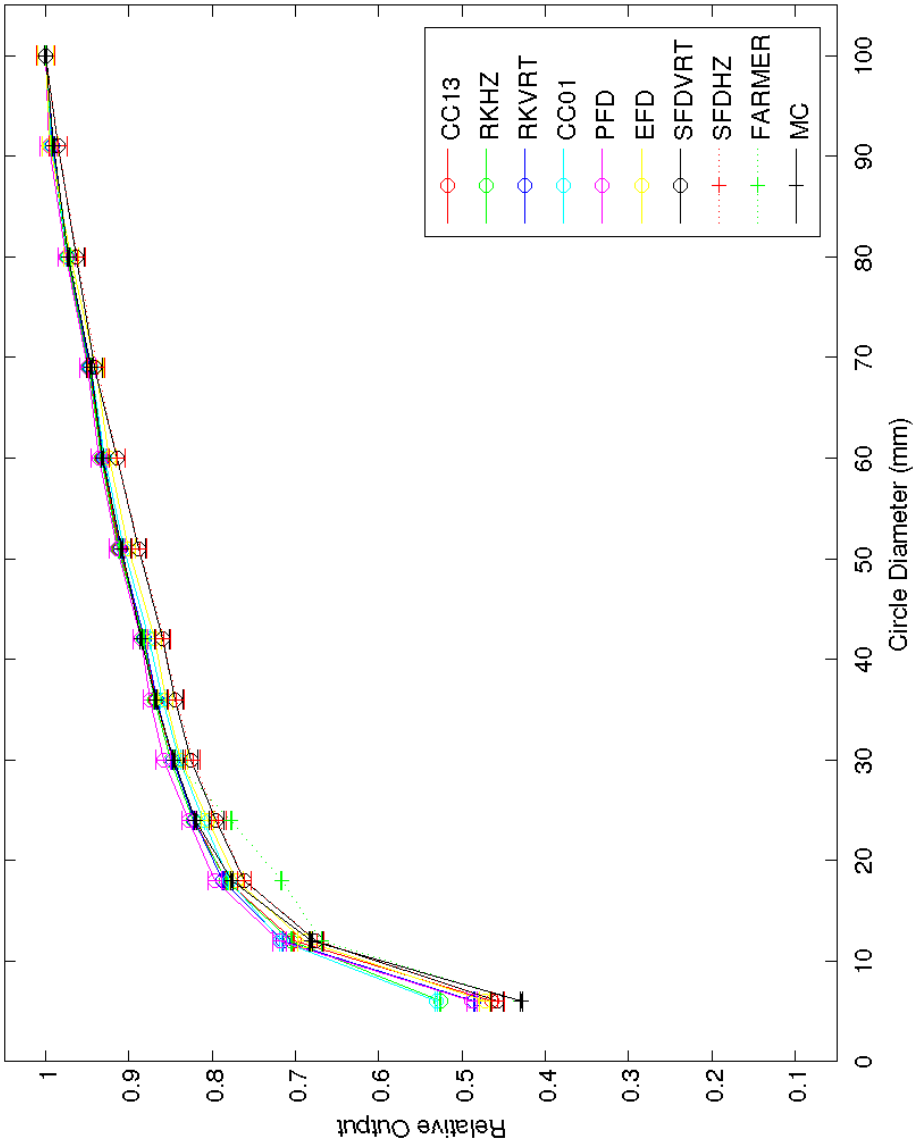

Figure 5.15: Measured Output factors of all detectors with application of volume averaging factors and with silicon correction factors applied to diode detectors.

There is a much closer agreement between all of the detectors and simulations with the application of both correction factors and for the most part of the curve most detectors agree within the experimental or simulation uncertainties. The exception to this is the Farmer chamber which deviates significantly for fields below 30mm ϕ despite agreeing well with the Monte Carlo simulation at the smallest field size. Despite the application of the correction factors, there is a difference of 20% between the lowest output factor of 0.428 (MC) with the highest factor of 0.526 measured with the RK chamber.

Table 5.7 tabulates the percentage difference between the factors measured and those simulated, which are graphically illustrated in figure 5.16. A fairly typical shape is shown of the differences between the detector measured output factors and MC simulations of generally less than 1% for the larger fields which increases rapidly for the smaller fields at around 30mm, depending on the detector. Compared to the MC simulations, it can be seen that the smaller ionisation chambers (CC01, CC13, RKHZ and RKVRT) show the best agreement with the diodes showing poorer comparisons to the MC factors. This is slightly in disagreement with the results reported by McKerracher and Thwaites (1999b), who found the SFD to be the most reliable detector when compared against a pinpoint ionisation chamber, although their chamber was different in design to the one used in this comparison.

The suitability of each detector for measurement, based on this investigation is tabulated in table 5.8, which is obtained by allowing the detector for use if it returns a relative output factor compared to the MC simulations of less than 1%. In the table this is illustrated by ✓. For detectors returning a difference slightly more or less than 1% but have differences at fields sizes on either of it that would allow or disallow their use, these are represented by a bracketed tick or cross. Differences of greater than 3% are shown with a double cross.

As can be seen none of the detectors are able to measure an output factor for the 6mm or 12mm ϕ fields to within 1% of the MC simulation, apart from the Farmer which exhibits large differences for fields smaller than 24mm, which would prohibit these field sizes for clinical use. However, the CC01, CC13, RKHZ and MC deliver factors within 1% of each other for the 18mm ϕ fields and larger with volume averaging factors applied. It could therefore be argued that this

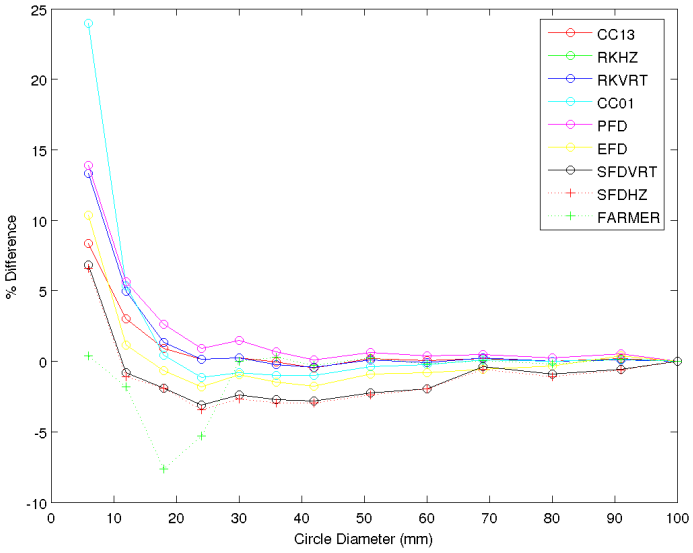

(a) Full Curve

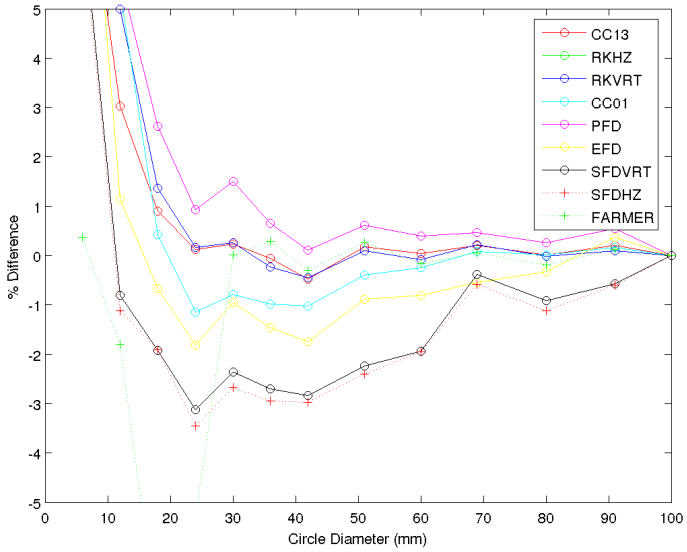

(b) Magnified

Figure 5.16: Percentage difference of output factors measured with each of the detectors compared to that derived from MC simulations.

would be the limit of the field sizes used locally within the department. This would require entry of this factor into the planning system and corresponding

validation for the range of usable field sizes to be extended as a consequence of this investigation.

5.3.3 Effect of Incident Source Size on Monte Carlo Simulations

5.3.3.1 Profiles

It has been shown by Wang and Leszczynski (2007) and Kim (2009a) that the doses simulated by Monte Carlo simulations are dependent on the incident source size. Chapter 4 has shown the variation in source size introduces a significant change in the shape of profiles, particularly near the surface of the phantom where, for large fields, the difference between the relative dose 15cm off axis may be as much as 10% for doses simulated using an incident source size of 0.5mm and 0.35mm. For smaller fields used in stereotactic radiotherapy, this effect is significantly smaller and a dose difference of 2% can be seen at 4cm off axis, which would be correspond to a field size (8cm) that would be rarely used in stereotactic techniques.

Figures 5.17 and 5.18 illustrate the simulations of profiles of a 100mm circular and 6mm circular fields at 100mm depth within a water phantom at 900mm from the source. As can be seen, there are differences between the data sets in both the penumbra and the *plateau* region of the profile which for the 100m circular field are 3% between the 0.5mm source and 3.5mm source at 35mm from the central axis. In the penumbra, the difference between the largest and smallest source sizes is approximately 2mm at the maximum deviation of the corresponding curves. The 6mm and 100mm circle field widths are tabulated in table 5.9 where a maximum deviation of 1mm, for the 100mm ϕ field and 2mm for the 6mm ϕ is observed between the smallest and largest incident source sizes in the 'Y' (MLC) direction. In the 'X' direction, the field widths for the 100mm circle are indistinguishable, whereas differences in the width of the 6mm diameter fields of more than 3mm (50% of the nominal field width) were seen. The shapes of the dose profile curves differ significantly in the penumbral regions. This is shown in figure 5.17(d), which is a magnification of the profiles illustrated in figure 5.17(b) for the 'Y' direction defined by μMLC. It can be seen that when using a smaller

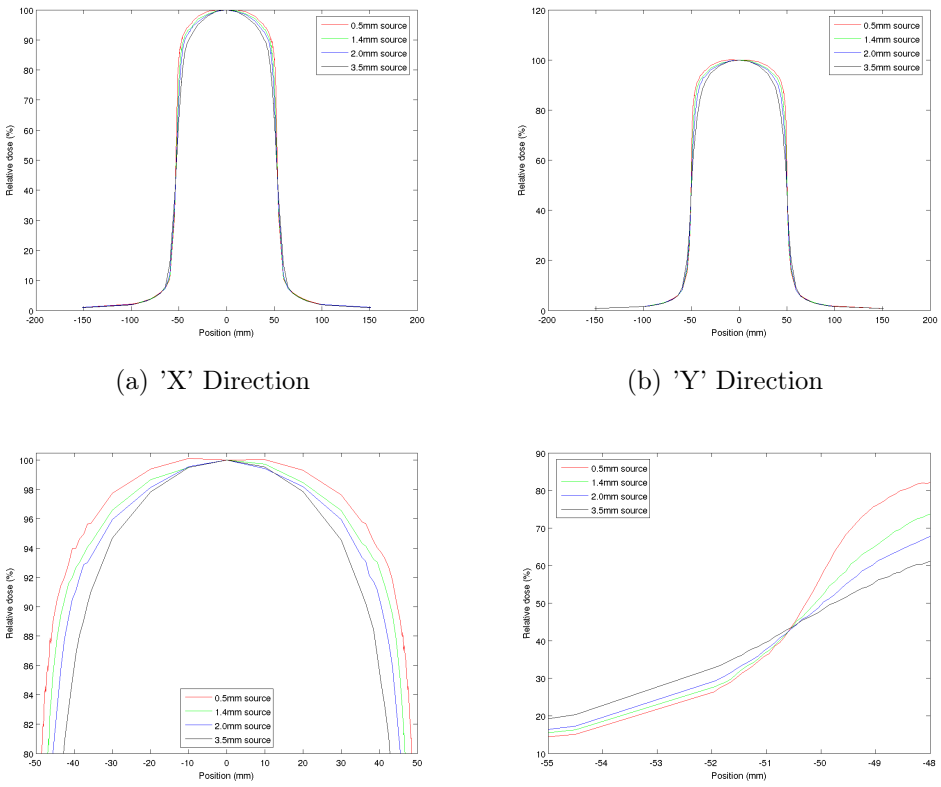

(a) 'X' Direction

(b) 'Y' Direction

(c) 'X' Direction

(d) 'Y' Direction

Figure 5.17: Simulated profiles of a 100mm ϕ circular field for a variety of incident source sizes, simulated at a depth of 100mm and an FSD of 900mm and normalised to the dose at the central axis. The lower diagrams are expanded versions of the figure above

incident electron source sharper edges of the fields are observed. The 1.4mm source, similar to that previously determined as the most appropriate size shows the closest agreement with the expected field size widths.

5.3.3.2 Depth Doses

The effect of incident source size on depth dose simulations was investigated by performing simulations of depth doses similar to those described in section 5.3.1.2 but the incident source size was varied as symmetric FWHM widths of 0.5mm, 1.4mm (closest to that found to give best agreement between simulated measured

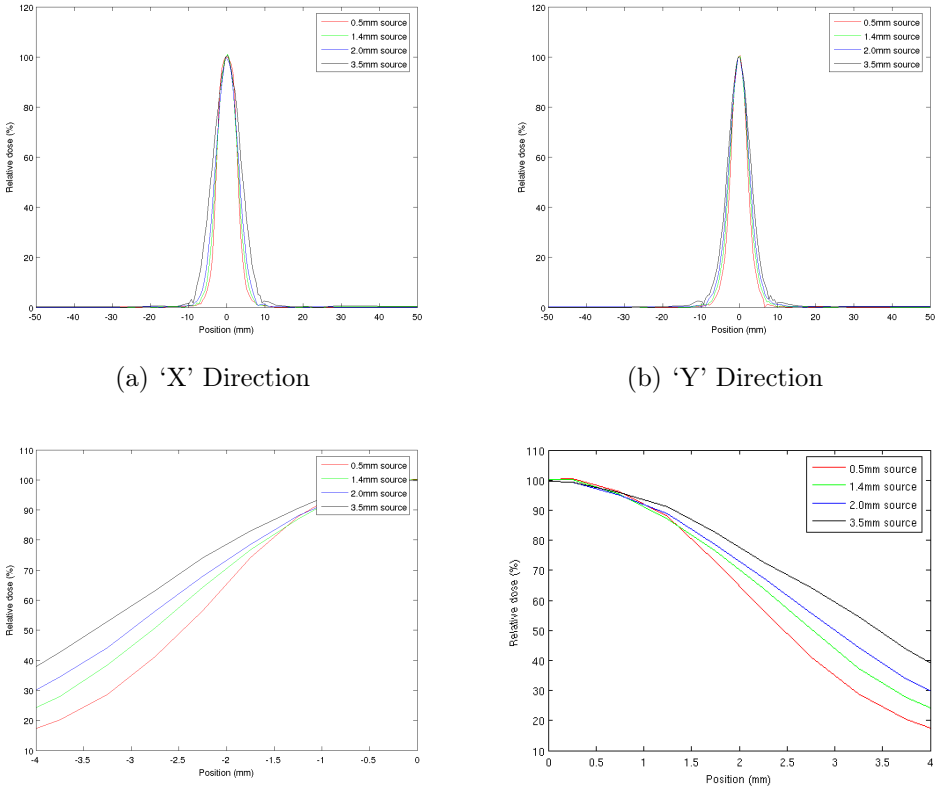

(a) 'X' Direction

(b) 'Y' Direction

(c) 'Y' Direction

(d) 'Y' Direction

Figure 5.18: Simulated profiles of a 6mm ϕ circular field for a variety of incident source sizes, simulated at a depth of 100mm and an FSD of 900mm and normalised to the dose at the central axis. Sub figures (c) and (d) are expanded illustrations of the penumbra on either side of the profile in the 'Y' direction.

doses), 2.0mm and 3.5mm. Results of this for a 100mm circle are illustrated in figure 5.20.

Although the curves are relatively noisy, it can be seen that they are relatively insensitive to the incident source width with a maximum deviation between the 0.5mm source and 3.5mm source curves of 1.8% comparable to the uncertainties of the simulations at this point of 1.2% and 0.8%.

Simulations for the 6mm circle show a greater deviation between the sources which are illustrated in figure 5.21.

Here it can be seen that there is a greater deviation in the curves which at

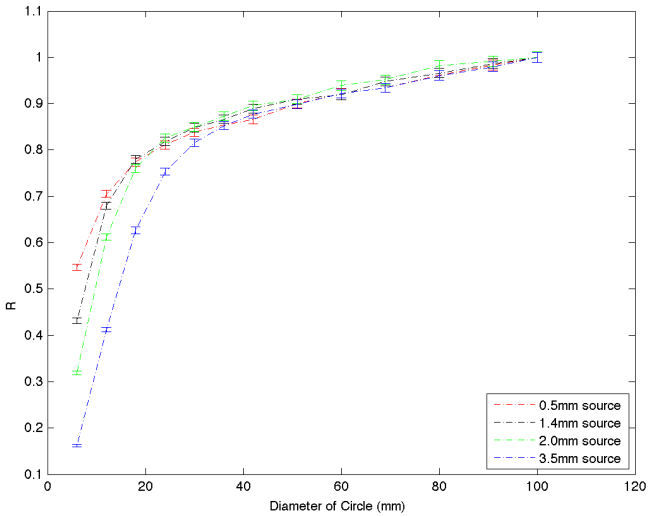

Figure 5.19: Simulated output factors using a variety of incident source sizes.

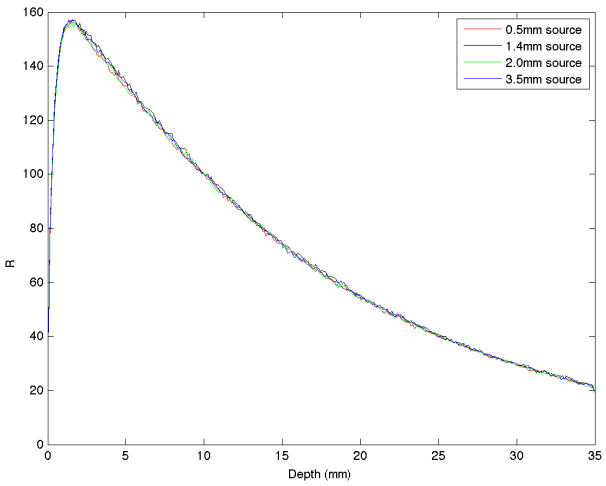

Figure 5.20: Simulated depth doses for a variety of incident source sizes for a 100mm ϕ circle, simulated at an FSD of 90cm and normalised to 100mm deep.

the depth of maximum dose, shown in figure 5.21(b) there is a difference of 4.1% between the 0.5mm and 3.5mm source widths, which have a maximum deviation of 18.5% of local dose at the deepest point in the phantom. Uncertainties at the depth of maximum were 0.5% and 0.7% for the 0.5mm and 3.5mm source size

simulations and 0.8% and 0.9% respectively at 350mm deep.

It can therefore be seen that Monte Carlo simulations of depth doses are strongly dependent on the incident source width for small fields where it is of more importance than the electron energy.

5.3.3.3 Output Factors

Variations in relative output factor with source size are more significant than that those observed for profile and depth dose measurements. This is illustrated in figure 5.19, which shows the relative output factors of circular fields of radius 100mm down to 6mm. For each curve, the simulated doses are normalised to the 100mm circular dose at the reference point for the incident source size. To avoid penumbral effects dominating the simulations a single voxel of 1mm x 1mm x 1mm was used to collect the doses in each simulation of a $100x10^6$ particles.

As can be seen the factors measured for the larger circles (greater than 30mm) there is good agreement between the data sets but as the field size is decreased there is a larger variation in the output factor, with the 3.5mm source producing a factor of only 27% of the 0.5mm factor, for the 6mm circular fields.

5.4 Conclusions

The main conclusion of this work is that the measurement and Monte Carlo simulation of small radiation fields can be problematic and should be undertaken with care. Section 5.3.1.1 has discussed the measurement of profiles using various detectors and compared them against Monte Carlo simulations. Profiles such as these are commonly used in the acquisition of raw data for input into a treatment planning system such as the BrainLAB iPLAN system which is used routinely within Velindre Cancer Centre for stereotactic planning.

Comparisons between the detectors and simulations indicate a strong dependence on detector geometry for measurements in the penumbra of the beam. The 100mm circle profiles show good agreement between the measurements and simulations over the central part of the beam but the shape of the penumbra differs in each case. This can be attributed to volume averaging

effects during measurement, which have the effect of broadening the width of the penumbra.

For the 6mm circle, where measurements are made up almost entirely of penumbral effects, there are marked differences between the measurement devices, with the larger devices deviating most from the Monte Carlo simulations. Interestingly the profiles obtained from iPLAN show the smallest width and would (to the planner's perspective) indicate that only 60% of the actual irradiated volume would be covered by such a field, causing larger fields to be used with a greater healthy tissue being irradiated than planned. Consequently, until this is investigated further and resolved, such small fields will not be used clinically with this system.

Similar results were obtained with the depth dose measurements and simulations. For large fields, such as the 100mm circle, excellent agreement between the detectors was observed apart from near the surface of the phantom where large differences were seen due to the different geometries of each of the detectors breaking the surface of the phantom and introducing errors in the measured curve.

For the smaller fields, such as the 6mm circle, significant deviations were observed between the detectors, with the smaller detectors (such as the CC01, and SFD diodes) giving the closest agreement with the Monte Carlo simulations. This would agree with the proposition that the large differences seen in these curves are due to the spatial resolution of these detectors. At the depth of dose maximum, differences of greater than 15% of local dose are observed and again would indicate that such fields be used with care. iPLAN underestimates the dose compared to the Monte Carlo simulations and diode measurements by approximately 8% and has a position of maximum dose closer to the surface than any of the detectors.

Relative output factor investigations have indicated a wide variation in the detectors compared to simulations, which can be attributed and accounted for to some degree by the application of volume averaging and detector material correction factors. These eliminate many of the differences between the data sets but again indicate extreme caution should be used when using the particularly small fields of less than 12mm ϕ.

Although requiring further work to tune the model and correction factors, MC simulations do offer a method for determining the areas of greatest uncertainty in small field measurement and give increasing confidence in dosimetry for some fields such as those in the 18mm - 42mm ϕ circle range, which should be used with care. MC offers a method for determining individual detector correction factors for volume and detector material effects.

Further detailed modelling of the detectors (such as using more exact models of the detector in the simulation phantom) could further enhance these factors, which together with a very well validated description of the accelerator geometry, incident electron energy and source size one could provide even more accurate factors and correct measurements for these effects. One problem to be overcome to do this would, of course, be the validation of the source size parameters used in the simulation. Comparison against uncertain measurements to determine these parameters may lead to a tautology with inappropriate factors being applied. Therefore, other techniques such as a direct measurement of the source using a pinhole camera technique as discussed by Lief and Lutz (2000) may be helpful in determining the source size, keeping this fixed and adjusting the incident electron energy only, in the validation simulations to arrive at a unique combination of energy and source size.

Circle ϕ(mm)	CC13	RKHZ	RKVRT	CC01	PFD	EFD	SFDVRT	SFDHZ	Farmer
100	0.0000	0.0000	0.0000	0.0000	0.0000	0.0000	0.0000	0.0000	0.0000
91	0.2108	0.2197	0.0973	0.1681	0.5460	0.3744	-0.5720	-0.6049	0.1259
80	0.0189	0.1454	-0.0128	0.0159	0.2599	-0.3207	-0.9186	-1.1149	-0.1850
69	0.1998	0.3387	0.2201	0.0757	0.4577	-0.5461	-0.3865	-0.5902	0.0569
60	0.0424	0.2121	-0.0801	-0.2390	0.3909	-0.8102	-1.9415	-1.9477	-0.1674
51	0.1809	0.3901	0.0943	-0.3950	0.6121	-0.8833	-2.2324	-2.3987	0.2647
42	-0.4780	-0.2882	-0.4439	-1.0221	0.1155	-1.7454	-2.8337	-2.9746	-0.2958
36	-0.0593	0.1147	-0.2387	-0.9755	0.6571	-1.4560	-2.6978	-2.9436	0.2920
30	0.2354	0.4744	0.2567	-0.7895	1.4991	-0.9590	-2.3622	-2.6705	0.0163
24	0.1231	0.2075	0.1605	-1.1439	0.9281	-1.8094	-3.1219	-3.4568	-5.2934
18	0.8973	0.8398	1.3591	0.4290	2.6149	-0.6645	-1.9294	-1.9099	-7.6442
12	3.0265	3.5017	4.9887	5.3439	5.6330	1.1415	-0.8043	-1.1179	-1.7958
6	8.3635	22.7664	13.3279	23.9695	13.9101	10.3633	6.8513	6.6120	0.3706

Table 5.7: Percentage differences between output factors measured with different detectors and Monte Carlo.

Circle ϕ(mm)	CC13	RKHZ	RKVRT	CC01	PFD	EFD	SFDVRT	SFDHZ	Farmer
100	✓	✓	✓	✓	✓	✓	✓	✓	✓
91	✓	✓	✓	✓	✓	✓	✓	✓	✓
80	✓	✓	✓	✓	✓	✓	✓	(✓)	✓
69	✓	✓	✓	✓	✓	✓	✓	✓	✓
60	✓	✓	✓	✓	✓	✓	✗	✗	✓
51	✓	✓	✓	✓	✓	✓	✗	✗	✓
42	✓	✓	✓	(✓)	✓	✓	✗	✗	✓
36	✓	✓	✓	✓	✓	✗	✗	✗	✓
30	✓	✓	✓	✓	✗	✗	✗	✗	✓
24	✓	✓	✓	(✓)	(✗)	✗	✗✗	✗✗	✗✗
18	✓	✓	✗	✓	✗	(✗)	✗	✗	✗✗
12	✗✗	✗✗	✗✗	✗✗	✗✗	✗	(✗)	✗	✗
6	✗✗	✗✗	✗✗	✗✗	✗✗	✗✗	✗✗	✗✗	(✗)

Table 5.8: Suitability of detectors examined for measurement as a function of field size. A ✓indicates an output factor within 1% of the MC factor and a ✗the converse. A (✓) or (✗) indicates a comparison slightly over or under 1% but has agreement either side of it, indicating use or otherwise. ✗✗indicates a significant difference (>3%) of the MC simulation.

FWHM Source Width	6mm x	6mm y	100mm x	100mm y
0.5mm	5.77	5.00	106.47	100.59
1.4mm	5.75	6.01	106.47	100.18
2.0mm	6.75	6.00	106.47	100.00
3.5mm	8.91	6.93	106.46	99.58

Table 5.9: Field widths measured for 6mm and 100mm ϕ circles in x and y directions measured with different incident electron source size widths.

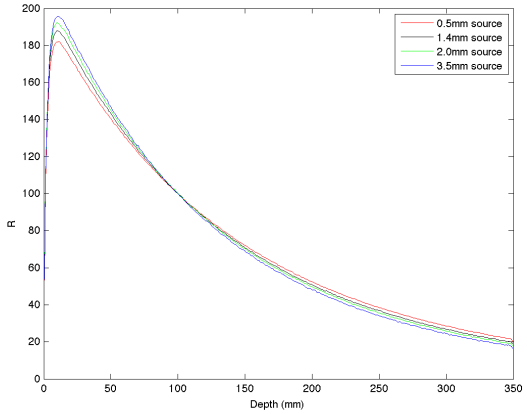

(a) Full Curve

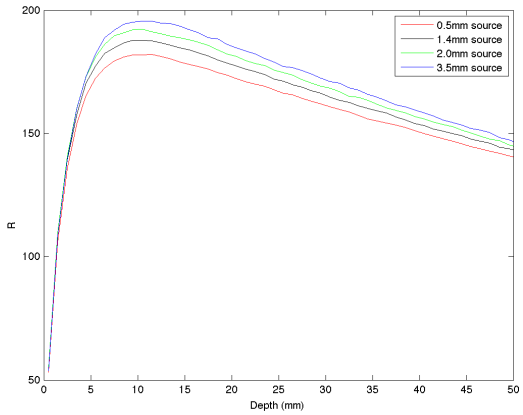

(b) Near Depth of Maximum Dose

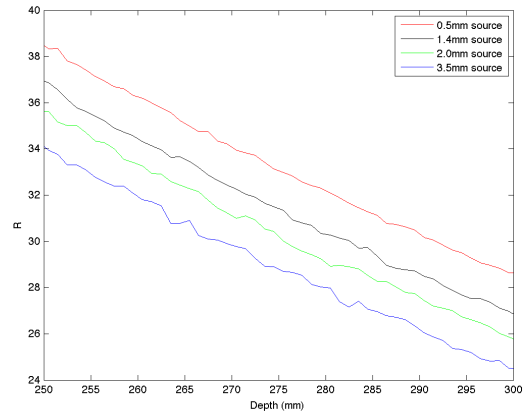

(c) Near 275mm deep

Figure 5.21: Simulated depth doses for a variety of incident source sizes for a 6mm ϕ circular field, simulated at an FSD of 90cm and normalised to 100mm deep.

Chapter 6

Applications of BLMLC II : Treatment Plan Verification

Contents

6.1 Treatment planning system

Treatment planning of cranial stereotactic radiotherapy at Velindre Hospital is performed using the BrainLAB iPLAN treatment planning system (TPS). The available functionality includes treatment planning with and without stereotactic localisation, image fusion of magnetic resonance images (MRI) with planning or diagnostic CT images and dose calculations using a pencil beam algorithm (Mohan et al., 1986),(Mohan and Chui, 1987).

It is generally recommended (Potter, 2000) that an independent calculation of monitor units is performed prior to the delivery of treatment for all forms of radiotherapy. Due to the issues associated with the dosimetry of small radiation fields outlined in Chapter 5, it may be difficult to perform this accurately using a standard approach of percentage depth doses (PDDs) (or tissue phantom ratios (TPRs)) and output factors. Furthermore, due to the nature of stereotactic radiotherapy, doses at points other than the prescription or normalisation point, such as those within or close to the sensitive structures within the irradiated volume, may be of equal or greater, importance. It has also been discussed in Chapter 2 that there are situations where the algorithms used within the iPLAN TPS suffer from large differences between calculated results and measurements with the lowest uncertainties, such as in regions of high tissue heterogeneity. Additionally, it is reasonably common for tables of output factors and TPRs to be obtained with the same detectors and phantoms as those used in the initial acquisition of the treatment planning data and thus these may not be entirely independent, even if a different calculation formalism is used.

For plans where a tabular output factor based check system is appropriate, such as at the centre of relative large fields, point doses off central axis may be problematic due to the difficulty of applying point corrections at positions where there are high dose gradients. This is frequently the case with small fields. It was shown in chapter 5 that the accuracy in this region is very dependent on the detector used in initial data acquisition.

A full MC simulation of the treatment delivered using the exact patient geometry and an accurate model can eliminate or minimise these issues and enable doses to be examined over the whole irradiated volume as well as at the prescription or normalisation point.

6.2 Methods and Materials

The use of a Monte Carlo system for routine verification of stereotactic treatments was investigated using the model of the accelerator and μMLC described in chapter 4 and the RTGrid processing framework described in chapter 3.

The work-flow of the investigation is shown in figure 6.1

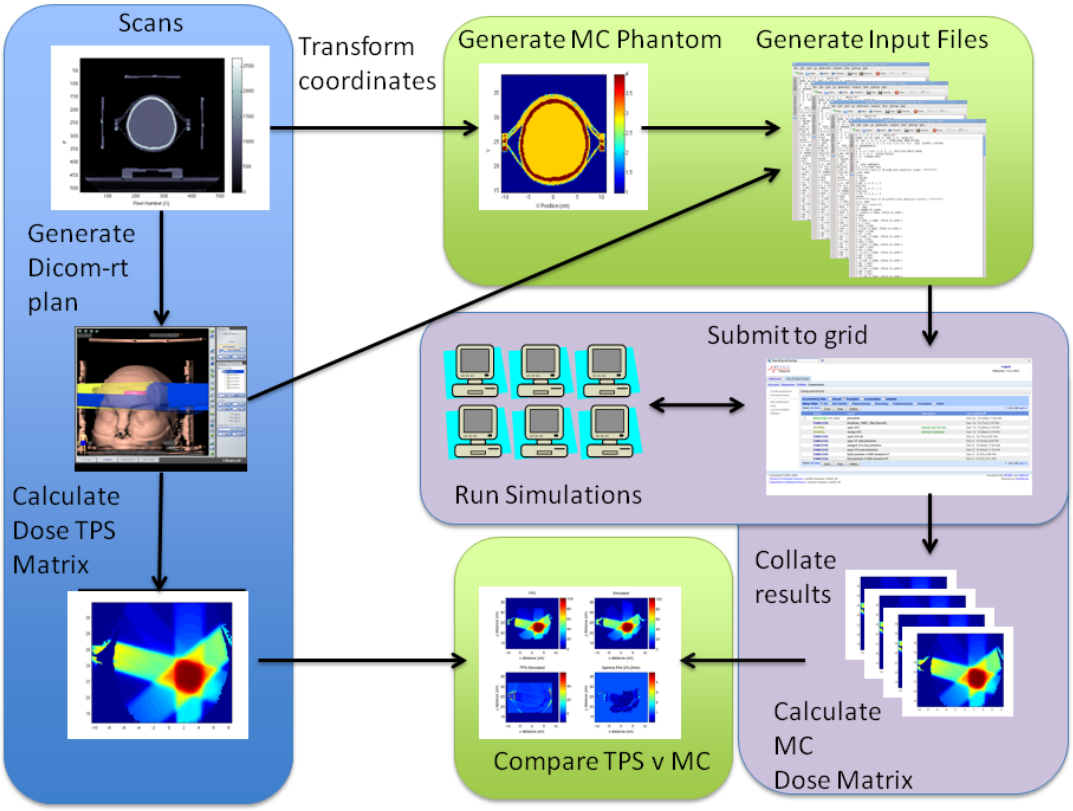

Figure 6.1: Work flow used in the verification of stereotactic plans using Monte Carlo simulations using the RTGrid distributed computing portal.

6.2.1 Phantoms

The patient specific simulations were performed using DOSXYZnrc phantom using patient anatomy derived from the original planning CT scans. A MATLAB[1] script was written, specifically for this project, to perform the necessary steps to generate the phantom; these were :

1. Collation of the CT data sets and sorting into the correct order
2. Removal of the stereotactic localising box from CT scans

[1]Mathworks software Ltd, Natick, Massachusetts, USA

3. Re-sampling of CT data to a convenient resolution (typically 256 x 256 pixels per slice, giving a typical resolution of around 1mm x 1mm)

4. Allocation of density and materials to each voxel

5. Conversion of data into format readable by DOSXYZnrc

The collation of the CT scans was done by simply exporting the data to the computer running the MATLAB software via a DICOM send of the data from the scanner to a DICOM listener on the host computer or by simply sending raw DICOM files between the systems. The DICOM server option was investigated as this offered the opportunity of developing a service running on the host computer to automatically generate a phantom on delivery of the CT scans at the host computer, although this has yet to realised in routine practice.

Patients undergoing a stereotactic treatment are scanned with the localising box applied to enable transformation of the acquired CT co-ordinates into stereotactic co-ordinates. As this will not be present in any subsequent treatment the next stage of the process is to remove the localising box from the patient CT data.

The Hounsfield units (HU) of these images were then converted into densities according to the calibration curve shown in figure 6.3, from which a linear fit was obtained over the two parts of the curves shown in equations 6.1:

$$\begin{aligned} density &= 0.00097661 * HU + 0.017966 \quad HU \leq 1024 \\ density &= 0.00047328 * HU + 0.55555 \quad HU > 1024 \end{aligned} \tag{6.1}$$

These figures were obtained by scanning a phantom comprising known densities, shown in figure 6.2, using the protocol used by the CT scanner for all stereotactic treatments and measuring the average Hounsfield unit over the volumes of interest and plotting these against the quoted density. The material of each voxel was then assigned according to a binning process based on the acquired HU described by table 6.1

The arrays of co-ordinate, density and material information were written to a file in the *.egsphant* format used by DOSXYZnrc for such simulations and

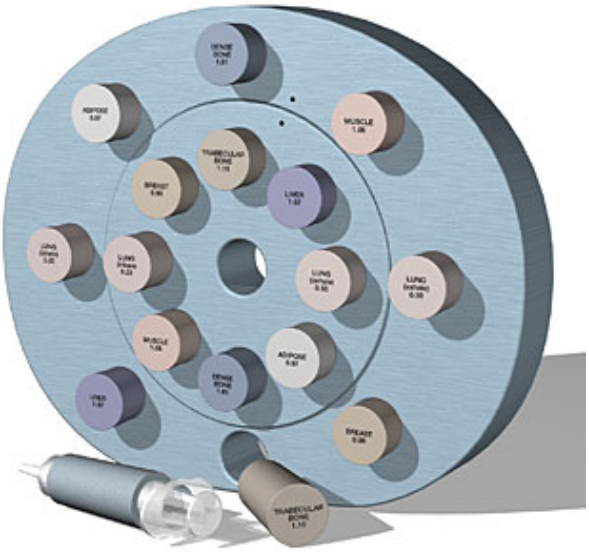

Figure 6.2: CIRS hounsfield unit phantom showing inserts of different densities.

incorporated into a DOSXYZnrc simulation using a BEAMnrc simulation as an input source.

HU Range	Material	PEGS4 Material
0-50	Air	AIR521ICRU
51-300	Lung	LUNG521ICRU
301-1125	Tissue	ICRUTISSUE521ICRU
1126	Bone	ICRPBONE521ICRU

Table 6.1: Materials used in the generation of phantoms for patient-specific DOSXYZnrc phantoms.

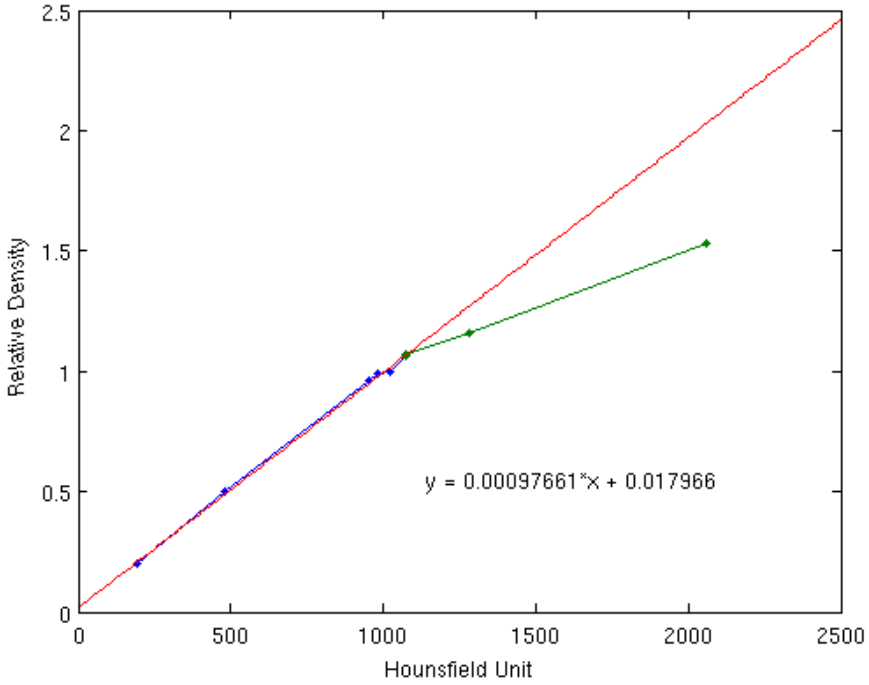

(a) Low HU range

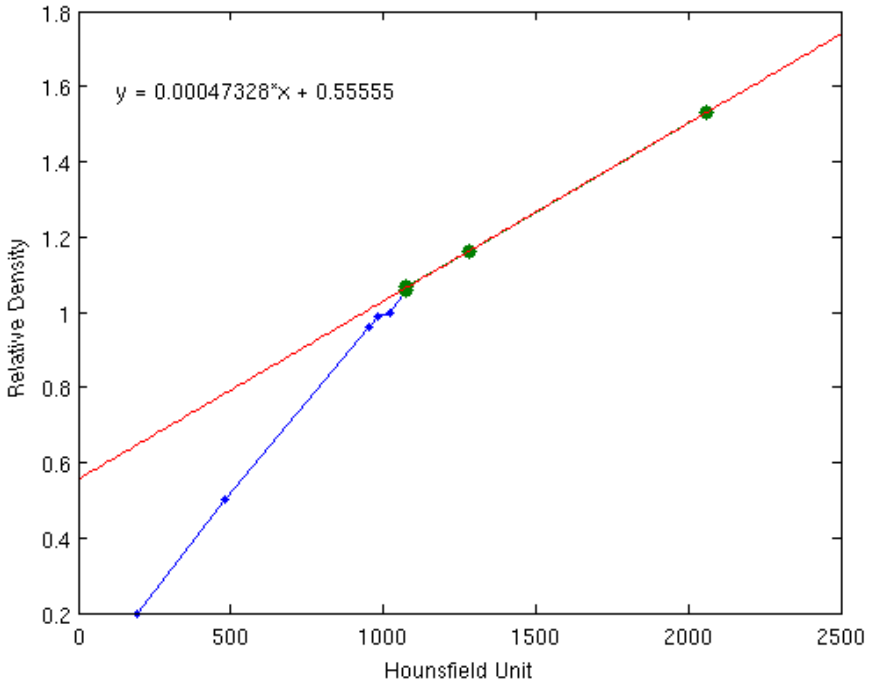

(b) High HU range

Figure 6.3: Hounsfield Unit (HU) conversion to density calibration curves.

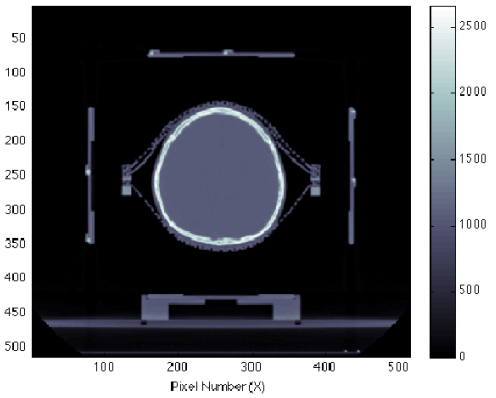

(a) Original CT with localiser attached to patient

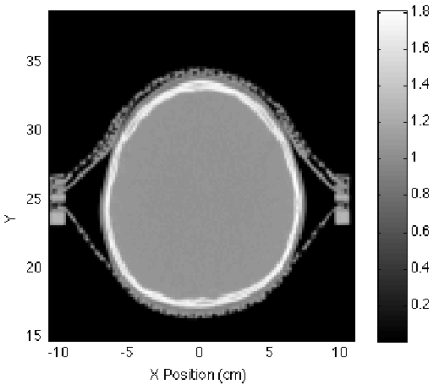

(b) CT with localiser removed

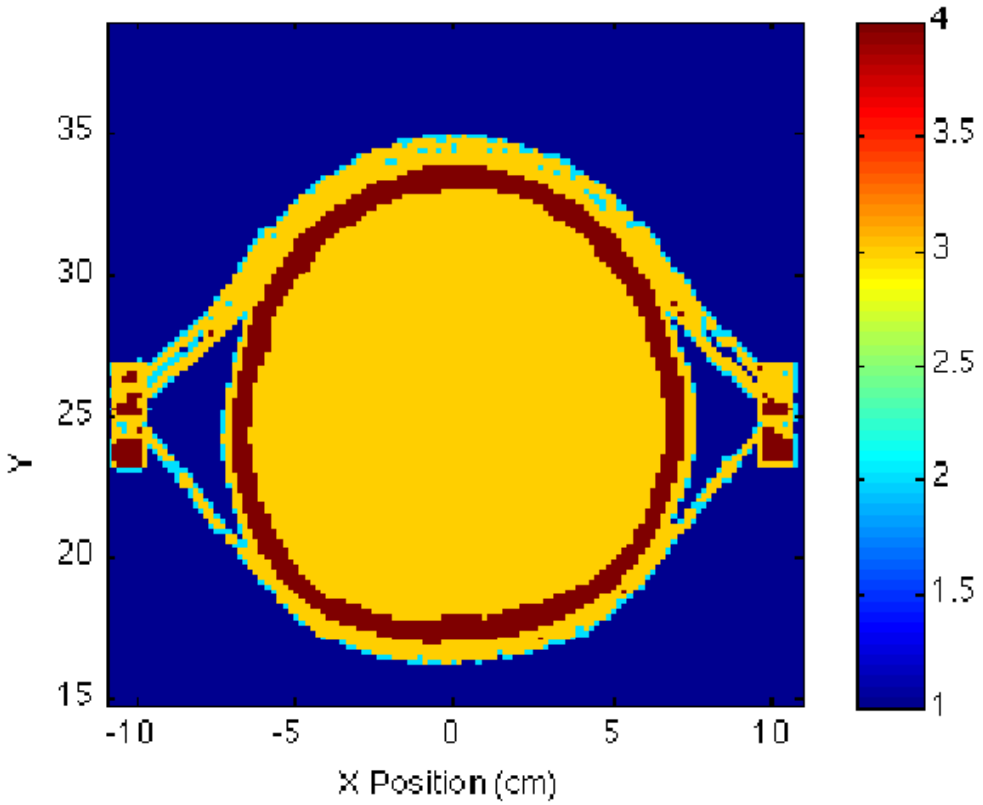

(c) Map of materials used in the simulation (1=Air, 2=Lung, 3=Tissue, 4=Bone)

Figure 6.4: Phantoms Used in Monte Carlo simulations of clinical plans.

6.2.2 Monte Carlo Simulations

The plan was simulated using the array of computers attached to the RTGrid described in chapter 3. To eliminate the requirement to transfer phase space files across the network, a full BEAMnrc simulation of the accelerator was provided as the source (ISOURCE=9) to the DOSXYZnrc simulation. The parameters used in the simulation are listed in table 3.1, which are identical to those used in the validation of the model.

For each treatment plan, a total of 250x10^6 particles were simulated for each case. These were divided in direct proportion to the number of monitor units planned for each beam so that the lowest simulation uncertainties were associated with the highest weighted beams. As the phantom for each patient occupied computer disk space of about 50Mb, each beam was divided into 100 jobs so that the size of the total returned phantoms for a five beam plan was around 25Gb. This was around the limit of storage space available for use. Typically, each individual job took about 3 hours of processor time. In practice, with the overhead of setting up the jobs and the requirement to wait until jobs submitted to the slower computers were completed, the total run time from the user perspective was approximately 4-5 hours. Once the complete set of runs for each plan was complete, the simulated doses were combined at each point with the phantom according to equation 4.1. For a phantom with 1mm x 1mm x 1mm voxels, the average uncertainty of doses greater than 20% of the dose at the prescription point was of the order of 1% .

6.2.3 Analysis

The outputs of the MC simulation were then compared to the doses calculated by the TPS. Doses were extracted from the TPS using the dose export function of iPLAN,which facilitated the export of dose points in an ASCII file easily readable by a script written in MATLAB into a 3 dimensional array. A calculation grid of 1mm x 1mm x 1mm was used and the doses sampled at 1mm x 1mm x 1mm for the output to the ASCII file. This export feature uses co-ordinates based on start and end positions specified by the user and may therefore not correspond directly with those of the TPS calculation matrix.

Doses from the Monte Carlo simulations were then similarly read into a 3D array and converted to absolute values using the method described in 4.3.4.5. During the phantom generation process the co-ordinates of DOSXYZnrc phantom were derived from the calculation matrix extracted from iPLAN. Therefore further re-sampling of the data was not required to perform subsequent comparisons.

Comparisons between the dose were made using the gamma method described by Low et al. (1998). This considers the distance to agreement (DTA) and absolute point differences between two data sets by calculating the multidimensional distances between the two data sets in terms of dose and distance scaled as a fraction of the acceptance criteria.

This is graphically illustrated in figure 6.5 illustrating a single measurement point $\vec{r_m}$ at the origin of the representation. The x and y axes represent the spatial locations $\vec{r_c}$ of the calculated distribution relative to the measured point. The remaining axis, δ, is the difference between the measured $[D_m(\vec{r_m})]$ and calculated $[D_c(\vec{r_c})]$ doses. The DTA criterion Δd_m, is represented by the shaded circle in the $\vec{r_c} - \vec{r_m}$ plane with a radius of Δd_M. Similarly the acceptance dose criterion is represented by a circle of radius ΔD_M in the $\delta - x$ plane.

The combined acceptance criteria can then be considered as:

$$\Gamma = \sqrt{\frac{r^2(\vec{r_m}, \vec{r})}{\Delta d_M^2} + \frac{\delta^2(\vec{r_m}, \vec{r})}{\Delta D_M^2}} \tag{6.2}$$

where

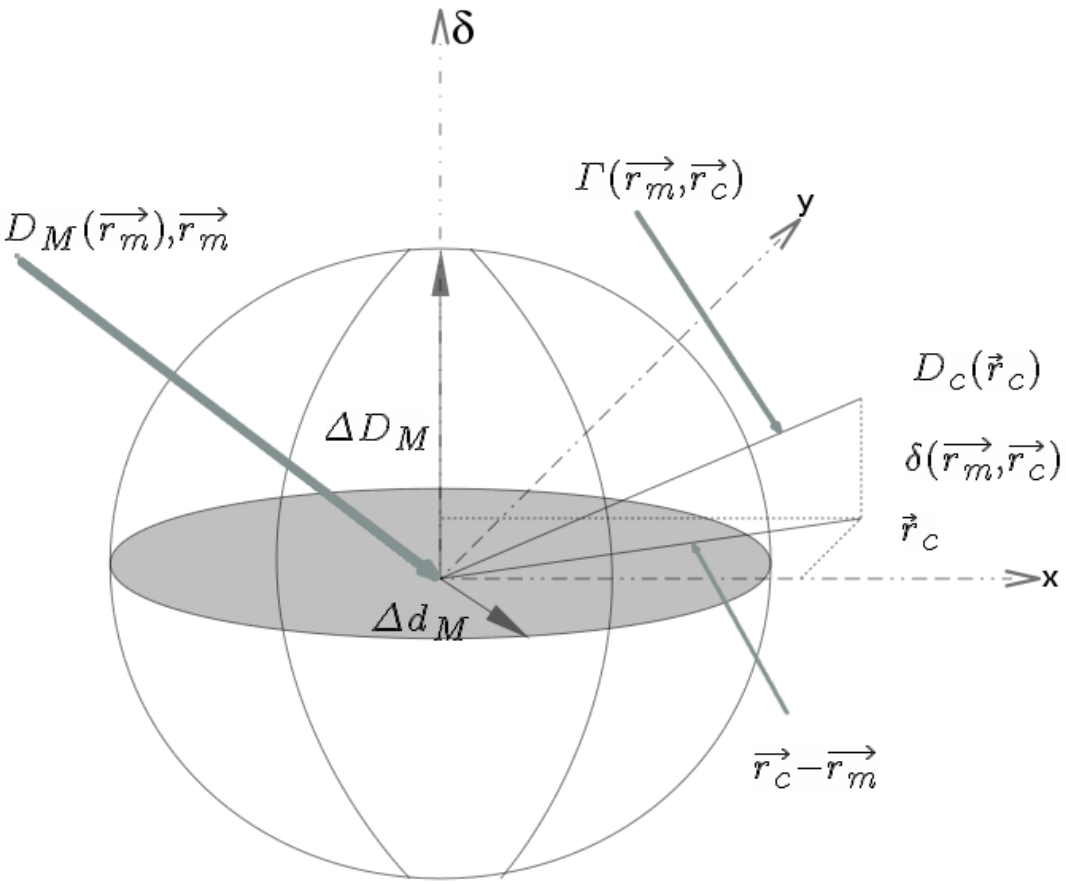

Figure 6.5: Graphical representation of the gamma concept from Low et al. (1998). See text for explanation of symbols

$$\vec{r}(\vec{r_m},\vec{r}) = |\vec{r} - \vec{r_m}| \tag{6.3}$$

and

$$\delta(\vec{r_m},\vec{r}) = D(\vec{r}) - D_m(\vec{r_m}) \tag{6.4}$$

where $\delta(\vec{r_m},\vec{r})$ is the dose difference at the position $\vec{r_m}$.

A quantity γ, or quality index can then be defined at each point in the evaluation plane $\vec{r_c} - \vec{r_m}$ for the measurement point $\vec{r_m}$ so that

$$\gamma(\vec{r_m}) = min\{\Gamma(\vec{r_m}, \vec{r_c})\}\forall\{\vec{r_c}\} \tag{6.5}$$

Therefore, it can be determined that if

$$\gamma(\vec{r_m}) \leq 1, \text{calculation passes} \tag{6.6}$$

$$\gamma(\vec{r_m}) > 1, \text{calculation fails} \tag{6.7}$$

A problem associated with the pencil beam algorithm of the iPLAN calculation system is that it calculates dose in water, whereas the Monte Carlo simulation calculates dose to tissue. This has a minor effect in doses within homogeneous regions of tissue with densities close to unity where the water to medium stopping power ratio ($\frac{S_{water}}{S_{medium}}$) is close to 1.0, whereas for materials such as air, the stopping power ratio is approximately 1.12 (Siebers et al., 2000).

This is illustrated in figure 6.6 which shows the results of a simulation and calculation of a beam incident on a cylindrical tissue phantom 150mm in diameter with a 60mm air cavity at the centre. As can be seen, the dose distribution of the TPS calculated doses within the air cavity of figure 6.6(b) significantly differ from those of the MC simulation of figure 6.6(c). Therefore, differences between the two data sets may be of little clinical significance as the dose discrepancies may occur within air cavities which are of little interest routinely. However, in a γ comparison this may lead to inappropriately low calculations of the percentage of points passing the criteria and plans with doses calculated correctly failing the analysis such as a criterion of 95% of points passing a 3% / 3mm γ test as is commonly used. Consequently, following calculation of the γ indices for each point, those relating to air were eliminated from the overall calculation. These air cavities are most likely to occur within the phantom between the thermoplastic shell and the patient surface where dose calculation accuracy is irrelevant. As the cranial region generally consists of tissue with a density similar to unity, and few air cavities this is unlikely to result in a loss in sensitivity of the method to

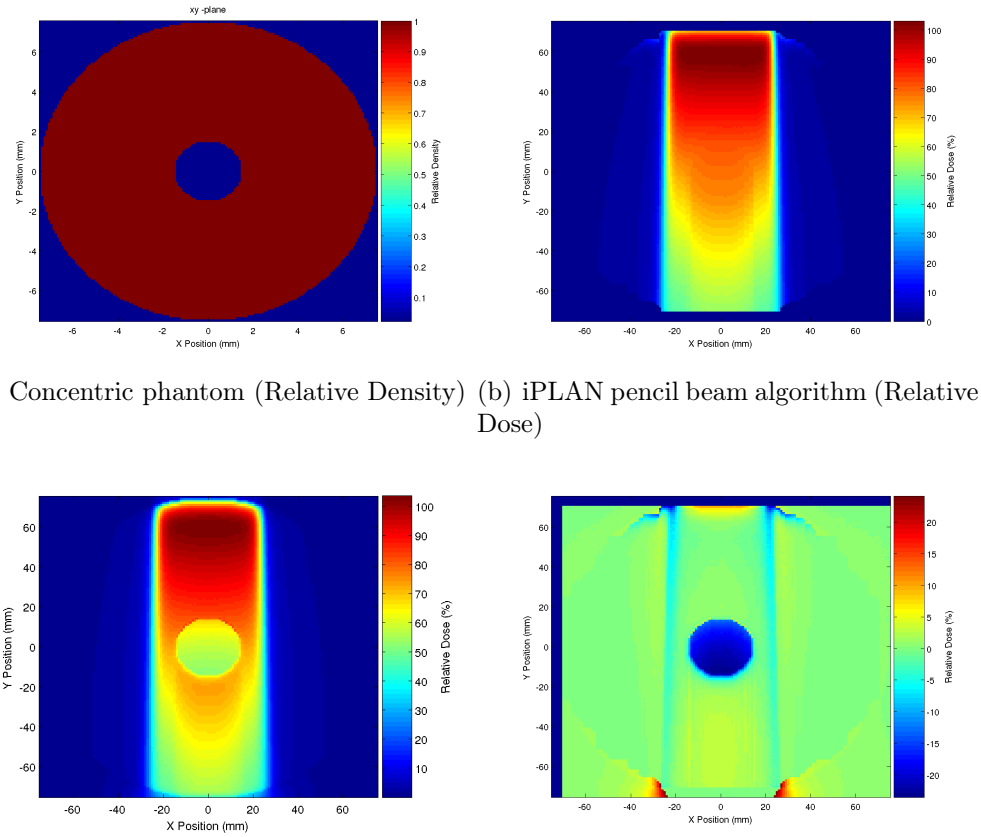

(a) Concentric phantom (Relative Density) (b) iPLAN pencil beam algorithm (Relative Dose)

(c) Monte Carlo Simulation (Relative Dose) (d) Monte Carlo Relative Dose - iPLAN Relative Dose

Figure 6.6: Comparison of calculated and simulated doses using a cylindrical phantom of unit density with an air cavity at the centre.

unknown calculation errors.

Some authors (Spezi, 2003), have converted the MC dose to dose to water prior to the comparison of doses calculated by the TPS. However within the cranium only a small conversion is required due to the anatomical composition of the tissues being close to unit density and therefore this was not done. .

In this investigation, γ values for each point were calculated with the measured doses, D_m in the above explanation replaced by simulated doses. For all points in which the TPS dose was greater than 10% of the prescription dose, gamma values using various criteria were calculated. The percentage of points passing these varying DTA and dose criteria (from 5% / 5mm to 1% / 1mm)

were calculated and tabulated for each patient.

6.3 Results

A total of 10 cranial patients were simulated using the above method. A typical result is shown in figure 6.7, illustrating the comparison between the dose calculated by the treatment planning system and that of the MC simulation. Figures 6.7(a) and 6.7(b) illustrate the output of both systems for this plan of a tumour within the cranium, with a prescribed dose of 7Gy per fraction. By inspection, there is good agreement between the data sets with a similar shape to the dose distribution for each case observed. This is confirmed in the percentage difference plot in figure 6.7(c), showing the percentage difference between the two data sets as a percentage of the prescribed dose (7Gy). Within the brain, there is little difference between the two sets of data. However, in the outer layers of the patient near beam entrance points there are larger differences, of the order of 20% within the shell, which due to the difference window of 2% used in the figure (chosen to exacerbate areas of dose difference in the brain), are not obviously seen. This may be due to a combination of issues. Firstly, there are difficulties associated with the measurement of depth dose and other data near the surface of a patient, which may have introduced errors into the systems and the predicted overdose of the treatment planning system may be a real issue. Secondly an inappropriate material may have been used due to the mapping of Hounsfield units to materials during the DOSXYZnrc phantom generation stage of the process. In general, the thermoplastic shell in this region has been assigned as either tissue or bone and may, therefore, result in an unrealistic dose deposition. Finally, there may be some sampling issues occurring near the interface of the patient and air, resulting in discrepancies between the data sets. This behaviour was seen on all patients but as these occurred within the shell rather than in the patient, this was not considered to be clinically significant and therefore not investigated further.

At points deeper within the patient some areas of difference can be seen with areas of ‘enhancement’ which relate to the position of the skull which can be attributed to a discrepancy introduced by the planning system in calculating

dose to water and not tissue.

The γ map shown in figure 6.7(d) for a pass / fail criterion of 2% / 2mm is shown. In general, a γ of less than one is returned apart from in areas within the shell where the dose to water - dose to medium issue is prevalent as discussed earlier and some regions within the bone where similar issues exist.

For each patient, the γ was analysed for all points within the phantom with doses greater than 20% of the prescription point. These are tabulated in table 8.1 in which it can be seen that there is excellent agreement between the data sets where for pass - fail criteria down to 2% / 2mm more than 95% of the points achieve a γ of less than or equal to 1. Patients 2 and 10 however return a significantly lower number of points passing the tightest gamma criterion (1% / 1mm) than the other patients, which is evident to a lesser extent at other gamma criteria. Both of these patients had an inferior tumour near air cavities, and indicate a poorer performance of the calculation algorithm in heterogeneous anatomy compared to the more homogeneous environment of the other patients.

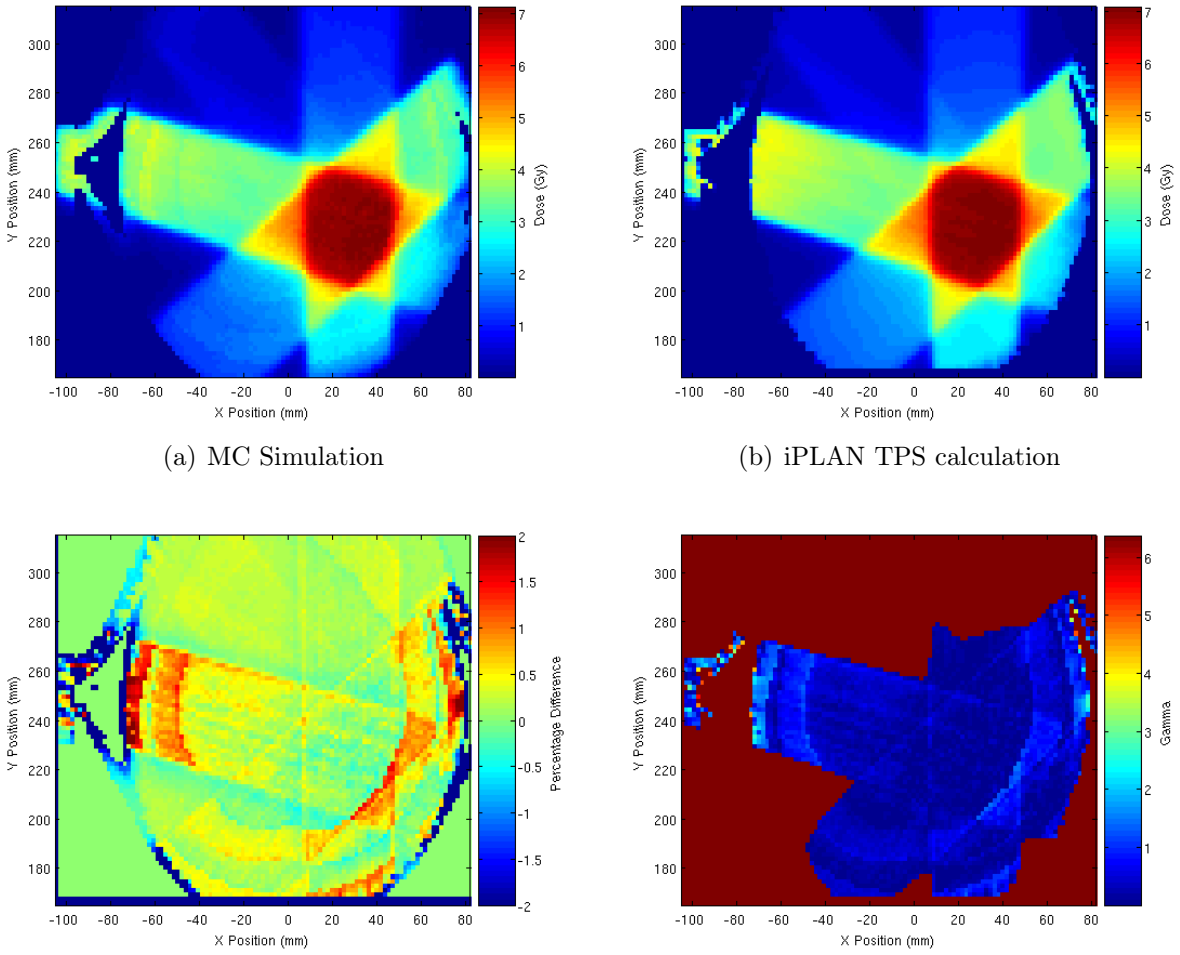

(a) MC Simulation

(b) iPLAN TPS calculation

(c) Percentage Difference

(d) Gamma Map (2% / 2mm)

Figure 6.7: Typical output of comparison between TPS and MC dose calculations.

Patient	5%/5mm	4%/4mm	3%/3mm	2%/2mm	1%/1mm
1	100.00	99.99	99.96	99.94	99.82
2	99.78	99.11	97.32	95.53	86.59
3	99.95	99.80	99.40	99.00	97.01
4	99.93	99.70	99.10	98.51	95.52
5	99.83	99.34	98.02	96.69	90.08
6	99.93	99.72	99.15	98.58	95.73
7	99.88	99.53	98.59	97.65	92.96
8	99.98	99.94	99.81	99.68	99.03
9	99.75	99.01	97.03	95.06	85.17
10	99.85	99.42	98.25	97.09	91.26

Table 6.2: Percentage of points passing the gamma test with various tolerances for each of the 10 patients investigated.

6.4 Conclusions

This work has shown that a Monte Carlo verification system can be used to independently validate cranial stereotactic plans on a routine basis. Using the RTGrid, results were returned within 4-5 hours of submission to the grid for subsequent analysis, which is an acceptable time frame for pre treatment checks of fractionated stereotactic radiotherapy, in which the plan and subsequent checks are most commonly performed over several days following the initial planning CT scan and the commencement of treatment. For single fraction treatments using invasive frames, in which the planning scan, beam optimisation and any necessary checks are made within a few hours of the treatment this approach may not be practical. However with our system and a 7 beam plan, 700 jobs are submitted to the grid and in general run simultaneously and immediately returning a result in 4 hours. However the RTGrid submit node is able to submit up to 1000 jobs at a time to the university-wide Condor pool, therefore it would be possible to split the simulation into smaller jobs with results being returned in 3-4 hours or less which may be feasible. This may not be sustainable in practice however as in this configuration there are other users of the RTGrid and the Condor pool which may block these jobs from running immediately. Should it be deemed that this system be used on a routine basis it may be necessary to put some thought

into ensuring the grid's availability for these tasks. An alternative approach to overcome the problem of simulation times would be to shorten the lengths, which will clearly increase the statistical uncertainties of the data returned requiring a loosening of the γ criteria to indicate acceptable agreement.

However, the good agreement of all patients analysed may indicate that in the relatively simple dosimetric situation of cranial stereotactic radiotherapy the need for such an approach may be unwarranted on a routine basis, although this investigation has confirmed that the data input into the planning system for the fields used clinically was correct, and that the planning system is functioning correctly in calculating doses in areas of tissue homogeneity.

The system may well be of use in validating software upgrades, or as the basis for ongoing routine quality control of the planning system. For situations such as in the head and neck or lung where much greater areas of tissue inhomogeneity exist, this system may be readily adapted for routine use or may provide definitive information during the validation of advanced calculation algorithms, such as point kernel based approaches and source model based Monte Carlo algorithms such as VMC (Kawrakow et al., 1996).

Chapter 7

Applications of BLMLC III: Influences of Monte Carlo Techniques on Treatment Tactics and Calculation Algorithms

Contents

7.1 Introduction

In recent years, the development of radiotherapy technology, such as the widespread adoption of conformal therapy and IMRT, has increased the number of treatment modality options available to the clinician. More recently, IMRT

has been combined with rotational techniques, which despite having been used for some years, have now been expanded to allow modulation of the dose rate and gantry speed. This rotation technique, commonly known as Volumetric Modulated Arc Therapy (VMAT) introduces many more degrees of freedom for the TPS optimiser to produce a plan meeting the clinical constraints of the treatment.

The use of VMAT has been embraced by the radiotherapy community, due to its ability to provide a superior dose distribution in terms of target coverage and sensitive organ avoidance than those achieved using IMRT (Otto, 2008). It can also be delivered in a shorter time.

In tandem with these developments, calculation algorithms used within treatment planning systems have also evolved, so that most TPSs commercially available utilise a 'type-b' algorithm such as the collapsed cone algorithm described in section 2.4.3, as well as the 'type-a' or pencil beam algorithms described in the same section. Type-b algorithms have greatly improved the accuracy of dose calculations within treatment planning systems, especially in treatment sites such as the lung, thorax and head and neck where there are large areas of tissue heterogeneity which are poorly modelled by type-a or pencil kernel based algorithms.

The interest in stereotactic radiotherapy applied to early stage lung tumours has increased greatly since the beginning of the 21st century after several papers (Norihisa et al., 2008; Banki et al., 2009; Whyte, 2010; Hof et al., 2004; Wulf et al., 2005), have shown significant improvement in tumour control for this group of patients, compared to conventional radiotherapy. This has been achieved by using a stereotactic technique to localise the tumour by the use of an external frame, or a frame-less technique in which fixed parts of the patient anatomy are used as an analogue to the frame. 4D CT, or other advanced imaging techniques are used to accurately locate the tumour during planning, and with the use of a stereotactic technique to position the patient, the set up uncertainties can be reduced. This allows the reduction of safety margins and an escalation in the doses applied to the tumour. The recently established stereotactic body radiotherapy consortium guidelines (UK SBRT Consortium, 2011) suggest a dose regime of 3 x 18Gy or 5 x 15Gy, giving a biological effective dose far higher than

a conventional conformal radiotherapy treatment (Wulf et al., 2005).

The consortium guidelines demand the use of a type-b algorithm to calculate the dose due to the inhomogeneities present within the tumour. This may include a Monte Carlo approach such as that of a VMC (Fippel, 1999) type-algorithm.

While the use of a type-b algorithm is clearly a requirement in such cases, these algorithms are not without their problems. For example early versions of the OMP type-b algorithm suffered from memory limitations imposed by the Windows XP [1] operating system, which although displaying the dose at the user specified grid, actually reduced the resolution of the calculation grid to the best possible with the available computing resources. Typically at VCC, actual resolutions of between 4mm x 4mm x 3mm and 6mm x 6mm x 3mm are observed for tumours within the lung, depending on the size of the patient anatomy.

This lack of dose resolution may not be a problem in the calculation of monitor units to the isocentre or prescription point within the tumour, as, at this point, any increased uncertainties are likely to be small. Despite increasing the uncertainty of dose calculation in the field edges (and therefore, in the selection of field width) the magnitude of any errors associated with this limitation are likely to be smaller than the expansion from clinical tumour volume (CTV), to planning target volume (PTV) used in the planning process.

However, these limitations in dose resolution may be a problem in investigating the most appropriate treatment tactic for such cases. Even with the enhanced collapsed cone algorithm (Nucletron, 2010) which enables a finer dose grid to be realised, the resolution of such calculations cannot be set to better than a few millimetres (even though the dose may be displayed at a higher resolution).

During the implementation phase of stereotactic body radiotherapy at VCC, the benefits of a VMAT treatment technique compared to a conformal technique were questioned. Clearly, the reduced treatment time of VMAT and therefore the reduced burden on the treatment machine and patient is a clear advantage of VMAT over a conformal technique. The increased complexity of validation and increased quality assurance of each patient may though, negate these benefits. However, due to the build-up effects of tumours within the lung there may be some benefit in a rotational technique compared to that of conformal therapy

[1] Microsoft Ltd, Redmond, WA 98052-6399, USA

using 4 - 8 beams. For the case of a rotational technique one might expect that the proportion of dose delivered to the periphery of a tumour from a beam directly incident on that part of the tumour would be less than that of a conformal technique, where the dose may fall off at the edges of the tumour and reduce the effectiveness of any treatment.

Due to the resolution issues of type-b algorithms, and the fact that much of the dose under investigation will be primarily in the build up region of the radiation field, a MC investigation was undertaken to investigate the benefits of VMAT or rotational techniques over conformal techniques, and to assess the performance of the different calculation algorithms in the situation of stereotactic body radiotherapy (SBRT) to the lung

7.2 Methods

For this investigation a phantom was constructed of three rings shown in figure 7.1.

The purpose of this design was to mimic the situation of a lung tumour, surrounded by low density lung tissues. The phantom therefore, consisted of a number of concentric cylinders with an inner cylinder of 40mm diameter constructed of tissue material, set as ICRU521TISSUE in subsequent MC simulations, a 120mm diameter, middle cylinder of lung (ICRU521LUNG) and a 250mm diameter outer cylinder of tissue (ICRU521TISSUE). The length of the 'tumour' (i.e. in the dimension into and out of the page) was 40mm. In order to examine doses near the extremities of the inner cylinder, a fine voxel size is required. If this is repeated throughout the phantom the size of the phantom would be large in terms of the physical storage space required on the simulating machine. Therefore, a scheme of irregular voxel dimensions was used. The voxels of the inner cylinder were 0.1mm x 0.1mm x 40mm, the middle cylinder were 1mm x 1mm x 40mm and the outer cylinder 10mm x 10mm x 40mm.

A phantom for use with DOSXYZnrc was created geometrically, using these dimensions and used for subsequent simulations. This phantom was then used to generate 'images' of the phantom in DICOM-RT format which could be read by a treatment planning system. Due to constraints of the planning system

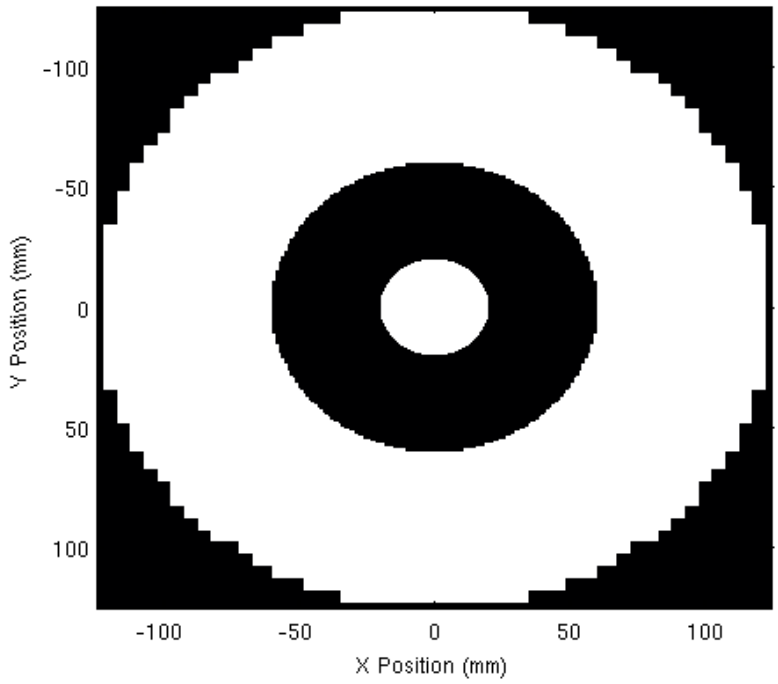

(a) XY image through isocentre plane

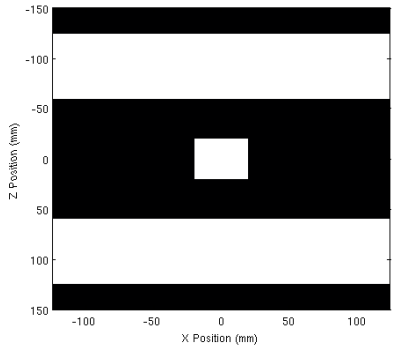

(b) XZ image through isocentre plane

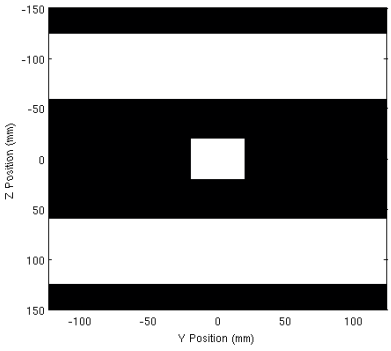

(c) YZ image through isocentre plane

Figure 7.1: Illustrations of the concentric phantom used for TPS based calculations and MC simulations analogous to an SBRT treatment of the lung. The images are shown in terms of relative density, the white areas are of density equal to 1.0 with lung equivalent material surrounding the 'tumour' in the centre.

requiring equally spaced pixels in each scan the phantom data were re-sampled to a resolution of 512 x 512 pixels for each slice equating to a resolution of 0.5mm x 0.5mm for all pixels. Due to the desire to compare a type-b algorithm, which was

not available on the iPLAN TPS, the Nucletron OnCentra Masterplan (OMP) TPS was used to calculate doses in the phantom using the enhanced pencil beam (PB) and enhanced collapsed cone (CC) algorithm of version 3.3SP3 of the software (Nucletron, 2010).

A field size 50mm x 50mm, was used in all cases with the isocentre of each beam placed at the centre of the tumour. Simulations and calculations were performed using 2, 3, 4, 8, 16, 32 beams together with a single beam, rotating 360 degrees around the tumour. This was achieved for the MC simulations by using source 10 of DOSXYZnrc, which allows for arc therapy to be simulated in a single run by specifying the range of angles and spacings. The parameters used for each of these are tabulated in table 7.1.

Number of Beams	Min Gantry	Max Gantry
2	0	180.00
3	0	240.00
4	0	270.00
8	0	315.00
16	0	337.50
32	0	348.75
rotation (360)	0	359.00

Table 7.1: Gantry angle parameters used for simulation of conformal and rotational technique using DOSXYZnrc source 10.

Thus, a full arc around the patient was simulated by dividing it into 360 beams entering the patient from 0 degrees to 359 degrees in 1 degree intervals. For the two beam plan, the arc was divided into two beams with 180 degree intervals. All of the beam arrangements began at 0 degrees and, therefore, the two beam plan consisted of beams at 0 and 180 degrees. Similarly, the three beam plan had portals entering the phantom at 0, 120 and 240 degrees with similarly arranged beams for each of the other plans, each beginning at 0 degrees.

The ‘dose cubes’ from the TPS and ‘.3ddose’ files from the MC simulations were then extracted and analysed to produce dose volume historgrams (DVHs) of the tumour and beam profiles of the dose delivered by each of the beam arrangements.

7.3 Results and Discussion

7.3.1 TPS Calculation Algorithms

The DVHs for all of the beams, using each calculation method and MC simulation are shown in 7.2. In figure 7.2(a) there is little separation between the curves but in the magnified image of figure 7.2(b), it can be seen that the curves separate due to the number of beams and calculation method used.

The most marked deviations can be seen in the curves for the two and three beam techniques, the DVHs for which, are shown in figure 7.2(c). It can clearly be seen that the PB algorithm produces a markedly different distribution to that of either the MC or the CC. The failure of the PB algorithm to model the build up effects of the radiation passing from a low density material into the lung would account for this difference between the algorithms. The CC calculation where the use of point kernels would account for this effect, agrees very well with the MC, although the MC DVH shows a slightly better coverage of the tumour than the CC.This may indicate that the situation of doses calculated using the CC algorithm in areas of tissue heterogeneity may not be as bad as calculated and could be an area of further investigation.

These effects are further illustrated in the diagrams of figure 7.3 which show the percentage differences between the doses within the tumour calculated by each of the methods. For clarity, doses outside the tumour region have been removed and the range of differences shown in each figure reduced from -5% to +5%. The red annulus around each tumour are regions where larger differences are present of the order of 20%.

For the rotational techniques, the thickness of this annulus is of the order of 0.2mm for the CC v MC comparison and 0.6mm for the CC v PB comparison. Considering the CC and PB were calculated on a 1mm grid, which required re-sampling to get to the 0.1mm resolution of the MC simulations, it is arguable whether this result is of any significance. However, the fact that the PB calculations do exhibit a thicker high difference annulus may add some credence to the argument that the CC is a more accurate calculation in this situation.

For the 2 beam approach, the difference between the PB and the other two

techniques is far more significant. Here, the annulus is significantly thicker in the case of the PB v MC compared to the CC v MC calculation where for the former case the annulus is up to 20mm thick, compared to up to 6mm thick for the latter. This would be consistent with the inability of the PB algorithm to model the build up effects in this situation.

The comparisons of PB v CC are shown in figures 7.3(c) and 7.3(f). In the former case small differences can be seen between the two data sets with an annulus of dose difference of 1% - 2% between them for the rotational technique near the edge of the tumour. For the two beam case of figure 7.3(f), much larger differences can be seen in the periphery of the tumour.

In the CC v MC comparison there is a dose difference of around 2% between the CC and MC near the edges, to the left and right of the figure, which although present to some extent in the PB calculation is of a smaller magnitude, generally less than 1% but with small areas of 2%. If one assumes the MC calculation as being the most accurate, it would appear that this discrepancy is introduced by the use of CC algorithm. However, this requires further investigation. For the 2 beam technique the differences between the two algorithms in the superficial layers swamp this effect in the comparison of the two algorithms but a similar discrepancy can be seen in the CC v MC comparison.

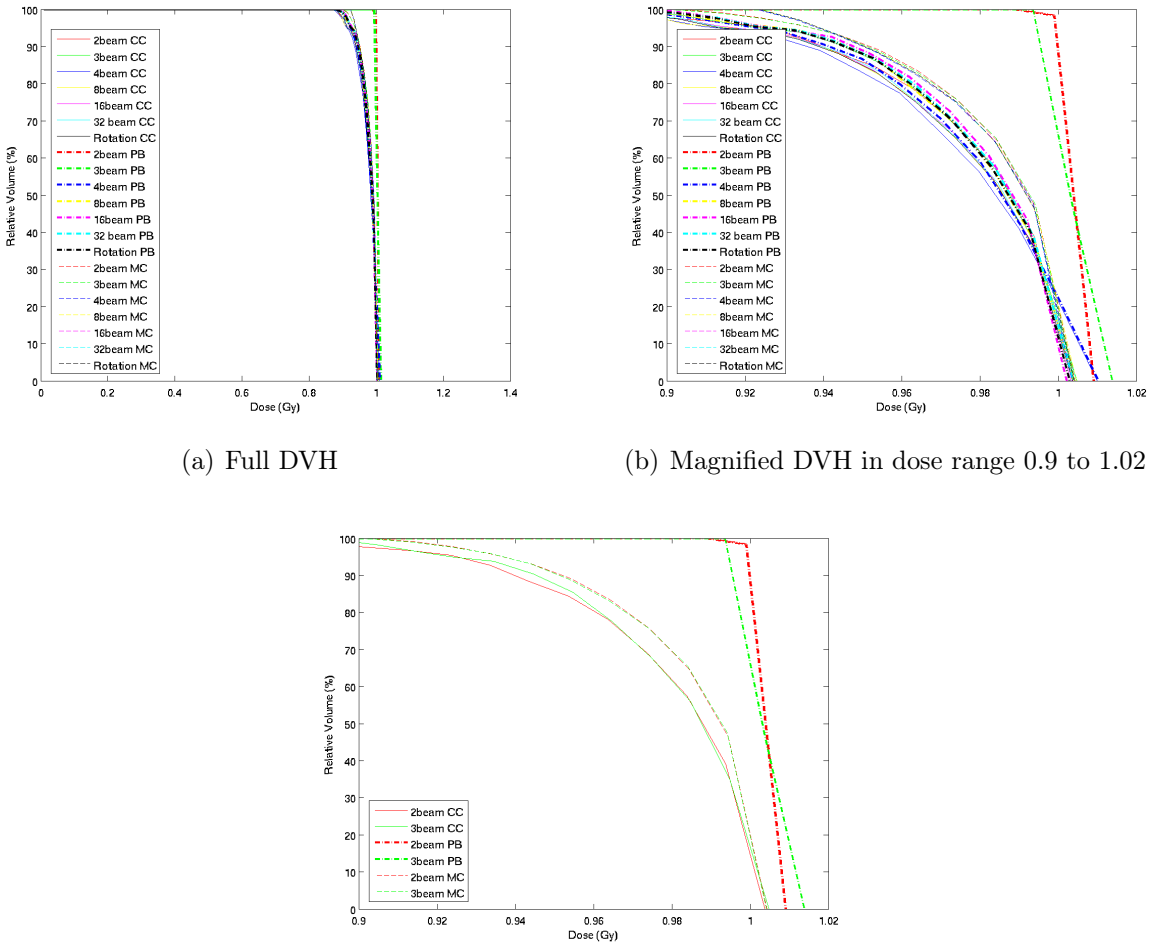

(a) Full DVH

(b) Magnified DVH in dose range 0.9 to 1.02

(c) DVH of 2 and 3 beam techniques

Figure 7.2: DVH of doses delivered using 2,3,4,8,16,32 and full rotational techniques calculated using a pencil beam (PB) and collapsed cone (CC) algorithms and Monte Carlo (MC) simulations of the beam arrangements.

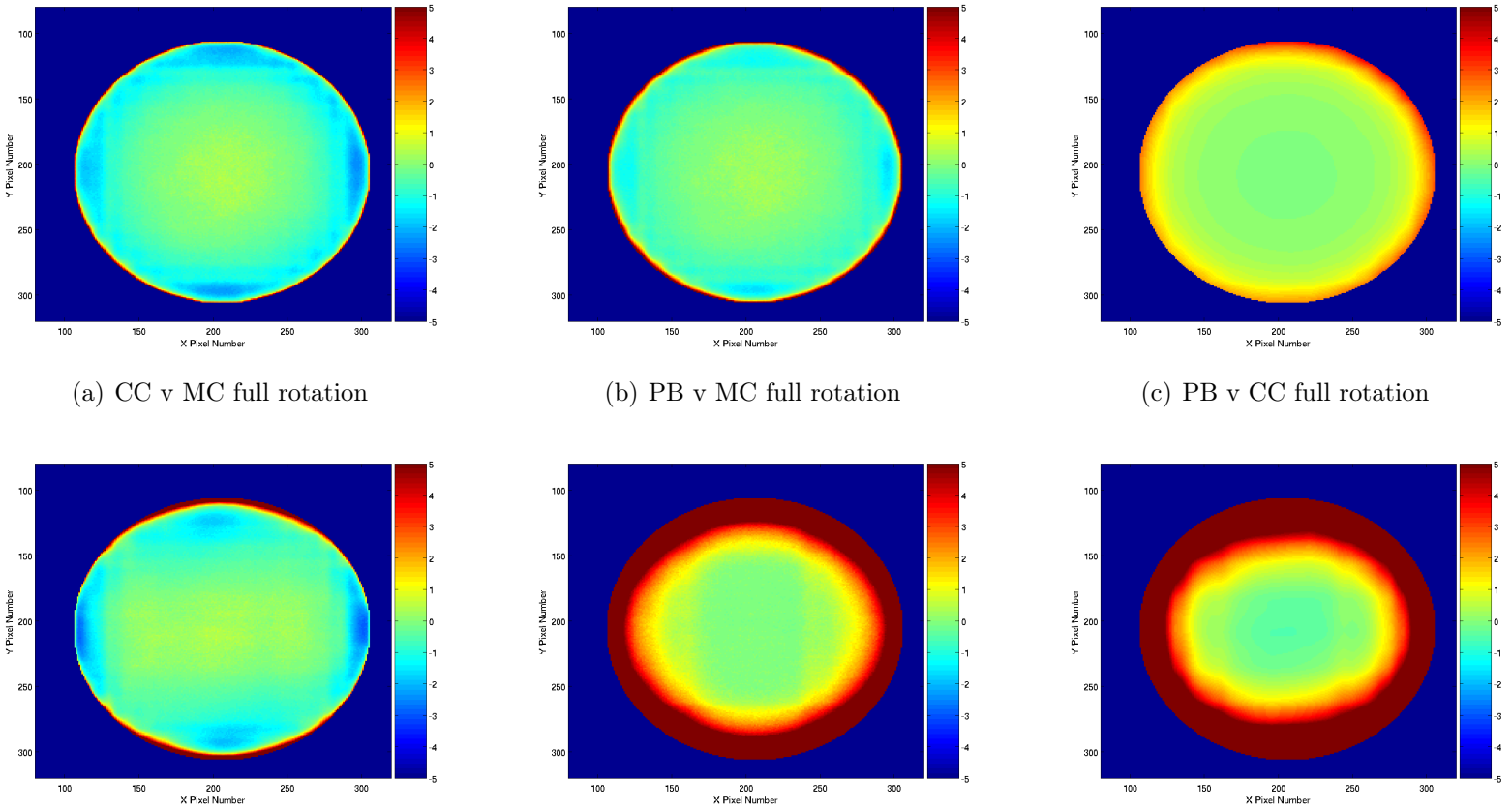

(a) CC v MC full rotation

(b) PB v MC full rotation

(c) PB v CC full rotation

(d) CC v MC 2 beam

(e) PB v MC 2 beam

(f) PB v CC 2 beam

Figure 7.3: Percentage differences to tumour region of phantom for the different calculation methods using a full rotational technique and a two field (ant-post) technique (0.1mm x 0.1mm matrix). For clarity doses outside the tumour region have been eliminated and shaded in dark blue.

The difference in resolution between the MC and TPS datasets being the source of the discrepancy, or masking some effects were then investigated by repeating the MC simulations with a 1mm x 1mm x 40mm in the region of the tumour, with co-ordinates exactly matching that of the calculation matrix of the TPS. Results of this are shown in figure 7.4. A similar behaviour is seen to the finer resolution comparisons in that there is an annulus of dose difference at the superficial layers of the tumour, which is significantly thicker for the PB v MC case than the CC v MC case for the 2 beam technique but the differences for the full rotation technique are much smaller. The discrepancies at the edges of the tumour, apparently introduced by the use of the CC algorithm are also present.

Although there are some differences between the two experiments, the thickness of the high dose difference annulus in the high resolution phantom has an average thickness of around 15mm compared to 10mm for the lower resolution case, this experiment has confirmed the use of the high resolution grid as a necessary method of comparison of the calculation algorithms.

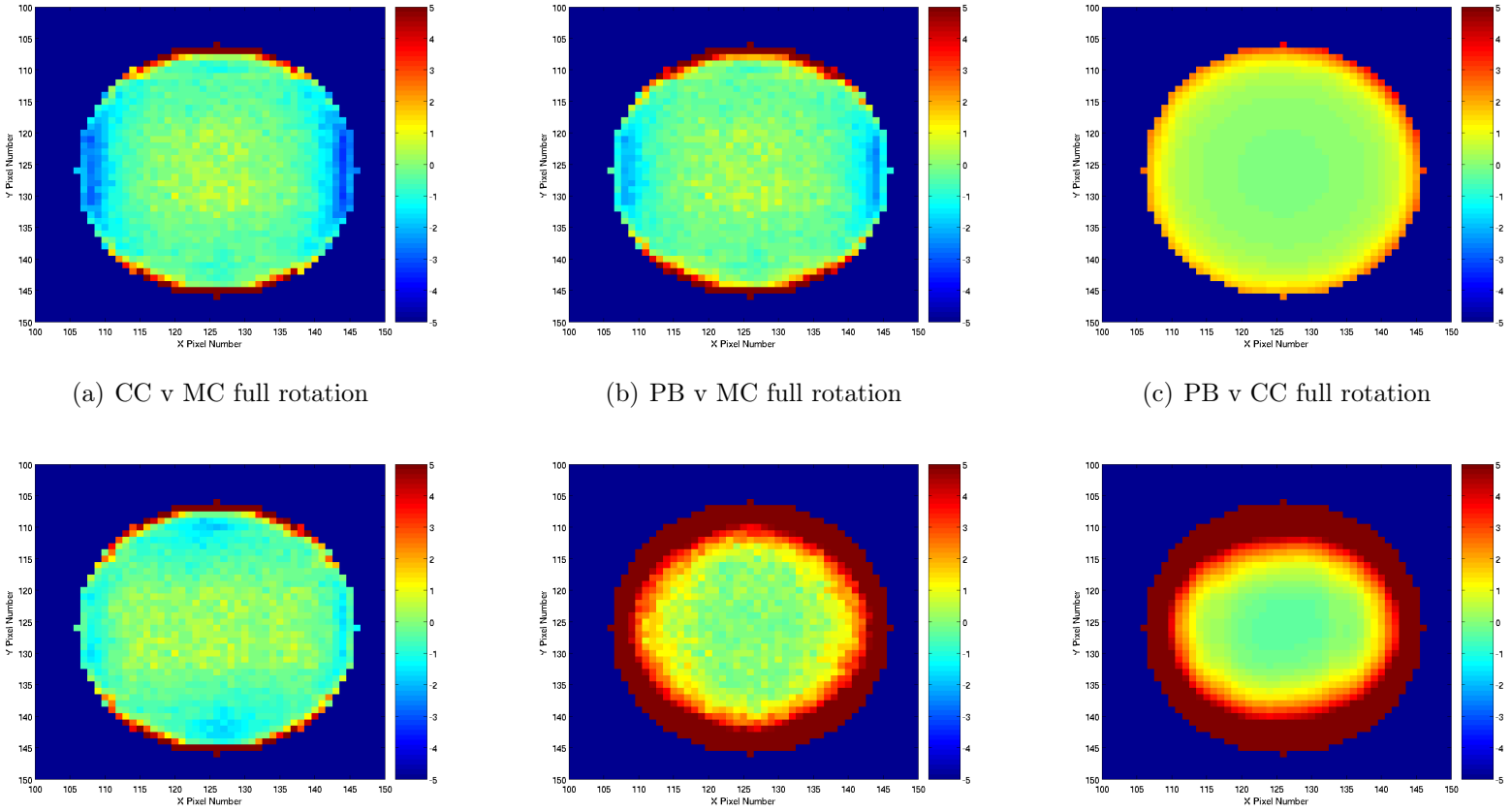

(a) CC v MC full rotation

(b) PB v MC full rotation

(c) PB v CC full rotation

(d) CC v MC 2 beam

(e) PB v MC 2 beam

(f) PB v CC 2 beam

Figure 7.4: Percentage differences to tumour region of phantom for the different calculation methods using a full rotational technique and a two field (ant-post) technique, (1mm x 1mm MC matrix). For clarity doses outside the tumour region have been eliminated and shaded in dark blue.

7.3.2 Treatment Tactics

Figure 7.5 illustrates the DVHs for the two, three, eight and full rotational techniques calculated using the MC simulations only. The coverage of the tumour is fairly similar for each of the techniques. However, the two and three beam situations do deviate somewhat from the situation with more beams as can be seen in figure 7.5(b), showing a that a higher volume of the tumour receives doses around 0.92Gy for cases with the higher number of beams than found with the rotational case.

For plans with four or more beams irradiating the tumour the DVHs returned are almost indistinguishable. This is shown in the plots of percentage differences between each of the conformal beams to the rotational case shown in figure 7.6. In this diagram a positive dose difference indicates an area of higher dose from the rotational plan and a negative dose the converse. It can be seen that in the case of the two and three beam plans, there are large differences in the saturated region of the annulus of up to -6% and +8% for the two beam plan and -2% to +4% in the case of the three beam plan. The four beam plan shows slight differences in the superficial area of the tumour but for techniques involving a greater number of beams beyond this, the distributions are indistinguishable.

These results would indicate that there is a disadvantage in having less than four beams in a plan, and that the addition of opposing beams helps over come the dose loss at the periphery of the tumour due to build up effects.

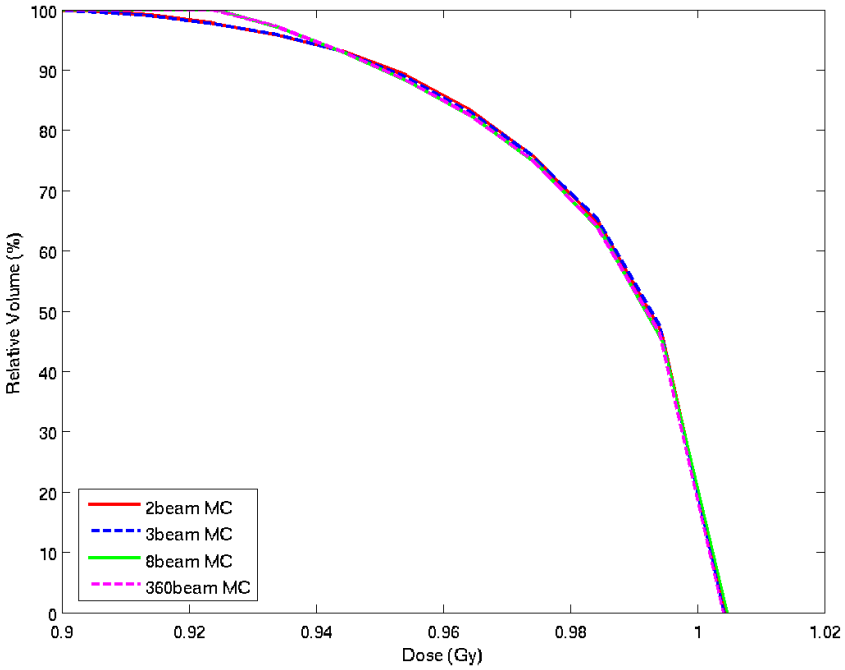

(a) Dose range 0.9Gy to 1.02Gy

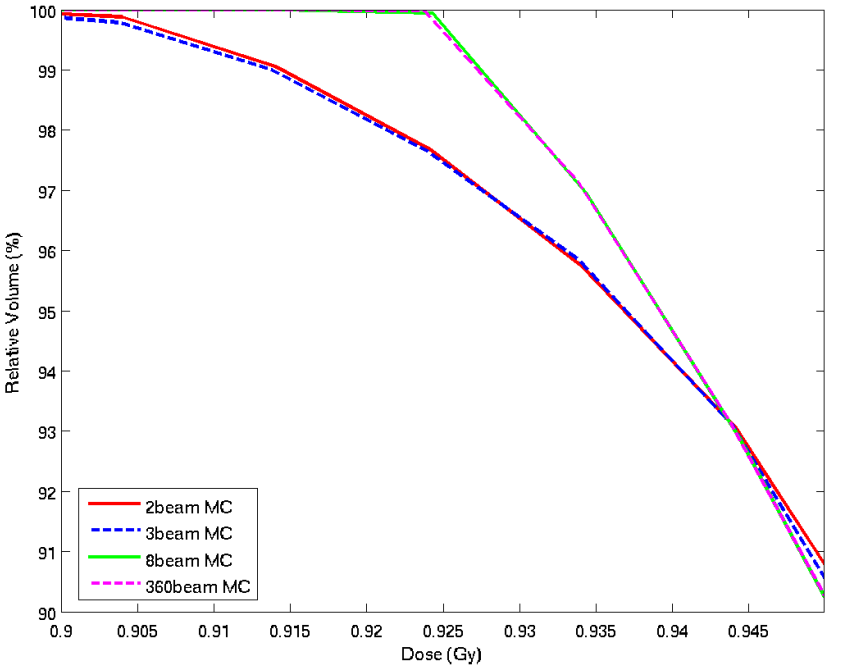

(b) Dose range 0.9Gy to 0.95Gy

Figure 7.5: DVH of doses delivered using 2,3,8 and full rotational techniques using MC simulations of the beam arrangements.

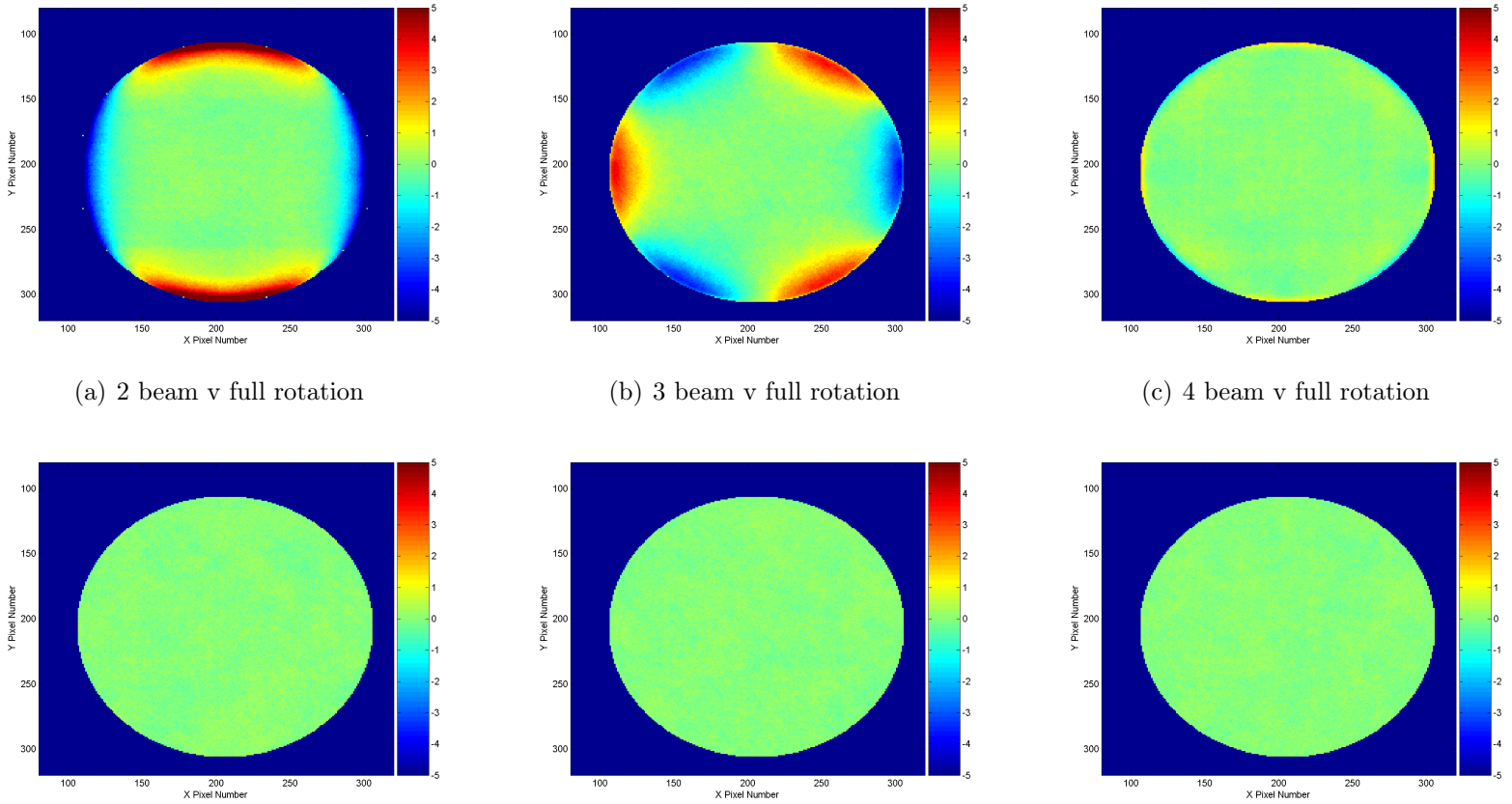

(a) 2 beam v full rotation

(b) 3 beam v full rotation

(c) 4 beam v full rotation

(d) 8 beam v full rotation

(e) 16 beam v full rotation

(f) 32 beam v full rotation

Figure 7.6: Percentage differences to tumour region of phantom comparing differing numbers of beams to full rotation (MC simulations).

7.4 Conclusions

This initial investigation has shown the following :

- There are significant differences between the PB and CC calculation algorithms at the periphery of tumours lying within low density regions. This difference is more significant for a smaller number of beams.
- For a fully rotational beam there is little difference between the doses reported by PB and CC. This may be of interest in systems such as OMP and Elekta Monaco[2] (both used at VCC), which may use a PB algorithm during its optimisation process to benefit from calculation speed objectives.
- Cold spots within tumours such as those investigated may be avoided by the use of more than four beams or more

[2]Elekta-CMS Ltd, Crawley, UK

Chapter 8

Applications of BLMLC IV: Portal Image Dosimetry for Stereotactic Radiotherapy

Contents

8.1 Portal Imaging

Portal imaging has been in use in radiotherapy for many years and is utilised to verify that the patient has been positioned correctly. Initially implemented using radiographic films placed in an exit plane of the beam distal to the patient, in more recent years electronic portal imaging devices (EPIDs) have been used to acquire an electronic image of the exit radiation, which can be compared to a digitally reconstructed radiograph (DRR) of the beam produced by the treatment planning system. A schematic diagram of this configuration is shown in figure 8.1.

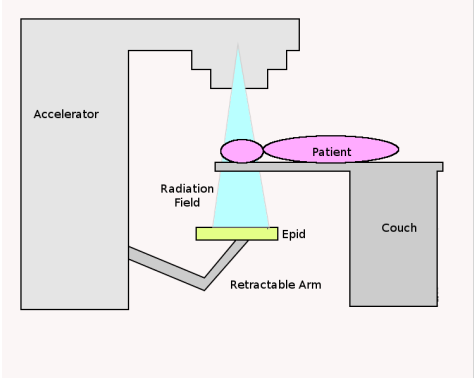

Figure 8.1: Schematic diagram of an EPID in clinical use.

Figure 8.2: Schematic diagram of an amorphous silicon electronic portal imaging device.

At Velindre Cancer Centre, all of the linear accelerators in clinical use are

equipped with megavoltage portal imaging devices based on amorphous silicon detectors, which are routinely used for the verification of patient position. Figure 8.2 illustrates the main components of the EPID on the Varian 600c linear accelerator used for cranial stereotactic treatments at Velindre Cancer Centre. The device consists of a copper plate, which is used to generate electrons from the incident photons that have transported through the patient, and to absorb any low energy scatter which may produce blurring on any subsequent image. The electrons are then incident on a scintillating layer of terbium doped gadolinium oxysulphide ($Gd_2O_2S : Tb$). This layer produces optical photons, which are then detected by a two-dimensional array of amorphous silicon (a-Si) coupled to photo-diodes, which are read out using an array of thin film transistors situated beneath the a-Si layer (Antonuk, 2002).

The detector provides an image af 512 columns x 384 rows of 0.784mm x 0.784mm pixels producing a maximum field size of 400mm x 300mm at the position of the detector. For a typical EPID position of 1400mm from the radiation source, this relates to a field size of approximately 280mm x 210mm, much larger than the fields used within stereotactic radiotherapy or radiosurgery.

The device is supported by a retractable arm which allows the detector assembly to be positioned within the gantry assembly when not in use and to a convenient position for the acquisition of verification images when required.

8.2 Portal Dosimetry

The response of the imager to dose is linear, as can be seen from the plot of EPID signal versus delivered dose shown in figure 8.3. This was obtained by placing 50mm of solid water equivalent material on the imager and irradiating the imager to a series of known doses at the exit of the solid water. The dose at the exit of the solid water was calculated using standard tables with the application of an inverse square law factor to account for increased distance between the radiation focus and the detector. This, therefore, assumes full scatter conditions in a homogeneous medium, which will not be the case in this circumstance, but any uncertainties associated with this technique will be constant across all measurements. As a check of the magnitude of the calculation,

this situation was simulated using a Monte Carlo model of the accelerator and imager. The difference between the calculated dose and simulated dose was within the statistical uncertainties of the simulation (0.5%). The points on the graph indicate the response of the detector to doses achieved from 0.06Gy (the dose delivered by 1 monitor unit in this configuration) to 10Gy once the flood and dark field corrections described below have been applied. The solid line is a least squares fit of the data showing the near perfect linear relationship between signal and applied dose over a range much wider than that practically used in stereotactic radiotherapy.

In order to calibrate the portal imager, a *dark field* and *flood field* is acquired. The dark field, taken with no radiation incident on the detector, is acquired in order to characterise the response of the imager and associated electronics with no radiation present. The flood field is obtained by irradiating the entire active area of the detector with an open field and is used to account for changes in sensitivity of the detector from pixel to pixel. In dosimetric mode, the images are obtained without these corrections applied which therefore needs to be done manually. The dose obtained from the imager is therefore obtained using the following equation:

$$Dose_{epid}(x,y) = \frac{Epid_{signal}(x,y) - dark_{field}(x,y)}{flood_{field}(x,y)} \times flood_{mean} \times d_{corr} \quad (8.1)$$

where

- $Dose_{epid}(x,y)$ is the dose measured by the detector at a point (x,y) on the imager panel
- $Epid_{signal}(x,y)$ is the signal measured by the EPID at (x,y)
- $dark_{field}(x,y)$ is the dark field measured by the detector with no incident on the detector at (x,y)
- $flood_{field}(x,y)$ is the flood field measured with the largest possible field incident on the detector (x,y)
- $flood_{mean}$ is the mean value of the flood field image.

- d_{corr} is the epid signal to dose correction factor obtained from a curve similar to that shown in figure 8.3

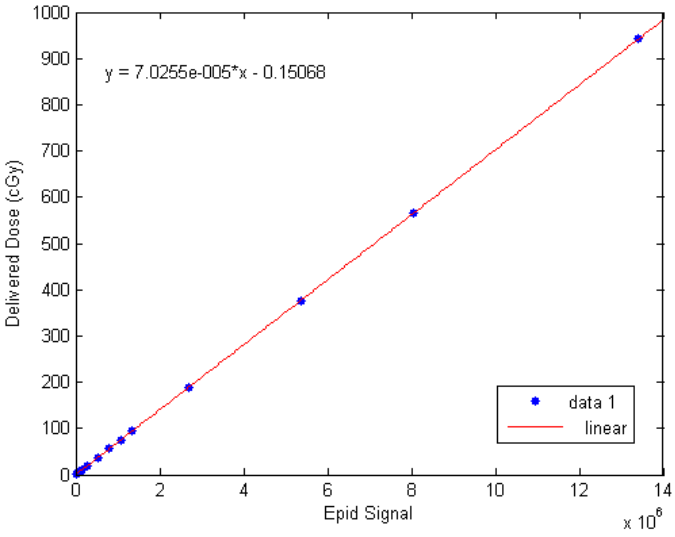

Figure 8.3: Plot of EPID signal versus dose.

An ideal detector would be water or tissue equivalent, whereas, in reality, the sensitive area of the EPID is constructed of a copper plate, a scintillating material and the a-Si layer used to capture the signal. All of these are of higher density than water or tissue and may, therefore, be prone to differences in response with changes in incident energy spectrum as the field size changes, in a similar way to that discussed in section 5.3.2.2 and in more detail by Chin (2005). Figure 8.4 illustrates this effect for the case of the EPID.

These data were obtained by simulating the situation of a 100mm slab of water equivalent material placed at 900mm FSD (i.e. the isocentre at the bottom of the solid water slab) and the EPID placed at a distance of 1400mm from the radiation source. In order to reduce the size of the phantom used in the simulations, and therefore enable the job to be run over a number of machines on the RT-Grid, voxels in the x-z direction, parallel to the slab surface were defined as a 3.136mm x 3.136mm voxels (equivalent to the dimensions of the central 4x4 pixels), symmetric around the central axis surrounded by voxels of 200mm width in which the dose was ignored. Dimensions in the y (vertical plane)

direction were maintained to be identical to the physical situation. Simulations were performed for the circular fields used in section 5.3.2.2 and an additional square field to which each of the simulated doses were normalised.

In section 5.3.2.2, the data are plotted against the diameter of the field but here it is plotted against the equivalent window width field ($EwwF$). This is a concept defined by Nicolini et al. (2006) as a fast and easy approximation to calculate equivalent squares for irregular fields.

Applied to the case of a M3 μMLC in which the leaves of the μMLC are in the 'Y' direction, the equivalent window width ($EwwF$) is defined as:

$$EwwF = \frac{2 \times X \times Y}{X + Y} \tag{8.2}$$

where X is the width of the field in the X (non μMLC) direction and Y is the mean of all apertures defined by opposing leaves that lie within the open part of the field.

The red line and points of figure 8.4 illustrate the set of output factors for the circular fields defined by the μMLC calculated using Monte Carlo simulations using a screen within the phantom made of $Gd_2O_2S : Tb$ compared to a screen constructed of water (green line). There is little difference between the output factors measured in both situations for fields larger than an $EwwF$ of greater than 25mm, below which, the two curves show a significant deviation.

Figure 8.4(b) illustrates a plot of the ratio of the output factors using a silicon and water screen in the simulations. A field size dependent conversion factor K_{sw} can be used to convert the doses measured in with the EPID to doses measured in water. This is defines as:

$$K_{sw} = \frac{relative\,dose\,to\,water}{relative\,dose\,to\,screen} \tag{8.3}$$

For fields of an $EwwF$ greater than 25mm this factor can be assumed to 1.00.

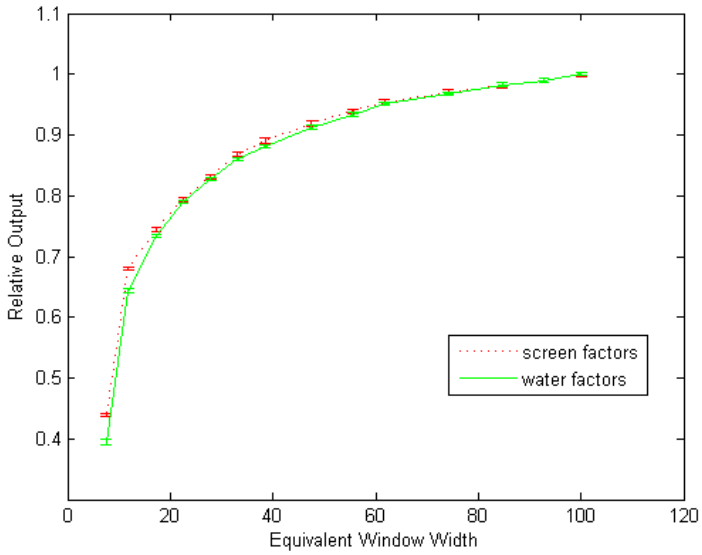

(a) Relative Output Factors

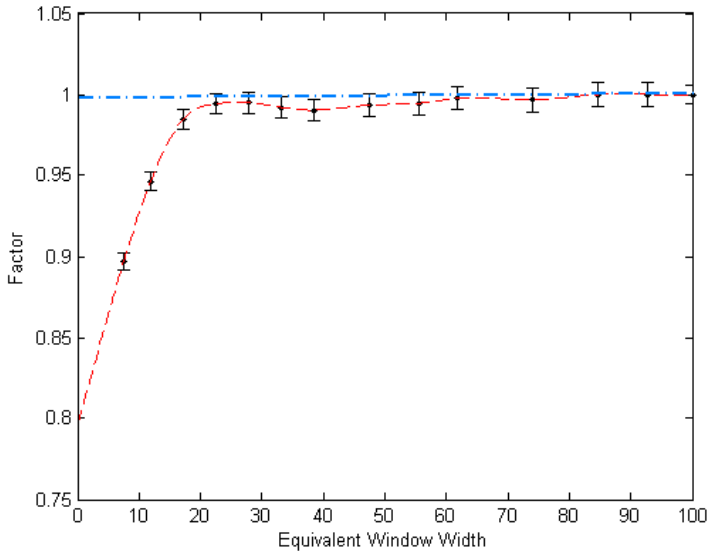

(b) Si - Water Correction Factors

Figure 8.4: Plot of EPID output factors simulated using a screen of actual composition, and of water against equivalent window width (EwwF) (top figure (a)). The bottom figure is the correction required to convert a dose measured with the EPID screen to a dose in water based on these measurements (again against EwwF).

8.3 In-vivo dosimetry

In recent years, the document "Towards Safer Radiotherapy" (Royal College of Radiologists, 2008) has recommended that all patients undergoing radiotherapy would benefit from in-vivo dosimetry to confirm that the correct dose has been applied. Clearly, this includes stereotactic radiotherapy and, by implication, radiosurgery. Methods such as tabular based dose checks, and pre-treatment individual patient Monte Carlo simulations, such as those described in chapter 6 can independently verify the dose calculation but are unable to detect errors due to an incorrect transfer of the dosimetric information to the treatment machine or an incorrect patient set up.

Consequently, in-vivo dosimetric measurement techniques have been developed and used routinely by many centres. These generally involve a detector, of limited spatial extent, such as a diode or thermoluminescent detector placed at the centre of the applied radiation field on the surface of the patient, and the dose measured compared to that planned at that point. This may be replaced or combined with a similar detector at the position of radiation exiting the patient. This approach is problematic in advanced radiotherapy techniques such as IMRT, in which the uncertainties associated with placing of the detector on the patient surface, combined with a modulated beam may make it difficult or impossible to realise a practical resolution of such methods to confirm doses (or otherwise) to within the desired level of around 5% or better. Other techniques, such as VMAT, in which modulating beams are rotated around the patient, have the added complication that there is no single entry or exit point for a beam and consequently make single point measurements even more problematic, if not impossible.

In order to solve some of these problems, *pseudo* in-vivo or exit dosimetric techniques have been developed by many authors, as reviewed by van Elmpt et al. (2008), which utilise the EPID as a dosimetric device. As an integral part of the machine, the EPID can usually be placed orthogonally to the central axis beyond the patient, where dosimetric information can be obtained and compared with the dose expected in this plane. However, this may not always be possible if extensive couch twists are utilised in the treatment plan, which may cause collisions with the patient or patient support apparatus.

As has been shown earlier, the response of the EPID is linear and has a small dependency on field size. Therefore, the dose in the exit plane can easily be determined with a careful calibration of the EPID. The difficulty is therefore in the determination of the expected dose in this plane.

8.4 The Application of EPID-based Exit Dosimetry in Stereotactic Radiotherapy

Rotational and modulated techniques are commonly applied to stereotactic radiotherapy and therefore suffer from the same issues as described in the previous section concerning IMRT and VMAT. Additionally, the fields used within stereotactic techniques are significantly smaller than conventional radiotherapy and, therefore, issues with the response of the detector in small fields (as discussed previously) may be prevalent.

Furthermore, there are increased uncertainties due to the positioning of a relatively large detector relative to the size of the radiation field on the central axis of the field where a small discrepancy in position may equate to a large change in dose due to the proximity of the field edge. Additionally, for these small fields, perturbations in the intensity of the incident beam, as a consequence of introducing the detector, may be more significant than in larger fields as the detector may cover a far more significant area of the incident beam. For treatments delivered over a small number of fractions (as is generally the case in stereotactic radiotherapy), and more so in radiosurgery this may be of significant enough magnitude to require a correction to the monitor units to ensure delivery of the correct dose, even if only used on the first fraction of a multi-fraction course, if the number of fractions is small. In conventional radiotherapy consisting of more highly fractionated regimes (typically between 15 and 37 fractions), any perturbations from a detector placed in a much larger field are likely to be insignificant

Therefore, an EPID based *pseudo* in-vivo exit dosimetry approach has several advantages.

1. The EPID is placed beyond the patient and therefore does not perturb the

incident beam

2. Dosimetric information concerning the entire beam can be obtained rather than just a point dose as in other methods. As dose is acquired from the whole radiation beam, any uncertainties such as movement within a fraction may be observed, and if necessary taken into account during analysis

3. The data are acquired electronically and can be analysed immediately using appropriate software and do not, necessarily require subsequent processing as is the case for TLDs, for example. The potential speed of data analysis may make the method appropriate for radiosurgery, in which the treatment may be interrupted part (e.g. 10%) of the way through treatment, the dose calculated and a decision made to continue treatment quickly

4. An electronic record of the measurement can be kept and stored as a record of for future analysis

5. The EPID is generally a standard part of a modern linear accelerator and use of it as a dosimetry device requires no further financial outlay

6. Use of the EPID as a surrogate in-vivo dosimetry measurement involves no physical contact with the patient

For these reasons, the use of an EPID based approach to in-vivo dosimetry was explored using a variety of methods to predict the dose at the imager plane. Three clinical cases, involving patients undergoing cranial stereotactic radiotherapy at Velindre Hospital were investigated as 'proofs of principle' for each of the methods. All of the patients were prescribed doses of between 28Gy and 32Gy to be delivered in daily fractions over four days for indications of a brain metastasis (one patient) and recurrent gliomas (two patients). For the case of the brain metastasis the patient had previously received whole brain radiotherapy.

These three patients had been subject to the standard dosimetric checks, which include a tabular dosimetry check and an electronic check of the parameters used to treat the patient following each fraction. Furthermore, these were part of the cohort of patients investigated in chapter 6 using a full

Monte Carlo simulation. Therefore, it can be verified that the correct doses were delivered to these patients on all fractions.

Three methods of pseudo in-vivo dose measurement were investigated:

1. Full Monte Carlo transport of dose through the patient
2. TPS based estimation of the dose at the imager plane
3. A single point dose equivalent path length based correction

8.4.1 Full Monte Carlo Simulation

In this method, the transport of radiation from each beam was simulated using the Monte Carlo model previously developed. This, together with a model of the portal imager, is used to determine an expected fluence at the imager plane and compared to that obtained during measurement.

8.4.1.1 Methods

For each patient, the planning CT scan was taken and converted to a DOSXYZnrc phantom using a method similar to that described in section 6.2.1. The difference in the method was that during phantom generation the DICOM-RT plan file of the treatment under investigation was read and the patient data rotated about the isocentre by the gantry angle described in the treatment plan so that a flat imaging panel could be easily constructed at the correct angle relative to the patient. The model of the imaging panel in use on the accelerator had previously been developed and validated within the department by Chin et al. (2003), Cufflin et al. (2010) and Cufflin (2011).

The gantry angle in the subsequent Monte Carlo simulations was changed to 0 degrees to maintain equivalence with the treatment plan. The generated phantoms of the first four beams of patient 1 are shown in the top row of figure 8.7.

Simulations were run using a BEAMnrc simulation of the linear accelerator head as the input source to a DOSXYZnrc simulation using the generated phantoms including the EPID. The simulation parameters were those shown

in table 3.1 and the RTGrid used to run the simulations. Due to the size of the phantoms generated being of the order of 50Mb each, the number of jobs for each beam was limited to 50. In this case, a six field plan would require 15Gb of storage on the server which would be near the limit of acceptability on the resources available to us. Using 10^8 particles, average uncertainties of approximately 1.5% in the imager plane were obtained. However, despite using this parallel technique, these took a real simulation time using the RT-Grid of over 48 hours.

Following simulation, each MC dose map of the imager screen was divided by a MC simulation of a flood field and multiplied by the mean of the flood field to ensure that the MC comparison data set was compared with a similarly processed data set from the imager.

For each fraction of treatment, portal images of each beam were obtained integrating the image over the entire duration of treatment. These were then converted to a calibrated dose, according to the procedure described in section 8.2. The two data sets were then compared and a gamma analysis done for each point in which the MC dose was greater than 20% of the dose at the central axis.

8.4.1.2 Results

Figure 8.5 illustrates the results for the first fraction of the first patient which are typical of the results obtained. An inspection of the absolute dose intensity maps of the MC phantom, and the dose maps obtained from the measurements shows good agreement, which is reflected in the map of percentage differences shown in the figure 8.5(c) and the gamma map in figure 8.5(d) in which for this example 93.9% of points pass a gamma criteria of 3% and 3mm. Phantoms, MC doses, EPID doses and gamma maps for the first fractions of the first four beams of patient 1 are shown in figure 8.7.

For this beam, gamma maps of criteria ranging from 1% / 1mm to 6% / 6mm are shown in figure 8.6 which show expected behaviour. At the 'looser' end of gamma criteria (6% / 6mm), 100% of points pass but at the 'tighter' end the figure is 53.5%

The average number of points passing each set of gamma criteria were

averaged over each fraction and listed for each beam in Table 8.1, together with the percentage of beams that pass the gamma criteria at the bottom.

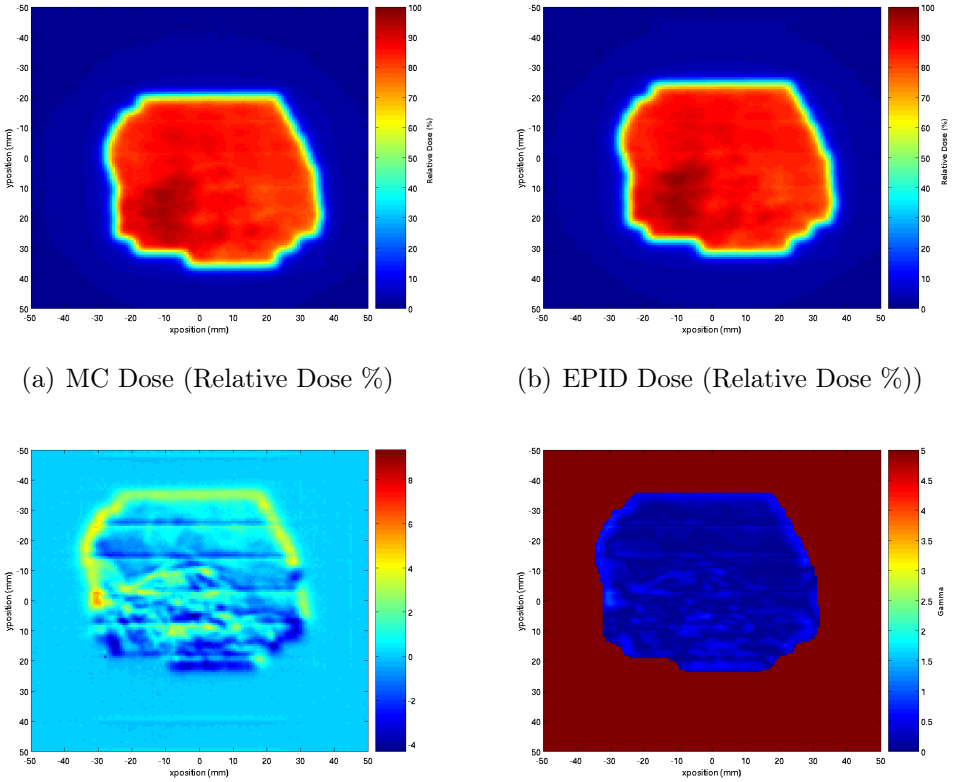

(a) MC Dose (Relative Dose %)

(b) EPID Dose (Relative Dose %))

(c) % difference

(d) Gamma Map (3% / 3mm)

Figure 8.5: Dose maps, % differences and gamma comparison of EPID and MC calculations for fraction 1, beam 1 of patient 1. In the gamma map, the value of gamma below the threshold dose of 10% is displayed in dark red for clarity

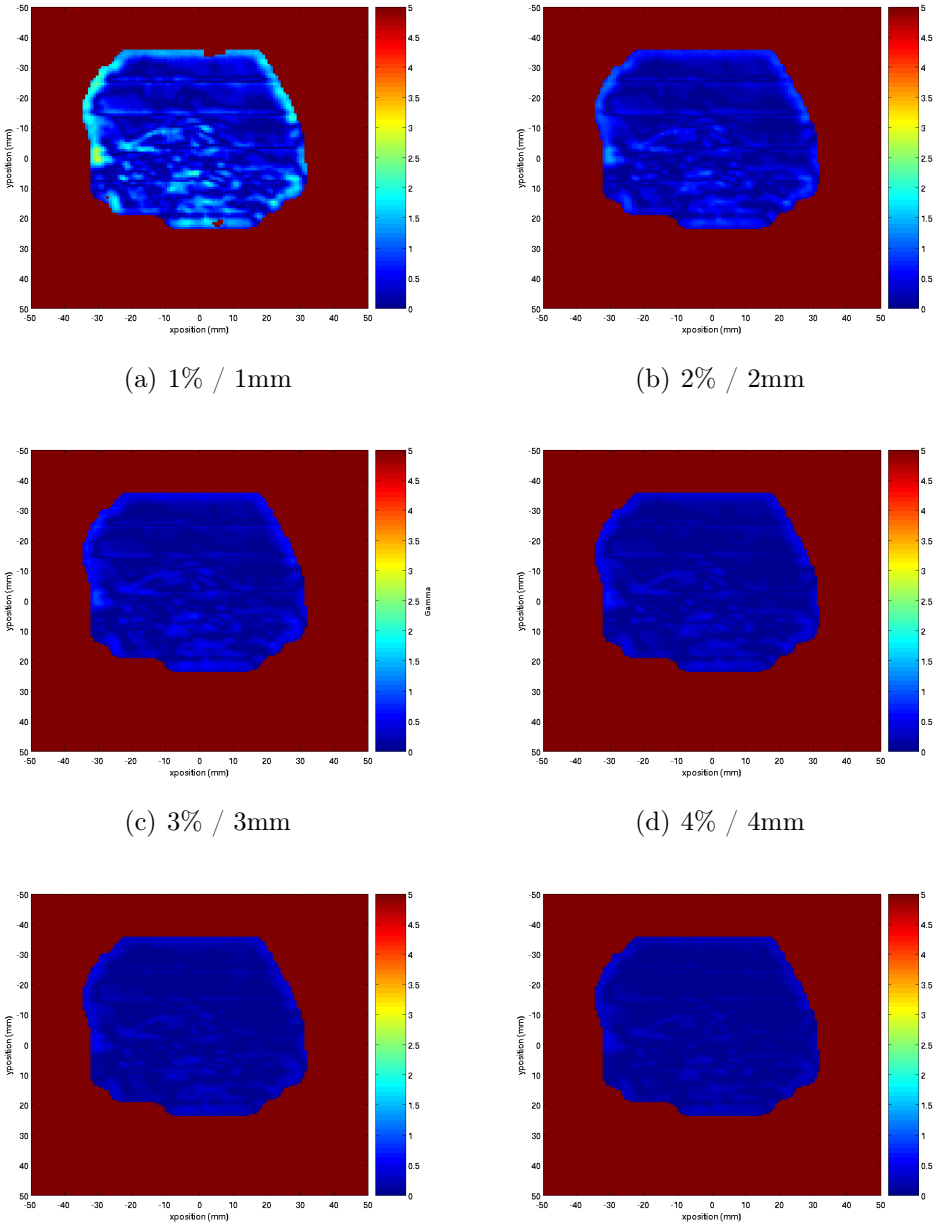

(a) 1% / 1mm

(b) 2% / 2mm

(c) 3% / 3mm

(d) 4% / 4mm

(e) 5% / 5mm

(f) 6% / 6mm

Figure 8.6: Gamma maps for various gamma criteria for fraction 1, patient 1 beam 1. In each map, the value of gamma below the threshold dose of 10% is displayed in dark red for clarity

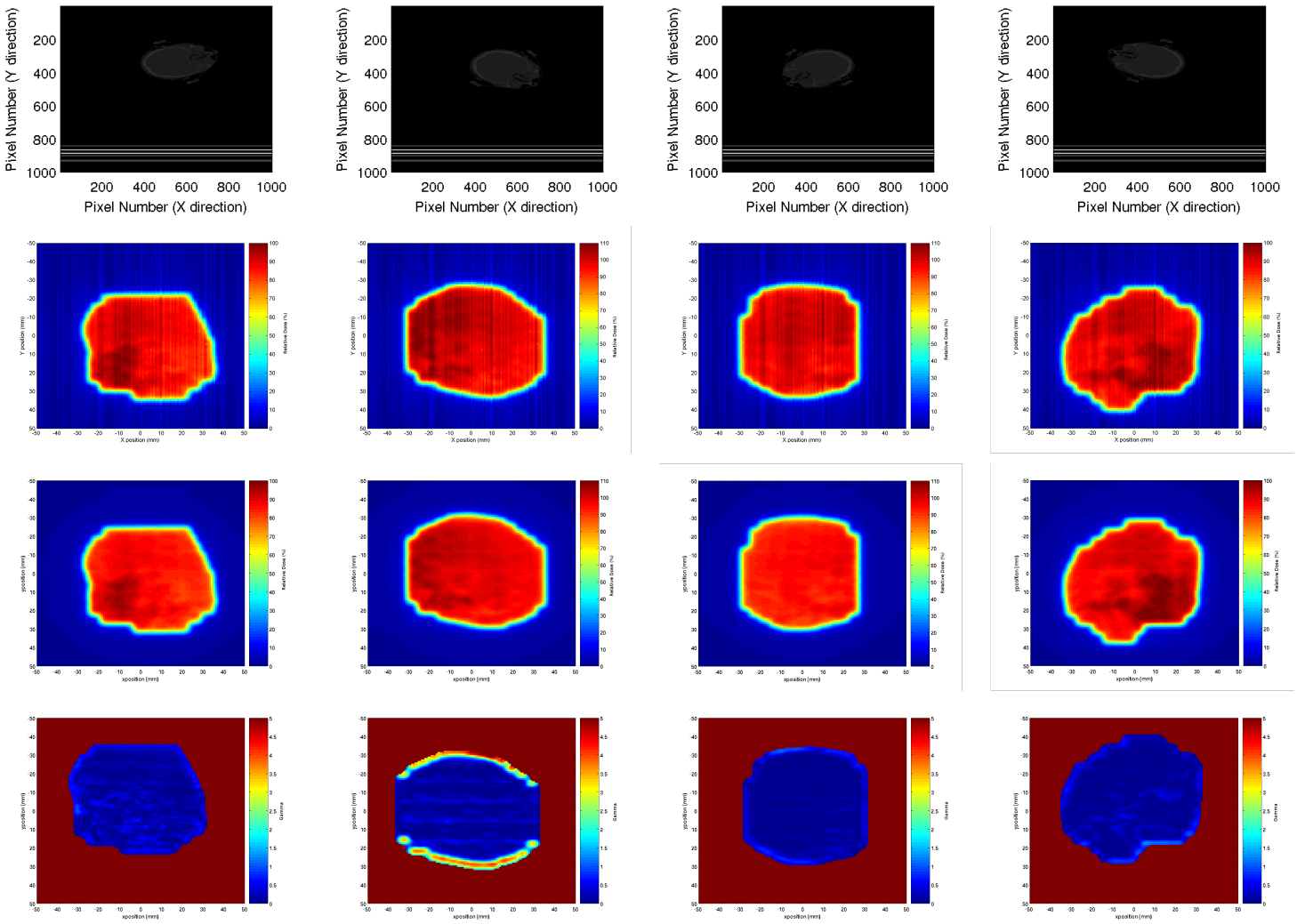

Figure 8.7: Phantoms, dose maps and gamma comparison of EPID MC simulations for patient 1. The top row is an illustration of the phantom used, the second and third rows the dose maps from the EPID and MC simulation respectively and the bottom row a gamma map of the comparison between the two data sets. In the gamma map, the value of gamma below the threshold dose of 10% is displayed in dark red for clarity

Patient	6%/6mm	5%/5mm	4%/4mm	3%/3mm	2%/2mm	1%/1mm
pat1 beam 1	100.00	99.80	99.10	93.65	79.94	54.68
pat1 beam 2	91.04	87.49	81.54	72.33	58.03	45.16
pat1 beam 3	98.32	96.61	92.97	91.20	79.04	63.41
pat1 beam 4	97.27	96.82	93.85	87.12	78.46	50.94
pat1 beam 5	98.56	97.60	94.42	93.46	82.85	61.25
pat2 beam 1	98.56	98.37	97.68	95.75	78.80	53.89
pat2 beam 2	97.45	97.25	96.57	94.67	77.90	53.28
pat2 beam 3	100.00	100.00	99.48	97.52	80.25	54.89
pat2 beam 4	97.95	97.74	97.06	95.15	78.30	53.55
pat2 beam 5	98.71	98.51	97.82	95.89	78.91	53.97
pat3 beam 1	100.00	100.00	100.00	98.28	80.87	55.31
pat3 beam 2	100.00	99.90	99.20	97.25	80.03	54.74
pat3 beam 3	100.00	100.00	99.76	97.79	80.47	55.04
pat3 beam 4	100.00	100.00	99.56	97.60	80.32	54.93
pat3 beam 5	99.06	98.84	98.16	96.22	79.18	54.16
pat3 beam 6	99.76	99.53	98.83	96.88	79.73	54.53
% of beams with γ>95%	93.75	93.75	75.00	62.50	0.00	0.00

Table 8.1: Percentage of points passing the gamma test with various tolerances for full MC transport method.

8.4.1.3 Discussion

The gamma comparisons in this study, do not show as good an agreement between simulated and measured data compared to that observed in the simulations of doses delivered to the patient described in Chapter 6. In the analysis performed in chapter 6, all plans had more than 95% of points passing a gamma criteria of 3% / 3mm compared to 62.5% of beams in this case. This is not a surprising result, as some of the random errors in a multi-beam situation may average out which is not the case when considering single beams and this situation involving a full transport through the patient to the imager is a far more complex situation compared to that simulated in Chapter 6.

It may, therefore, be appropriate to loosen the gamma criteria used to indicate a successful validation for each single beam to 95% of points passing a gamma criteria of 5% and 5mm as used by Cufflin et al. (2010) for the case of IMRT

verification. For the cases examined, only one beam, beam 2 of patient 1 would fail with these criteria. It can be seen from figure 8.7 that there appears to be a positional issue of a few millimetres evident, and may, in fact, indicate that some degree of positional error occurred during treatment delivery, although this discrepancy was present on all fractions observed. As the data were analysed some time after the patient had been treated, there was no opportunity to explore this individual case further. This discrepancy varied from 3mm - 4mm at the imager plane which relates to 2.1mm to 2.9mm at the isocentre. This is however within the 5mm margin expansion used to determine the planning target volume.

In stereotactic radiotherapy and radiosurgery, it is common practice for doses to be prescribed to a position other than the isocentre, commonly the extremities of the tumour to ensure that the most amount of tumour possible receives at least the prescription dose. In such cases, it is common for there to be hot spots within the tumour of 120% or more. A dose discrepancy of 5% in the imager plane could, therefore, be considered acceptable on the grounds that a far greater dose inhomogeneity is allowed in these patients than conventional radiotherapy. Furthermore, the complexity of the simulation is greater than that of the calculation and therefore subject to greater uncertainties, therefore a 5% agreement between the data sets is entirely acceptable

However, there is a greater requirement for positional accuracy than in conventional radiotherapy suggesting that an adjustment of the distance to agreement (dta) gamma criterion to a tighter value may be appropriate. Table 8.2 tabulates the gamma for various spatial tolerances from 5mm to 2mm for 5% dose differences; as the dimensions of the voxels of the MC phantom were 2mm, distance to agreement criterion of less than 2mm is inappropriate.

As can be seen, only two of the beams fail the gamma criteria of 5% /4mm, 3 at 5% /3mm and 4 at 5% /2mm. The distance to agreement figure is, of course, measured at the imager plane, which in these instances is at 1400mm which relates to dta figures of 3.6mm, 2.9mm, 2.1mm and 1.4mm for the 5mm, 4mm, 3mm and 2mm tolerances respectively, at the isocentre. Therefore, it can be seen that a gamma criteria of 5% / 3mm (at the imager plane) would indicate acceptable agreement between doses measured with the EPID and simulated, relating to positional uncertainties of around 2mm at the isocentre.

Patient	5%/5mm	5%/4mm	5%/3mm	5%/2mm
pat1 beam 1	99.80	97.80	97.14	96.47
pat1 beam 2	87.49	87.10	86.97	86.84
pat1 beam 3	96.61	96.32	96.23	96.13
pat1 beam 4	96.82	96.78	96.76	96.75
pat1 beam 5	97.60	96.74	96.45	96.16
pat2 beam 1	98.37	95.92	95.10	94.29
pat2 beam 2	97.25	94.29	93.31	92.32
pat2 beam 3	100.00	99.95	99.93	99.91
pat2 beam 4	97.74	95.28	94.46	93.64
pat2 beam 5	98.51	96.65	96.03	95.40
pat3 beam 1	100.00	98.32	97.76	97.20
pat3 beam 2	99.90	99.17	98.92	98.68
pat3 beam 3	100.00	97.53	96.71	95.89
pat3 beam 4	100.00	99.21	98.95	98.68
pat3 beam 5	98.84	96.58	95.83	95.07
pat3 beam 6	99.53	97.55	96.89	96.23
% of beams with γ>95%	93.75	87.50	81.25	75.00

Table 8.2: Percentage of points passing the gamma test with varying dta tolerances for a dose difference criterion of 5% for the MC transport method.

These results, therefore, indicate that this approach may be used as a successful method of individual patient validation. The disadvantage of this technique however is the time required to generate the phantoms (two hours) and for the simulations to run which may be upwards of 48 hours. As this method would primarily be used as a secondary validation of treatment plan transfer and patient set up, one may argue that it is somewhat exhaustive to simulate doses to arrive at uncertainties of less than 1.5% with the subsequent expectation of poorer gamma results. Further work is required to indicate the simulation time necessary to ensure that all correctly delivered treatments passed the gamma criteria chosen.

Additionally, the phantom may be reduced in size by restricting its dimensions to only a few centimetres outside the beam edges, which would enable the simulation to be split up into a greater number of jobs to avoid the physical limitations of the RTGrid server. Again, further investigation would be required

to arrive at the best compromise between phantom, phantom voxel size and simulation uncertainty to derive the optimal figures.

8.4.2 TPS EPID calculation

An alternative approach to obviate the speed difficulties of the full Monte Carlo simulation described in the previous section is to calculate the doses at the imaging plane using a TPS or similar. It has been shown by Dahlgren et al. (2006), Cufflin (2011) and Cufflin et al. (2010) that for IMRT plans optimised and calculated using the Nucletron[1] OnCentra MasterPlan TPS (OMP) a good agreement between dose predicted by the EPID and TPS can be obtained using the collapsed cone (Ahnesjo, 1989) algorithm. Larger differences were observed between the doses calculated on the TPS using the pencil beam algorithm (Ahnesjo and Trepp, 1991), which is implemented in a similar way as on the iPLAN system. However, due to the potential benefit in speed, this method applied to this situation was investigated.

8.4.2.1 Methods

For this investigation, the CT scans suitable for import into the iPLAN TPS were generated using a similar method of rotating the patient around the isocentre and adding the EPID at the required position. Due to the TPS's calculation algorithm only computing dose to water, a uniform slab of water was used to represent the imager material. The data acquired by the EPID was then converted to water equivalent information using the factors described in section 8.2.

Using the 'phantom mapping' function of the TPS, the clinical plan was transferred to this new case and the clinical beam geometry set to the clinical isocentre. All beam parameters were kept the same as in the treatment plan with the exception of the gantry angle which was set to 0 degrees to maintain the appropriate geometry relative to the EPID. A TPS flood field was obtained from a calculation by the TPS of a 28cm x 21cm field at the isocentre (40cm

[1]Nucletron BV Ltd

x 30cm at the imager plane) incident on the imager geometry and the dose calculated by the TPS, $Dose_{TPS}$ derived from the following equation:

$$Dose_{TPS}(x,y) = \frac{TPS_{dose}(x,y)}{floodTPS(x,y)} \times floodTPS_{mean} \tag{8.4}$$

where

- $Dose_{TPS}(x,y)$ is the corrected dose calculated by the TPS at a point (x,y) on the imager panel
- $TPS_{dose}(x,y)$ is the uncorrected dose calculated by the TPS at the imager plane on the EPID at (x,y)
- $floodTPS(x,y)$ is the dose calculated by the TPS at a point (x,y) on the imager panel from the largest possible field incident on the detector
- $floodTPS_{mean}$ is the mean value of the $floodTPS(x,y)$ field image.

By applying this flood field correction, differences between the TPS calculated results and those acquired by the EPID due to the averaging out of the beam 'horns' by the flood field are removed.

The two data sets were then compared using a gamma analysis for each point in which the TPS dose was greater than 20% of the dose at the central axis.

8.4.2.2 Results

Figure 8.8 illustrates the dose and gamma maps for patient 1, fraction 1. There appears to be a fair visual agreement between the relative intensities of the two data sets but as can be seen from figure 8.8(c) there is a greater absolute dose discrepancy between the two data sets compared to that found when the full MC simulation was used. This is reflected in the gamma comparison of figure 8.8(d) which shows significantly worse results than that observed with the full MC calculation of figure 8.5(d), where the percentage passing the 3% / 3mm criterion was 93.9% compared to 86.1%, in this instance, for the first fraction. The full set of gamma comparisons for this beam averaged over all fractions is shown in figure 8.9 and tabulated for all beams in all plans investigated in table

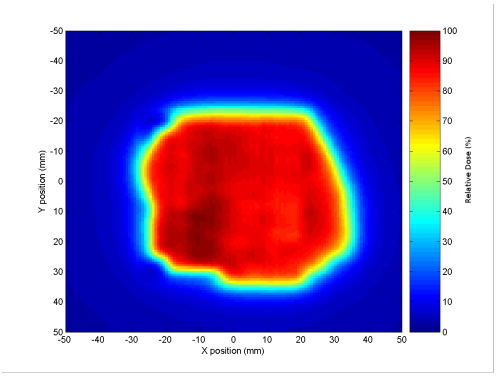

(a) TPS (Relative Dose %)

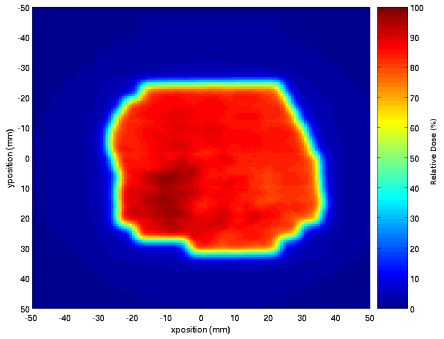

(b) EPID (Relative Dose %)

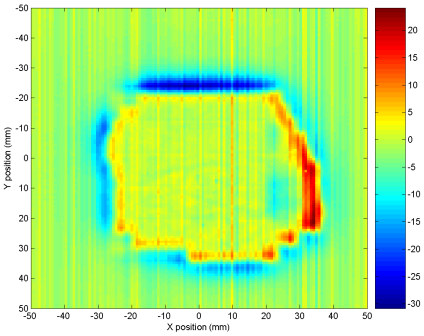

(c) % Difference

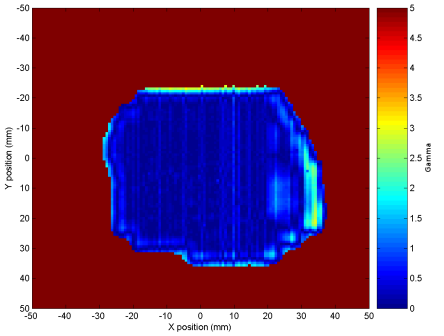

(d) Gamma (3% /3mm)

Figure 8.8: Dose maps, % differences and gamma comparisons of EPID and TPS calculations for beam 1, patient 1. In the gamma map, the value of gamma below the threshold dose of 10% is displayed in dark red for clarity

8.3. Similarly, as for the MC transport investigation, the phantoms, dose maps and gamma maps for the first four fractions of patient 1 are shown in figure 8.10.

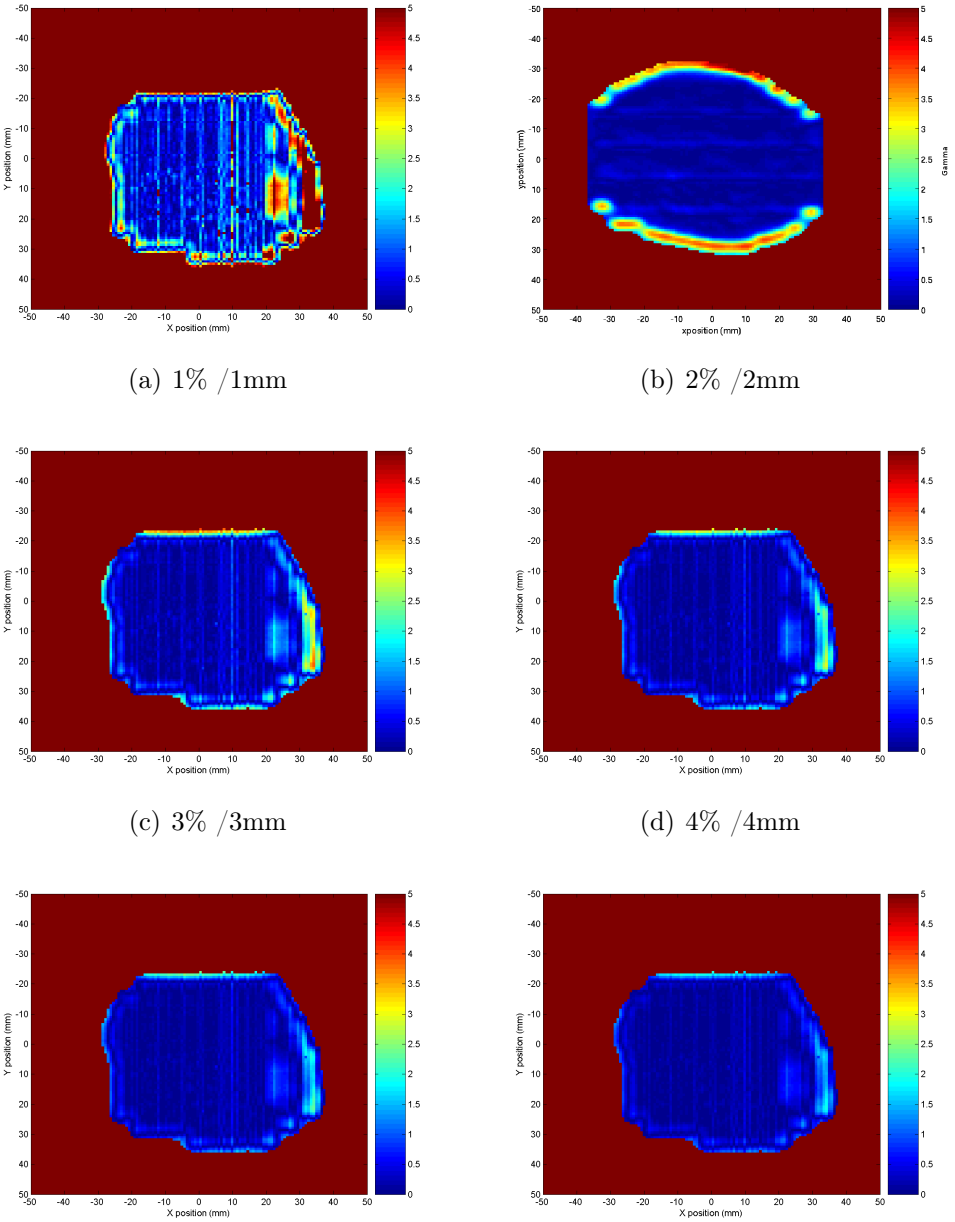

(a) 1% /1mm

(b) 2% /2mm

(c) 3% /3mm

(d) 4% /4mm

(e) 5% / 5mm

(f) 6% / 6mm

Figure 8.9: Gamma maps for various gamma criteria for beam 1, patient 1.In each map, the value of gamma below the threshold dose of 10% is displayed in dark red for clarity

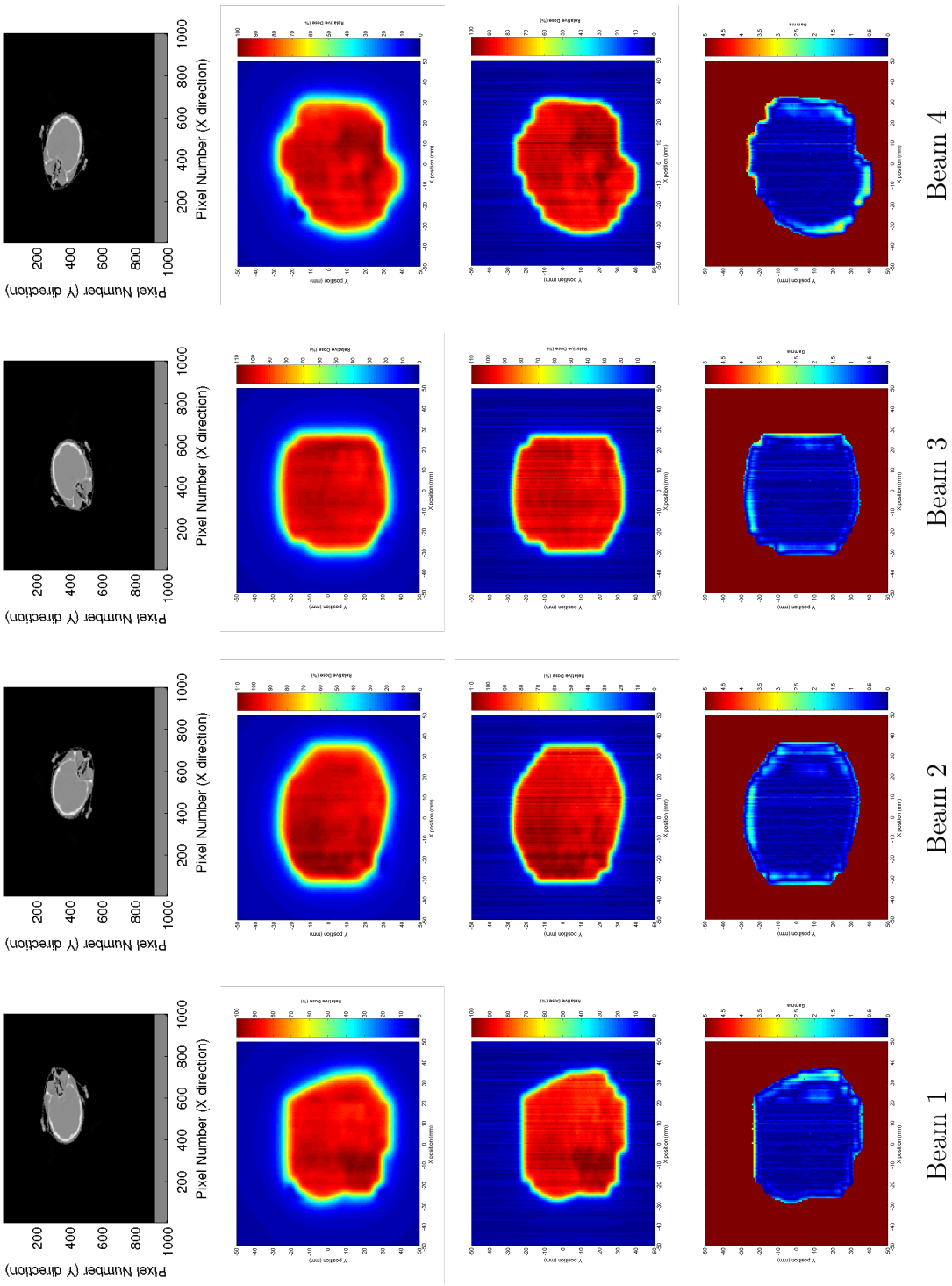

Figure 8.10: Phantoms, dose maps and gamma comparison of EPID MC simulations for patient 1.The top row is an illustration of the phantom used, the second and third rows the dose maps from the EPID and TPS calculation respectively and the bottom row a gamma map of the comparison between the two data sets

Patient	6%/5mm	5%/5mm	4%/4mm	3%/3mm	2%/2mm	1%/1mm
pat1 beam 1	95.30	93.10	90.40	85.74	62.10	56.60
pat1 beam 2	92.17	88.90	80.12	73.32	57.97	38.30
pat1 beam 3	98.02	95.76	92.98	88.18	63.87	58.22
pat1 beam 4	98.84	96.56	93.76	88.92	64.41	58.70
pat1 beam 5	99.69	97.39	94.56	89.68	64.96	59.21
pat2 beam 1	97.37	95.12	92.36	87.60	63.45	57.83
pat2 beam 2	98.78	96.50	93.70	88.87	64.37	58.67
pat2 beam 3	99.33	97.04	94.22	89.36	64.73	58.99
pat2 beam 4	97.11	94.87	92.12	87.36	63.28	57.67
pat2 beam 5	97.08	94.84	92.09	87.34	63.26	57.66
pat3 beam 1	99.97	97.66	94.83	89.94	65.14	59.37
pat3 beam 2	97.55	95.30	92.53	87.76	63.57	57.94
pat3 beam 3	96.81	94.58	91.83	87.09	63.08	57.50
pat3 beam 4	97.88	95.62	92.85	88.06	63.78	58.13
pat3 beam 5	99.77	97.47	94.64	89.76	65.01	59.25
pat3 beam 6	99.25	96.96	94.15	89.29	64.67	58.95
% of beams with γ>95%	93.75	68.75	0.00	0.00	0.00	0.00

Table 8.3: Percentage of points passing the gamma test with various tolerances for dose. TPS calculation of dose to EPID.

An apparent systematic difference between TPS dose and EPID dose was investigated by extracting the central voxels from the TPS dose and the EPID dose. The percentage difference between the average doses in the central 5x5 EPID pixels equivalent to an area of 3.92mm x 3.92mm and the central 4mm x 4mm of the TPS dose were calculated and tabulated in table 8.4.

The differences of table 8.4 were then averaged to produce a correction factor of 3.67% which was then uniformly applied to the TPS calculated doses. The gamma analysis was then repeated and tabulated in 8.5. As can be seen excellent figures are returned by the application of this empirically derived correction factor.

8.4.2.3 Discussion

There is a relatively poor agreement between measured and calculated results using this technique. The reason for this is not clear but Cufflin et al. (2010)

Patient	fract 1	fract 2	fract 3	fract 4
pat1 beam 1	-3.72%	-3.47%	-2.37%	-4.36%
pat1 beam 2	-4.39%	-2.77%	-3.94%	-4.14%
pat1 beam 3	-3.86%	-3.41%	-4.13%	-3.59%
pat1 beam 4	-2.78%	-3.72%	-3.95%	-3.27%
pat1 beam 5	-4.60%	-2.35%	-4.53%	-3.22%
pat2 beam 1	-3.24%	-2.57%	-3.46%	-4.12%
pat2 beam 2	-2.67%	-4.03%	-4.46%	-3.62%
pat2 beam 3	-4.04%	-3.81%	-4.17%	-3.84%
pat2 beam 4	-3.72%	-3.84%	-3.95%	-4.97%
pat2 beam 5	-4.60%	-4.46%	-4.56%	-4.37%
pat3 beam 1	-3.16%	-3.77%	-3.21%	-4.27%
pat3 beam 2	-3.02%	3.66%	-2.96%	-4.61%
pat3 beam 3	-3.05%	-3.41%	-3.88%	-3.71%
pat3 beam 4	-4.82%	-3.75%	-3.13%	-3.90%
pat3 beam 5	-4.87%	-2.53%	-3.03%	-3.15%
pat3 beam 6	-3.57%	-3.87%	-2.59%	-2.54%

Table 8.4: Percentage differences between doses calculated at the centre of the EPID and by the TPS and those measured with the EPID.

showed with their investigation that the pencil beam algorithm of OMP was the source of similar discrepancies. The imaging panel is within the build up region of the detector and, as such, a systematic difference of a few percent could be considered a better agreement than would be expected in this situation as the build up effect is not modelled in a pencil beam or type-a algorithm.

An improvement in the agreement between TPS dose and EPID dose could be explored by the use of a more complex algorithm within the TPS. Unfortunately, however, the iPLAN TPS does not have a type b or collapsed cone type algorithm and VCC have not currently purchased the iPLAN Voxel Monte Carlo (VMC) option, which could be used to explore this discrepancy further. The fact that the full MC simulations agree with the EPID measurements and the doses calculated within the patient in chapter 6 agree between the TPS and MC would also tend to point to the fact that this discrepancy is due to the weaknesses in the calculation algorithm of the TPS. Other treatment planning systems available within the department do not contain models of the μMLC, which is solely used for stereotactic radiotherapy. Therefore, it was not possible to change the TPS

Patient	6%/5mm	5%/5mm	4%/4mm	3%/3mm	2%/2mm	1%/1mm
pat1 beam 1	100.00	100.00	100.00	100.00	85.54	58.51
pat1 beam 2	96.8	95.70	94.90	93.82	77.01	49.51
pat1 beam 3	100.00	100.00	100.00	100.00	85.93	58.77
pat1 beam 4	100.00	100.00	100.00	100.00	86.31	59.03
pat1 beam 5	100.00	100.00	100.00	100.00	86.30	59.03
pat2 beam 1	100.00	100.00	100.00	100.00	87.04	59.53
pat2 beam 2	100.00	99.82	99.82	99.82	85.39	58.40
pat2 beam 3	100.00	100.00	100.00	100.00	85.56	58.52
pat2 beam 4	100.00	100.00	100.00	100.00	87.63	59.94
pat2 beam 5	100.00	100.00	100.00	100.00	88.75	60.70
pat3 beam 1	100.00	100.00	100.00	100.00	86.68	59.28
pat3 beam 2	100.00	100.00	100.00	100.00	86.58	59.22
pat3 beam 3	100.00	99.54	99.54	99.54	85.15	58.24
pat3 beam 4	100.00	95.65	95.65	95.65	81.82	55.96
pat3 beam 5	100.00	95.79	95.79	95.79	81.94	56.04
pat3 beam 6	100.00	93.87	93.70	93.47	79.95	54.69
% of beams with γ>95%	100.00	93.75	87.50	87.50	0.00	0.00

Table 8.5: Percentage of points passing the gamma test with various tolerances for dose. TPS EPID calculations with correction factor applied.

to further confirm this conclusion.

The use of a correction factor to adjust the TPS dose may be of some promise in resolving this discrepancy and, when applied, only two beams fail to have 95% of points passing the 3% / 3mm gamma comparison. Figure 8.10 also shows that the beam with an apparent positioning error has also been identified, which is reflected in the visual examination of the gamma map and in the reported average gamma figures tabulated.

A plot of varying distance to agreement figures in the gamma comparison at a discrepancy of 5% (prior to the correction factor being applied) is shown in table 8.6. Unlike the MC comparisons only 19% of beams pass the 5% / 3mm criteria. This would suggest that the empirically derived correction factor and the adjusted gamma criteria would need to be applied to achieve good agreement between the data sets.

This method is also considerably faster than the MC method in that a

Patient	5%/5mm	5%/4mm	5%/3mm	5%/2mm
pat1 beam 1	93.10	90.63	89.81	88.99
pat1 beam 2	88.90	86.50	85.70	84.90
pat1 beam 3	95.76	92.73	91.72	90.70
pat1 beam 4	96.56	95.54	95.21	94.87
pat1 beam 5	97.39	94.24	93.19	92.14
pat2 beam 1	95.12	91.27	89.99	88.71
pat2 beam 2	96.50	96.40	96.37	96.34
pat2 beam 3	97.04	92.02	90.35	88.67
pat2 beam 4	94.87	90.05	88.44	86.84
pat2 beam 5	94.84	90.65	89.26	87.86
pat3 beam 1	97.66	94.89	93.96	93.04
pat3 beam 2	95.30	94.80	94.64	94.47
pat3 beam 3	94.58	89.66	88.01	86.37
pat3 beam 4	95.62	94.46	94.08	93.69
pat3 beam 5	97.47	94.80	93.91	93.02
pat3 beam 6	96.96	96.88	96.86	96.83
% of beams with γ>95%	68.75	18.75	18.75	12.50

Table 8.6: Percentage of points passing the gamma test with varying dta tolerances for a dose difference criterion of 5% for the TPS calculation method.

comparison dose map can be produced within a few hours of the plan being completed with only the scans containing the EPID needing generation. The calculation time of the iPLAN system prior to dose export is instantaneous.

8.4.3 Path length approximation

For an in-vivo measurement, the intention is to confirm the validity of the overall dose delivered rather than the fluence across the beam. Another approach to solve the problems associated with the previous methods is to predict the doses based on a simple measurement obtained from the patient scans to obtain an expected dose, at a single point, and compare that to the dose measured by the EPID during treatment.

8.4.3.1 Theory

For the majority of cranial stereotactic radiotherapy and radiosurgery cases, EPID dosimetry at the centre of the field, can be greatly simplified due to the fact that

- The patient composition is fairly homogeneous in this region
- The thickness of sites treated being within the cranium is relatively constant at around 150 - 250mm
- The range of field sizes is fairly small and is limited by the μMLC to be less than 100mm and is limited locally (due to dosimetric issues) to be greater than an equivalent circle of 25mm diameter
- All fields are generally positioned around the isocentre and therefore 'off axis' and 'back scatter' factors, arising as a consequence of the effects of the support arm changing position relative to the fields do not need to be taken into account

Consequently, if there is no couch rotation involved, the imager may be placed in almost the same position on a daily basis allowing a set of dosimetric factors to be measured in this situation, closely analogous to the treatment situation.

To derive dosimetric quantities in this situation, a dose calculation formalism analogous to a TPR (Khan, 2010), based approach is applied. In standard conditions, the dose at the isocentre of a phantom can be calculated by rearranging equation 2.3 to give:

$$Dose = MU \times f_{cal} \times TPR(fs, depth) \times S_c(cs) \times S_p(fs) \times f_{ISL} \tag{8.5}$$

where

- $Dose$ is the dose at the isocentre
- f_{cal} is the dose delivered per monitor unit under standard conditions
- TPR is the tissue phantom ratio for a field size fs at $depth$

- S_c is the collimator scatter factor for a collimator setting cs
- S_p is the phantom scatter factor for a field size of fs
- f_{ISL} is the inverse square law factor for points at non isocentric distances.

All of these quantities can be approximated by measurements made with the EPID. In order to do this, the machine and EPID were set up according to figure 8.11(a) with layers of a water equivalent material, WTe (McEwen and DuSautoy, 2003), placed on the treatment couch with the isocentre placed in the centre of the slab.

In a conventional dose calculation, a machine calibration factor would be calculated at the isocentre, at a depth within the phantom, such as point B in figure 8.11(b) with a significant amount of phantom material beyond the measurement point to provide sufficient back scatter. However, in this situation, the exit dose at point C is of more interest than that at the centre of the phantom. A calibration curve, similar to that in figure 8.3, was derived, by positioning the isocentre of the machine at point C, and irradiating a 100mm slab of solid water with a 100mm x 100mm square field defined by the μMLC and standard collimators. A series of known doses, found by adjusting the number of MU according to standard tables, were then used to irradiate the block, with these doses measured by the EPID. A relationship between calculated dose and EPID signal could then be derived with the effects of missing back scatter at point C being taken into account by this calibration procedure, to give an EPID signal to dose conversion factor $f_{epiddose}$.

Analogues of TPRs were then measured by keeping the isocentre at point C on the stack of solid water and delivering a fixed number of monitor units whilst varying the thickness of solid water, the length of line AB in figure 8.11(b), with the doses again acquired using the EPID. These are shown in figure 8.12 such that a relationship between EPID dose and phantom thickness can be determined.

The expected dose at the EPID from a beam of $EwwF$ field size, from MU monitor units passing through a patient of radiological depth d_{rad} can therefore be determined by:

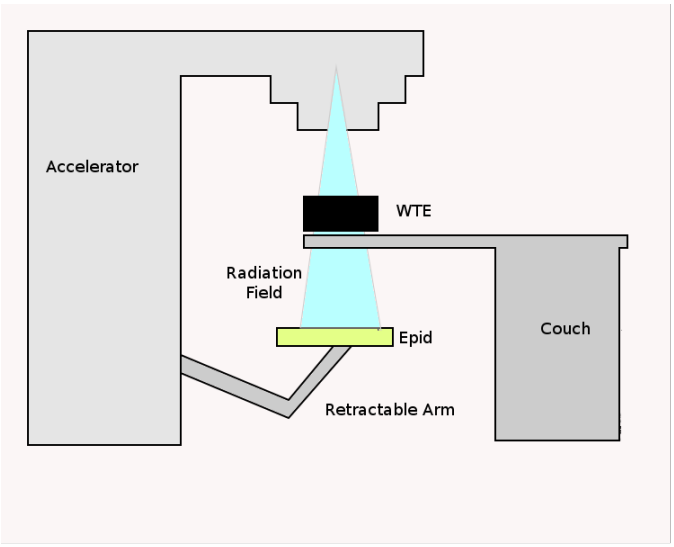

(a) Position of WTe

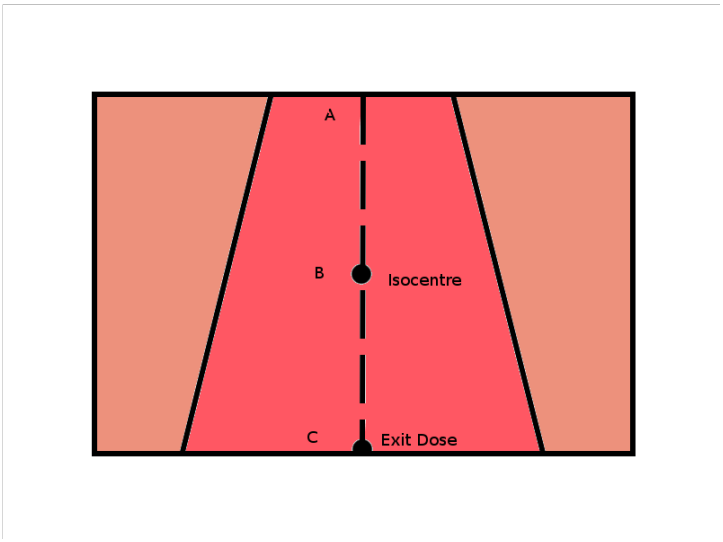

(b) Points within WTe)

Figure 8.11: Experimental set up for acquisition of data for path length method.

$$Dose_{epid} = f_{epiddose} \times TPR_{epid}(EwwF, d_{rad}) \times f_{EwwF} \times ISL(d_{geom}) \qquad (8.6)$$

where

- $Dose_{epid}$ is the epid dose expected at the imager plane

- $f_{epiddose}$ is the epid signal to dose conversion factor
- TPR_{epid} is the Tissue Phantom Ratio measured with the EPID for a field size of equivalent window width $EwwF$ and a radiological depth d_{rad}
- f_{EwwF} is the field size factor
- ISL is the inverse square law factor based on the geometric distance d_{geom} between the isocentre and the position of the exit plane in the clinical situation.

The field size factor $f_{fieldsize}$ is analogous to a total scatter factor S_{cp}, which holds true for calculations at the isocentre but is not the case in this situation. However, the screen field size factors, illustrated in figure 8.4(a) are used in this situation and simulated with this beam arrangement. Therefore, these effects are taken into account. As the support arm is held in the same place for both the acquisition of data and during measurement the effects of differing amounts of back scatter into the sensitive volume of the EPID as a function of the position of the support arm can also be neglected.

8.4.3.2 Methods

For each beam, from each fraction, the expected doses were calculated using equation 8.6 and compared with that measured using the EPID. The radiological and geometric depths were obtained by ray tracing the central axis through the MC phantoms generated for the MC transport investigation discussed previously.

8.4.3.3 Results

The results of the calculations for each beam and each fraction are tabulated in table 8.7. There appears to be a random variation between the dose expected and that measured at the EPID, possibly as a result of the approximation of the collimator and phantom scatter factors to a single factor based on the $EwwF$ and uncertainties in the calculation of geometric depth and other factors used in the calculation

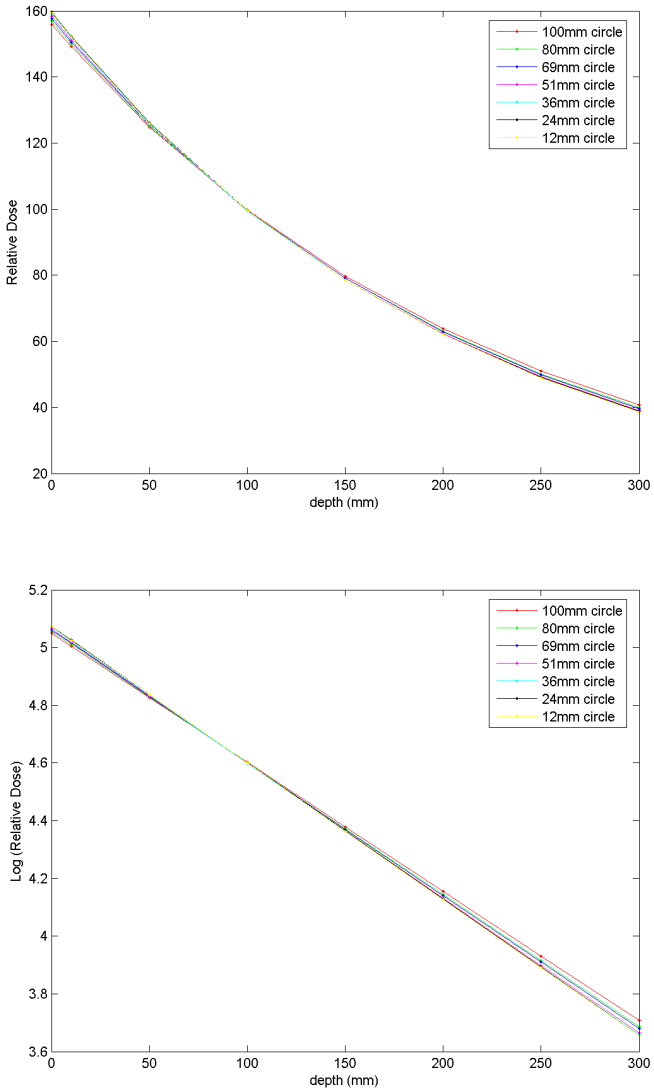

Figure 8.12: TPR equivalent measured with EPID (linear and natural logarithm scales for relative dose).

8.4.3.4 Discussion

This method shows relatively good agreement at a single point at the imager plane. The greatest discrepancy between measured and calculated doses is 3.61%, which is of a similar magnitude to the accuracy achieved using other methods such as in-vivo diodes and TLDs. The time taken to calculate these doses was

Patient	fract 1	fract 2	fract 3	fract 4
pat1 beam 1	2.15%	2.44%	1.86%	2.15%
pat1 beam 2	-2.73%	-2.22%	-2.53%	-2.53%
pat1 beam 3	-1.74%	-1.36%	-1.20%	-1.43%
pat1 beam 4	-0.44%	-0.30%	-0.85%	-0.56%
pat1 beam 5	2.33%	2.98%	0.54%	1.91%
pat2 beam 1	-0.76%	-2.21%	-2.13%	-1.14%
pat2 beam 2	-0.61%	-0.30%	-0.25%	-1.30%
pat2 beam 3	-0.24%	-1.25%	-0.03%	-1.25%
pat2 beam 4	-1.10%	0.52%	-1.02%	0.85%
pat2 beam 5	-1.06%	-1.72%	-1.24%	0.66%
pat3 beam 1	-2.11%	-3.30%	-0.03%	-1.28%
pat3 beam 2	2.51%	2.38%	2.26%	3.61%
pat3 beam 3	-0.55%	-0.26%	-0.83%	1.30%
pat3 beam 4	-1.45%	0.65%	-2.01%	-0.92%
pat3 beam 5	1.24%	0.92%	2.48%	1.55%
pat3 beam 6	0.35%	0.72%	0.77%	1.60%

Table 8.7: Percentage differences between predicted and measured values using path length approximation model - no back scatter correction and assumes Scp is unchanged at exit plane.

small once the MC phantoms had been generated and of the order of less than two minutes per plan. However, were this to be used as the sole method of in-vivo dosimetry, a method of radiological depth calculation would need to be developed to enable fast calculation. This information may be fairly readily obtained by placing calculation points on the patient anatomy using the TPS, or by developing software to automatically calculate the radiological depth from the CT planning scans, but this has yet to be investigated and developed.

8.4.4 Discussion

All three methods investigated have shown that they are capable of providing assurance that the delivered doses are within acceptable limits or identifying those outside tolerance which require further investigation. A summary of their performance is shown in table 8.8.

The full Monte Carlo transport approach, although the most accurate

technique is, unsurprisingly, the most time consuming and resource intensive. It may be argued that the time required to simulate the exact clinical situation is not warranted as the level of validation required is of a much lower precision than that offered by the technique. It does, however, offer a completely independent dose calculation of doses at the imager plane and may be of value in particularly complex cases or in the introduction of new technique into a department. As a full transport of incident radiation through the patient is involved from a complete model of the accelerator head, a high degree of confidence can be placed in the accuracy of the system for difficult cases, such as those involving heterogeneous tissue e.g. for stereotactic techniques in the lung and other sites. Using an appropriate set of gamma criteria, the approach can identify delivery errors to within realistic tolerances.

The TPS technique has the advantage of a fast calculation of the predicted doses but requires an empirically derived correction factor to get the measured doses to within expected limits. In many respects, the application of such a factor is counter intuitive to the concept of in vivo dosimetry as the application of a factor derived from the inability of the TPS to calculate doses correctly in this situation may cancel out any other discrepancies in dose calculation introduced by the TPS. The MC technique has shown, for these three patients at least, that the miscalculation is associated with the weaknesses in the calculation algorithm in calculating doses in a relatively complex situation involving large amounts of inhomogeneity. Although this technique may be usable for a type-a algorithm with a correction factor applied, there appears to be little advantage in adopting this system over the path length approximation until these dosimetric errors are investigated further and a a solution without the need for an empirical correction factor found. The use of a type-b or VMC type calculation may overcome these difficulties, and for tumour sites outside the cranium, where still further areas of inhomogeneity exist, the method needs further investigation.

The path length approximation technique provides the advantage of a fast calculation and good agreement between the doses measured with the EPID and those predicted by the technique. Despite suffering from the disadvantage of offering only a single point calculation, for fixed, small unmodulated fields it may be argued that this is the most appropriate technique for cranial stereotactic radiotherapy and radiosurgery.

With the increasing interest in extra-cranial stereotactic radiotherapy an interesting piece of further work would be to extend this investigation into areas of high tissue inhomogeneity such as those found in the lung to determine if the same behaviour and agreement between predicted doses and those measured at the imager plane are observed.

	MC Transport	TPS calculation	Path length
Accuracy	Excellent (<3%)	Fair (<5%)	Good (<4%)
Preparation Speed	2 hours	2 hours	10 Minutes
Calculation Time	48 hours	2 Minutes	Instant
Independence	Excellent	Fair	Good
Information	Excellent (Full beam)	Excellent (Full beam)	Fair (Point dose)

Table 8.8: Comparison of EPID dose prediction methods.

..

8.5 Conclusions

This work has shown that the three methods investigated can be used, with varying degrees of accuracy to validate the delivered doses to a patient for cranial stereotactic radiotherapy. A gamma comparison criteria of 95% points passing 5% / 3mm for the MC transport would appear to be an appropriate measure for determining the accuracy of dose delivery in this situation.The TPS calculation is less successful, probably as a consequence of the calculation algorithm, which may be solved by the use of more advanced calculation algorithms or the acceptance of less rigorous gamma criteria. For the cases considered 93.8% of beams passed a gamma criteria of 6% / 6mm. The path length approximation confirmed doses were correct on the central axis to within 3.6% and could be used as a check of correct dose delivery to within a similar tolerance.

Monte Carlo methods have enabled a solution to be derived using a full MC transport of radiation through the patient and also in the derivation of 'water to screen' correction factors.

Chapter 9

Conclusions and Further Work

Contents

9.1 Conclusions

The work has concentrated on the application of Monte Carlo dose calculation methods in stereotactic radiotherapy, primarily within the cranium, but with some investigations into the application of MC methods in extra-cranial stereotaxy in inhomogeneous media, such as that found in the lung.

In Chapter 4, a model of the accelerator and the BrainLAB μMLC was developed and shown to have very good agreement between experimental measurements and simulations. As with the rest of this study, the use of high performance computing techniques using Condor and the RTGrid allowed detailed tuning of the model to arrive at parameters which could be used with confidence in subsequent parts of the work. A model of the μMLC was developed which modelled the exact geometry of the device, enabling rapid (compared to some approximations of other authors) and accurate simulations of doses delivered by the device. The development of this component module was the largest aspect of the work and it would be interesting to compare with the results

of Kairn et al. (2010) who showed excellent agreement between measurement and simulation using existing component modules.

The exact geometry within the BLMLC component module did however provide confidence that the effects of collimator design on the output from small fields would be modelled exactly, which was the basis for the study in Chapter 5. In this chapter the performance of several detectors was examined in the measurement of relative and absolute doses and compared to those simulated using BLMLC and a model of the accelerator. Correction factors for volume averaging and detector composition were derived which could be applied profitably within the clinic. More importantly however, these studies have helped define the circumstances, in terms of field size, in which the measurements made by the detectors could be used with confidence. Locally at VCC this has confirmed our current practice of field size limitations (perhaps even suggesting that we have been too cautious in setting field size limits), and provides a secure platform to implement smaller fields if required.

Further clinical implications of the model were discussed in Chapter 6 in which a system for routine verification of plans calculated using the BrainLAB iPLAN system was developed. Excellent agreement was achieved between the doses calculated by the TPS and using the MC system, giving confidence in the validity of the dosimetric performance of the TPS. Dose calculations in volumes with a high degree of tissue homogeneity are not troublesome and with the exception of field size limitations should not unduly cause problems for a pencil beam or type-a calculation algorithm. It could be argued therefore, that such a system is unwarranted for such treatments but there are likely to be occasions where treatments are required in areas of high tissue heterogeneity (such as found just inferiorly to the brain) where the MC method can add to the validation of the TPS calculation. Similarly, when small fields are used, the system may be of use as is the case when new beam data or calculation algorithms are introduced into the department where this system can provide a completely independent calculation for comparison.

In Chapter 7 the situation of extra cranial stereotactic treatments in the lung or other heterogeneous media was examined. Using the MC simulations enabled a fine dose grid to be calculated and comparisons made against the dose produced

by a TPS. From this work it was shown that at least a type-b algorithm should be used in calculation of doses to the lung, although the requirement for this may reduce as the number of beams is increased. It was shown that beyond three beams there is little advantage in the use of additional beams to overcome the surface effects of such treatments but that the image and calculation resolution may be significant in properly modelling such situations.

Chapter 8 dealt with the subject of dosimetry using Electronic Portal Imaging Devices (EPIDs). Three methods were compared ranging from a full MC simulation to a simple path length correction. All of the methods investigated showed some promise as a routine system. However, whereas the MC solution had limitations associated with the time required to set up and run the simulations, and the path length approximation has a weakness of only considering a single point, the TPS calculation relies on an empirically derived correction factor, based on previous data to enable a satisfactory result. The work has shown however that EPID based transit dosimetry can be used in the routine verification of treatment delivery of stereotactic radiotherapy and radiosurgery. The application of MC methods was able to realise one method and facilitate the other two, by producing water to imager, and field size correction factors.

9.2 Further Work

There are several areas investigated in this study, which open up possibilities for further work. A comparison of the models of the μMLC produced in this study with those of Belec et al. (2005) and Kairn et al. (2010) would be an interesting study and the limitations of the approximations made in the less exact models compared with that of BLMLC.

For the small field investigation a more exact model of the diodes would be an interesting study to determine, in more detail the effects of the material manufacture on dose measurement in various conditions. This may enable the output data to converge further on the MC simulations.

Both the plan verification and the EPID based dosimetry sections, have clear uses in extra cranial stereotactic radiotherapy. In these situations of greater uncertainty in the TPS dose calculation the MC approach may be used to

independently validate the TPS calculated dose prior to treatment. On treatment the extension of the EPID based work may provide a valuable addition to the tools available to verify that doses have been delivered correctly. However, due to the complexity of the clinical situation, certainly it would be expected that the path length approximation method and the TPS calculation method would require further investigation to determine their feasibility. The MC method should be applicable in this situation. As has been shown by Cufflin et al. (2010) a type-b algorithm is necessary for good agreements of the TPS or similar methods but this would need to be available on the TPS as prerequisite to implementing the technique.

Chapter 10

Dissemination of Work

Contents

10.1 Presentations

'Monte Carlo Verification of Stereotactic Radiotherapy' Tony Millin, Jason Belec, Geraint Lewis, Frank Verhaegen; presented at MCNEG (Monte Carlo users group), Birmingham, UK; April 2005

'Verification of Stereotactic Radiotherapy using Monte Carlo methods', Tony Millin, Geraint Lewis; presented at BrainLAB users meeting, Seville, Spain; June 2005.

'A New BEAMnrc Component Module to Model Complex Multi Leaf Collimator Geometry', Tony Millin, Geraint Lewis; presented at MCNEG, London UK; March 2007

'Verification of Stereotactic Radiotherapy using Distributed Computing Methods', Tony Millin, Geraint Lewis; presented at BrainLAB users meeting, Rome, Italy; June 2007.

'Verification of Stereotactic Radiotherpy in a Distributed Computing Environment', Tony Millin, Geraint Lewis; presented at International Stereotactic Society (ISRS) biennial meeting, San Francisco, USA; July 2007

'Applications of a new BEAMnrc Component Module (BLMLC) in the Verification of Stereotactic Radiotherapy and Stereotactic Radiosurgery', Tony Millin, Geraint Lewis, Rebecca Cufflin; presented at 2nd European Workshop on Monte Carlo Treatment Planning, Cardiff UK; October 2009

'Applications of high throughput computing in the verification of stereotactically guided radiotherapy. Tony Millin; presented at Institute of Physics and Engineering in Medicine annual meeting, (High Performance Computing Session), Nottingham, UK; September 2010

'Electronic Portal Image Dosimetry for Cranial Stereotactic Radiotherapy / Radiosurgery' Tony Millin, Rebecca Cufflin, Geraint Lewis; presented at IPEM meeting 'Stereotactic Radiotherapy: new equipment, novel techniques', London, UK; March 2011

10.2 Publications

Millin, A.E., and Lewis D. G. 2010. Routine Dosimetric Verification of Stereotactic Treatments Using Monte Carlo Methods in a Distributed Computing Environment. Radiosurgery 7: 28.

References

Ahnesjo, A., Saxner, M., and Trepp, A. A pencil beam model for photon dose calculation. *Medical physics*, 19:263 (1992).
URL: *http://link.aip.org/link/?MPHYA6/19/263/1* 47

Ahnesjo, A. and Trepp, A. Acquisition of the effective lateral energy fluence distribution for photon beam dose calculations by convolution models. *Physics in Medicine and Biology*, 36:973 (1991).
URL: *http://iopscience.iop.org/0031-9155/36/7/006* 207

Ahnesjo, Anders. Collapsed cone convolution of radiant energy for photon dose calculation in heterogeneous media. *Medical Physics*, 16(4):577–592 (1989). 47, 207

Andrews, Gregory R. *Foundations of Multithreaded, Parallel, and Distributed Programming*. Addison Wesley (2000). ISBN ISBN 0-201-35752-6. 54

Antonuk, Larry E. Electronic portal imaging devices: a review and historical perspective of contemporary technologies and research. *Physics in medicine and biology*, 47(6):R31–65 (March 2002). ISSN 0031-9155.
URL: *http://www.ncbi.nlm.nih.gov/pubmed/11936185* 12, 191

Baldock, C, De Deene, Y, Doran, S, Ibbott, G, Jirasek, a, Lepage, M, McAuley, K B, Oldham, M, and Schreiner, L J. Polymer gel dosimetry. *Physics in medicine and biology*, 55(5):R1–63 (2010). ISSN 1361-6560. doi: 10.1088/0031-9155/55/5/R01.
URL: *http://www.ncbi.nlm.nih.gov/pubmed/20150687* 29, 30

Banki, F, Luketich, J D, Chen, H, Christie, N, and Pennathur, A. Stereotactic radiosurgery for lung cancer. *Minerva Chirurgica*, 64(6):589–598 (2009). 174

Batho, H F. Lung corrections in cobalt 60 beam therapy. *Journal of Canadian Association of Radiology*, 15:79–83 (1964). 42

Belec, Jason, Patrocinio, Horacio, and Verhaegen, Frank. Development of a Monte Carlo model for the Brainlab microMLC. *Physics in Medicine and Biology*, 50:787–799 (2005).
URL: *http://stacks.iop.org/0031-9155/50/787* 67, 89, 104, 106, 226

Bentley, R E and Milan, J. An interactive digital computer system for radiotherapy treatment planning. *The British journal of radiology*, 44(527):826–33 (November 1971). ISSN 0007-1285.
URL: *http://www.ncbi.nlm.nih.gov/pubmed/5001288* 39

Bielajew, A F, Hirayama, H, Nelson, W R, and Rogers, D W O. History , overview and recent improvements of EGS4 National Laboratory for High Energy Physics. Technical Report June, Institute for National Measurement Standards, National Research Council of Canada (1994). 52

Bjarngard, J, Tsai, Jen-San, and Rice, R K. Doses on the central axes of narrow 6MV x-ray beams. *Medical Physics*, 17(5):794–799 (1990). 28

Bortfeld, Thomas and Webb, Steve. Single-Arc IMRT? *Physics in medicine and biology*, 54(1):N9–20 (2009). ISSN 0031-9155. doi:10.1088/0031-9155/54/1/N02.
URL: *http://www.ncbi.nlm.nih.gov/pubmed/19075362* 15

Cameron, C. Sweeping-window arc therapy: an implementation of rotational IMRT with automatic beam-weight calculation. *Physics in medicine and biology*, 50(18):4317–36 (September 2005). ISSN 0031-9155. doi:10.1088/0031-9155/50/18/006.
URL: *http://www.ncbi.nlm.nih.gov/pubmed/16148396* 15

Cassell, K J, Hobday, P A, and Parker, R P. The implementation of a generalised Batho inhomogeneity correction for radiotherapy planning with direct use of CT numbers. *Physics in medicine and biology*, 26(5):825–33 (September 1981). ISSN 0031-9155.
URL: *http://www.ncbi.nlm.nih.gov/pubmed/7291303* 42

Chin, P W, Lewis, D G, and Spezi, E. Correction for dose-response variations in a scanning liquid ion chamber EPID as a function of linac gantry angle. *Physics in Medicine and Biology*, 49(8):N93–N103 (April 2004). ISSN 0031-9155. doi:10.1088/0031-9155/49/8/N01. 31

Chin, P W, Spezi, E, and Lewis, D G. Monte Carlo simulation of portal dosimetry on a rectilinear voxel geometry: a variable gantry angle solution. *Physics in medicine and biology*, 48(16):N231–8 (August 2003). ISSN 0031-9155.
URL: *http://www.ncbi.nlm.nih.gov/pubmed/12974586* 199

Chin, Pik Wai. *Monte Carlo portal dosimetry*. Ph.D. thesis, University of Wales (2005). doi:10.1118/1.2040709. 193

Chiu-Tsao, Sou-Tung, Ho, Yunsil, Shankar, Ravi, Wang, Lin, and Harrison, Louis B. Energy dependence of response of new high sensitivity radiochromic films for megavoltage and kilovoltage radiation energies. *Medical Physics*, 32(11):3350 (2005). ISSN 00942405. doi:10.1118/1.2065467.
URL: *http://link.aip.org/link/MPHYA6/v32/i11/p3350/s1&Agg=doi* 29

Chui, C.S. and Mohan, R. Off-center ratios for three-dimensional dose calculations. *Medical physics*, 13:409 (1986).
URL: *http://link.aip.org/link/?MPHYA6/13/409/1* 42

Clarkson, JR. A note on depth doses in fields of irregular shape. *British Journal of Radiology*, 14(164):265 (1941).
URL: *http://bjr.birjournals.org/cgi/content/abstract/14/164/265* 41

Colombo, F, Benedetti, A, Pozza, F, Avanzo, R C, Marchetti, C, Chierego, G, and Zanardo, A. External stereotactic irradiation by linear accelerator. *Neurosurgery*, 16:154 (1985). 9, 13

Cosgrove, V P, Jahn, U, Pfaender, M, Bauer, S, Budach, V, and Wurm, R E. Commissioning of a micro multi-leaf collimator and planning system for stereotactic radiosurgery. *Radiotherapy and Oncology*, 50:325–335 (1999). 13, 18, 104, 106

Crop, F, Reynaert, N, Pittomvils, G, Paelinck, L, De Wagter, C, Vakaet, L, and Thierens, H. The influence of small field sizes, penumbra, spot size

and measurement depth on perturbation factors for microionization chambers. *Physics in medicine and biology*, 54(9):2951–69 (2009). ISSN 0031-9155. doi: 10.1088/0031-9155/54/9/024.
URL: *http://www.ncbi.nlm.nih.gov/pubmed/19384005* 33

Cufflin, R S. *Development of Techniques for the Verification of Intensity Modulated Radiotherapy*. Phd thesis, Cardiff University (2011). 199, 207

Cufflin, R S, Spezi, E, Millin, A E, and Lewis, D G. An investigation of the accuracy of Monte Carlo portal dosimetry for verification of IMRT with extended fields. *Physics in medicine and biology*, 55(16):4589–600 (August 2010). ISSN 1361-6560. doi:10.1088/0031-9155/55/16/S12.
URL: *http://www.ncbi.nlm.nih.gov/pubmed/20668335* 32, 104, 106, 199, 204, 207, 212, 227

Dahlgren, Christina Vallhagen, Eilertsen, Karsten, Jorgensen, Trude Dahl, and Ahnesjö, Anders. Portal dose image verification: the collapsed cone superposition method applied with different electronic portal imaging devices. *Physics in medicine and biology*, 51(2):335–49 (January 2006). ISSN 0031-9155. doi:10.1088/0031-9155/51/2/010.
URL: *http://www.ncbi.nlm.nih.gov/pubmed/16394342* 207

Das, Indra J., Ding, George X., and Ahnesjo, Anders. Small fields: Nonequilibrium radiation dosimetry. *Medical Physics*, 35(1):206 (2008). ISSN 00942405. doi:10.1118/1.2815356.
URL: *http://link.aip.org/link/MPHYA6/v35/i1/p206/s1&Agg=doi* 34

Day, MJ. A note on the calculation of dose in x-ray fields. *British Journal of Radiology*, 23(270):368 (1950).
URL: *http://bjr.birjournals.org/cgi/content/abstract/23/270/368* 42

Deng, Jun, Guerrero, Thomas, Ma, C-M, and Nath, Ravinder. Modelling 6 MV photon beams of a stereotactic radiosurgery system for Monte Carlo treatment planning. *Physics in Medicine and Biology*, 49:1689–1704 (2004).
URL: *http://stacks.iop.org/0031-9155/49/1689* 89

Downes, P, Yaikhom, G, Giddy, JP, Walker, DW, Spezi, E, and Lewis, DG. High performance computing for Monte Carlo radiotherapy calculations.

Philosophical Transactions of the Royal Society A: Mathematical, Physical and Engineering Sciences, 367(1897):2607 (2009). doi:10.1098/rsta.2009.0028.
URL: *http://dx.doi.org/10.1098/rsta.2009.0028* 50, 56, 61

Dutreix, A, Bjarngard, BE, Bridier, A, Mijnheer, B, Shaw, JE, and Svensson, H. Monitor unit calculation for high energy photon beams. Technical report, ESTRO Booklet No. 3. Garant Publishers N.V.; 1997 (1997). 19

Fiandra, Christian, Ricardi, Umberto, Ragona, Riccardo, Anglesio, Silvia, Romana Giglioli, Francesca, Calamia, Elisa, and Lucio, Francesco. Clinical use of EBT model Gafchromic film in radiotherapy. *Medical Physics*, 33(11):4314 (2006). ISSN 00942405. doi:10.1118/1.2362876.
URL: *http://link.aip.org/link/MPHYA6/v33/i11/p4314/s1&Agg=doi* 29

Fippel, M. Fast Monte Carlo dose calculation for photon beams based on the VMC electron algorithm. *Medical physics*, 26(8):1466–75 (August 1999). ISSN 0094-2405.
URL: *http://www.ncbi.nlm.nih.gov/pubmed/10501045* 175

Fong, P M, Keil, D C, Does, M D, and Gore, J C. Polymer gels for magnetic resonance imaging of radiation dose distributions at normal room atmosphere. *Physics in medicine and biology*, 46(12):3105–13 (December 2001). ISSN 0031-9155.
URL: *http://www.ncbi.nlm.nih.gov/pubmed/11768494* 30

Gager, L. David, Wright, Ann, E, and Almond, Peter R. Silicon diode detectors used in radiological physics measurments. Part 1: Development of an energy compensating shield. *Medical Physics*, 4(6):494–498 (1977). 26

Gill, S S, Thomas, D G, Warrington, A P, and Brada, M. Relocatable Frame for stereotactic external beam radiotherapy. *International Journal of Radiation Oncology*Biology*Physics*, 20(3):599–603 (1991). 16

Gray, K and Smith, C W. Accuracy of dose calculation methods for retracted tissue compensators. *Physics in medicine and biology*, 39(12):2355–65 (December 1994). ISSN 0031-9155.
URL: *http://www.ncbi.nlm.nih.gov/pubmed/15551559* 42

Heath, Emily and Seuntjens, Jan. Development and validation of a BEAMnrc component module for accurate Monte Carlo modelling of the Varian dynamic Millennium multileaf collimator. *Physics in medicine and biology*, 48(24):4045–63 (December 2003). ISSN 0031-9155.
URL: *http://www.ncbi.nlm.nih.gov/pubmed/14727750* 89, 92, 104

Heydarian, M, Hoban, P W, and Beddoe, A H. A comparison of dosimetry techniques in stereotactic radiosurgery. *Physics in Medicine and Biology*, 41:93–110 (1996).
URL: *http://stacks.iop.org/0031-9155/41/93* 33

Hof, H, Herfarth, K, and Debus, J. Stereotactic irradiation of lung tumors. *Der Radiologe*, 44(5):484–490 (2004). 174

Horsley, V and Clarke, R H. The structure and functions of the cerebellum examined by a new method. *Brain*, 31:45 (1908). 3

Huang, Vicky W, Seuntjens, Jan, Devic, Slobodan, and Verhaegen, Frank. Experimental determination of electron source parameters for accurate Monte Carlo calculation of large field electron therapy. *Physics in medicine and biology*, 50(5):779–86 (March 2005). ISSN 0031-9155. doi:10.1088/0031-9155/50/5/004.
URL: *http://www.ncbi.nlm.nih.gov/pubmed/15798254* 74

IBA Dosimetry GmbH. *Field Detectors: EFD, PFD, SFD, RFD* (2010). 136

Johns, H E and Cunningham, J R. *The physics of radiology*. Thomas Springfield, Illinois (1969). 9

Jursinic, Paul A. Angular dependence of dose sensitivity of surface diodes. *Medical Physics*, 36(6):2165 (2009). ISSN 00942405. doi:10.1118/1.3125644.
URL: *http://link.aip.org/link/MPHYA6/v36/i6/p2165/s1&Agg=doi* 26

Kairn, T., Kenny, J., Crowe, S. B., Fielding, A. L., Franich, R. D., Johnston, P. N., Knight, R. T., Langton, C. M., Schlect, D., and Trapp, J. V. Technical Note: Modeling a complex micro-multileaf collimator using the standard BEAMnrc distribution. *Medical Physics*, 37(4):1761 (2010). ISSN 00942405. doi:10.1118/1.3355873.

URL: *http://link.aip.org/link/MPHYA6/v37/i4/p1761/s1&Agg=doi* 67, 225, 226

Kawrakow, I. On the de-noising of Monte Carlo calculated dose distributions. *Physics in medicine and biology*, 47(17):3087–103 (September 2002). ISSN 0031-9155.
URL: *http://www.ncbi.nlm.nih.gov/pubmed/12361212* 85

Kawrakow, I. The EGSnrc Code System : Monte Carlo Simulation of Electron and Photon Transport. pages 2001–2009 (2010). 52, 53

Kawrakow, I., Fippel, M., and Friedrich, K. 3D electron dose calculation using a Voxel based Monte Carlo algorithm (VMC). *Medical physics*, 23:445 (1996).
URL: *http://link.aip.org/link/?MPHYA6/23/445/1* 51, 172

Kawrakow, I, Mainegra-Hing, E, Rogers, DWO, Tessier, F, and Walters, B R. The EGSnrc Code System : Monte Carlo Simulation of Electron and Photon Transport. Technical report, National Research Council of Canada, Ottawa (2010).
URL: *http://irs.inms.nrc.ca/software/egsnrc/documentation/pirs701.pdf* 67

Keall, P J, Siebers, J V, Arnfield, M, Kim, J O, and Mohan, R. Monte Carlo dose calculations for dynamic IMRT treatments. *Physics in medicine and biology*, 46(4):929–41 (April 2001). ISSN 0031-9155.
URL: *http://www.ncbi.nlm.nih.gov/pubmed/11324969* 89

Khan, Faiz M. *The physics of radiation therapy*. Wolters Kluwer. Lippincott Williams & Wilkins, Philadelphia, 4th edition (2010). 2, 29, 216

Kim, Sangroh. Characteristics of elliptical sources in BEAMnrc Monte Carlo system :. (August 2008):1046–1052 (2009a). doi:10.1118/1.3086110. 145

Kim, Sangroh. Characteristics of elliptical sources in BEAMnrc Monte Carlo system: Implementation and application. *Medical Physics*, 36(4):1046 (2009b). ISSN 00942405. doi:10.1118/1.3086110.
URL: *http://link.aip.org/link/MPHYA6/v36/i4/p1046/s1&Agg=doi* 74

Kirby, M and Williams, P C. The use of an electronic portal imaging device for exit dosimetry and quality control measurements. *International Journal of Radiation Oncology*Biology*Physics*, 31(3):593–603 (1995). 31

Kirby, M C and Glendinning, a G. Developments in electronic portal imaging systems. *The British journal of radiology*, 79 Spec No:S50–65 (September 2006). ISSN 1748-880X. doi:10.1259/bjr/21517185.
URL: *http://www.ncbi.nlm.nih.gov/pubmed/16980685* 30

Kontrisova, Kristina, Stock, Markus, Dieckmann, Karin, Bogner, Joachim, Pötter, Richard, and Georg, Dietmar. Dosimetric comparison of stereotactic body radiotherapy in different respiration conditions: a modeling study. *Radiotherapy and oncology : journal of the European Society for Therapeutic Radiology and Oncology*, 81(1):97–104 (October 2006). ISSN 0167-8140. doi: 10.1016/j.radonc.2006.08.006.
URL: *http://www.ncbi.nlm.nih.gov/pubmed/16962675* 20

Kumar, Shaleen, Burke, Kevin, Nalder, Colin, Jarrett, Paula, Mubata, Cephas, A'hern, Roger, Humphreys, Mandy, Bidmead, Margaret, and Brada, Michael. Treatment accuracy of fractionated stereotactic radiotherapy. *Radiotherapy and oncology : journal of the European Society for Therapeutic Radiology and Oncology*, 74(1):53–9 (January 2005). ISSN 0167-8140. doi:10.1016/j.radonc.2004.06.008.
URL: *http://www.ncbi.nlm.nih.gov/pubmed/15683670* 17

la Porte, C. Technical possibilities and limitations of stereotaxy. *Acta neurochirurgica*, 124:3–6 (1993). 4

Leal, A, Sanchez-Doblado, F, Arrans, R, Rosello, J, Pavon, E, and Lagares, J. Routine IMRT verification by means of an automated Monte Carlo simulation system. *International Journal of Radiation OncologyBiologyPhysics*, 56(1):58–68 (2003). ISSN 03603016. doi:10.1016/S0360-3016(03)00067-1.
URL: *http://linkinghub.elsevier.com/retrieve/pii/S0360301603000671* 50

Leksell, L. A stereotaxic apparatus for intracerebral surgery. *Acta Chir Scand*, 99:229–233 (1949). 4

Leksell, L. The stereotaxic method and radiosurgery of the brain. *Acta Chirurgica Scandinavica*, 102:316 (1951). 8

Levy, M L, Chen, J C T, Moffitt, K, Corber, Z, and McComb, G J. Stereoscopic head-mounted display incorporated into microsurgical procedures: technical note. *Neurosurgery*, 43:392 (1998). 4

Lief, E P and Lutz, W R. Determination of effective electron source size using multislit and pinhole cameras. *Medical physics*, 27(10):2372–5 (October 2000). ISSN 0094-2405.
URL: *http://www.ncbi.nlm.nih.gov/pubmed/11099206* 151

Liu, H H, Mackie, T R, and McCullough, E C. A dual source photon beam model used in convolution/superposition dose calculations for clinical megavoltage x-ray beams. *Medical physics*, 24(12):1960–74 (December 1997). ISSN 0094-2405.
URL: *http://www.ncbi.nlm.nih.gov/pubmed/9434979* 84

Liu, H H, Mackie, T R, and McCullough, E C. Modeling photon output caused by backscattered radiation into the monitor chamber from collimator jaws using a Monte Carlo technique. *Medical physics*, 27(4):737–44 (May 2000). ISSN 0094-2405.
URL: *http://www.ncbi.nlm.nih.gov/pubmed/10798696* 84, 86, 87

LoSasso, T, Chui, C S, Kutcher, G J, Leibel, S A, Fuks, Z, and Ling, C C. The use of a multi-leaf collimator for conformal radiotherapy of carcinomas of the prostate and nasopharynx. *International journal of radiation oncology, biology, physics*, 25:161 (1993). 10

Louwe, R. J. W., Tielenburg, R., van Ingen, K. M., Mijnheer, B. J., and van Herk, M. B. The stability of liquid-filled matrix ionization chamber electronic portal imaging devices for dosimetry purposes. *Medical Physics*, 31(4):819 (2004). ISSN 00942405. doi:10.1118/1.1668411.
URL: *http://link.aip.org/link/MPHYA6/v31/i4/p819/s1&Agg=doi* 31

Low, D a, Harms, W B, Mutic, S, and Purdy, J a. A technique for the quantitative evaluation of dose distributions. *Medical physics*, 25(5):656–61 (May 1998). ISSN 0094-2405.
URL: *http://www.ncbi.nlm.nih.gov/pubmed/9608475* 164, 165

Ma, C-M and Nahum, AE. Bragg-Gray theory and ion chamber dosimetry for photon beams. *Phys. Med. Niol*, 36:413–28 (1991). 25, 33

Manolopoulos, S, Wojnecki, C, Hugtenburg, R, Jaafar Sidek, M a, Chalmers, G, Heyes, G, and Green, S. Small field measurements with a novel silicon position sensitive diode array. *Physics in medicine and biology*, 54(3):485–95 (February 2009). ISSN 0031-9155. doi:10.1088/0031-9155/54/3/002.
URL: *http://www.ncbi.nlm.nih.gov/pubmed/19124947* 34

McCurdy, B. M. C., Luchka, K., and Pistorius, S. Dosimetric investigation and portal dose image prediction using an amorphous silicon electronic portal imaging device. *Medical Physics*, 28(6):911 (2001). ISSN 00942405. doi:10.1118/1.1374244.
URL: *http://link.aip.org/link/MPHYA6/v28/i6/p911/s1&Agg=doi* 104

McEwen, M R and DuSautoy, a R. Characterization of the water-equivalent material WTe for use in electron beam dosimetry. *Physics in medicine and biology*, 48(13):1885–93 (July 2003). ISSN 0031-9155.
URL: *http://www.ncbi.nlm.nih.gov/pubmed/12884922* 217

McKerracher, C and Thwaites, D I. Assessment of new small-field detectors against standard-field detectors for practical stereotactic beam data acquisition. *Physics in Medicine and Biology*, 44:2143–2160 (1999a).
URL: *http://stacks.iop.org/0031-9155/44/2143* 19, 33

McKerracher, C and Thwaites, D I. Assessment of new small-field detectors against standard-field detectors for practical stereotactic beam data acquisition. *Physics in medicine and biology*, 44(9):2143–60 (September 1999b). ISSN 0031-9155.
URL: *http://www.ncbi.nlm.nih.gov/pubmed/10495110* 143

McKerracher, Carolyn and Thwaites, David I. Notes on the construction of solid-state detectors. *Radiotherapy and oncology : journal of the European Society for Therapeutic Radiology and Oncology*, 79(3):348–51 (June 2006). ISSN 0167-8140. doi:10.1016/j.radonc.2006.05.008.
URL: *http://www.ncbi.nlm.nih.gov/pubmed/16797095* 71, 136

McKerracher, Carolyn and Thwaites, David I. Head scatter factors for small MV photon fields. Part I: a comparison of phantom types and methodologies. *Radiotherapy and oncology : journal of the European Society for Therapeutic Radiology and Oncology*, 85(2):277–85 (November 2007a). ISSN 0167-8140. doi:10.1016/j.radonc.2007.09.005.
URL: *http://www.ncbi.nlm.nih.gov/pubmed/17983677* 19

McKerracher, Carolyn and Thwaites, David I. Head scatter factors for small MV photon fields. Part II: the effects of source size and detector. *Radiotherapy and oncology : journal of the European Society for Therapeutic Radiology and Oncology*, 85(2):286–91 (November 2007b). ISSN 0167-8140. doi:10.1016/j.radonc.2007.09.006.
URL: *http://www.ncbi.nlm.nih.gov/pubmed/17983678* 19

McKerracher, Carolyn and Thwaites, David I. Phantom scatter factors for small MV photon fields. *Radiotherapy and oncology : journal of the European Society for Therapeutic Radiology and Oncology*, 86(2):272–5 (March 2008). ISSN 0167-8140. doi:10.1016/j.radonc.2007.10.040.
URL: *http://www.ncbi.nlm.nih.gov/pubmed/18061694* 19

McLaughlin, William L, Sayeg, J A, McCullough, E C, Kline, R W, Wu, Andrew, and Maitz, A H. The use of a radiochromic detector for the determination of stereotactic dose characteristics. *Medical Physics*, 21(3):379–388 (1994). 28

Meigooni, Ali S, Sanders, M F, Ibbott, G S, and Szeglin, S R. Dosimetric characteristics of an improved radiochromic film. *Medical Physics*, 23(11):1883–1888 (1996). 28

Millin, A E and Smith, C W. A beam profile generation algorithm for wedged half-beam blocked asymmetric fields. *Physics in Medicine and Biology*, 39:63–74 (1994). 42

Minniti, Giuseppe, Valeriani, Maurizio, Clarke, Enrico, D'Arienzo, Marco, Ciotti, Michelangelo, Montagnoli, Roberto, Saporetti, Francesca, and Enrici, Riccardo Maurizi. Fractionated stereotactic radiotherapy for skull base tumors: analysis of treatment accuracy using a stereotactic mask fixation system. *Radiation oncology (London, England)*, 5:1 (January 2010). ISSN 1748-717X.

doi:10.1186/1748-717X-5-1.
URL: *http://www.ncbi.nlm.nih.gov/pubmed/20070901* 17

Mohan, R., Chui, C., and Lidofsky, L. Differential pencil beam dose computation model for photonsons. *Medical physics*, 13:64 (1986).
URL: *http://link.aip.org/link/?MPHYA6/13/64/1* 156

Mohan, R. and Chui, C.S. Use of fast Fourier transforms in calculating dose distributions for irregularly shaped fields for three-dimensional treatment planning. *Medical physics*, 14:70 (1987).
URL: *http://link.aip.org/link/?MPHYA6/14/70/1* 156

Mukumoto, Nobutaka, Tsujii, Katsutomo, Saito, Susumu, Yasunaga, Masayoshi, Takegawa, Hideki, Yamamoto, Tokihiro, Numasaki, Hodaka, and Teshima, Teruki. A preliminary study of in-house Monte Carlo simulations: an integrated Monte Carlo verification system. *International journal of radiation oncology, biology, physics*, 75(2):571–9 (October 2009). ISSN 1879-355X. doi: 10.1016/j.ijrobp.2009.02.088.
URL: *http://www.ncbi.nlm.nih.gov/pubmed/19735883* 67

Nelson, WR, Hirayama, H, and Rogers, DWO. The EGS4 code system. *SLAC-265, Stanford Linear Accelerator* (1985).
URL: *http://www.osti.gov/energycitations/product.biblio.jsp?osti_id=6137659* 18

Netherlands Commission on Radiation Dosimetry. Recommendations for the determination and use of scatter correction factors of megavoltage photon beams. Technical report, NCS Report No. 12 (1998). 19

Nicolini, Giorgia, Fogliata, Antonella, Vanetti, Eugenio, Clivio, Alessandro, and Cozzi, Luca. GLAaS: An absolute dose calibration algorithm for an amorphous silicon portal imager. Applications to IMRT verifications. *Medical Physics*, 33(8):2839 (2006). ISSN 00942405. doi:10.1118/1.2218314.
URL: *http://link.aip.org/link/MPHYA6/v33/i8/p2839/s1&Agg=doi* 32, 104, 194

Niroomand-Rad, A, Blackwell, C R, Coursey, B M, Gall, K P, Galvin, J M, McLaughlin, W L, Meigooni, a S, Nath, R, Rodgers, J E, and Soares, C G.

Radiochromic film dosimetry: recommendations of AAPM Radiation Therapy Committee Task Group 55. American Association of Physicists in Medicine. *Medical physics*, 25(11):2093–115 (November 1998). ISSN 0094-2405.
URL: *http://www.ncbi.nlm.nih.gov/pubmed/9829234* 27, 28

Norihisa, Yoshiki, Nagata, Yasushi, Takayama, Kenji, Matsuo, Yukinori, Sakamoto, Takashi, Sakamoto, Masato, Mizowaki, Takashi, Yano, Shinsuke, and Hiraoka, Masahiro. Stereotactic body radiotherapy for oligometastatic lung tumors. *International journal of radiation oncology, biology, physics*, 72(2):398–403 (October 2008). ISSN 0360-3016. doi:10.1016/j.ijrobp.2008.01.002.
URL: *http://www.ncbi.nlm.nih.gov/pubmed/18374506* 174

Nucletron, BV. *OnCentra MasterPlan Physics Manual* (2010). 175, 178

Otto, Karl. Volumetric modulated arc therapy: IMRT in a single gantry arc. *Medical Physics*, 35(1):310 (2008). ISSN 00942405. doi:10.1118/1.2818738.
URL: *http://link.aip.org/link/MPHYA6/v35/i1/p310/s1&Agg=doi* 174

Pai, Sujatha, Das, Indra J., Dempsey, James F., Lam, Kwok L., LoSasso, Thomas J., Olch, Arthur J., Palta, Jatinder R., Reinstein, Lawrence E., Ritt, Dan, and Wilcox, Ellen E. TG-69: Radiographic film for megavoltage beam dosimetry. *Medical Physics*, 34(6):2228 (2007). ISSN 00942405. doi:10.1118/1.2736779.
URL: *http://link.aip.org/link/MPHYA6/v34/i6/p2228/s1&Agg=doi* 26

Pappas, E., Maris, T. G., Zacharopoulou, F., Papadakis, A, Manolopoulos, S., Green, S., and Wojnecki, C. Small SRS photon field profile dosimetry performed using a PinPoint air ion chamber, a diamond detector, a novel silicon-diode array (DOSI), and polymer gel dosimetry. Analysis and intercomparison. *Medical Physics*, 35(10):4640 (2008). ISSN 00942405. doi:10.1118/1.2977829.
URL: *http://link.aip.org/link/MPHYA6/v35/i10/p4640/s1&Agg=doi* 34

Pena, Javier, Gonzalez-Castano, Diego M., Gomez, Faustino, Sanchez-Doblado, Francisco, and Hartmann, Guenther H. Automatic determination of primary electron beam parameters in Monte Carlo simulation. *Medical Physics*,

34(3):1076 (2007). ISSN 00942405. doi:10.1118/1.2514155.
URL: *http://link.aip.org/link/MPHYA6/v34/i3/p1076/s1&Agg=doi* 68

Perks, Julian, Rosenberg, Ivan, and Warrington, Jim. Dose quality assurance for stereotactic radiotherapy treatments. *Physics in Medicine and Biology*, 44:N209–N215 (1999).
URL: *http://stacks.iop.org/0031-9155/44/N209* 18

Picard, C, Olivier, A, and Bertrand, G. The first human stereotaxic apparatus. *Journal of Neurosurgery*, 59:673–676 (1983). 3

Potter, R. Physics Aspects of Quality Control in Radiotherapy. *European Journal of Radiology*, 36(1):65 (October 2000). ISSN 0720048X. doi:10.1016/S0720-048X(00)00146-7.
URL: *http://linkinghub.elsevier.com/retrieve/pii/S0720048X00001467* 157

Rogers, D W O. Fifty years of Monte Carlo simulations for medical physics. *Physics in medicine and biology*, 51(13):R287–301 (July 2006). ISSN 0031-9155. doi:10.1088/0031-9155/51/13/R17.
URL: *http://www.ncbi.nlm.nih.gov/pubmed/16790908* 49

Rogers, D W O, Walters, B, and Kawrakow, I. BEAMnrc Users Manual. *Source* (2009). 53, 62, 91

Rogers, DWO, Faddegon, BA, Ding, GX, Ma, CM, and We, J. BEAM: A Monte Carlo code to simulate radiotherapy treatment units. *Medical Physics*, 22(5):503–524 (1995).
URL: *http://link.aip.org/link/?MPHYA6/22/503/1* 67

Royal College of Radiologists. Towards Safer Radiotherapy. Technical report, Royal College of Radiologists (2008). 34, 196

Sabet, Mahsheed, Menk, FW, and Greer, P.B. Evaluation of an a-Si EPID in direct detection configuration as a water-equivalent dosimeter for transit dosimetry. *Medical physics*, 37:1459 (2010). doi:10.1118/1.3327456.
URL: *http://link.aip.org/link/?MPHYA6/37/1459/1* 31

Saini, Amarjit S. and Zhu, Timothy C. Energy dependence of commercially available diode detectors for in-vivo dosimetry. *Medical Physics*, 34(5):1704

(2007). ISSN 00942405. doi:10.1118/1.2719365.
URL: *http://link.aip.org/link/MPHYA6/v34/i5/p1704/s1&Agg=doi* 26

Sanchez-Doblado, F, Andreo, P, Capote, R, Leal, A, Perucha, M, Arrans, R, Nunez, L, Mainegra, E, Lagares, J I, and Carrasco, E. Ionization chamber dosimetry of small photon fields: a Monte Carlo study on stopping-power ratios for radiosurgery and IMRT beams. *Physics in Medicine and Biology*, 48:2081–2099 (2003).
URL: *http://stacks.iop.org/0031-9155/48/2081* 33

Scott, Alison J. D., Nahum, Alan E., and Fenwick, John D. Using a Monte Carlo model to predict dosimetric properties of small radiotherapy photon fields. *Medical Physics*, 35(10):4671 (2008). ISSN 00942405. doi:10.1118/1.2975223.
URL: *http://link.aip.org/link/MPHYA6/v35/i10/p4671/s1&Agg=doi* 33

Seuntjens, Jan and Verhaegen, Frank. Comments on 'ionization chamber dosimetry of small photon fields: a Monte Carlo study on stopping-power ratios for radiosurgery and IMRT beams'. *Physics in medicine and biology*, 48(21):L43–5; author reply L46–8 (November 2003). ISSN 0031-9155.
URL: *http://www.ncbi.nlm.nih.gov/pubmed/14653570* 33

Sheikh-Bagheri, Daryoush and Rogers, D. W. O. Sensitivity of megavoltage photon beam Monte Carlo simulations to electron beam and other parameters. *Medical Physics*, 29(3):379 (2002). ISSN 00942405. doi:10.1118/1.1446109.
URL: *http://link.aip.org/link/MPHYA6/v29/i3/p379/s1&Agg=doi* 68

Shrieve, D, Kooy, H M, Tarbell, NJ, and Loeffler, J. Fractionated stereotactic radiotherapy. *Advanced Neurosurgical Navigation*, page 451 (1998). 13

Siddon, R L. Generalised Batho correction factor. *Physics in medicine and biology*, 29(12):1575–9 (December 1984). ISSN 0031-9155.
URL: *http://www.ncbi.nlm.nih.gov/pubmed/6514787* 42

Siebers, Jeffrey V., Kim, Jong Oh, Ko, Lung, Keall, Paul J., and Mohan, Radhe. Monte Carlo computation of dosimetric amorphous silicon electronic portal images. *Medical Physics*, 31(7):2135 (2004). ISSN 00942405. doi:10.1118/1.1764392.

URL: *http://link.aip.org/link/MPHYA6/v31/i7/p2135/s1&Agg=doi* 32, 50, 104

Siebers, JV, Keall, PJ, Nahum, AE, and Mohan, R. Converting absorbed dose to medium to absorbed dose to water for Monte Carlo based photon beam dose calculations. *Physics in medicine and biology*, 45:983 (2000).
URL: *http://iopscience.iop.org/0031-9155/45/4/313* 166

Spezi, E. *A Monte Carlo investigation of the accuracy of intensity modulated radiotherapy.* Ph.D. thesis, University of Wales, College of Medicine (2003). 167

Spezi, E, Lewis, D G, and Smith, C W. Monte Carlo simulation and dosimetric verification of radiotherapy beam modifiers. *Physics in medicine and biology*, 46(11):3007–29 (November 2001). ISSN 0031-9155.
URL: *http://www.ncbi.nlm.nih.gov/pubmed/11720360* 50, 67

Spiegel, E A, Wycis, H T, Marks, M, and Lee, A J. Stereotaxic apparatus for operations on the human brain. *Science*, 106:349–350 (1947). 4

Stasi, M., Baiotto, B., Barboni, G., and Scielzo, G. The behavior of several microionization chambers in small intensity modulated radiotherapy fields. *Medical Physics*, 31(10):2792 (2004). ISSN 00942405. doi:10.1118/1.1788911.
URL: *http://link.aip.org/link/MPHYA6/v31/i10/p2792/s1&Agg=doi* 33

Symonds-Tayler, J R, Partridge, M, and Evans, P M. An electronic portal imaging device for transit dosimetry. *Physics in medicine and biology*, 42(11):2273–83 (November 1997). ISSN 0031-9155.
URL: *http://www.ncbi.nlm.nih.gov/pubmed/12408300* 31

Talairach, J and Tournoux, P. *Co-planar stereotaxic atlas of the human brain.* Thieme New York (1988). 5

Thain, Douglas. Distributed computing in practice: the Condor experience. *Concurrency and Computation: Practice and Experience*, 11(2-4):79–356 (February 2005). doi:10.1002/cpe.938. 54

Thomas, D G, Anderson, R E, and Du Boulay, G H. CT-guided stereotactic neurosurgery: experience in 24 cases with a new stereotactic system. *British Medical Journal*, 47:9–16 (1984). 6

Traberg Hansen, Anders, Petersen, Jørgen B, Hø yer, Morten, and Christensen, Jens Juul. Comparison of two dose calculation methods applied to extracranial stereotactic radiotherapy treatment planning. *Radiotherapy and oncology : journal of the European Society for Therapeutic Radiology and Oncology*, 77(1):96–8 (October 2005). ISSN 0167-8140. doi:10.1016/j.radonc.2005.04.018. **URL:** *http://www.ncbi.nlm.nih.gov/pubmed/16246744* 18

UK SBRT Consortium. UK SBRT Consortium. Stereotactic Body Radiation Therapy (SBRT) for Patients with Early Stage Non-small Cell Lung Cancer: A Resource. 2nd update Oct 2010. (2011) (2011). 174

van Elmpt, Wouter, McDermott, Leah, Nijsten, Sebastiaan, Wendling, Markus, Lambin, Philippe, and Mijnheer, Ben. A literature review of electronic portal imaging for radiotherapy dosimetry. *Radiotherapy and oncology : journal of the European Society for Therapeutic Radiology and Oncology*, 88(3):289–309 (September 2008). ISSN 0167-8140. doi:10.1016/j.radonc.2008.07.008. **URL:** *http://www.ncbi.nlm.nih.gov/pubmed/18706727* 196

Verhaegen, F, Das, I J, and Palmans, H. Monte Carlo dosimetry study of a 6 MV stereotactic radiosurgery unit. *Physics in Medicine and Biology*, 43:2755–2768 (1998). **URL:** *http://stacks.iop.org/0031-9155/43/2755* 33, 34, 89

Verhaegen, Frank and Seuntjens, Jan. Monte Carlo modelling of external radiotherapy photon beams. *Physics in Medicine and Biology*, 48:R107–R164 (2003). **URL:** *http://stacks.iop.org/0031-9155/48/R107* 49, 50, 74

Walters, B R B and Rogers, D W O. QA for the BEAM system; component modules, variance reduction options and source routines. *NRCC Report PIRS-509k* (1999). 101, 102

Walters, BRB, Kawrakow, I, and Rogers, DWO. DOSXYZnrc users manual. *NRC Report PIRS*, 794 (2005).

URL: *http://irs.inms.nrc.ca/software/beamnrc-V4-2.3.1/documentation/pirs794.pdf* 67

Wang, Lilie L. W. and Leszczynski, Konrad. Estimation of the focal spot size and shape for a medical linear accelerator by Monte Carlo simulation. *Medical Physics*, 34(2):485 (2007). ISSN 00942405. doi:10.1118/1.2426407.
URL: *http://link.aip.org/link/MPHYA6/v34/i2/p485/s1&Agg=doi* 74, 145

Wang, Lu, Li, Jinsheng, Paskalev, Kamen, Hoban, Peter, Luo, Wei, Chen, Lili, McNeeley, Shawn, Price, Robert, and Ma, Charlie. Commissioning and quality assurance of a commercial stereotactic treatment-planning system for extracranial IMRT. *Journal of applied clinical medical physics / American College of Medical Physics*, 7(1):21–34 (January 2006a). ISSN 1526-9914.
URL: *http://www.ncbi.nlm.nih.gov/pubmed/16518314* 17

Wang, Lu, Li, Jinsheng, Paskalev, Kamen, Hoban, Peter, Luo, Wei, Chen, Lili, McNeeley, Shawn, Price, Robert, and Ma, Charlie. Commissioning and quality assurance of a commercial stereotactic treatment-planning system for extracranial IMRT. *Journal of applied clinical medical physics / American College of Medical Physics*, 7(1):21–34 (January 2006b). ISSN 1526-9914.
URL: *http://www.ncbi.nlm.nih.gov/pubmed/16518314* 18

Warrington, AP and Laing, RW. Quality assurance in fractionated stereotactic radiotherapy. *Radiotherapy and Oncology*, 30:239 (1994).
URL: *http://linkinghub.elsevier.com/retrieve/pii/0167814094904642* 8, 16

Webb, S. The physical basis of IMRT and inverse planning. *British Journal of Radiology*, 76:678 (2003). 10

Whyte, Richard I. Stereotactic radiosurgery for lung tumors. *Seminars in Thoracic and Cardiovascular Surgery*, 22(1):59–66 (2010).
URL: *http://www.ncbi.nlm.nih.gov/pubmed/20813318* 174

Wulf, Joern, Baier, Kurt, Mueller, Gerd, and Flentje, Michael P. Dose-response in stereotactic irradiation of lung tumors. Technical Report 1, Department of Radiotherapy, University of Wuerzburg, Wuerzburg, Germany. (2005).
URL: *http://www.ncbi.nlm.nih.gov/pubmed/16209896* 174, 175

Xia, P, Geis, P, Xing, L, Ma, C, Findley, D, Forster, K, and Boyer, A. Physical characteristics of a miniature multileaf collimator. *Medical Physics*, 26:65 (1999). 13

Zhu, Y., Jiang, X.Q., and Van Dyk, J. Portal dosimetry using a liquid ion chamber matrix: Dose response studies. *Medical Physics*, 22:1101 (1995). **URL:** *http://link.aip.org/link/?MPHYA6/22/1101/1* 31

Zhu, Yimin, Kirov, Assen S, Meigooni, Ali S, and Williamson, Jeffrey F. Quantitative evaluation of radiochromic film response for two-dimensional dosimetry. 24(2):223–231 (1997). 28

Appendices

Appendix - Source Code of BLMLC subroutines and macros

```
%E
/*****************************************************************************
 *
 *  $Id: BLMLC_cm.mortran,v 1.3 2005/11/10 05:19:11 bwalters Exp $
 *
 *****************************************************************************/
;
"   Revision 1.4 last edited  2001/06/29 21:43:27
"   Last changed by bwalters and currently locked by
"     started from BLMLC_cm.mortran  (SID 1.8 last edited 00/12/11)"
%C80

" ***************************************************************************"

"                           BLMLC_cm.mortran                                "

" ***************************************************************************"
"                                                                           "
"                              SUMMARY                                      "
"                              =======                                      "
"    A Component module to be used in conjunction with OMEGA/BEAM           "
"    for Monte Carlo simulations of photon and electron beams (used in      "
"    radiotherapy)transported through a BrainLAB M3 Multileaf               "
"    Collimator system. This CM takes into account the multiple             "
"    tongue and groove geometry and offers a choice of divergent or         "
"    rounded leaf ends.                                                     "
"    It also accounts for the leaf driving screw hole, tips and support     "
"    railings explicitly.                                                   "
"                                                                           "
"    M3s vary depending on the accelerator to which they are attached       "
"    To simplify this, distances are hard wired into the code rather        "
"    than have a very complicated input file.                               "
"                                                                           "
"       Information from BrainLAB on the above will be required             "
"       This CM was originally written by                                   "
"                                                                           "
"             Ajay Kapur, Stanford University                               "
"             Charlie Ma, Stanford University                               "
"             Room A0-42                                                    "
"             Division of Radiation Physics                                 "
"             Department of Radiation Oncology                              "
"             Stanford University                                           "
"             300 Pasteur Drive                                             "
"             Stanford, CA 94305                                            "
"             Tel: (650) 498-6378                                           "
"             FAX: (650) 498-4015                                           "
"             Email: kapur@reyes.stanford.edu                               "
"                                                                           "
"               extensively reworked by                                     "
"                Blake Walters, NRC Ottawa                                  "
"               bwalters@irs.phy.nrc.ca                                     "
"                                                                           "
"          More extensive reworking to account for BrainLAB M3              "
"                                                                           "
"                                                                           "
"                                                                           "
"        ---------------------------------------------------------          "
```



```
"         Velindre Cancer Centre                                            "
"         Files needed:                                                     "
"         1. BLMLC_cm.mortran                                               "
"         2. BLMLC_cm.macros
"                                    "
"         ---------------------------------------------------------         "

"*****************************************************************"
"*****************************************************************"
"
"                           ****************              ""toc:
"                           *              *              ""toc:
"                           *   BLMLC      *             ""toc:
"                           *               *             ""toc:
"                           ****************              ""toc:
"
"
"*****************************************************************
"*****************************************************************
"
"
"                          GENERAL DESCRIPTION
"                          *******************
"
"   This set of routines is used in conjunction with BEAM.MORTRAN to
"   simulate one component module of a clinical linear accelerator:
"
"   This component module can be added to the simulation by including these
"   routines in the MORTRAN file BEAM_CM.MORTRAN and including the MORTRAN
"   replacement macros associated with this component module in the file
"   BEAM_COMMON.MORTRAN.  The order of the component modules in either of
"   these files is unimportant.  To explicitly include this component module
"   the simulation it must be included in the $CM_LIST replacement statement.
"   The component modules in this list are stacked sequentially for the
"   simulation, one on top of the other, and must not overlap.
"
"   1>. This module can be used as single or double focus multileaf
"       collimators.
"   2>. Used as x or y direction parallel to the leaf.
"   3>. it can have max 100 leaf pair which are equal width, symmetrical
"       arranged with y axis or x axis. For more than 26 leaf pairs some work will be required
"   4>. Each leaf has two separate parts which can be moved in the leaf
"       direction independently.
"   5>. Rules to obey:
"          i.  You must enter your MLC dimensions in the YREG and ZREG sections
"
" Similar in approach to DYNVMLC but added lots of special cases for the M3
" You MUST edit the ZREG and YREG for your MLC
;
"I>
"I> Geometry of BLMLC:
"I> **********************
"I>                                  top view
"I>
"I>            ------------------------------------------------
"I>                                 |
"I>            ------------------------------------------------
```



```
"I>                             |           |
"I>           -----------------           ----------------------
"I>                      |        opening     |
"I>           ---------------     (IR=1)      -----------------
"I>                        |                  |
"I>           ------leaves--------       ------------------------
"I>                (IR=2)       |     |
"I>           ---------------------------------------------------
"I>                                 |
"I>           ---------------------------------------------------
"I>
;
"I>       cross-section through leaves taken perpendicular to leaves
"I>
"I>                                 * ZFOCUS(1)
"I>                              .   .   .
"I>                          .    . .|. .    .
"I> - - - - - - -     .      .    . | .   .      .
"I> airgap(IR=3)  .      .      .   |  .     .      .
"I>     -------- ------ ------ ---|--- ------ ------ ---------
"I>   leaf      / leaf / leaf /leaf|leaf\ leaf  \ leaf \  leaf
"I>   1    /    2  /     3  /  4  | 5   \  6     \  7    \  8
"I>    /        /          /      |      \          \        \
"I>    -------- ---------- -------|------- ---------- --------- -
"I>                            Z-axis
;
"I>            cross-section through leaf taken || to leaf
"I>             I)  FOR FOCUSED DIVERGENT LEAF ENDS :
"I>
"I>                                 * ZFOCUS(2)
"I>  - - - - - - - - - - - - -     . | .
"I>  airgap(IR=4)                  .  |  .
"I>     -----------------------    |    -------------------------
"I>                           /     |     \
"I>        Leaf B  (-ve)     /      |      \    Leaf A (+ve)
"I>                         /       |       \
"I>    --------------------         |        ------------------------
"I>                            Z-axis

"I>              II)  FOR ROUNDED LEAF ENDS :
"I>
"I>                                 *
"I>  - - - - - - - - - - - -       |
"I>  airgap(IR=4)                  |
"I>     -------------              |               --------------
"I>      --------\     \           |             /
"I>    hole IR=3 | A   |           |            |<------Leafradius
"I>     ---------/     /           |             \    B
"I>     -------------              |               --------------
"I>                            Z-axis
;
"I>   IR is the region number within the CM.  There are three local regions
"I>   shown above.
"I>
"I>
"I>            ------------------------------------------------------
"I>            |              Region            | Description         |
```



```
"I>            |--------------------------------|----------------------|
"I>            |  absolute       | local        |                      |
"I>            |-----------------|--------------|                      |
"I>            |                 |              |                      |
"I>            |IRSTART_MLC      | IR_MLC       |  as shown in above   |
"I>            |  +IR_MLC-1      |              |    (1 to 4)          |
"I>            |                 |              |                      |
"I>            |                 |              |                      |
"I>            ------------------------------------------------------
"I>
;

" Subroutines:
" ************
"                     INPUT_$BLMLC
"                     ISUMRY_$BLMLC
"                     HOWFAR_$BLMLC
"                     WHERE_AM_I_$BLMLC
"
"       Called from BEAM's subroutines:
"                     INPUT
"                     ISUMRY
"                     HOWFAR
"
"       Subroutines called:
"                     WHERE_AM_I (a BEAM subroutine)
"
"*****************************************************************
"
"                           RESTRICTIONS ON USE/KNOWN BUGS
"                           ******************
"
"*****************************************************************
;
"
"                             INPUT FROM UNIT 5
"                             *****************
"
"I>
"I>

;
"*****************************************************************
"************************  ERROR CONDITIONS  *********************
"*****************************************************************
"
"                             SIMULATION PARAMETERS
"                             *********************
"
" Geometry checks:
" ****************
"
"   1)  Overlapping component modules
"
"*****************************************************************
;
%E "Start of subroutine HOWFAR_$BLMLC (Rev 1.4)"
```

```
"*********************************************************************
"********************Component Module BLMLC ***************************
"*********************************************************************
"
"                          Subroutine HOWFAR_$BLMLC
"                          ************************
"
" HOWFAR routine for stacked planar media.
"
" Determine if current region number is within component module BLMLC,
" evaluate DIST, distance to region boundary along current trajectory.
" USTEP must not exceed DIST.
"
"   There are N_$BLMLC local regions + an air gap (if present):
"
"  local             absolute                                  description
"--------------- ------------------------------------------- ---------------
"IR_$BLMLC IR_start_CM(ICM_$BLMLC)+IR_$BLMLC-1 exclude front air gap
"--------------- ------------------------------------------- ---------------
"   Geometrical co-ordinates, as set in INPUT_$BLMLC are:
"
"   ZFRONT_$BLMLC     front of CM (upstream surface, air region)
"   ZMIN_$BLMLC       front of cone
"   ZBACK_$BLMLC      back of cone
"   RMAX_$BLMLC       radius of last cylinder (largest)
"
"*********************************************************************
;
;SUBROUTINE HOWFAR_$BLMLC;

"V>$GEO_SHIFT_1_(#)
"V>=============
"V>{p1} the value to compare with ustep
"V> if {p1}+1.0e-5 < ustep shift it, otherwise no shift
;
REPLACE {$GEO_SHIFT_1_(#)} WITH {
  ;IF({P1}~=0.00 ) [
    IF({P1}+1.0E-5< USTEP) [{P1}={P1}+1.0E-5;]
   ]
   ELSE [{P1}={P1}+1.0E-5;];

}

;IMPLICIT NONE;
;COMIN/CMs,CM_$BLMLC,EPCONT,STACK/;
"T>
"T>*********************************
"T>TYPE DECLARATIONS FOR HOWFAR_$BLMLC
"T>*********************************
"T>
INTEGER
   COUNT,
   IRL,        "T>local region number (absolute), required by HOWNEAR macro
   I, J,        "T>loop control
   REGION_$BLMLC,     "T>region number within CM (relative)
   NEWREGION_$BLMLC,     "T>region number within CM (relative)
   NX,NY,NZ,        "T> Subindices for region
```



```
   OUTOFCMFLAG,     "T> Flag to denote particle out of CM
   OUTOFMLCFLAG,    "T> Flag to denote particle out of MLC
   LEAFIS,          "T> Leaf number
   LHS,RHS,     "T> Macro variables to find + and - closest boundary index
   ZLHS,ZRHS,
   YLHS,YRHS,LEAF_CHWITH,LEAF_DE, "for leaf boundary indicees
   IDIR,        "T> direction sign, used in call to where_am_i
   XREG_MIN, XREG_MAX,
   YREG_MIN, YREG_MAX,
   ZREG_MIN, ZREG_MAX,  "Indicees of end boundary regions"
   YREG_STRT,
   LEAF_TOP, LEAF_MIDDLE, LEAF_BOTTOM;


DOUBLE PRECISION
   DIST,      "T>Distance to z boundary along current particle trajectory
   UVL(2),    "T>temporary variable
   TRYY1,TRYY2,
   XoN,XoP,    "T> Negative and Positive leaf centers (rounded leaf)
   Zo,          "T> z position of rounded leaf tip
   XP,XN,YP,YN,ZP,ZN,    "T>+ and - distances in x,y, z directions
   XDIST,YDIST,ZDIST,    "T> x,y, Z distances to nearest boundaries
   DIST1,DIST2,DIST3,    "T> Variables to control particle propagation
   STEP2,               "T>  "
   TLHS,TRHS,           "T> temporary macro variables like lhs,rhs
   DISCRIMINANT,        "T> Variable for rounded leaf
   TEMP,TEMP1, TEMP2, TEMP3, TEMP4, TEMP5, HOLE,
   STEP_UNIT,
   XYL(2),     "T> rearranged x and y coordinates
   XYFL(2),
   Z_LEAF_BOTTOM,
   Z_LEAF_TOP,
   XL, XR,
   ZFL;

" prepare the local variables "
"============================="

IRL = IR(NP); "local region number (absolute)"
IR_$BLMLC = IRL - IRSTART_$BLMLC + 1;   "rel. local region number"
IF(ORIENT_$BLMLC=1) [
    XYL(1)=Y(NP); XYL(2)=X(NP);UVL(1)=V(NP);UVL(2)=U(NP);
]
ELSE[
 XYL(1)=X(NP); XYL(2)=Y(NP);UVL(1)=U(NP);UVL(2)=V(NP);
]
LEAF_TOP=6;
LEAF_MIDDLE=10;
LEAF_BOTTOM=15;
STEP_UNIT=0.0;
COUNT = 0;
OUTOFCMFLAG=0;
OUTOFMLCFLAG=0;
"Initialise NX,NY,NZ to try and avoid segmentation fault"
"Turned out not to be the cause but leave in anyway"
"================================================="
NX=0;
```



```
NY=0;
NZ=0;
"Now set up index numbers of boundaries etc"
"==========================================================="
XREG_MIN=1;
XREG_MAX=5;
YREG_MIN=1;
YREG_MAX=8;
YREG_STRT=6;
ZREG_MIN=1;
ZREG_MAX=16;
"==========================================================="
" Boundary-crossing check
" **********************
"
" Determine if current region number is within component module ,if so
" evaluate DIST, distance to region boundary along current trajectory.
" USTEP must not exceed DIST.
"

" the following block double check:
"==================================
"      1. the particle is out of the CM or regions in z direction
"      2.                          the regions in xy directions
"     if so reset the ir #, and print out the warning message.
"comment: this block is not time consumming, can be kept in the final version
"=======
"
"  now do the air gap check if existed.
"======================================
"

IF(N_GAP_$BLMLC=1 & IR_$BLMLC=4 ) ["Check the air gap first"
    IF(W(NP)>0.0) ["Particle going forward"
            DIST = (ZMIN_$BLMLC - Z(NP))/W(NP); "distance to front of CM"
            IF(DIST <= 0.0) [
                USTEP=0.0;
                $BLMLC_FIND(IR_$BLMLC, 0.0);
                    IF( IR_$BLMLC=1 )[ "in air"
                    IRNEW =IRSTART_$BLMLC;
                    RETURN;
                ]
                    ELSE[
                    IRNEW =IRSTART_$BLMLC+1;
                    RETURN;
                ]
            ] "double check if a particle is out of the AIR GAP"
        ]
    ELSEIF(W(NP)<0.0) [ "particle going backward"
            DIST = (ZFRONT_$BLMLC - Z(NP))/W(NP); "distance to front of CM"
            IF(DIST <= 0.0) [
                USTEP=1.E-16;
                CALL WHERE_AM_I(ICM_$BLMLC,-1);
                RETURN;
            ] " double check if a particle is out of the CM"
        ]
]
```



```
ELSEIF(IR_$BLMLC=1 | IR_$BLMLC=2 | IR_$BLMLC=3) [
    IF(W(NP) > 0.0) ["particle going forward"
            DIST = (ZMAX_$BLMLC - Z(NP))/W(NP); "distance to back of CM"
            IF(DIST>USTEP) [
            STEP_UNIT=USTEP;
        ]
            ELSE [
            STEP_UNIT=DIST;
        ]
            IF(DIST <=0.0) [
                USTEP=1.E-16;"ensures call to AUSGAB on leaving CM"
                CALL WHERE_AM_I(ICM_$BLMLC,1);
                RETURN;
            ] "double check if a particle is out of the CM"
        ]
    ELSEIF(W(NP) < 0.0) [ "particle going backward"
            DIST = (ZMIN_$BLMLC - Z(NP))/W(NP); "distance to back of CM "
            IF(DIST>USTEP) [
            STEP_UNIT=USTEP;
        ]
            ELSE [
            STEP_UNIT=DIST;
        ]
            IF(DIST <= 0.0) [
                USTEP=0.0;
                IF(N_GAP_$BLMLC = 1) [
                    IRNEW =IREND_$BLMLC;
                RETURN;
            ]
                ELSE[
                USTEP=1.E-16;
                CALL WHERE_AM_I(ICM_$BLMLC,-1);
                RETURN;
            ]
            ] " double check if a particle is out of the main body to air gap"
        ]
    ELSE[
        STEP_UNIT=USTEP;
    ]  " for w(np)=0.0 case"
]

" end of z direction check
"=========================

$BLMLC_FIND(REGION_$BLMLC,0.0);

IF(REGION_$BLMLC=4) [ "Particle is in the air gap "
    REGION_$BLMLC=IRSTART_$BLMLC-1+REGION_$BLMLC;
    IF(W(NP) > 0.0)[
            IF(DIST <= USTEP ) ["particle to be moved to region boundary"
            $GEO_SHIFT_1_(DIST);
            USTEP = DIST;
            $BLMLC_FIND(NEWREGION_$BLMLC,USTEP);
                IF( NEWREGION_$BLMLC=1) [
                IRNEW =IRSTART_$BLMLC;
                RETURN;
            ]
```

```
                ELSE[
                IRNEW =IRSTART_$BLMLC+1;
                RETURN;
            ]
            ]
            ELSE[
            RETURN;
        ];
        ] "end of particle going forward"
        ELSEIF(W(NP) < 0.0) ["particle going backward"
            IF(DIST <= USTEP ) ["particle to be moved to region boundary"
                $GEO_SHIFT_1_(DIST);
                USTEP = DIST;
                CALL WHERE_AM_I(ICM_$BLMLC,-1);
                RETURN;
            ]
            ELSE [
            RETURN;
        ]
        ] " end of going backward"
        ELSE[
        RETURN;
    ]   " W=0.0 CASE "
]" end of region 4"


IF(OUTOFMLCFLAG=1) [
    STEP2=STEP_UNIT;
    TEMP1=(SURPARA1_$BLMLC(1,YREG_MIN)*(ZFL-ZFOCUS_$BLMLC(1))-XYFL(1));
    IF( (UVL(1)-SURPARA1_$BLMLC(1,YREG_MIN)*W(NP))~=0.0 ) [
            TEMP1=TEMP1/(UVL(1)-SURPARA1_$BLMLC(1,YREG_MIN)*W(NP));
    ]
    ELSE [
         TEMP1 = -1000.00
    ]
    TEMP2=(SURPARA1_$BLMLC(TOT_LEAF_$BLMLC,YREG_MAX)*
            (ZFL-ZFOCUS_$BLMLC(1))-XYFL(1));
    IF((UVL(1)-SURPARA1_$BLMLC(TOT_LEAF_$BLMLC,YREG_MAX)*W(NP))~=0.0) [
            TEMP2=TEMP2/(UVL(1)-SURPARA1_$BLMLC(TOT_LEAF_$BLMLC,YREG_MAX)*W(NP));
    ]
    ELSE [
        TEMP2 = -1000.00
    ]
    IF( STEP2>=0.0)[
            TEMP=STEP2;
            IF( TEMP1>=0 ) [
            TEMP=MIN(TEMP,TEMP1);
        ]
            IF( TEMP2>=0 ) [
            TEMP=MIN(TEMP,TEMP2);
        ]
    ]
    ELSEIF ( (TEMP1>0.0) & (TEMP2>0.0) ) [
        TEMP=MIN(TEMP1,TEMP2);
    ]
    ELSE [
        TEMP=MAX(TEMP2,TEMP1);
```



```
    ]
        STEP2 = TEMP;
    $GEO_SHIFT_1_(STEP2);
    $BLMLC_FIND(IRNEW,STEP2);
    IRNEW=IRNEW+IRSTART_$BLMLC-1;
    USTEP=STEP2;
]
CALL MINDISTANCE_$BLMLC(DIST1,LEAFIS,NX,NY,NZ,ZFL,XYFL,UVL);
"$BLMLC_MINDISTANCE(DIST1);"
IF((DIST1>=STEP_UNIT) | (DIST1<0)) [
        STEP2=STEP_UNIT;
        $GEO_SHIFT_1_(STEP2);
        $BLMLC_FIND(IRNEW,STEP2);
        USTEP=STEP2;
        IF(OUTOFCMFLAG=1)[ "call where_am_i"
            IDIR=SIGN(1.0,W(NP));
            CALL WHERE_AM_I(ICM_$BLMLC,IDIR);
            RETURN;
        ]
        ELSE[
            IRNEW=IRNEW+IRSTART_$BLMLC-1;
            RETURN;
        ]
]
ELSEIF( (STEP_UNIT>DIST1) & (DIST1>=0)) [
        REGION_$BLMLC=REGION_$BLMLC+IRSTART_$BLMLC-1;
        LOOP[
            DIST1=DIST1+1.0E-5; "we have to shift it regardless to avoid "
                        "infinite loops"
            IF(DIST1>=STEP_UNIT)[
            EXIT;
        ]
            ELSE[
                $BLMLC_FIND(NEWREGION_$BLMLC,DIST1);
                NEWREGION_$BLMLC=NEWREGION_$BLMLC+IRSTART_$BLMLC-1;
                IF( OUTOFCMFLAG=1 ) [
                EXIT;
            ]
                ELSEIF( (NEWREGION_$BLMLC~=REGION_$BLMLC) | OUTOFMLCFLAG=1 )[
                    USTEP = MIN(USTEP,DIST1);
                "take min. because we shifted DIST1"
                    IRNEW = NEWREGION_$BLMLC;
                    RETURN;
                ]
                ELSE [
                CALL MINDISTANCE_$BLMLC(DIST2,LEAFIS,NX,NY,NZ,ZFL,XYFL,UVL);
                    "$BLMLC_MINDISTANCE(DIST2);"
                    DIST1=DIST1+DIST2;
                ];
            ]
        ];
"trying to delete a close bracket her to get round error - 22/12/06"
"if it gets here, then it exited either because OUTOFCMFLAG=1"
"or because DIST1 >= STEP_UNIT, in either case DIST1 >= STEP_UNIT"
        DIST1=STEP_UNIT;
        $GEO_SHIFT_1_(DIST1);
        USTEP = DIST1;
```



```
        IF( OUTOFCMFLAG=0 ) [
            $BLMLC_FIND(NEWREGION_$BLMLC,DIST1);
            "still have to check if we have left the CM in case STEP_UNIT"
            "was the distance to the bottom of the CM"
            IF(OUTOFCMFLAG=1)[
                IDIR=SIGN(1.0,W(NP));
                CALL WHERE_AM_I(ICM_$BLMLC,IDIR);
                RETURN;
            ]
            ELSE["not leaving CM"
                NEWREGION_$BLMLC=NEWREGION_$BLMLC+IRSTART_$BLMLC-1;
                IRNEW = NEWREGION_$BLMLC;
                RETURN;
            ]
    ]
        ELSE[ "call where_am_i"
            "since flag is based on distance to Z bdy, DIST1 is >= STEP_UNIT now"
            IDIR=SIGN(1.0,W(NP));
            CALL WHERE_AM_I(ICM_$BLMLC,IDIR);
            RETURN;
        ]

]; "End of IF loop for step_unit>dist1

;
"   end of HOWFAR_$BLMLC
"   ==================
"
251 FORMAT(F8.3,',',F8.3,',',F8.3,',',I3,',',I3,',',I3,',',I3,',',I3);
252 FORMAT(F8.3,',',F8.3,',',F8.3,',',I3,',',I3,',',I3,',',I3,',',A1);
RETURN;
END; "End of subroutine HOWFAR_$BLMLC"
%E "Start of WHERE_AM_I_$BLMLC (Rev 1.4)"
"*************************************************************************
"
"                          Subroutine WHERE_AM_I_$BLMLC
"                          ************************
"
" WHERE_AM_I routine for a stacked right cylinder slabs.
"
" WHERE_AM_I_$BLMLC determines the new region number when a particle
" traverses a component module boundary.  The scheme is as follows:
"
"      Whenever a particle is to be transported to a component module
"      boundary in HOWFAR, the subroutine WHERE_AM_I is called.  The
"      current component module and particle direction (backwards or
"      forwards) are transferred to WHERE_AM_I in the CALL statement.
"      WHERE_AM_I determines which component module the particle is
"      about to enter and calls the WHERE_AM_I_$BLMLC subroutine for
"      that component module, transferring the particle direction.
"      The region number that the particle is about to enter is
"      determined in WHERE_AM_I_$BLMLC from the knowledge of which
"      surface the particle is entering through (front if IDIR=1,
"      back if IDIR=-1) and the (X,Y) coordinates of the particle.
"      The current particle being transported is NP (in /STACK/).
"
"*************************************************************************
```



```
;SUBROUTINE WHERE_AM_I_$BLMLC(IDIR);
;
;IMPLICIT NONE;
;COMIN/CM_$BLMLC,EPCONT,STACK,CMs/;
"T>
"T>************************************
"T>TYPE DECLARATIONS FOR WHERE_AM_I_$BLMLC
"T>************************************
"T>
INTEGER NX,NY,NZ,   "T>Indices of subregions
        I,J,
        OUTOFCMFLAG, "Flags to denote out of CM and
        OUTOFMLCFLAG, " MLC respectively
        LEAFIS,       " Leaf number
        IDIR,   "T>direction of particle, +1=forward, -1=backward
    XREG_MIN, XREG_MAX,
    YREG_MIN, YREG_MAX,YREG_STRT,
    ZREG_MIN, ZREG_MAX; "Indicees of end boundary regions"
DOUBLE PRECISION   XYL(2), XYFL(2), ZFL, UVL(2), XoN, XoP, Zo, TEMP1, TEMP2,
                   TEMP3, TEMP4, HOLE, Z_LEAF_BOTTOM,Z_LEAF_TOP;



"Now set up index numbers of boundaries etc"
"======================================================="
XREG_MIN=1;
XREG_MAX=5;
YREG_MIN=1;
YREG_MAX=8;
YREG_STRT=6;
ZREG_MIN=1;
ZREG_MAX=16;
"======================================================="
IF(ORIENT_$BLMLC=1) [
    XYL(1)=Y(NP);
    XYL(2)=X(NP);
    UVL(1)=V(NP);
    UVL(2)=U(NP);
]
ELSE[
    XYL(1)=X(NP);
    XYL(2)=Y(NP);
    UVL(1)=U(NP);
    UVL(2)=V(NP);
]
IF (IDIR=1) [
 "particle entering this CM through front face (upstream)"
   IF(N_GAP_$BLMLC = 0) [ "no air gap this CM"
        IF(IRSTART_$BLMLC=2)[   " the first CM"
        $BLMLC_FIND(IR_$BLMLC,0.0);
    ]
        ELSE[
        $BLMLC_FIND(IR_$BLMLC, USTEP);
    ]
        IF(IR_$BLMLC=1)[
        IRNEW=IRSTART_$BLMLC;
```

```
        RETURN;
    ]
        ELSE[
        IRNEW=IRSTART_$BLMLC+1;
        RETURN;
    ]
   ]         " end of the no air gap case"
   ELSE [ "this CM has an air gap at the front"
      IRNEW = IREND_$BLMLC;
        ]
]

ELSE [ "particle entering CM through back face (downstream)"
   $BLMLC_FIND(IR_$BLMLC, USTEP);
   IF(IR_$BLMLC=1)
     [IRNEW=IRSTART_$BLMLC; RETURN;]
   ELSE[ IRNEW=IRSTART_$BLMLC+1; RETURN; ]
 ];
251 FORMAT(F8.3,',',F8.3,',',F8.3,',',I3,',',I3,',',I3,',',I3,',',I3);
252 FORMAT(F8.3,',',F8.3,',',F8.3,',',I3,',',I3,',',I3,',',I3,',',A1);
RETURN;
;
END; "End of subroutine WHERE_AM_I_$BLMLC"
%E "Start of subroutine INPUT_$BLMLC (Rev 1.4)"

"***********************************************************************

"                          Subroutine INPUT_$BLMLC
"
"***********************************************************************
"***********************************************************************

"  A CM input subroutine for a series of 2 or more slabs.
"
"  It must fill all parameters in COMMON/CMs/ associated with this CM.
"
"  Routine prints error messages on unit 6 for
"      format error on input
"      end of file hit
"      error in logic of input file
"
"  The format of the input is presented in the section INPUT FROM UNIT 5
"   in the above documentation.
"
"***********************************************************************

;SUBROUTINE INPUT_$BLMLC;
;

;IMPLICIT NONE;
;COMIN/ BOUNDS,CMs,CM_$BLMLC,GEOM,IO_INFO,MEDIA,MISC,SCORE,USER,EGS-IO/;

"  ************************************************************* "
"              TYPE DECLARATIONS FOR INPUT_$BLMLC
"  ************************************************************* "

DOUBLE PRECISION  NEG_$BLMLC,     "T>Leaf B tip
```



```
                  POS_$BLMLC,     "T>Leaf A Tip
                  TEMP1,
                  TEMP2;

INTEGER I,J,K,L,        "T>DO loop indices
        IRA,            "T>Absolute region number
        MED_FLAG,       "T>flag used by media-sort macro $MED_INPUT
        MED_INDEX,    "T>medium index, set after medium sort by $MED_INPUT
        NUM_$BLMLC,  "T>number of adjacent leaves with same opening coordinates
        LEAFTYPE,     "T>temporary input variable for LEAFTYPE
        MIN_INDEX,    "T>index of leaf with min. opening coordinate
        MAX_INDEX,   "T>index of leaf with max. opening coordinate
    XREG_MIN, XREG_MAX,
    YREG_MIN, YREG_MAX,YREG_STRT,
    ZREG_MIN, ZREG_MAX; "Indicees of end boundary regions"
" ************************************************************ "

"                 STEP I : INITIALIZE PARAMETERS
"                          ====================
 ICM_$BLMLC = ICM;

" ************************************************************ "
"Now set up index numbers of boundaries etc"
"========================================================="
XREG_MIN=1;
XREG_MAX=5;
YREG_MIN=1;
YREG_MAX=8;
YREG_STRT=6;
ZREG_MIN=1;
ZREG_MAX=16;
"========================================================="

"I. GET THE TITLE "
"================ "
;
EPS=0.00001;
OUTPUT;(/' Next component is a BRAINLAB M3 type MLC'/' Title: ',$);
MINPUT ($BLMLC) TITLE_$BLMLC;(60A1);
          "MINPUT is a replacement macro with EOF and
          "ERR branching to :EOF_{P1}: and :ERR_{P1}:
OUTPUT TITLE_$BLMLC;(' ',60A1);
            "OUTPUT is a replacement macro which writes to"
            "unit 5.  Used here for echo of user input"
"WRITE(IOUTLIST,'(60A1)') TITLE_$BLMLC;
            "Unit 7 is temporary file of user input
OUTPUT;(/' Do you wish to plot some co ordinates out for debugging?',$);
MINPUT ($BLMLC) PLT_$BLMLC;(I3);
IF (PLT_$BLMLC ~= 0) [
    OPEN(UNIT=73,FILE='blmlc2.lis',
        FORM='FORMATTED',STATUS='UNKNOWN');
]
OUTPUT PLT_$BLMLC; (I5/);

"II. CHOOSE THE BLMLC ORIENTATION "
"============================== "
```



```
OUTPUT; (' Input leaf orientation (0=parallel to y, 1=parallel to x) and '/
         ' no. of groups of leaves with equal width on one line'/' :',$);
MINPUT ($BLMLC) ORIENT_$BLMLC, NGROUP_$BLMLC; (2I5);
OUTPUT ORIENT_$BLMLC,NGROUP_$BLMLC; (2I5/);
IF(ORIENT_$BLMLC~=1) [
      ORIENT_$BLMLC=0;
      OUTPUT;(/' Orientation defaults to 0.'/);
 ];
IF(NGROUP_$BLMLC<=0) [
      NGROUP_$BLMLC=1;
      OUTPUT;(/' No. of groups defaults to 1.'/);
 ];
WRITE(IOUTLIST,'(2I5)')ORIENT_$BLMLC,NGROUP_$BLMLC;

"III. DESIGNATE REGION NUMBERS "
"============================== "

N_$BLMLC = 3;
          "Number of regions in this CM (excluding front air gap)
ICM_$BLMLC = ICM;      "CM index for this component module
IRSTART_$BLMLC = IR_start_CM(ICM_$BLMLC);
                    "Index of first region in this CM,
                    "set by previous CM or in MAIN if ICM=1
IERR_GEOM(ICM_$BLMLC) = 0; "Geometry-checking flag, 0 if no error detected

"IV. GET DISTANCE FROM THE REFERENCE PLANE, z=0 "
"============================================== "
;
OUTPUT; (' Z position of top of BRAINLAB MLC (>=0) : ',$);
;MINPUT ($BLMLC) ZMIN_$BLMLC;(F12.5);
OUTPUT ZMIN_$BLMLC;(F12.5/);
WRITE(IOUTLIST,'(F12.5)') ZMIN_$BLMLC;
IF(Z_min_CM(ICM_$BLMLC)>ZMIN_$BLMLC) [
   IF(ICM_$BLMLC=1) [
      Z_min_CM(ICM_$BLMLC)=ZMIN_$BLMLC;
      OUTPUT ICM_$BLMLC, Z_min_CM(ICM_$BLMLC);
       (//' ***WARNING IN CM ',I4,' ($BLMLC):'/
           ' Z_min_CM(1)  > distance to front of MLC '/
           ' Z_min_CM(1) reset to ',F8.5,' cm'//);
      WRITE(IOUTLIST,
         ' (//'' ***WARNING IN CM '',I4,'' ($BLMLC):''/
          '' Z_min_CM(1)  > distance to front of collimator''/
          '' Z_min_CM(1) reset to '',F8.5,'' cm''//)')
          ICM_$BLMLC, Z_min_CM(ICM_$BLMLC);
     ]
    ELSE[
      OUTPUT ICM_$BLMLC;
       (//' ***** WARNING WARNING WARNING *****'/
          ' ***ERROR IN CM ',I4,' ($BLMLC):'/
          ' Overlaps with previous CM'/
          ' Error will be propagated'//);
      WRITE(IOUTLIST,
         ' (//'' ***WARNING IN CM '',I4,'' ($BLMLC):''/
          '' Overlaps with previous CM''//)')
          ICM_$BLMLC;
      IERR_GEOM(ICM_$BLMLC)=IERR_GEOM(ICM_$BLMLC)+1;
     ]
```



```
 ]
;
" ************************************************************ "

"              STEP TWO : GET BLMLC GEOMETRY INFORMATION
"                         ============================

" ************************************************************ "

" I. THICKNESS OF LEAVES "
" ======================= "
;

OUTPUT; (' MLC Leaf thickness (cm):',$);
MINPUT ($BLMLC) ZTHICK_$BLMLC; (F15.0);
OUTPUT ZTHICK_$BLMLC;(F15.5, ' cm'/);
WRITE(IOUTLIST,'(F15.5)') ZTHICK_$BLMLC;

" Validate the user-input thickness "

IF(ZTHICK_$BLMLC<0.0) [
    OUTPUT ICM_$BLMLC;(//' ***ERROR IN CM ',I4,' ($BLMLC):'/
                       ' ZTHICK < 0.0'//);
    IERR_GEOM(ICM_$BLMLC)=IERR_GEOM(ICM_$BLMLC)+1;
 ];

ZMAX_$BLMLC = ZMIN_$BLMLC + ZTHICK_$BLMLC;
;
" Instead of the input for geometric parameters"
"to be supplied in the input card"
" geometry will be hard wired in for now."
" If this routine is successful this should be"
" removed and the user encouraged to enter geometry"
" via input card - Tony Millin Sept 06"
"   "
" 1EAF 1 18-04
    ZREG_$BLMLC(1,1)=ZMIN_$BLMLC;
    ZREG_$BLMLC(1,2)=ZREG_$BLMLC(1,1)+0.1;
    ZREG_$BLMLC(1,3)=ZREG_$BLMLC(1,1)+0.1675;
    ZREG_$BLMLC(1,4)=ZREG_$BLMLC(1,1)+0.9575;
    ZREG_$BLMLC(1,5)=ZREG_$BLMLC(1,1)+1.2575;
    ZREG_$BLMLC(1,6)=ZREG_$BLMLC(1,1)+1.9775;
    ZREG_$BLMLC(1,7)=ZREG_$BLMLC(1,1)+2.2775;
    ZREG_$BLMLC(1,8)=ZREG_$BLMLC(1,1)+3.0675;
    ZREG_$BLMLC(1,9)=ZREG_$BLMLC(1,1)+3.3675;
    ZREG_$BLMLC(1,10)=ZREG_$BLMLC(1,1)+4.0875;
    ZREG_$BLMLC(1,11)=ZREG_$BLMLC(1,1)+4.3875;
    ZREG_$BLMLC(1,12)=ZREG_$BLMLC(1,1)+5.1775;
    ZREG_$BLMLC(1,13)=ZREG_$BLMLC(1,1)+5.4475;
    ZREG_$BLMLC(1,14)=ZREG_$BLMLC(1,1)+6.1975;
    ZREG_$BLMLC(1,15)=ZREG_$BLMLC(1,1)+6.3000;
    ZREG_$BLMLC(1,16)=ZREG_$BLMLC(1,1)+ZTHICK_$BLMLC;
"1EAF 2 18-03
    ZREG_$BLMLC(2,1)=ZMIN_$BLMLC;
    ZREG_$BLMLC(2,2)=ZREG_$BLMLC(2,1)+0.1;
    ZREG_$BLMLC(2,3)=ZREG_$BLMLC(2,1)+0.2025;
    ZREG_$BLMLC(2,4)=ZREG_$BLMLC(2,1)+0.9225;
```

```
    ZREG_$BLMLC(2,5)=ZREG_$BLMLC(2,1)+1.2225;
    ZREG_$BLMLC(2,6)=ZREG_$BLMLC(2,1)+2.0125;
    ZREG_$BLMLC(2,7)=ZREG_$BLMLC(2,1)+2.3125;
    ZREG_$BLMLC(2,8)=ZREG_$BLMLC(2,1)+3.0325;
    ZREG_$BLMLC(2,9)=ZREG_$BLMLC(2,1)+3.3325;
    ZREG_$BLMLC(2,10)=ZREG_$BLMLC(2,1)+4.1225;
    ZREG_$BLMLC(2,11)=ZREG_$BLMLC(2,1)+4.4225;
    ZREG_$BLMLC(2,12)=ZREG_$BLMLC(2,1)+5.1425;
    ZREG_$BLMLC(2,13)=ZREG_$BLMLC(2,1)+5.4425;
    ZREG_$BLMLC(2,14)=ZREG_$BLMLC(2,1)+6.2325;
    ZREG_$BLMLC(2,15)=ZREG_$BLMLC(2,1)+6.3000;
    ZREG_$BLMLC(2,16)=ZREG_$BLMLC(2,1)+ZTHICK_$BLMLC;
"1EAF 3 18-02
    ZREG_$BLMLC(3,1)=ZMIN_$BLMLC;
    ZREG_$BLMLC(3,2)=ZREG_$BLMLC(3,1)+0.1;
    ZREG_$BLMLC(3,3)=ZREG_$BLMLC(3,1)+0.1675;
    ZREG_$BLMLC(3,4)=ZREG_$BLMLC(3,1)+0.9575;
    ZREG_$BLMLC(3,5)=ZREG_$BLMLC(3,1)+1.2575;
    ZREG_$BLMLC(3,6)=ZREG_$BLMLC(3,1)+1.9775;
    ZREG_$BLMLC(3,7)=ZREG_$BLMLC(3,1)+2.2775;
    ZREG_$BLMLC(3,8)=ZREG_$BLMLC(3,1)+3.0675;
    ZREG_$BLMLC(3,9)=ZREG_$BLMLC(3,1)+3.3675;
    ZREG_$BLMLC(3,10)=ZREG_$BLMLC(3,1)+4.0875;
    ZREG_$BLMLC(3,11)=ZREG_$BLMLC(3,1)+4.3875;
    ZREG_$BLMLC(3,12)=ZREG_$BLMLC(3,1)+5.1775;
    ZREG_$BLMLC(3,13)=ZREG_$BLMLC(3,1)+5.4475;
    ZREG_$BLMLC(3,14)=ZREG_$BLMLC(3,1)+6.1975;
    ZREG_$BLMLC(3,15)=ZREG_$BLMLC(3,1)+6.3000;
    ZREG_$BLMLC(3,16)=ZREG_$BLMLC(3,1)+ZTHICK_$BLMLC;
"1EAF 4 17-01
    ZREG_$BLMLC(4,1)=ZMIN_$BLMLC;
    ZREG_$BLMLC(4,2)=ZREG_$BLMLC(4,1)+0.1;
    ZREG_$BLMLC(4,3)=ZREG_$BLMLC(4,1)+0.2025;
    ZREG_$BLMLC(4,4)=ZREG_$BLMLC(4,1)+0.9225;
    ZREG_$BLMLC(4,5)=ZREG_$BLMLC(4,1)+1.2225;
    ZREG_$BLMLC(4,6)=ZREG_$BLMLC(4,1)+2.0125;
    ZREG_$BLMLC(4,7)=ZREG_$BLMLC(4,1)+2.3125;
    ZREG_$BLMLC(4,8)=ZREG_$BLMLC(4,1)+3.0325;
    ZREG_$BLMLC(4,9)=ZREG_$BLMLC(4,1)+3.3325;
    ZREG_$BLMLC(4,10)=ZREG_$BLMLC(4,1)+4.1225;
    ZREG_$BLMLC(4,11)=ZREG_$BLMLC(4,1)+4.4225;
    ZREG_$BLMLC(4,12)=ZREG_$BLMLC(4,1)+5.1425;
    ZREG_$BLMLC(4,13)=ZREG_$BLMLC(4,1)+5.4425;
    ZREG_$BLMLC(4,14)=ZREG_$BLMLC(4,1)+6.2325;
    ZREG_$BLMLC(4,15)=ZREG_$BLMLC(4,1)+6.3000;
    ZREG_$BLMLC(4,16)=ZREG_$BLMLC(4,1)+ZTHICK_$BLMLC;
"1EAF 5 17-06
    ZREG_$BLMLC(5,1)=ZMIN_$BLMLC;
    ZREG_$BLMLC(5,2)=ZREG_$BLMLC(5,1)+0.1;
    ZREG_$BLMLC(5,3)=ZREG_$BLMLC(5,1)+0.1675;
    ZREG_$BLMLC(5,4)=ZREG_$BLMLC(5,1)+0.9575;
    ZREG_$BLMLC(5,5)=ZREG_$BLMLC(5,1)+1.2575;
    ZREG_$BLMLC(5,6)=ZREG_$BLMLC(5,1)+1.9775;
    ZREG_$BLMLC(5,7)=ZREG_$BLMLC(5,1)+2.2775;
    ZREG_$BLMLC(5,8)=ZREG_$BLMLC(5,1)+3.0675;
    ZREG_$BLMLC(5,9)=ZREG_$BLMLC(5,1)+3.3675;
    ZREG_$BLMLC(5,10)=ZREG_$BLMLC(5,1)+4.0875;
```



```
    ZREG_$BLMLC(5,11)=ZREG_$BLMLC(5,1)+4.3875;
    ZREG_$BLMLC(5,12)=ZREG_$BLMLC(5,1)+5.1775;
    ZREG_$BLMLC(5,13)=ZREG_$BLMLC(5,1)+5.4475;
    ZREG_$BLMLC(5,14)=ZREG_$BLMLC(5,1)+6.1975;
    ZREG_$BLMLC(5,15)=ZREG_$BLMLC(5,1)+6.3000;
    ZREG_$BLMLC(5,16)=ZREG_$BLMLC(5,1)+ZTHICK_$BLMLC;
"1EAF 6 17-05
    ZREG_$BLMLC(6,1)=ZMIN_$BLMLC;
    ZREG_$BLMLC(6,2)=ZREG_$BLMLC(6,1)+0.1;
    ZREG_$BLMLC(6,3)=ZREG_$BLMLC(6,1)+0.2025;
    ZREG_$BLMLC(6,4)=ZREG_$BLMLC(6,1)+0.9225;
    ZREG_$BLMLC(6,5)=ZREG_$BLMLC(6,1)+1.2225;
    ZREG_$BLMLC(6,6)=ZREG_$BLMLC(6,1)+2.0125;
    ZREG_$BLMLC(6,7)=ZREG_$BLMLC(6,1)+2.3125;
    ZREG_$BLMLC(6,8)=ZREG_$BLMLC(6,1)+3.0325;
    ZREG_$BLMLC(6,9)=ZREG_$BLMLC(6,1)+3.3325;
    ZREG_$BLMLC(6,10)=ZREG_$BLMLC(6,1)+4.1225;
    ZREG_$BLMLC(6,11)=ZREG_$BLMLC(6,1)+4.4225;
    ZREG_$BLMLC(6,12)=ZREG_$BLMLC(6,1)+5.1425;
    ZREG_$BLMLC(6,13)=ZREG_$BLMLC(6,1)+5.4425;
    ZREG_$BLMLC(6,14)=ZREG_$BLMLC(6,1)+6.2325;
    ZREG_$BLMLC(6,15)=ZREG_$BLMLC(6,1)+6.3000;
    ZREG_$BLMLC(6,16)=ZREG_$BLMLC(6,1)+ZTHICK_$BLMLC;
"1EAF 7 16-04
    ZREG_$BLMLC(7,1)=ZMIN_$BLMLC;
    ZREG_$BLMLC(7,2)=ZREG_$BLMLC(7,1)+0.1;
    ZREG_$BLMLC(7,3)=ZREG_$BLMLC(7,1)+0.1675;
    ZREG_$BLMLC(7,4)=ZREG_$BLMLC(7,1)+0.9575;
    ZREG_$BLMLC(7,5)=ZREG_$BLMLC(7,1)+1.2575;
    ZREG_$BLMLC(7,6)=ZREG_$BLMLC(7,1)+1.9775;
    ZREG_$BLMLC(7,7)=ZREG_$BLMLC(7,1)+2.2775;
    ZREG_$BLMLC(7,8)=ZREG_$BLMLC(7,1)+3.0675;
    ZREG_$BLMLC(7,9)=ZREG_$BLMLC(7,1)+3.3675;
    ZREG_$BLMLC(7,10)=ZREG_$BLMLC(7,1)+4.0875;
    ZREG_$BLMLC(7,11)=ZREG_$BLMLC(7,1)+4.3875;
    ZREG_$BLMLC(7,12)=ZREG_$BLMLC(7,1)+5.1775;
    ZREG_$BLMLC(7,13)=ZREG_$BLMLC(7,1)+5.4475;
    ZREG_$BLMLC(7,14)=ZREG_$BLMLC(7,1)+6.1975;
    ZREG_$BLMLC(7,15)=ZREG_$BLMLC(7,1)+6.3000;
    ZREG_$BLMLC(7,16)=ZREG_$BLMLC(7,1)+ZTHICK_$BLMLC;
"1EAF 8 16-03
    ZREG_$BLMLC(8,1)=ZMIN_$BLMLC;
    ZREG_$BLMLC(8,2)=ZREG_$BLMLC(8,1)+0.1;
    ZREG_$BLMLC(8,3)=ZREG_$BLMLC(8,1)+0.2025;
    ZREG_$BLMLC(8,4)=ZREG_$BLMLC(8,1)+0.9225;
    ZREG_$BLMLC(8,5)=ZREG_$BLMLC(8,1)+1.2225;
    ZREG_$BLMLC(8,6)=ZREG_$BLMLC(8,1)+2.0125;
    ZREG_$BLMLC(8,7)=ZREG_$BLMLC(8,1)+2.3125;
    ZREG_$BLMLC(8,8)=ZREG_$BLMLC(8,1)+3.0325;
    ZREG_$BLMLC(8,9)=ZREG_$BLMLC(8,1)+3.3325;
    ZREG_$BLMLC(8,10)=ZREG_$BLMLC(8,1)+4.1225;
    ZREG_$BLMLC(8,11)=ZREG_$BLMLC(8,1)+4.4225;
    ZREG_$BLMLC(8,12)=ZREG_$BLMLC(8,1)+5.1425;
    ZREG_$BLMLC(8,13)=ZREG_$BLMLC(8,1)+5.4425;
    ZREG_$BLMLC(8,14)=ZREG_$BLMLC(8,1)+6.2325;
    ZREG_$BLMLC(8,15)=ZREG_$BLMLC(8,1)+6.3000;
    ZREG_$BLMLC(8,16)=ZREG_$BLMLC(8,1)+ZTHICK_$BLMLC;
```



```
"1EAF 9 16-02
    ZREG_$BLMLC(9,1)=ZMIN_$BLMLC;
    ZREG_$BLMLC(9,2)=ZREG_$BLMLC(9,1)+0.1;
    ZREG_$BLMLC(9,3)=ZREG_$BLMLC(9,1)+0.1675;
    ZREG_$BLMLC(9,4)=ZREG_$BLMLC(9,1)+0.9575;
    ZREG_$BLMLC(9,5)=ZREG_$BLMLC(9,1)+1.2575;
    ZREG_$BLMLC(9,6)=ZREG_$BLMLC(9,1)+1.9775;
    ZREG_$BLMLC(9,7)=ZREG_$BLMLC(9,1)+2.2775;
    ZREG_$BLMLC(9,8)=ZREG_$BLMLC(9,1)+3.0675;
    ZREG_$BLMLC(9,9)=ZREG_$BLMLC(9,1)+3.3675;
    ZREG_$BLMLC(9,10)=ZREG_$BLMLC(9,1)+4.0875;
    ZREG_$BLMLC(9,11)=ZREG_$BLMLC(9,1)+4.3875;
    ZREG_$BLMLC(9,12)=ZREG_$BLMLC(9,1)+5.1775;
    ZREG_$BLMLC(9,13)=ZREG_$BLMLC(9,1)+5.4475;
    ZREG_$BLMLC(9,14)=ZREG_$BLMLC(9,1)+6.1975;
    ZREG_$BLMLC(9,15)=ZREG_$BLMLC(9,1)+6.3000;
    ZREG_$BLMLC(9,16)=ZREG_$BLMLC(9,1)+ZTHICK_$BLMLC;
"1EAF 10 16-01
    ZREG_$BLMLC(10,1)=ZMIN_$BLMLC;
    ZREG_$BLMLC(10,2)=ZREG_$BLMLC(10,1)+0.1;
    ZREG_$BLMLC(10,3)=ZREG_$BLMLC(10,1)+0.2025;
    ZREG_$BLMLC(10,4)=ZREG_$BLMLC(10,1)+0.9225;
    ZREG_$BLMLC(10,5)=ZREG_$BLMLC(10,1)+1.2225;
    ZREG_$BLMLC(10,6)=ZREG_$BLMLC(10,1)+2.0125;
    ZREG_$BLMLC(10,7)=ZREG_$BLMLC(10,1)+2.3125;
    ZREG_$BLMLC(10,8)=ZREG_$BLMLC(10,1)+3.0325;
    ZREG_$BLMLC(10,9)=ZREG_$BLMLC(10,1)+3.3325;
    ZREG_$BLMLC(10,10)=ZREG_$BLMLC(10,1)+4.1225;
    ZREG_$BLMLC(10,11)=ZREG_$BLMLC(10,1)+4.4225;
    ZREG_$BLMLC(10,12)=ZREG_$BLMLC(10,1)+5.1425;
    ZREG_$BLMLC(10,13)=ZREG_$BLMLC(10,1)+5.4425;
    ZREG_$BLMLC(10,14)=ZREG_$BLMLC(10,1)+6.2325;
    ZREG_$BLMLC(10,15)=ZREG_$BLMLC(10,1)+6.3000;
    ZREG_$BLMLC(10,16)=ZREG_$BLMLC(10,1)+ZTHICK_$BLMLC;
"1EAF 11 06-06
    ZREG_$BLMLC(11,1)=ZMIN_$BLMLC;
    ZREG_$BLMLC(11,2)=ZREG_$BLMLC(11,1)+0.1;
    ZREG_$BLMLC(11,3)=ZREG_$BLMLC(11,1)+0.1675;
    ZREG_$BLMLC(11,4)=ZREG_$BLMLC(11,1)+0.9575;
    ZREG_$BLMLC(11,5)=ZREG_$BLMLC(11,1)+1.2575;
    ZREG_$BLMLC(11,6)=ZREG_$BLMLC(11,1)+1.9775;
    ZREG_$BLMLC(11,7)=ZREG_$BLMLC(11,1)+2.2775;
    ZREG_$BLMLC(11,8)=ZREG_$BLMLC(11,1)+3.0675;
    ZREG_$BLMLC(11,9)=ZREG_$BLMLC(11,1)+3.3675;
    ZREG_$BLMLC(11,10)=ZREG_$BLMLC(11,1)+4.0875;
    ZREG_$BLMLC(11,11)=ZREG_$BLMLC(11,1)+4.3875;
    ZREG_$BLMLC(11,12)=ZREG_$BLMLC(11,1)+5.1775;
    ZREG_$BLMLC(11,13)=ZREG_$BLMLC(11,1)+5.4475;
    ZREG_$BLMLC(11,14)=ZREG_$BLMLC(11,1)+6.1975;
    ZREG_$BLMLC(11,15)=ZREG_$BLMLC(11,1)+6.3000;
    ZREG_$BLMLC(11,16)=ZREG_$BLMLC(11,1)+ZTHICK_$BLMLC;
"1EAF 12 06-05
    ZREG_$BLMLC(12,1)=ZMIN_$BLMLC;
    ZREG_$BLMLC(12,2)=ZREG_$BLMLC(12,1)+0.1;
    ZREG_$BLMLC(12,3)=ZREG_$BLMLC(12,1)+0.2025;
    ZREG_$BLMLC(12,4)=ZREG_$BLMLC(12,1)+0.9225;
    ZREG_$BLMLC(12,5)=ZREG_$BLMLC(12,1)+1.2225;
```



```
    ZREG_$BLMLC(12,6)=ZREG_$BLMLC(12,1)+2.0125;
    ZREG_$BLMLC(12,7)=ZREG_$BLMLC(12,1)+2.3125;
    ZREG_$BLMLC(12,8)=ZREG_$BLMLC(12,1)+3.0325;
    ZREG_$BLMLC(12,9)=ZREG_$BLMLC(12,1)+3.3325;
    ZREG_$BLMLC(12,10)=ZREG_$BLMLC(12,1)+4.1225;
    ZREG_$BLMLC(12,11)=ZREG_$BLMLC(12,1)+4.4225;
    ZREG_$BLMLC(12,12)=ZREG_$BLMLC(12,1)+5.1425;
    ZREG_$BLMLC(12,13)=ZREG_$BLMLC(12,1)+5.4425;
    ZREG_$BLMLC(12,14)=ZREG_$BLMLC(12,1)+6.2325;
    ZREG_$BLMLC(12,15)=ZREG_$BLMLC(12,1)+6.3000;
    ZREG_$BLMLC(12,16)=ZREG_$BLMLC(12,1)+ZTHICK_$BLMLC;
"1EAF 13 06-04
    ZREG_$BLMLC(13,1)=ZMIN_$BLMLC;
    ZREG_$BLMLC(13,2)=ZREG_$BLMLC(13,1)+0.1;
    ZREG_$BLMLC(13,3)=ZREG_$BLMLC(13,1)+0.1675;
    ZREG_$BLMLC(13,4)=ZREG_$BLMLC(13,1)+0.9575;
    ZREG_$BLMLC(13,5)=ZREG_$BLMLC(13,1)+1.2575;
    ZREG_$BLMLC(13,6)=ZREG_$BLMLC(13,1)+1.9775;
    ZREG_$BLMLC(13,7)=ZREG_$BLMLC(13,1)+2.2775;
    ZREG_$BLMLC(13,8)=ZREG_$BLMLC(13,1)+3.0675;
    ZREG_$BLMLC(13,9)=ZREG_$BLMLC(13,1)+3.3675;
    ZREG_$BLMLC(13,10)=ZREG_$BLMLC(13,1)+4.0875;
    ZREG_$BLMLC(13,11)=ZREG_$BLMLC(13,1)+4.3875;
    ZREG_$BLMLC(13,12)=ZREG_$BLMLC(13,1)+5.1775;
    ZREG_$BLMLC(13,13)=ZREG_$BLMLC(13,1)+5.4475;
    ZREG_$BLMLC(13,14)=ZREG_$BLMLC(13,1)+6.1975;
    ZREG_$BLMLC(13,15)=ZREG_$BLMLC(13,1)+6.3000;
    ZREG_$BLMLC(13,16)=ZREG_$BLMLC(13,1)+ZTHICK_$BLMLC;
"1EAF 14 06-03
    ZREG_$BLMLC(14,1)=ZMIN_$BLMLC;
    ZREG_$BLMLC(14,2)=ZREG_$BLMLC(14,1)+0.1;
    ZREG_$BLMLC(14,3)=ZREG_$BLMLC(14,1)+0.2025;
    ZREG_$BLMLC(14,4)=ZREG_$BLMLC(14,1)+0.9225;
    ZREG_$BLMLC(14,5)=ZREG_$BLMLC(14,1)+1.2225;
    ZREG_$BLMLC(14,6)=ZREG_$BLMLC(14,1)+2.0125;
    ZREG_$BLMLC(14,7)=ZREG_$BLMLC(14,1)+2.3125;
    ZREG_$BLMLC(14,8)=ZREG_$BLMLC(14,1)+3.0325;
    ZREG_$BLMLC(14,9)=ZREG_$BLMLC(14,1)+3.3325;
    ZREG_$BLMLC(14,10)=ZREG_$BLMLC(14,1)+4.1225;
    ZREG_$BLMLC(14,11)=ZREG_$BLMLC(14,1)+4.4225;
    ZREG_$BLMLC(14,12)=ZREG_$BLMLC(14,1)+5.1425;
    ZREG_$BLMLC(14,13)=ZREG_$BLMLC(14,1)+5.4425;
    ZREG_$BLMLC(14,14)=ZREG_$BLMLC(14,1)+6.2325;
    ZREG_$BLMLC(14,15)=ZREG_$BLMLC(14,1)+6.3000;
    ZREG_$BLMLC(14,16)=ZREG_$BLMLC(14,1)+ZTHICK_$BLMLC;
"1EAF 15 06-02
    ZREG_$BLMLC(15,1)=ZMIN_$BLMLC;
    ZREG_$BLMLC(15,2)=ZREG_$BLMLC(15,1)+0.1;
    ZREG_$BLMLC(15,3)=ZREG_$BLMLC(15,1)+0.1675;
    ZREG_$BLMLC(15,4)=ZREG_$BLMLC(15,1)+0.9575;
    ZREG_$BLMLC(15,5)=ZREG_$BLMLC(15,1)+1.2575;
    ZREG_$BLMLC(15,6)=ZREG_$BLMLC(15,1)+1.9775;
    ZREG_$BLMLC(15,7)=ZREG_$BLMLC(15,1)+2.2775;
    ZREG_$BLMLC(15,8)=ZREG_$BLMLC(15,1)+3.0675;
    ZREG_$BLMLC(15,9)=ZREG_$BLMLC(15,1)+3.3675;
    ZREG_$BLMLC(15,10)=ZREG_$BLMLC(15,1)+4.0875;
    ZREG_$BLMLC(15,11)=ZREG_$BLMLC(15,1)+4.3875;
```

```
    ZREG_$BLMLC(15,12)=ZREG_$BLMLC(15,1)+5.1775;
    ZREG_$BLMLC(15,13)=ZREG_$BLMLC(15,1)+5.4475;
    ZREG_$BLMLC(15,14)=ZREG_$BLMLC(15,1)+6.1975;
    ZREG_$BLMLC(15,15)=ZREG_$BLMLC(15,1)+6.3000;
    ZREG_$BLMLC(15,16)=ZREG_$BLMLC(15,1)+ZTHICK_$BLMLC;
"LEAF 16 06-01
    ZREG_$BLMLC(16,1)=ZMIN_$BLMLC;
    ZREG_$BLMLC(16,2)=ZREG_$BLMLC(16,1)+0.1;
    ZREG_$BLMLC(16,3)=ZREG_$BLMLC(16,1)+0.2025;
    ZREG_$BLMLC(16,4)=ZREG_$BLMLC(16,1)+0.9225;
    ZREG_$BLMLC(16,5)=ZREG_$BLMLC(16,1)+1.2225;
    ZREG_$BLMLC(16,6)=ZREG_$BLMLC(16,1)+2.0125;
    ZREG_$BLMLC(16,7)=ZREG_$BLMLC(16,1)+2.3125;
    ZREG_$BLMLC(16,8)=ZREG_$BLMLC(16,1)+3.0325;
    ZREG_$BLMLC(16,9)=ZREG_$BLMLC(16,1)+3.3325;
    ZREG_$BLMLC(16,10)=ZREG_$BLMLC(16,1)+4.1225;
    ZREG_$BLMLC(16,11)=ZREG_$BLMLC(16,1)+4.4225;
    ZREG_$BLMLC(16,12)=ZREG_$BLMLC(16,1)+5.1425;
    ZREG_$BLMLC(16,13)=ZREG_$BLMLC(16,1)+5.4425;
    ZREG_$BLMLC(16,14)=ZREG_$BLMLC(16,1)+6.2325;
    ZREG_$BLMLC(16,15)=ZREG_$BLMLC(16,1)+6.3000;
    ZREG_$BLMLC(16,16)=ZREG_$BLMLC(16,1)+ZTHICK_$BLMLC;
"LEAF 17 16-06
    ZREG_$BLMLC(17,1)=ZMIN_$BLMLC;
    ZREG_$BLMLC(17,2)=ZREG_$BLMLC(17,1)+0.1;
    ZREG_$BLMLC(17,3)=ZREG_$BLMLC(17,1)+0.1675;
    ZREG_$BLMLC(17,4)=ZREG_$BLMLC(17,1)+0.9575;
    ZREG_$BLMLC(17,5)=ZREG_$BLMLC(17,1)+1.2575;
    ZREG_$BLMLC(17,6)=ZREG_$BLMLC(17,1)+1.9775;
    ZREG_$BLMLC(17,7)=ZREG_$BLMLC(17,1)+2.2775;
    ZREG_$BLMLC(17,8)=ZREG_$BLMLC(17,1)+3.0675;
    ZREG_$BLMLC(17,9)=ZREG_$BLMLC(17,1)+3.3675;
    ZREG_$BLMLC(17,10)=ZREG_$BLMLC(17,1)+4.0875;
    ZREG_$BLMLC(17,11)=ZREG_$BLMLC(17,1)+4.3875;
    ZREG_$BLMLC(17,12)=ZREG_$BLMLC(17,1)+5.1775;
    ZREG_$BLMLC(17,13)=ZREG_$BLMLC(17,1)+5.4475;
    ZREG_$BLMLC(17,14)=ZREG_$BLMLC(17,1)+6.1975;
    ZREG_$BLMLC(17,15)=ZREG_$BLMLC(17,1)+6.3000;
    ZREG_$BLMLC(17,16)=ZREG_$BLMLC(17,1)+ZTHICK_$BLMLC;
"LEAF 18 16-05
    ZREG_$BLMLC(18,1)=ZMIN_$BLMLC;
    ZREG_$BLMLC(18,2)=ZREG_$BLMLC(18,1)+0.1;
    ZREG_$BLMLC(18,3)=ZREG_$BLMLC(18,1)+0.2025;
    ZREG_$BLMLC(18,4)=ZREG_$BLMLC(18,1)+0.9225;
    ZREG_$BLMLC(18,5)=ZREG_$BLMLC(18,1)+1.2225;
    ZREG_$BLMLC(18,6)=ZREG_$BLMLC(18,1)+2.0125;
    ZREG_$BLMLC(18,7)=ZREG_$BLMLC(18,1)+2.3125;
    ZREG_$BLMLC(18,8)=ZREG_$BLMLC(18,1)+3.0325;
    ZREG_$BLMLC(18,9)=ZREG_$BLMLC(18,1)+3.3325;
    ZREG_$BLMLC(18,10)=ZREG_$BLMLC(18,1)+4.1225;
    ZREG_$BLMLC(18,11)=ZREG_$BLMLC(18,1)+4.4225;
    ZREG_$BLMLC(18,12)=ZREG_$BLMLC(18,1)+5.1425;
    ZREG_$BLMLC(18,13)=ZREG_$BLMLC(18,1)+5.4425;
    ZREG_$BLMLC(18,14)=ZREG_$BLMLC(18,1)+6.2325;
    ZREG_$BLMLC(18,15)=ZREG_$BLMLC(18,1)+6.3000;
    ZREG_$BLMLC(18,16)=ZREG_$BLMLC(18,1)+ZTHICK_$BLMLC;
"LEAF 19 16-04
```



```
    ZREG_$BLMLC(19,1)=ZMIN_$BLMLC;
    ZREG_$BLMLC(19,2)=ZREG_$BLMLC(19,1)+0.1;
    ZREG_$BLMLC(19,3)=ZREG_$BLMLC(19,1)+0.1675;
    ZREG_$BLMLC(19,4)=ZREG_$BLMLC(19,1)+0.9575;
    ZREG_$BLMLC(19,5)=ZREG_$BLMLC(19,1)+1.2575;
    ZREG_$BLMLC(19,6)=ZREG_$BLMLC(19,1)+1.9775;
    ZREG_$BLMLC(19,7)=ZREG_$BLMLC(19,1)+2.2775;
    ZREG_$BLMLC(19,8)=ZREG_$BLMLC(19,1)+3.0675;
    ZREG_$BLMLC(19,9)=ZREG_$BLMLC(19,1)+3.3675;
    ZREG_$BLMLC(19,10)=ZREG_$BLMLC(19,1)+4.0875;
    ZREG_$BLMLC(19,11)=ZREG_$BLMLC(19,1)+4.3875;
    ZREG_$BLMLC(19,12)=ZREG_$BLMLC(19,1)+5.1775;
    ZREG_$BLMLC(19,13)=ZREG_$BLMLC(19,1)+5.4475;
    ZREG_$BLMLC(19,14)=ZREG_$BLMLC(19,1)+6.1975;
    ZREG_$BLMLC(19,15)=ZREG_$BLMLC(19,1)+6.3000;
    ZREG_$BLMLC(19,16)=ZREG_$BLMLC(19,1)+ZTHICK_$BLMLC;
"LEAF 20 16-03
    ZREG_$BLMLC(20,1)=ZMIN_$BLMLC;
    ZREG_$BLMLC(20,2)=ZREG_$BLMLC(20,1)+0.1;
    ZREG_$BLMLC(20,3)=ZREG_$BLMLC(20,1)+0.2025;
    ZREG_$BLMLC(20,4)=ZREG_$BLMLC(20,1)+0.9225;
    ZREG_$BLMLC(20,5)=ZREG_$BLMLC(20,1)+1.2225;
    ZREG_$BLMLC(20,6)=ZREG_$BLMLC(20,1)+2.0125;
    ZREG_$BLMLC(20,7)=ZREG_$BLMLC(20,1)+2.3125;
    ZREG_$BLMLC(20,8)=ZREG_$BLMLC(20,1)+3.0325;
    ZREG_$BLMLC(20,9)=ZREG_$BLMLC(20,1)+3.3325;
    ZREG_$BLMLC(20,10)=ZREG_$BLMLC(20,1)+4.1225;
    ZREG_$BLMLC(20,11)=ZREG_$BLMLC(20,1)+4.4225;
    ZREG_$BLMLC(20,12)=ZREG_$BLMLC(20,1)+5.1425;
    ZREG_$BLMLC(20,13)=ZREG_$BLMLC(20,1)+5.4425;
    ZREG_$BLMLC(20,14)=ZREG_$BLMLC(20,1)+6.2325;
    ZREG_$BLMLC(20,15)=ZREG_$BLMLC(20,1)+6.3000;
    ZREG_$BLMLC(20,16)=ZREG_$BLMLC(20,1)+ZTHICK_$BLMLC;
"LEAF 21 17-02
    ZREG_$BLMLC(21,1)=ZMIN_$BLMLC;
    ZREG_$BLMLC(21,2)=ZREG_$BLMLC(21,1)+0.1;
    ZREG_$BLMLC(21,3)=ZREG_$BLMLC(21,1)+0.1675;
    ZREG_$BLMLC(21,4)=ZREG_$BLMLC(21,1)+0.9575;
    ZREG_$BLMLC(21,5)=ZREG_$BLMLC(21,1)+1.2575;
    ZREG_$BLMLC(21,6)=ZREG_$BLMLC(21,1)+1.9775;
    ZREG_$BLMLC(21,7)=ZREG_$BLMLC(21,1)+2.2775;
    ZREG_$BLMLC(21,8)=ZREG_$BLMLC(21,1)+3.0675;
    ZREG_$BLMLC(21,9)=ZREG_$BLMLC(21,1)+3.3675;
    ZREG_$BLMLC(21,10)=ZREG_$BLMLC(21,1)+4.0875;
    ZREG_$BLMLC(21,11)=ZREG_$BLMLC(21,1)+4.3875;
    ZREG_$BLMLC(21,12)=ZREG_$BLMLC(21,1)+5.1775;
    ZREG_$BLMLC(21,13)=ZREG_$BLMLC(21,1)+5.4475;
    ZREG_$BLMLC(21,14)=ZREG_$BLMLC(21,1)+6.1975;
    ZREG_$BLMLC(21,15)=ZREG_$BLMLC(21,1)+6.3000;
    ZREG_$BLMLC(21,16)=ZREG_$BLMLC(21,1)+ZTHICK_$BLMLC;
"LEAF 22 17-01
    ZREG_$BLMLC(22,1)=ZMIN_$BLMLC;
    ZREG_$BLMLC(22,2)=ZREG_$BLMLC(22,1)+0.1;
    ZREG_$BLMLC(22,3)=ZREG_$BLMLC(22,1)+0.2025;
    ZREG_$BLMLC(22,4)=ZREG_$BLMLC(22,1)+0.9225;
    ZREG_$BLMLC(22,5)=ZREG_$BLMLC(22,1)+1.2225;
    ZREG_$BLMLC(22,6)=ZREG_$BLMLC(22,1)+2.0125;
```



```
    ZREG_$BLMLC(22,7)=ZREG_$BLMLC(22,1)+2.3125;
    ZREG_$BLMLC(22,8)=ZREG_$BLMLC(22,1)+3.0325;
    ZREG_$BLMLC(22,9)=ZREG_$BLMLC(22,1)+3.3325;
    ZREG_$BLMLC(22,10)=ZREG_$BLMLC(22,1)+4.1225;
    ZREG_$BLMLC(22,11)=ZREG_$BLMLC(22,1)+4.4225;
    ZREG_$BLMLC(22,12)=ZREG_$BLMLC(22,1)+5.1425;
    ZREG_$BLMLC(22,13)=ZREG_$BLMLC(22,1)+5.4425;
    ZREG_$BLMLC(22,14)=ZREG_$BLMLC(22,1)+6.2325;
    ZREG_$BLMLC(22,15)=ZREG_$BLMLC(22,1)+6.3000;
    ZREG_$BLMLC(22,16)=ZREG_$BLMLC(22,1)+ZTHICK_$BLMLC;
"LEAF 23 17-06
    ZREG_$BLMLC(23,1)=ZMIN_$BLMLC;
    ZREG_$BLMLC(23,2)=ZREG_$BLMLC(23,1)+0.1;
    ZREG_$BLMLC(23,3)=ZREG_$BLMLC(23,1)+0.1675;
    ZREG_$BLMLC(23,4)=ZREG_$BLMLC(23,1)+0.9575;
    ZREG_$BLMLC(23,5)=ZREG_$BLMLC(23,1)+1.2575;
    ZREG_$BLMLC(23,6)=ZREG_$BLMLC(23,1)+1.9775;
    ZREG_$BLMLC(23,7)=ZREG_$BLMLC(23,1)+2.2775;
    ZREG_$BLMLC(23,8)=ZREG_$BLMLC(23,1)+3.0675;
    ZREG_$BLMLC(23,9)=ZREG_$BLMLC(23,1)+3.3675;
    ZREG_$BLMLC(23,10)=ZREG_$BLMLC(23,1)+4.0875;
    ZREG_$BLMLC(23,11)=ZREG_$BLMLC(23,1)+4.3875;
    ZREG_$BLMLC(23,12)=ZREG_$BLMLC(23,1)+5.1775;
    ZREG_$BLMLC(23,13)=ZREG_$BLMLC(23,1)+5.4475;
    ZREG_$BLMLC(23,14)=ZREG_$BLMLC(23,1)+6.1975;
    ZREG_$BLMLC(23,15)=ZREG_$BLMLC(23,1)+6.3000;
    ZREG_$BLMLC(23,16)=ZREG_$BLMLC(23,1)+ZTHICK_$BLMLC;
"LEAF 24 18-05
    ZREG_$BLMLC(24,1)=ZMIN_$BLMLC;
    ZREG_$BLMLC(24,2)=ZREG_$BLMLC(24,1)+0.1;
    ZREG_$BLMLC(24,3)=ZREG_$BLMLC(24,1)+0.2025;
    ZREG_$BLMLC(24,4)=ZREG_$BLMLC(24,1)+0.9225;
    ZREG_$BLMLC(24,5)=ZREG_$BLMLC(24,1)+1.2225;
    ZREG_$BLMLC(24,6)=ZREG_$BLMLC(24,1)+2.0125;
    ZREG_$BLMLC(24,7)=ZREG_$BLMLC(24,1)+2.3125;
    ZREG_$BLMLC(24,8)=ZREG_$BLMLC(24,1)+3.0325;
    ZREG_$BLMLC(24,9)=ZREG_$BLMLC(24,1)+3.3325;
    ZREG_$BLMLC(24,10)=ZREG_$BLMLC(24,1)+4.1225;
    ZREG_$BLMLC(24,11)=ZREG_$BLMLC(24,1)+4.4225;
    ZREG_$BLMLC(24,12)=ZREG_$BLMLC(24,1)+5.1425;
    ZREG_$BLMLC(24,13)=ZREG_$BLMLC(24,1)+5.4425;
    ZREG_$BLMLC(24,14)=ZREG_$BLMLC(24,1)+6.2325;
    ZREG_$BLMLC(24,15)=ZREG_$BLMLC(24,1)+6.3000;
    ZREG_$BLMLC(24,16)=ZREG_$BLMLC(24,1)+ZTHICK_$BLMLC;
"LEAF 25 18-04
    ZREG_$BLMLC(25,1)=ZMIN_$BLMLC;
    ZREG_$BLMLC(25,2)=ZREG_$BLMLC(25,1)+0.1;
    ZREG_$BLMLC(25,3)=ZREG_$BLMLC(25,1)+0.1675;
    ZREG_$BLMLC(25,4)=ZREG_$BLMLC(25,1)+0.9575;
    ZREG_$BLMLC(25,5)=ZREG_$BLMLC(25,1)+1.2575;
    ZREG_$BLMLC(25,6)=ZREG_$BLMLC(25,1)+1.9775;
    ZREG_$BLMLC(25,7)=ZREG_$BLMLC(25,1)+2.2775;
    ZREG_$BLMLC(25,8)=ZREG_$BLMLC(25,1)+3.0675;
    ZREG_$BLMLC(25,9)=ZREG_$BLMLC(25,1)+3.3675;
    ZREG_$BLMLC(25,10)=ZREG_$BLMLC(25,1)+4.0875;
    ZREG_$BLMLC(25,11)=ZREG_$BLMLC(25,1)+4.3875;
    ZREG_$BLMLC(25,12)=ZREG_$BLMLC(25,1)+5.1775;
```



```
    ZREG_$BLMLC(25,13)=ZREG_$BLMLC(25,1)+5.4475;
    ZREG_$BLMLC(25,14)=ZREG_$BLMLC(25,1)+6.1975;
    ZREG_$BLMLC(25,15)=ZREG_$BLMLC(25,1)+6.3000;
    ZREG_$BLMLC(25,16)=ZREG_$BLMLC(25,1)+ZTHICK_$BLMLC;
"LEAF 26"
    ZREG_$BLMLC(26,1)=ZMIN_$BLMLC;
    ZREG_$BLMLC(26,2)=ZREG_$BLMLC(26,1)+0.1;
    ZREG_$BLMLC(26,3)=ZREG_$BLMLC(26,1)+0.2025;
    ZREG_$BLMLC(26,4)=ZREG_$BLMLC(26,1)+0.9225;
    ZREG_$BLMLC(26,5)=ZREG_$BLMLC(26,1)+1.2225;
    ZREG_$BLMLC(26,6)=ZREG_$BLMLC(26,1)+2.0125;
    ZREG_$BLMLC(26,7)=ZREG_$BLMLC(26,1)+2.3125;
    ZREG_$BLMLC(26,8)=ZREG_$BLMLC(26,1)+3.0325;
    ZREG_$BLMLC(26,9)=ZREG_$BLMLC(26,1)+3.3325;
    ZREG_$BLMLC(26,10)=ZREG_$BLMLC(26,1)+4.1225;
    ZREG_$BLMLC(26,11)=ZREG_$BLMLC(26,1)+4.4225;
    ZREG_$BLMLC(26,12)=ZREG_$BLMLC(26,1)+5.1425;
    ZREG_$BLMLC(26,13)=ZREG_$BLMLC(26,1)+5.4425;
    ZREG_$BLMLC(26,14)=ZREG_$BLMLC(26,1)+6.2325;
    ZREG_$BLMLC(26,15)=ZREG_$BLMLC(26,1)+6.3000;
    ZREG_$BLMLC(26,16)=ZREG_$BLMLC(26,1)+ZTHICK_$BLMLC;



TOT_LEAF_$BLMLC=26;
OUTPUT; (' set tot leaf to 26',$)


" III. START POSITION OF LEAVES"
" ============================="
;
OUTPUT; ('About to start entering leaf positions etc',$)
OUTPUT ZMIN_$BLMLC; (/' Input the starting X (ORIENT_$BLMLC=0) or '/
         ' Y (ORIENT_$BLMLC=1) position at z = ',F15.0, ' cm : ', $);
MINPUT ($BLMLC) START_$BLMLC; (F15.0);
OUTPUT START_$BLMLC; (F12.5);
WRITE(IOUTLIST,'(F15.8)') START_$BLMLC;

" Checking the validity of user-input"

IF(ABS(START_$BLMLC)-RMAX_CM(ICM_$BLMLC)>1.E-5) [
  OUTPUT ICM_$BLMLC;
   (//'***ERROR IN CM ',I4,' ($BLMLC)'/
   ' START POSITION EXCEEDS CM BOUNDARY'//);
   IERR_GEOM(ICM_$BLMLC)=IERR_GEOM(ICM_$BLMLC)+1;
 ];

"IV. INTER-LEAF AIR GAP "
"====================== "

OUTPUT; (/'Input the inter-leaf air gap(>=0.0) : ',$);
  "leaf gap defined at ZMIN"
MINPUT ($BLMLC) LEAFGAP_$BLMLC; (F15.0);
OUTPUT LEAFGAP_$BLMLC; (F12.5);
WRITE(IOUTLIST,'(F15.8)') LEAFGAP_$BLMLC;

IF (LEAFGAP_$BLMLC<0.0) [
```

```
      LEAFGAP_$BLMLC=0;
      OUTPUT ICM_$BLMLC;
         ('***ERROR IN CM ',I4,' ($BLMLC)'/
         ' Inter-leaf air gap is negative - reset to 0   '//);
         IERR_GEOM(ICM_$BLMLC)=IERR_GEOM(ICM_$BLMLC)+1;
      ];
"V. TYPE OF LEAF ENDS - ROUNDED VS FLAT DIVERGENT "
"================================================ "
"THIS NEEDS REWRITING TO ACCOUNT FOR THREE REGIONS OF BRAINLAB MLC!"
"DO LATER ..................................... 26/11/06"
"================================================================="
OUTPUT; ('Input the type of leaf end desired : only opt 1 supported ',/,
          '   0 --- Rounded leaf end or ',/
          '   1 --- Focused leaf end  ');
OUTPUT; ('Input your choice : ', $);
MINPUT ($BLMLC) ENDTYPE_$BLMLC; (I5);
WRITE(IOUTLIST, '(I5)') ENDTYPE_$BLMLC;
OUTPUT ENDTYPE_$BLMLC; (I5/);
"Leave rounded end code in for now as it may be needed - can't see why though"

IF(ENDTYPE_$BLMLC=1) [

    OUTPUT; ('Input the angle of the upper part of leaves (rads) :',$);
    MINPUT ($BLMLC) THETA_TOP_$BLMLC; (F15.0);
    OUTPUT THETA_TOP_$BLMLC;(F12.5/);
    OUTPUT; ('Input the angle of the lower part of leaves (rads) :',$);
    MINPUT ($BLMLC) THETA_BOTTOM_$BLMLC; (F15.0);
    OUTPUT THETA_BOTTOM_$BLMLC;(F12.5/);

    WRITE(IOUTLIST,'(F15.5)')THETA_TOP_$BLMLC;
    WRITE(IOUTLIST,'(F15.5)')THETA_BOTTOM_$BLMLC;


 ]
ELSE  [ "Defaults to rounded ends "

   OUTPUT (ZTHICK_$BLMLC/2);
          (' Input the radius >= ', F12.5, ' cm ', /
          ' of the leaf ends : ',$);

   MINPUT ($BLMLC) LEAFRADIUS_$BLMLC; (F15.0);
   OUTPUT LEAFRADIUS_$BLMLC; (F15.0/);
   WRITE(IOUTLIST,'(F15.8)') LEAFRADIUS_$BLMLC;

   IF((LEAFRADIUS_$BLMLC < (0.5*ZTHICK_$BLMLC)) |
      (LEAFRADIUS_$BLMLC < 0.0)) [

" This is done to ensure that the leaf end is rounded all the"
" way from zmin_$BLMLC to zmax_$BLMLC. "
" Otherwise the curvature will fall short."

     LEAFRADIUS_$BLMLC=0.5*ZTHICK_$BLMLC;
     OUTPUT ICM_$BLMLC,LEAFRADIUS_$BLMLC;
      ('***ERROR IN CM ',I4,' ($BLMLC)'/
      ' LEAFRADIUS_$BLMLC is less than minimum acceptable'/
      ' RESET TO ', F15.5, ' cm for now'//);
     IERR_GEOM(ICM_$BLMLC)=IERR_GEOM(ICM_$BLMLC)+1;
```



```
    ]
    IF(HOLEPOS_FULL_$BLMLC>=LEAFRADIUS_$BLMLC) [
      HOLEPOS_FULL_$BLMLC=LEAFRADIUS_$BLMLC-0.1;
      OUTPUT ICM_$BLMLC,LEAFRADIUS_$BLMLC;
      ('***ERROR IN CM ',I4,' ($BLMLC)'/
      ' Hole position in FULL leaves is greater than leaf'/
      ' radius. Reset to ',F12.5,' cm for now'//);
      IERR_GEOM(ICM_$BLMLC)=IERR_GEOM(ICM_$BLMLC)+1;
    ]
    IF(HOLEPOS_ISO_$BLMLC>=LEAFRADIUS_$BLMLC) [
      HOLEPOS_ISO_$BLMLC=LEAFRADIUS_$BLMLC-0.1;
      OUTPUT ICM_$BLMLC,LEAFRADIUS_$BLMLC;
      ('***ERROR IN CM ',I4,' ($BLMLC)'/
      ' Hole position in ISOCENTER leaves is greater than leaf'/
      ' radius. Reset to ',F12.5,' cm for now'//);
      IERR_GEOM(ICM_$BLMLC)=IERR_GEOM(ICM_$BLMLC)+1;
    ]
    IF(HOLEPOS_TAR_$BLMLC>=LEAFRADIUS_$BLMLC) [
      HOLEPOS_TAR_$BLMLC=LEAFRADIUS_$BLMLC-0.1;
      OUTPUT ICM_$BLMLC,LEAFRADIUS_$BLMLC;
      ('***ERROR IN CM ',I4,' ($BLMLC)'/
      ' Hole position in TARGET leaves is greater than leaf'/
      ' radius. Reset to ',F12.5,' cm for now'//);
      IERR_GEOM(ICM_$BLMLC)=IERR_GEOM(ICM_$BLMLC)+1;
    ]
 ]; " End of checking the leaf end ;

ZFOCUS_$BLMLC(2)=0.0; "temporary set to avoid crash in summary

"VI. FOCUS FOR DIVERGENT LEAF SIDES "
"==================================== "

OUTPUT; (' Input the Z focus point of the leaf sides: ',$);
MINPUT  ($BLMLC) ZFOCUS_$BLMLC(1); (F15.0);
OUTPUT ZFOCUS_$BLMLC(1); (F12.5/);
WRITE(IOUTLIST,'(F15.5)') ZFOCUS_$BLMLC(1);
IF(ABS(ZFOCUS_$BLMLC(1)-ZMIN_$BLMLC)<1.E-5) [
   ZFOCUS_$BLMLC(1)=ZMIN_$BLMLC-1.E-4;
   OUTPUT ICM_$BLMLC,ZFOCUS_$BLMLC(1);
      (//' ***ERROR IN CM ',I4,' ($BLMLC)'/
       ' ZFOCUS(1) cannot be equal to ZMIN_$BLMLC'/
       ' ZFOCUS(1) reset to ',F15.5,' cm for now'//);
   IERR_GEOM(ICM_$BLMLC)=IERR_GEOM(ICM_$BLMLC)+1;
 ]
ELSEIF(ZFOCUS_$BLMLC(1)>ZMIN_$BLMLC & ZFOCUS_$BLMLC(1)<ZMAX_$BLMLC) [
   ZFOCUS_$BLMLC(1)=ZMAX_$BLMLC;
   OUTPUT ICM_$BLMLC,ZFOCUS_$BLMLC(1);
      (//' ***ERROR IN CM ',I4,' ($BLMLC)'/
       ' ZFOCUS(1) is between ZMIN_$BLMLC and ZMAX_$BLMLC'/
       ' This will cause leaf sides to overlap'/
       ' ZFOCUS(1) reset to ',F15.5,' cm for now'//);
   IERR_GEOM(ICM_$BLMLC)=IERR_GEOM(ICM_$BLMLC)+1;
 ];

"VII. CALCULATE THE Z-AXIS COORDINATES OF DIFFERENT SUB-REGIONS "
"============================================================== "
"this is done on a leaf-by-leaf basis      done already see above"
```



```
"VIII. CALC PARAMETERS IN DIRECTION PERPENDICULAR TO LEAF ORIENTATION"
"================================================================="
" as above

"Y Positions of leaves"
"====================="
"LEAF 1 -18-04"
    YREG_$BLMLC(1,1)=START_$BLMLC;
    YREG_$BLMLC(1,2)=YREG_$BLMLC(1,1)+0.023386;
    YREG_$BLMLC(1,3)=YREG_$BLMLC(1,1)+0.047224;
    YREG_$BLMLC(1,4)=YREG_$BLMLC(1,1)+0.116995;
    YREG_$BLMLC(1,5)=YREG_$BLMLC(1,1)+0.211534;
    YREG_$BLMLC(1,6)=YREG_$BLMLC(1,1)+0.281305;
    YREG_$BLMLC(1,7)=YREG_$BLMLC(1,1)+0.305143;
    YREG_$BLMLC(1,8)=YREG_$BLMLC(1,1)+0.328529;
    LEAFTYPE_$BLMLC(1)=2;
"LEAF 2 -18-03"
    YREG_$BLMLC(2,1)=YREG_$BLMLC(1,YREG_STRT)+LEAFGAP_$BLMLC;
    YREG_$BLMLC(2,2)=YREG_$BLMLC(2,1)+0.023836;
    YREG_$BLMLC(2,3)=YREG_$BLMLC(2,1)+0.047131;
    YREG_$BLMLC(2,4)=YREG_$BLMLC(2,1)+0.117406;
    YREG_$BLMLC(2,5)=YREG_$BLMLC(2,1)+0.211945;
    YREG_$BLMLC(2,6)=YREG_$BLMLC(2,1)+0.282220;
    YREG_$BLMLC(2,7)=YREG_$BLMLC(2,1)+0.305514;
    YREG_$BLMLC(2,8)=YREG_$BLMLC(2,1)+0.329350;
    LEAFTYPE_$BLMLC(2)=1;
"LEAF 3 -18-02
    YREG_$BLMLC(3,1)=YREG_$BLMLC(2,YREG_STRT)+LEAFGAP_$BLMLC;
    YREG_$BLMLC(3,2)=YREG_$BLMLC(3,1)+0.023386;
    YREG_$BLMLC(3,3)=YREG_$BLMLC(3,1)+0.047224;
    YREG_$BLMLC(3,4)=YREG_$BLMLC(3,1)+0.116995;
    YREG_$BLMLC(3,5)=YREG_$BLMLC(3,1)+0.211534;
    YREG_$BLMLC(3,6)=YREG_$BLMLC(3,1)+0.281305;
    YREG_$BLMLC(3,7)=YREG_$BLMLC(3,1)+0.305143;
    YREG_$BLMLC(3,8)=YREG_$BLMLC(3,1)+0.328529;
    LEAFTYPE_$BLMLC(3)=2;
"LEAF 4 -17-01
    YREG_$BLMLC(4,1)=YREG_$BLMLC(3,YREG_STRT)+LEAFGAP_$BLMLC;
    YREG_$BLMLC(4,2)=YREG_$BLMLC(4,1)+0.023830;
    YREG_$BLMLC(4,3)=YREG_$BLMLC(4,1)+0.047106;
    YREG_$BLMLC(4,4)=YREG_$BLMLC(4,1)+0.091321;
    YREG_$BLMLC(4,5)=YREG_$BLMLC(4,1)+0.185860;
    YREG_$BLMLC(4,6)=YREG_$BLMLC(4,1)+0.230076;
    YREG_$BLMLC(4,7)=YREG_$BLMLC(4,1)+0.253351;
    YREG_$BLMLC(4,8)=YREG_$BLMLC(4,1)+0.277181;
    LEAFTYPE_$BLMLC(4)=1;
"LEAF 5 -17-06
    YREG_$BLMLC(5,1)=YREG_$BLMLC(4,YREG_STRT)+LEAFGAP_$BLMLC;
    YREG_$BLMLC(5,2)=YREG_$BLMLC(5,1)+0.023447;
    YREG_$BLMLC(5,3)=YREG_$BLMLC(5,1)+0.047228;
    YREG_$BLMLC(5,4)=YREG_$BLMLC(5,1)+0.090936;
    YREG_$BLMLC(5,5)=YREG_$BLMLC(5,1)+0.185474;
    YREG_$BLMLC(5,6)=YREG_$BLMLC(5,1)+0.229182;
    YREG_$BLMLC(5,7)=YREG_$BLMLC(5,1)+0.252963;
    YREG_$BLMLC(5,8)=YREG_$BLMLC(5,1)+0.276410;
    LEAFTYPE_$BLMLC(5)=2;
```



```
"LEAF 6 -17-05
    YREG_$BLMLC(6,1)=YREG_$BLMLC(5,YREG_STRT)+LEAFGAP_$BLMLC;
    YREG_$BLMLC(6,2)=YREG_$BLMLC(6,1)+0.023830;
    YREG_$BLMLC(6,3)=YREG_$BLMLC(6,1)+0.047106;
    YREG_$BLMLC(6,4)=YREG_$BLMLC(6,1)+0.091321;
    YREG_$BLMLC(6,5)=YREG_$BLMLC(6,1)+0.185860;
    YREG_$BLMLC(6,6)=YREG_$BLMLC(6,1)+0.230076;
    YREG_$BLMLC(6,7)=YREG_$BLMLC(6,1)+0.253351;
    YREG_$BLMLC(6,8)=YREG_$BLMLC(6,1)+0.277181;
    LEAFTYPE_$BLMLC(6)=1;
"LEAF 7 -16-04
    YREG_$BLMLC(7,1)=YREG_$BLMLC(6,YREG_STRT)+LEAFGAP_$BLMLC;
    YREG_$BLMLC(7,2)=YREG_$BLMLC(7,1)+0.023429;
    YREG_$BLMLC(7,3)=YREG_$BLMLC(7,1)+0.047223;
    YREG_$BLMLC(7,4)=YREG_$BLMLC(7,1)+0.051730;
    YREG_$BLMLC(7,5)=YREG_$BLMLC(7,1)+0.146268;
    YREG_$BLMLC(7,6)=YREG_$BLMLC(7,1)+0.150775;
    YREG_$BLMLC(7,7)=YREG_$BLMLC(7,1)+0.174569;
    YREG_$BLMLC(7,8)=YREG_$BLMLC(7,1)+0.197998;
    LEAFTYPE_$BLMLC(7)=2;
"LEAF 8 - 16-03
    YREG_$BLMLC(8,1)=YREG_$BLMLC(7,YREG_STRT)+LEAFGAP_$BLMLC;
    YREG_$BLMLC(8,2)=YREG_$BLMLC(8,1)+0.023835;
    YREG_$BLMLC(8,3)=YREG_$BLMLC(8,1)+0.047114;
    YREG_$BLMLC(8,4)=YREG_$BLMLC(8,1)+0.052140;
    YREG_$BLMLC(8,5)=YREG_$BLMLC(8,1)+0.146679;
    YREG_$BLMLC(8,6)=YREG_$BLMLC(8,1)+0.151705;
    YREG_$BLMLC(8,7)=YREG_$BLMLC(8,1)+0.174984;
    YREG_$BLMLC(8,8)=YREG_$BLMLC(8,1)+0.198819;
    LEAFTYPE_$BLMLC(8)=1;
"LEAF 9 -16-02
    YREG_$BLMLC(9,1)=YREG_$BLMLC(8,YREG_STRT)+LEAFGAP_$BLMLC;
    YREG_$BLMLC(9,2)=YREG_$BLMLC(9,1)+0.023429;
    YREG_$BLMLC(9,3)=YREG_$BLMLC(9,1)+0.047223;
    YREG_$BLMLC(9,4)=YREG_$BLMLC(9,1)+0.051730;
    YREG_$BLMLC(9,5)=YREG_$BLMLC(9,1)+0.146268;
    YREG_$BLMLC(9,6)=YREG_$BLMLC(9,1)+0.150775;
    YREG_$BLMLC(9,7)=YREG_$BLMLC(9,1)+0.174569;
    YREG_$BLMLC(9,8)=YREG_$BLMLC(9,1)+0.197998;
    LEAFTYPE_$BLMLC(9)=2;
"LEAF 10 - 16-01
    YREG_$BLMLC(10,1)=YREG_$BLMLC(9,YREG_STRT)+LEAFGAP_$BLMLC;
    YREG_$BLMLC(10,2)=YREG_$BLMLC(10,1)+0.023835;
    YREG_$BLMLC(10,3)=YREG_$BLMLC(10,1)+0.048114;
    YREG_$BLMLC(10,4)=YREG_$BLMLC(10,1)+0.052140;
    YREG_$BLMLC(10,5)=YREG_$BLMLC(10,1)+0.146679;
    YREG_$BLMLC(10,6)=YREG_$BLMLC(10,1)+0.151705;
    YREG_$BLMLC(10,7)=YREG_$BLMLC(10,1)+0.174984;
    YREG_$BLMLC(10,8)=YREG_$BLMLC(10,1)+0.198819;
    LEAFTYPE_$BLMLC(10)=1;
"LEAF 11 - 06-06
    YREG_$BLMLC(11,1)=YREG_$BLMLC(10,YREG_STRT)+LEAFGAP_$BLMLC;
    YREG_$BLMLC(11,2)=YREG_$BLMLC(11,1)+0.023429;
    YREG_$BLMLC(11,3)=YREG_$BLMLC(11,1)+0.047223;
    YREG_$BLMLC(11,4)=YREG_$BLMLC(11,1)+0.051730;
    YREG_$BLMLC(11,5)=YREG_$BLMLC(11,1)+0.146268;
    YREG_$BLMLC(11,6)=YREG_$BLMLC(11,1)+0.150775;
```

```
    YREG_$BLMLC(11,7)=YREG_$BLMLC(11,1)+0.174569;
    YREG_$BLMLC(11,8)=YREG_$BLMLC(11,1)+0.197998;
    LEAFTYPE_$BLMLC(11)=2;
"LEAF 12 -06-05
    YREG_$BLMLC(12,1)=YREG_$BLMLC(11,YREG_STRT)+LEAFGAP_$BLMLC;
    YREG_$BLMLC(12,2)=YREG_$BLMLC(12,1)+0.023835;
    YREG_$BLMLC(12,3)=YREG_$BLMLC(12,1)+0.047114;
    YREG_$BLMLC(12,4)=YREG_$BLMLC(12,1)+0.052140;
    YREG_$BLMLC(12,5)=YREG_$BLMLC(12,1)+0.146679;
    YREG_$BLMLC(12,6)=YREG_$BLMLC(12,1)+0.151705;
    YREG_$BLMLC(12,7)=YREG_$BLMLC(12,1)+0.174984;
    YREG_$BLMLC(12,8)=YREG_$BLMLC(12,1)+0.198819;
    LEAFTYPE_$BLMLC(12)=1;
"LEAF 13 -06-04
    YREG_$BLMLC(13,1)=YREG_$BLMLC(12,YREG_STRT)+LEAFGAP_$BLMLC;
    YREG_$BLMLC(13,2)=YREG_$BLMLC(13,1)+0.023429;
    YREG_$BLMLC(13,3)=YREG_$BLMLC(13,1)+0.047223;
    YREG_$BLMLC(13,4)=YREG_$BLMLC(13,1)+0.051730;
    YREG_$BLMLC(13,5)=YREG_$BLMLC(13,1)+0.146268;
    YREG_$BLMLC(13,6)=YREG_$BLMLC(13,1)+0.150775;
    YREG_$BLMLC(13,7)=YREG_$BLMLC(13,1)+0.174569;
    YREG_$BLMLC(13,8)=YREG_$BLMLC(13,1)+0.197998;
    LEAFTYPE_$BLMLC(13)=2;
"LEAF 14 -06-03
    YREG_$BLMLC(14,1)=YREG_$BLMLC(13,YREG_STRT)+LEAFGAP_$BLMLC;
    YREG_$BLMLC(14,2)=YREG_$BLMLC(14,1)+0.023835;
    YREG_$BLMLC(14,3)=YREG_$BLMLC(14,1)+0.048114;
    YREG_$BLMLC(14,4)=YREG_$BLMLC(14,1)+0.052140;
    YREG_$BLMLC(14,5)=YREG_$BLMLC(14,1)+0.146679;
    YREG_$BLMLC(14,6)=YREG_$BLMLC(14,1)+0.151705;
    YREG_$BLMLC(14,7)=YREG_$BLMLC(14,1)+0.174984;
    YREG_$BLMLC(14,8)=YREG_$BLMLC(14,1)+0.198819;
    LEAFTYPE_$BLMLC(14)=1;
"LEAF 15 -06-02
    YREG_$BLMLC(15,1)=YREG_$BLMLC(14,YREG_STRT)+LEAFGAP_$BLMLC;
    YREG_$BLMLC(15,2)=YREG_$BLMLC(15,1)+0.023429;
    YREG_$BLMLC(15,3)=YREG_$BLMLC(15,1)+0.047223;
    YREG_$BLMLC(15,4)=YREG_$BLMLC(15,1)+0.051730;
    YREG_$BLMLC(15,5)=YREG_$BLMLC(15,1)+0.146268;
    YREG_$BLMLC(15,6)=YREG_$BLMLC(15,1)+0.150775;
    YREG_$BLMLC(15,7)=YREG_$BLMLC(15,1)+0.174569;
    YREG_$BLMLC(15,8)=YREG_$BLMLC(15,1)+0.197998;
    LEAFTYPE_$BLMLC(15)=2;
"LEAF 16 -06-01
    YREG_$BLMLC(16,1)=YREG_$BLMLC(15,YREG_STRT)+LEAFGAP_$BLMLC;
    YREG_$BLMLC(16,2)=YREG_$BLMLC(16,1)+0.023835;
    YREG_$BLMLC(16,3)=YREG_$BLMLC(16,1)+0.047114;
    YREG_$BLMLC(16,4)=YREG_$BLMLC(16,1)+0.052140;
    YREG_$BLMLC(16,5)=YREG_$BLMLC(16,1)+0.146679;
    YREG_$BLMLC(16,6)=YREG_$BLMLC(16,1)+0.151705;
    YREG_$BLMLC(16,7)=YREG_$BLMLC(16,1)+0.174984;
    YREG_$BLMLC(16,8)=YREG_$BLMLC(16,1)+0.198819;
    LEAFTYPE_$BLMLC(16)=1;
"LEAF 17 -16-06
    YREG_$BLMLC(17,1)=YREG_$BLMLC(16,YREG_STRT)+LEAFGAP_$BLMLC;
    YREG_$BLMLC(17,2)=YREG_$BLMLC(17,1)+0.023429;
    YREG_$BLMLC(17,3)=YREG_$BLMLC(17,1)+0.047223;
```



```
    YREG_$BLMLC(17,4)=YREG_$BLMLC(17,1)+0.051730;
    YREG_$BLMLC(17,5)=YREG_$BLMLC(17,1)+0.146268;
    YREG_$BLMLC(17,6)=YREG_$BLMLC(17,1)+0.150775;
    YREG_$BLMLC(17,7)=YREG_$BLMLC(17,1)+0.174569;
    YREG_$BLMLC(17,8)=YREG_$BLMLC(17,1)+0.197998;
    LEAFTYPE_$BLMLC(17)=2;
"LEAF 18 -16-05
    YREG_$BLMLC(18,1)=YREG_$BLMLC(17,YREG_STRT)+LEAFGAP_$BLMLC;
    YREG_$BLMLC(18,2)=YREG_$BLMLC(18,1)+0.023835;
    YREG_$BLMLC(18,3)=YREG_$BLMLC(18,1)+0.047114;
    YREG_$BLMLC(18,4)=YREG_$BLMLC(18,1)+0.052140;
    YREG_$BLMLC(18,5)=YREG_$BLMLC(18,1)+0.146679;
    YREG_$BLMLC(18,6)=YREG_$BLMLC(18,1)+0.151705;
    YREG_$BLMLC(18,7)=YREG_$BLMLC(18,1)+0.174984;
    YREG_$BLMLC(18,8)=YREG_$BLMLC(18,1)+0.198819;
    LEAFTYPE_$BLMLC(18)=1;
"LEAF 19 -16-04
    YREG_$BLMLC(19,1)=YREG_$BLMLC(18,YREG_STRT)+LEAFGAP_$BLMLC;
    YREG_$BLMLC(19,2)=YREG_$BLMLC(19,1)+0.023429;
    YREG_$BLMLC(19,3)=YREG_$BLMLC(19,1)+0.047223;
    YREG_$BLMLC(19,4)=YREG_$BLMLC(19,1)+0.051730;
    YREG_$BLMLC(19,5)=YREG_$BLMLC(19,1)+0.146268;
    YREG_$BLMLC(19,6)=YREG_$BLMLC(19,1)+0.150775;
    YREG_$BLMLC(19,7)=YREG_$BLMLC(19,1)+0.174569;
    YREG_$BLMLC(19,8)=YREG_$BLMLC(19,1)+0.197998;
    LEAFTYPE_$BLMLC(19)=2;
"LEAF 20 -16-03
    YREG_$BLMLC(20,1)=YREG_$BLMLC(19,YREG_STRT)+LEAFGAP_$BLMLC;
    YREG_$BLMLC(20,2)=YREG_$BLMLC(20,1)+0.023835;
    YREG_$BLMLC(20,3)=YREG_$BLMLC(20,1)+0.047114;
    YREG_$BLMLC(20,4)=YREG_$BLMLC(20,1)+0.052140;
    YREG_$BLMLC(20,5)=YREG_$BLMLC(20,1)+0.146679;
    YREG_$BLMLC(20,6)=YREG_$BLMLC(20,1)+0.151705;
    YREG_$BLMLC(20,7)=YREG_$BLMLC(20,1)+0.174984;
    YREG_$BLMLC(20,8)=YREG_$BLMLC(20,1)+0.198819;
    LEAFTYPE_$BLMLC(20)=1;
"LEAF 21 -17-02
    YREG_$BLMLC(21,1)=YREG_$BLMLC(20,YREG_STRT)+LEAFGAP_$BLMLC;
    YREG_$BLMLC(21,2)=YREG_$BLMLC(21,1)+0.023447;
    YREG_$BLMLC(21,3)=YREG_$BLMLC(21,1)+0.047228;
    YREG_$BLMLC(21,4)=YREG_$BLMLC(21,1)+0.090936;
    YREG_$BLMLC(21,5)=YREG_$BLMLC(21,1)+0.185474;
    YREG_$BLMLC(21,6)=YREG_$BLMLC(21,1)+0.229182;
    YREG_$BLMLC(21,7)=YREG_$BLMLC(21,1)+0.252963;
    YREG_$BLMLC(21,8)=YREG_$BLMLC(21,1)+0.276410;
    LEAFTYPE_$BLMLC(21)=2;
"LEAF 22 -17-01
    YREG_$BLMLC(22,1)=YREG_$BLMLC(21,YREG_STRT)+LEAFGAP_$BLMLC;
    YREG_$BLMLC(22,2)=YREG_$BLMLC(22,1)+0.023830;
    YREG_$BLMLC(22,3)=YREG_$BLMLC(22,1)+0.047106;
    YREG_$BLMLC(22,4)=YREG_$BLMLC(22,1)+0.091321;
    YREG_$BLMLC(22,5)=YREG_$BLMLC(22,1)+0.185860;
    YREG_$BLMLC(22,6)=YREG_$BLMLC(22,1)+0.230076;
    YREG_$BLMLC(22,7)=YREG_$BLMLC(22,1)+0.253351;
    YREG_$BLMLC(22,8)=YREG_$BLMLC(22,1)+0.277181;
    LEAFTYPE_$BLMLC(22)=1;
"LEAF 23 - 17-06
```



```
    YREG_$BLMLC(23,1)=YREG_$BLMLC(22,YREG_STRT)+LEAFGAP_$BLMLC;
    YREG_$BLMLC(23,2)=YREG_$BLMLC(23,1)+0.023447;
    YREG_$BLMLC(23,3)=YREG_$BLMLC(23,1)+0.047228;
    YREG_$BLMLC(23,4)=YREG_$BLMLC(23,1)+0.090936;
    YREG_$BLMLC(23,5)=YREG_$BLMLC(23,1)+0.185474;
    YREG_$BLMLC(23,6)=YREG_$BLMLC(23,1)+0.229182;
    YREG_$BLMLC(23,7)=YREG_$BLMLC(23,1)+0.252963;
    YREG_$BLMLC(23,8)=YREG_$BLMLC(23,1)+0.276410;
    LEAFTYPE_$BLMLC(23)=2;
"LEAF 24 - 18-05
    YREG_$BLMLC(24,1)=YREG_$BLMLC(23,YREG_STRT)+LEAFGAP_$BLMLC;
    YREG_$BLMLC(24,2)=YREG_$BLMLC(24,1)+0.023836;
    YREG_$BLMLC(24,3)=YREG_$BLMLC(24,1)+0.047131;
    YREG_$BLMLC(24,4)=YREG_$BLMLC(24,1)+0.117406;
    YREG_$BLMLC(24,5)=YREG_$BLMLC(24,1)+0.211945;
    YREG_$BLMLC(24,6)=YREG_$BLMLC(24,1)+0.282220;
    YREG_$BLMLC(24,7)=YREG_$BLMLC(24,1)+0.305514;
    YREG_$BLMLC(24,8)=YREG_$BLMLC(24,1)+0.329350;
    LEAFTYPE_$BLMLC(24)=1;
"LEAF 25 - 18-04
    YREG_$BLMLC(25,1)=YREG_$BLMLC(24,YREG_STRT)+LEAFGAP_$BLMLC;
    YREG_$BLMLC(25,2)=YREG_$BLMLC(25,1)+0.023386;
    YREG_$BLMLC(25,3)=YREG_$BLMLC(25,1)+0.047224;
    YREG_$BLMLC(25,4)=YREG_$BLMLC(25,1)+0.116995;
    YREG_$BLMLC(25,5)=YREG_$BLMLC(25,1)+0.211534;
    YREG_$BLMLC(25,6)=YREG_$BLMLC(25,1)+0.281305;
    YREG_$BLMLC(25,7)=YREG_$BLMLC(25,1)+0.305143;
    YREG_$BLMLC(25,8)=YREG_$BLMLC(25,1)+0.328529;
    LEAFTYPE_$BLMLC(25)=2;
"LEAF 26 - 18-03
    YREG_$BLMLC(26,1)=YREG_$BLMLC(25,YREG_STRT)+LEAFGAP_$BLMLC;
    YREG_$BLMLC(26,2)=YREG_$BLMLC(26,1)+0.023836;
    YREG_$BLMLC(26,3)=YREG_$BLMLC(26,1)+0.047131;
    YREG_$BLMLC(26,4)=YREG_$BLMLC(26,1)+0.117406;
    YREG_$BLMLC(26,5)=YREG_$BLMLC(26,1)+0.211945;
    YREG_$BLMLC(26,6)=YREG_$BLMLC(26,1)+0.282220;
    YREG_$BLMLC(26,7)=YREG_$BLMLC(26,1)+0.305514;
    YREG_$BLMLC(26,8)=YREG_$BLMLC(26,1)+0.329350;
    LEAFTYPE_$BLMLC(26)=1;

"   DO  I=1,26[
"       DO J=1,8 [
"           WRITE(73,1251) YREG_$BLMLC(I,J);
"       ]
"   ]
1251    FORMAT(F8.3,',');

    WRITE(IOUTLIST,'(2F15.5)') YREG_$BLMLC(1,1),YREG_$BLMLC(26,8);

TEMP1 = (ZMIN_$BLMLC-ZFOCUS_$BLMLC(1));"
"SET TEMP1 to 1.00 for now - may need to improve to get exact dimensions"
"TEMP1 = 1.0;"
DO I=1,26[
    DO J=1,8[
        SURPARA1_$BLMLC(I,J)=YREG_$BLMLC(I,J)/TEMP1;
    ];
];
```



```
"IX. INPUT THE COORDINATES NEG_$BLMLC AND POS_$BLMLC "
"================================================== "

DO I=1, TOT_LEAF_$BLMLC [
        LEAFB_$BLMLC(I)=0.0;
    LEAFA_$BLMLC(I)=0.0;
]

OUTPUT; (' Input for MLC A and B leaf tips '/);
IF(ORIENT_$BLMLC=1)[
    IF(ENDTYPE_$BLMLC=1)[
      OUTPUT;(' Input min. X, max. X of top of opening in leaves,');
    ]
    ELSE[
      OUTPUT;(' Input min. X, max. X of rounded leaf ends,');
    ]
]
ELSE[
    IF(ENDTYPE_$BLMLC=1)[
      OUTPUT;(' Input min. Y, max. Y of top of opening in leaves,');
    ]
    ELSE[
      OUTPUT;(' Input min. Y, max. Y of rounded leaf ends,');
    ]
]
OUTPUT;(' # of adjacent leaves with these coordinates:');
I=1;
LOOP[
  OUTPUT I;('   For leaf',I4,' :',$)
  MINPUT ($BLMLC) NEG_$BLMLC, POS_$BLMLC, NUM_$BLMLC; (2F15.0,I5);
  IF(NUM_$BLMLC<=0) NUM_$BLMLC=1;
  OUTPUT NEG_$BLMLC, POS_$BLMLC, NUM_$BLMLC; (2F12.5,I5);
  WRITE(IOUTLIST,'(2F15.5,I5)')NEG_$BLMLC, POS_$BLMLC,NUM_$BLMLC;
  IF(NEG_$BLMLC > POS_$BLMLC)[
     NEG_$BLMLC = POS_$BLMLC;
     OUTPUT ICM_$BLMLC,I,I+NUM_$BLMLC-1,NEG_$BLMLC;
      ('// ***ERROR IN CM ',I4,' ($BLMLC)'/
   ' Min. and max. opening coordinates in leaves ',I4,' - ',I4,' overlap'/
   ' Both coordinates set to ',F15.5,' cm for now'//);
     IERR_GEOM(ICM_$BLMLC)=IERR_GEOM(ICM_$BLMLC)+1;
                                ]

  IF(ABS(NEG_$BLMLC)>RMAX_CM(ICM_$BLMLC)|
     ABS(POS_$BLMLC)>RMAX_CM(ICM_$BLMLC)) [

     OUTPUT ICM_$BLMLC,I,I+NUM_$BLMLC-1;
      ('// ***ERROR IN CM ',I4,' ($BLMLC)'/
       ' Tip of leaves ',I4,' - ',I4,' are outside CM '//);

     IERR_GEOM(ICM_$BLMLC)=IERR_GEOM(ICM_$BLMLC)+1;
                                        ];
  DO J=I,I+NUM_$BLMLC-1["define opening for all leaves in group"
    IF(J>TOT_LEAF_$BLMLC) EXIT;
    LEAFB_$BLMLC(J)=NEG_$BLMLC;
    LEAFA_$BLMLC(J)=POS_$BLMLC;
  ]
```

```
  I=J;
]WHILE(I<=TOT_LEAF_$BLMLC);"End of Coordinate inputs for || direction "

IF(ENDTYPE_$BLMLC=1)[
"Not sure why this is here as zfocus_$blmlc"
" will not be used may cause problems"
DO I=1, TOT_LEAF_$BLMLC [

SURPARA2_B_$BLMLC(I)=LEAFB_$BLMLC(I)/(ZMIN_$BLMLC-ZFOCUS_$BLMLC(2) );

SURPARA2_A_$BLMLC(I)=LEAFA_$BLMLC(I)/(ZMIN_$BLMLC-ZFOCUS_$BLMLC(2) );

                        ];
                    ];


"X. ESTABLISH TOP OF FIRST CM
"==============================

ZFRONT_$BLMLC = Z_min_CM(ICM_$BLMLC);

"
"XI. ESTABLISH START OF NEXT CM
"================================

Z_min_CM(ICM_$BLMLC+1) = ZMAX_$BLMLC;

"
"XII. GET ECUT, PCUT, DOSE SCORING ZONE AND MATERIAL IN EACH REGION
"================================================================

IRA = IRSTART_$BLMLC-1;
DO IR_$BLMLC = 1,N_$BLMLC ["loop through regions to get information"
   IRA = IRA+1;
   IF(IR_$BLMLC=1) [
       OUTPUT IR_$BLMLC;
        (/' Region',I4,' (MLC opening):'/
          ' ECUT, PCUT (MeV), DOSE ZONE (0=NO DOSE SCORED), IREGION_TO_BIT'/
          ' :',$);
   ]
   ELSEIF(IR_$BLMLC=2) [
       OUTPUT IR_$BLMLC;
        (/' Region',I4,' (MLC leaves):'/
' ECUT, PCUT (MeV), DOSE ZONE (0=NO DOSE SCORED), IREGION_TO_BIT, IGNOREGAPS'/
         ' :',$);
   ]
   ELSE[
       OUTPUT IR_$BLMLC;
        (/' Region',I4,' (driving screw holes):'/
         ' ECUT, PCUT (MeV), DOSE ZONE (0=NO DOSE SCORED), IREGION_TO_BIT'/
         ' :',$);
   ]
   IF(IR_$BLMLC~=2)[
      MINPUT ($BLMLC) ECUT(IRA),PCUT(IRA),DOSE_ZONE(IRA),IREGION_TO_BIT(IRA);
      (2F15.0,2I5);
      OUTPUT ECUT(IRA),PCUT(IRA),DOSE_ZONE(IRA),IREGION_TO_BIT(IRA);
             (2F15.5,2I5);
```



```
      WRITE(IOUTLIST,'(2F15.5,2I5)')
             ECUT(IRA),PCUT(IRA),DOSE_ZONE(IRA),IREGION_TO_BIT(IRA);
   ]
   ELSE[
      MINPUT ($BLMLC) ECUT(IRA),PCUT(IRA),DOSE_ZONE(IRA),
                      IREGION_TO_BIT(IRA),IGNOREGAPS_$BLMLC; (2F15.0,3I5);
      OUTPUT ECUT(IRA),PCUT(IRA),DOSE_ZONE(IRA),IREGION_TO_BIT(IRA),
             IGNOREGAPS_$BLMLC; (2F15.5,3I5);
      WRITE(IOUTLIST,'(2F15.5,3I5)')
    ECUT(IRA),PCUT(IRA),DOSE_ZONE(IRA),IREGION_TO_BIT(IRA),IGNOREGAPS_$BLMLC;
   ]
   IF(ECUT(IRA) < ECUTIN) [ECUT(IRA)=ECUTIN;];
   IF(PCUT(IRA) < PCUTIN) [PCUT(IRA)=PCUTIN;];
   OUTPUT IR_$BLMLC; (' material of region ',I3,' ',$);
     $MED_INPUT($BLMLC); " inputs character array MED_IN from unit 5, loops"
  "through array MEDIA(24,I) to check if medium was previously input."
  "If so, sets MED_INDEX to index of previous medium.  If not,"
  "increments NMED and sets MED_INDEX to NMED."
   MED(IRA) = MED_INDEX; " medium of the planar slab"
 ] "end of loop over IR_$BLMLC"
;

IF(IGNOREGAPS_$BLMLC=1 & IREJCT_GLOBAL>0)[
   IF(ORIENT_$BLMLC=1)["leaves parallel to X"
       OUTPUT;(/' *******Range rejection in $BLMLC will ignore all'/
                ' air gaps if the particle is in the leaves and has'/
                ' X < min. X of leaf openings (not including leaf ends)'/
                ' or X > max. X of leaf openings (not including ends)'/);
   ]
   ELSE["leaves parallel to Y"
       OUTPUT;(/' *******Range rejection in $BLMLC will ignore all'/
                ' air gaps if the particle is in the leaves and has'/
                ' Y < min. Y of leaf openings (not including leaf ends)'/
                ' or Y > max. Y of leaf openings (not including ends)'/);
   ]
   DO I=1,TOT_LEAF_$BLMLC["loop through leaves to find index of those with"
                          "max. +ve opening and min. -ve opening"
       IF(I=1)[
           MIN_INDEX=I;200 FORMAT(' ',I1,A3,A1,10(F7.2,','));
           MAX_INDEX=I;
       ]
       ELSE[
           IF(LEAFB_$BLMLC(I)<LEAFB_$BLMLC(I-1))MIN_INDEX=I;
           IF(LEAFA_$BLMLC(I)>LEAFA_$BLMLC(I-1))MAX_INDEX=I;
       ]
   ]
   IF(ENDTYPE_$BLMLC=1)["straight, focused ends"
"       MIN_PLANE_$BLMLC=MIN(LEAFB_$BLMLC(MIN_INDEX),"
"                        SURPARA2_B_$BLMLC(MIN_INDEX)*"
"                       (ZMIN_$BLMLC+ZTHICK_$BLMLC-ZFOCUS_$BLMLC(2)));"
"       MAX_PLANE_$BLMLC=MAX(LEAFB_$BLMLC(MAX_INDEX),"
"                         SURPARA2_B_$BLMLC(MAX_INDEX)*"
"                         (ZMIN_$BLMLC+ZTHICK_$BLMLC-ZFOCUS_$BLMLC(2)));"
     MIN_PLANE_$BLMLC=MIN(LEAFB_$BLMLC(MIN_INDEX),
                         SURPARA2_B_$BLMLC(MIN_INDEX)*
                        (ZMIN_$BLMLC+ZTHICK_$BLMLC));
       MAX_PLANE_$BLMLC=MAX(LEAFB_$BLMLC(MAX_INDEX),
```



```
                        SURPARA2_B_$BLMLC(MAX_INDEX)*
                        (ZMIN_$BLMLC+ZTHICK_$BLMLC));
   ]
   ELSE["rounded leaf ends"
       MIN_PLANE_$BLMLC=LEAFB_$BLMLC(MIN_INDEX)-LEAFRADIUS_$BLMLC+
                        SQRT(LEAFRADIUS_$BLMLC**2-(ZTHICK_$BLMLC/2.)**2);
       MAX_PLANE_$BLMLC=LEAFA_$BLMLC(MIN_INDEX)+LEAFRADIUS_$BLMLC-
                        SQRT(LEAFRADIUS_$BLMLC**2-(ZTHICK_$BLMLC/2.)**2);
   ]
   write(*,*)' min,max ',MIN_PLANE_$BLMLC,MAX_PLANE_$BLMLC;
]
ELSE["set to default"
   IGNOREGAPS_$BLMLC=0;
]
"
"XIII. SET UP AIR GAP TO PREVIOUS CM IF PRESENT
"  ========================================
"
"  The air gap has the highest region number in the CM, even though its
"  the top of the component module.  This is to allow the assignment of
"  region numbers on input of the parameters of each local region
"  (mainly to assign the medium number of the region).
"  The air gap is then assigned after all of the
"  CM parameters have been input.
"
"note that if this is the first CM (ICM_$mlc=1) then the gap thickness
"Z_gap_THICK(ICM_$BLMLC) = 0, which is used as a flag for no air gap

Z_gap_THICK(ICM_$BLMLC) = ZMIN_$BLMLC - Z_min_CM(ICM_$BLMLC);
IF (Z_gap_THICK(ICM_$BLMLC) < = 0.0) [
   Z_gap_THICK(ICM_$BLMLC) = 0.;
   N_GAP_$BLMLC = 0; "no air gap for this CM"
  ]
ELSE [
   N_GAP_$BLMLC = 1; "this CM has an air gap"
   IRA = IRSTART_$BLMLC+N_$BLMLC; "absolute region number of air gap"
   MED(IRA) = AIR_INDEX; "medium is air"
 ];
"
"XIV. SET UP REGION NUMBERS
"============================
"
"  This CM has N_$BLMLC+N_GAP_$mlc regions
"
;
"Index last region
IREND_$BLMLC = (IRSTART_$BLMLC -1) + N_$BLMLC+N_GAP_$BLMLC;
NREG = NREG+N_$BLMLC+N_GAP_$BLMLC;
                          "Total no of regions in full geometry up
                          "to and including this CM
IF (NREG <= $MXREG) [
   IR_start_CM(ICM_$BLMLC+1) = IREND_$BLMLC+1;
  ]    "have not exceeded maximum region number
       "Index of first region in next CM:"
ELSE [
   OUTPUT ICM_$BLMLC,NREG,$MXREG;
   (//' ***ERROR IN CM ',I4,' ($BLMLC):'/
```



```
   T2,I4,' regions requested, only ',I4,' available'//);
   IERR_GEOM(ICM_$BLMLC)=IERR_GEOM(ICM_$BLMLC)+1;
 ];

"
"XV.  ESTABLISH CM BOUNDARY
"============================
"
RMAX_CM_FLAG(ICM_$BLMLC) = 2; "put a square boundary about CM
"
"XVI. ESTABLISH DOSE SCORING ZONES AND BIT SETTING FOR EACH REGION
"================================================================
"
IRA = IRSTART_$BLMLC-1; "absolute region number"
DO IR_$BLMLC=1,N_$BLMLC ["loop over local region number"
   IRA = IRA+1;
   "dose-scoring zones"
   NDOSE_ZONE = MAX(DOSE_ZONE(IRA),NDOSE_ZONE); "Number of dose zones"
   MAX_BIT = MAX(IREGION_TO_BIT(IRA),MAX_BIT); " current maximum"
   "charged particle range rejection parameters"
   ESAVE(IRA)=ESAVE_GLOBAL; "Particles with total energies below ESAVE are"
                            "considered for range rejection"
   ECUTRR(IRA)=ECUT(IRA); "Minimum energy on exit from region GXD"
   E_min_out(ICM_$BLMLC)=ECUT(IRA); "Minimum energy on exit from CM"
  ] "end of loop over IR_$BLMLC

"XVII. ESTABLISH SUB-REGION IR VALUES
"====================================
DO L=1,TOT_LEAF_$BLMLC [
      DO I=1,5 [ "NX"
           DO J =1,7 [ "NY"
                DO K = 1,15 [ "NZ"
                  SUBINDEX_$BLMLC(L,I,J,K)=1; "
                  ];
             ];
         ];
       ];
;
"Now define regions containing leaf medium"
DO L=1,TOT_LEAF_$BLMLC[" Do For All Leaves"
    DO I=2,5[
    IF (    LEAFTYPE_$BLMLC(L)=1)[
        SUBINDEX_$BLMLC(L,I,1,5)=2;
        SUBINDEX_$BLMLC(L,I,1,9)=2;
        SUBINDEX_$BLMLC(L,I,1,13)=2;
        SUBINDEX_$BLMLC(L,I,2,2)=2;
        SUBINDEX_$BLMLC(L,I,2,4)=2;
        SUBINDEX_$BLMLC(L,I,2,5)=2;
        SUBINDEX_$BLMLC(L,I,2,6)=2;
        SUBINDEX_$BLMLC(L,I,2,8)=2;
        SUBINDEX_$BLMLC(L,I,2,9)=2;
        SUBINDEX_$BLMLC(L,I,2,10)=2;
        SUBINDEX_$BLMLC(L,I,2,12)=2;
        SUBINDEX_$BLMLC(L,I,2,13)=2;
        SUBINDEX_$BLMLC(L,I,2,14)=2;
        SUBINDEX_$BLMLC(L,I,3,2)=2;
        SUBINDEX_$BLMLC(L,I,3,3)=2;
```

```
        SUBINDEX_$BLMLC(L,I,3,4)=2;
        SUBINDEX_$BLMLC(L,I,3,5)=2;
        SUBINDEX_$BLMLC(L,I,3,6)=2;
        SUBINDEX_$BLMLC(L,I,3,7)=2;
        SUBINDEX_$BLMLC(L,I,3,8)=2;
        SUBINDEX_$BLMLC(L,I,3,9)=2;
        SUBINDEX_$BLMLC(L,I,3,10)=2;
        SUBINDEX_$BLMLC(L,I,3,11)=2;
        SUBINDEX_$BLMLC(L,I,3,12)=2;
        SUBINDEX_$BLMLC(L,I,3,13)=2;
        SUBINDEX_$BLMLC(L,I,3,14)=2;
        SUBINDEX_$BLMLC(L,I,4,1)=2;
        SUBINDEX_$BLMLC(L,I,4,2)=2;
        SUBINDEX_$BLMLC(L,I,4,3)=2;
        SUBINDEX_$BLMLC(L,I,4,4)=2;
        SUBINDEX_$BLMLC(L,I,4,5)=2;
        SUBINDEX_$BLMLC(L,I,4,6)=2;
        SUBINDEX_$BLMLC(L,I,4,7)=2;
        SUBINDEX_$BLMLC(L,I,4,8)=2;
        SUBINDEX_$BLMLC(L,I,4,9)=2;
        SUBINDEX_$BLMLC(L,I,4,10)=2;
        SUBINDEX_$BLMLC(L,I,4,11)=2;
        SUBINDEX_$BLMLC(L,I,4,12)=2;
        SUBINDEX_$BLMLC(L,I,4,13)=2;
        SUBINDEX_$BLMLC(L,I,4,14)=2;
        SUBINDEX_$BLMLC(L,I,4,15)=2;
        SUBINDEX_$BLMLC(L,I,5,2)=2;
        SUBINDEX_$BLMLC(L,I,5,3)=2;
        SUBINDEX_$BLMLC(L,I,5,4)=2;
        SUBINDEX_$BLMLC(L,I,5,5)=2;
        SUBINDEX_$BLMLC(L,I,5,6)=2;
        SUBINDEX_$BLMLC(L,I,5,7)=2;
        SUBINDEX_$BLMLC(L,I,5,8)=2;
        SUBINDEX_$BLMLC(L,I,5,9)=2;
        SUBINDEX_$BLMLC(L,I,5,10)=2;
        SUBINDEX_$BLMLC(L,I,5,11)=2;
        SUBINDEX_$BLMLC(L,I,5,12)=2;
        SUBINDEX_$BLMLC(L,I,5,13)=2;
        SUBINDEX_$BLMLC(L,I,5,14)=2;
        SUBINDEX_$BLMLC(L,I,6,2)=2;
        SUBINDEX_$BLMLC(L,I,6,4)=2;
        SUBINDEX_$BLMLC(L,I,6,5)=2;
        SUBINDEX_$BLMLC(L,I,6,6)=2;
        SUBINDEX_$BLMLC(L,I,6,8)=2;
        SUBINDEX_$BLMLC(L,I,6,9)=2;
        SUBINDEX_$BLMLC(L,I,6,10)=2;
        SUBINDEX_$BLMLC(L,I,6,12)=2;
        SUBINDEX_$BLMLC(L,I,6,13)=2;
        SUBINDEX_$BLMLC(L,I,6,14)=2;
        SUBINDEX_$BLMLC(L,I,7,5)=2;
        SUBINDEX_$BLMLC(L,I,7,9)=2;
        SUBINDEX_$BLMLC(L,I,7,13)=2;
    ]
    ELSE [
        SUBINDEX_$BLMLC(L,I,1,3)=2;
        SUBINDEX_$BLMLC(L,I,1,7)=2;
        SUBINDEX_$BLMLC(L,I,1,11)=2;
```



```
        SUBINDEX_$BLMLC(L,I,2,2)=2;
        SUBINDEX_$BLMLC(L,I,2,3)=2;
        SUBINDEX_$BLMLC(L,I,2,4)=2;
        SUBINDEX_$BLMLC(L,I,2,6)=2;
        SUBINDEX_$BLMLC(L,I,2,7)=2;
        SUBINDEX_$BLMLC(L,I,2,8)=2;
        SUBINDEX_$BLMLC(L,I,2,10)=2;
        SUBINDEX_$BLMLC(L,I,2,11)=2;
        SUBINDEX_$BLMLC(L,I,2,12)=2;
        SUBINDEX_$BLMLC(L,I,2,14)=2;
        SUBINDEX_$BLMLC(L,I,3,2)=2;
        SUBINDEX_$BLMLC(L,I,3,3)=2;
        SUBINDEX_$BLMLC(L,I,3,4)=2;
        SUBINDEX_$BLMLC(L,I,3,5)=2;
        SUBINDEX_$BLMLC(L,I,3,6)=2;
        SUBINDEX_$BLMLC(L,I,3,7)=2;
        SUBINDEX_$BLMLC(L,I,3,8)=2;
        SUBINDEX_$BLMLC(L,I,3,9)=2;
        SUBINDEX_$BLMLC(L,I,3,10)=2;
        SUBINDEX_$BLMLC(L,I,3,11)=2;
        SUBINDEX_$BLMLC(L,I,3,12)=2;
        SUBINDEX_$BLMLC(L,I,3,13)=2;
        SUBINDEX_$BLMLC(L,I,3,14)=2;
        SUBINDEX_$BLMLC(L,I,4,1)=2;
        SUBINDEX_$BLMLC(L,I,4,2)=2;
        SUBINDEX_$BLMLC(L,I,4,3)=2;
        SUBINDEX_$BLMLC(L,I,4,4)=2;
        SUBINDEX_$BLMLC(L,I,4,5)=2;
        SUBINDEX_$BLMLC(L,I,4,6)=2;
        SUBINDEX_$BLMLC(L,I,4,7)=2;
        SUBINDEX_$BLMLC(L,I,4,8)=2;
        SUBINDEX_$BLMLC(L,I,4,9)=2;
        SUBINDEX_$BLMLC(L,I,4,10)=2;
        SUBINDEX_$BLMLC(L,I,4,11)=2;
        SUBINDEX_$BLMLC(L,I,4,12)=2;
        SUBINDEX_$BLMLC(L,I,4,13)=2;
        SUBINDEX_$BLMLC(L,I,4,14)=2;
        SUBINDEX_$BLMLC(L,I,4,15)=2;
        SUBINDEX_$BLMLC(L,I,5,2)=2;
        SUBINDEX_$BLMLC(L,I,5,3)=2;
        SUBINDEX_$BLMLC(L,I,5,4)=2;
        SUBINDEX_$BLMLC(L,I,5,5)=2;
        SUBINDEX_$BLMLC(L,I,5,6)=2;
        SUBINDEX_$BLMLC(L,I,5,7)=2;
        SUBINDEX_$BLMLC(L,I,5,8)=2;
        SUBINDEX_$BLMLC(L,I,5,9)=2;
        SUBINDEX_$BLMLC(L,I,5,10)=2;
        SUBINDEX_$BLMLC(L,I,5,11)=2;
        SUBINDEX_$BLMLC(L,I,5,12)=2;
        SUBINDEX_$BLMLC(L,I,5,13)=2;
        SUBINDEX_$BLMLC(L,I,5,14)=2;
        SUBINDEX_$BLMLC(L,I,6,2)=2;
        SUBINDEX_$BLMLC(L,I,6,3)=2;
        SUBINDEX_$BLMLC(L,I,6,4)=2;
        SUBINDEX_$BLMLC(L,I,6,6)=2;
        SUBINDEX_$BLMLC(L,I,6,7)=2;
        SUBINDEX_$BLMLC(L,I,6,8)=2;
```



```
        SUBINDEX_$BLMLC(L,I,6,10)=2;
        SUBINDEX_$BLMLC(L,I,6,11)=2;
        SUBINDEX_$BLMLC(L,I,6,12)=2;
        SUBINDEX_$BLMLC(L,I,6,14)=2;
        SUBINDEX_$BLMLC(L,I,7,3)=2;
        SUBINDEX_$BLMLC(L,I,7,7)=2;
        SUBINDEX_$BLMLC(L,I,7,11)=2;
    ]
];

"Now set driving screw hole to air - Not right at moment change later"
   DO J=3,3 [
      SUBINDEX_$BLMLC(L,2,J,6)=2;
      SUBINDEX_$BLMLC(L,5,J,6)=2;
     ]
]
  "   ========================
"
RETURN;

"XVIII. ERROR MESSAGES
"==================
"
:EOF_$BLMLC:
;OUTPUT ICM;
  (//' *** ERROR *** unexpected end of file reading input for CM',I3);
STOP;

:ERROR_$BLMLC:
;OUTPUT ICM;(//' *** ERROR *** format error on input for CM',I3);
STOP;
END;  "End of INPUT_$BLMLC"

%E "Start of subroutine ISUMRY_$BLMLC (Rev 1.4)"
"*********************************************************************
"
"                          Subroutine ISUMRY_$BLMLC
"                          ************************
"
" Summarize input, write graphics file for EGS_Windows, and set parameters
" that require medium information obtained from HATCH call.
"
"*********************************************************************

;SUBROUTINE ISUMRY_$BLMLC;

;IMPLICIT NONE;
;COMIN/ BOUNDS,CMs,CM_$BLMLC,GEOM,IO_INFO,MEDIA,MISC,SCORE,UPHIOT,USER/;
"T>
"T>*********************************
"T>TYPE DECLARATIONS FOR ISUMRY_$BLMLC
"T>*********************************
"T>
INTEGER
   ICOLOUR, "T>colour of CM for EGS_Windows
"   ID,     already defined gf  T>index of dose scoring zone
   IRA,     "T>absolute region number
```



```
   I,J,     "T>DO loop index
   ISTART,IEND; "T>indices for outputting info"

$REAL  VOL_$BLMLC(3), "T> region volumes
       YY1(9),          "T> YY1 and YY2 index subregion along perpendicular..
       YY2(9),          "T> direction to MLC orientation
       YY3(9),          "T> specific for target leaf
       YY4(9),          "T>
       YY5(9),          "T> same for full leaf
       YY6(9),          "T>
       YY7(9),          "T> same for isocenter leaf
       YY8(9),         "T>
       Zo,             "T> THe z-coordinate of the leaf center
       XoP,XoN,        "T> The center of the rounded leaves ends along leaf
       M1,M2,          "T> Variables related to partial(rounded) leaf volume
       THETASUB,       "T> Angle at leaf end subtended by Z boundaries of reg.
       TOTALVOL,       "T> Total volume of MLC CM
       ZSQUARE,ZCUBE,AREA,    "T> Variables related to partial leaf volumes
       TEMP,TEMP1,TEMP2,TEMP3,"T> Variables related to partial leaf volumes
       HOLD;            "T> to hold a TEMP value


RETURN;
END;

%E "Start of subroutine HOWNEAR_$BLMLC (Rev 1.4)"
"*********************************************************************"
"                                                                     "
"                          Subroutine HOWNEAR_$BLMLC              "
"                          ****************************               "
"                                                                     "
" Calculates min. distance to nearest region boundary                  "
" Used to be HOWNEAR macro, but is now called from that macro.         "
"                                                                     "
"*********************************************************************"
" Rewritten for BLMLC module"
"============================"
"First of all assume single leaf"
;SUBROUTINE HOWNEAR_$BLMLC(DIST_sngl);
;
$IMPLICIT-NONE;

COMIN/CMs,CM_$BLMLC,STACK,IO_INFO,EGS-IO/;

$REAL   DIST_sngl; "T> min. distance to nearest region boundary"
DOUBLE PRECISION   XYL1,XYL2, "T> X(NP) and Y(NP)"
                   XoN, XoP, DIST,
                   UVL1,UVL2,
          Z_LEAF_BOTTOM,
          Z_LEAF_TOP,
                   TEMP1,TEMP2,TEMP3,TEMP4,
                   TEMP5,TEMP6,HOLE, "T> temp. distance variables"
                   XL,XR,Lo,Ro,Zo;          "T>temp distance variables"
$INTEGER I,J,K, "T> looping index"
        NZ, "T> index of subregion in Z direction"
        NY, "T> index of subregion perpendicular to leaf opening direction"
        NX, "T> index of subregion in direction of leaf opening"
```

```
        LEAFIS, "T> leaf no. where particle is located"
     LEAF_TOP,
     LEAF_MIDDLE,
     LEAF_BOTTOM, "BOTTOM Z INDICES OF REGIONS OF LEAF FOR CALCULATING X REGION"
     LEAF_STRT, "INDEX OF START OF LEAF GROOVE"
     LAST_LEAF,
     LEFT_BORD, RIGHT_BORD,
         I1,I2; "T> used to mark min. max. Z boundaries for calculating dist"

    LEAF_TOP=6;
    LEAF_MIDDLE=10;
    LEAF_BOTTOM=15;
    LEAF_STRT=6;
    LAST_LEAF=26;

IR_$BLMLC=IR(NP)-IRSTART_$BLMLC+1;
IF(IR_$BLMLC=4) [ "in the air gap at the top"
  DIST=MIN(Z(NP)-ZFRONT_$BLMLC,ZMIN_$BLMLC-Z(NP));
  ]
ELSE[
    IF(ORIENT_$BLMLC=1) [
        XYL1=Y(NP);XYL2=X(NP);UVL1=V(NP);UVL2=U(NP);
        ]
    ELSE [
        XYL1=X(NP);XYL2=Y(NP);UVL1=U(NP);UVL2=V(NP);
        ];
    IF(IGNOREGAPS_$BLMLC=1 & XYL2 < MIN_PLANE_$BLMLC &
    XYL1 > SURPARA1_$BLMLC(1,1)*(Z(NP)-ZFOCUS_$BLMLC(1)) &
    XYL1 < SURPARA1_$BLMLC(TOT_LEAF_$BLMLC,8)*(Z(NP)-ZFOCUS_$BLMLC(1)) &
    IR_$BLMLC=2)[
        "particle within negative leaves, ignore air gaps for range rejection"
        "distance to most -ve leaf side...note this is to the tip of the tongue"
        TEMP1=SURPARA1_$BLMLC(1,1);
        TEMP1=ABS((TEMP1*(Z(NP)-ZFOCUS_$BLMLC(1))-XYL1)/SQRT(1+TEMP1**2));
        "distance to most +ve leaf side...note this is to the back of the last"
        "leaf...ie not to the groove"
        TEMP2=SURPARA1_$BLMLC(TOT_LEAF_$BLMLC,8);
        TEMP2=ABS((TEMP2*(Z(NP)-ZFOCUS_$BLMLC(1))-XYL1)/SQRT(1+TEMP2**2));
        DIST=MIN(Z(NP)-ZMIN_$BLMLC,ZMIN_$BLMLC+ZTHICK_$BLMLC-Z(NP),
            MIN_PLANE_$BLMLC-XYL2,TEMP1,TEMP2);
            ]
    ELSEIF(IGNOREGAPS_$BLMLC=1 & XYL2 > MAX_PLANE_$BLMLC &
    XYL1 > SURPARA1_$BLMLC(1,1)*(Z(NP)-ZFOCUS_$BLMLC(1)) &
    XYL1 < SURPARA1_$BLMLC(TOT_LEAF_$BLMLC,8)*(Z(NP)-ZFOCUS_$BLMLC(1)) &
    IR_$BLMLC=2)[
        "particle within positive leaves, ignore air gaps for range rejection"
        "distance to most -ve leaf side...note this is to the tip of the tongue"
        TEMP1=SURPARA1_$BLMLC(1,1);
        TEMP1=ABS((TEMP1*(Z(NP)-ZFOCUS_$BLMLC(1))-XYL1)/SQRT(1+TEMP1**2));

        "distance to most +ve leaf side...note this is to the back of the last"
        "leaf...ie not just to the groove"
        TEMP2=SURPARA1_$BLMLC(TOT_LEAF_$BLMLC,8);
        TEMP2=ABS((TEMP2*(Z(NP)-ZFOCUS_$BLMLC(1))-XYL1)/SQRT(1+TEMP2**2));

        DIST=MIN(Z(NP)-ZMIN_$BLMLC,ZMIN_$BLMLC+ZTHICK_$BLMLC-Z(NP),
        XYL2-MAX_PLANE_$BLMLC,TEMP1,TEMP2);
```



```
    ]
    ELSE["do not ignore air gaps for range rejection"
        LEAFIS=0; "Determine which leaf we are in, I is index of leaf number"
"in order to find out if we are in a gap (leafis=0)"
" we must find out z first and then y pos"
        IF(Z(NP)<ZREG_$BLMLC(1,1))[
                NZ=1;
        ]
        ELSEIF(Z(NP)>ZREG_$BLMLC(1,16))[
            NZ=15;
        ]
        ELSE[
                DO J = 1,15 [ "Determine which Z region we are in for leaf I"
                IF((ZREG_$BLMLC(1,J)<=Z(NP))&(Z(NP)<=ZREG_$BLMLC(1,J+1)))[
                        NZ=J;
                EXIT;
                ];
                ];
        ]
" Find out which leaf we are in"

        LEFT_BORD=1;
        RIGHT_BORD=8;
        LEAFIS=0;
        NY=0;
        DO I=1,26 [
            TEMP1=SURPARA1_$BLMLC(I,LEFT_BORD)*(Z(NP)-ZFOCUS_$BLMLC(1));
            TEMP2=SURPARA1_$BLMLC(I,RIGHT_BORD)*(Z(NP)-ZFOCUS_$BLMLC(1));
            IF ((XYL1 >= TEMP1) & (XYL1 <TEMP2))[
                LEAFIS=I;
                EXIT;
            ]
        ]


        IF (LEAFIS > 0) [
"Now we know which leaf we are in (leafis) determine ny
            DO I=1,7 [
                TEMP1=SURPARA1_$BLMLC(LEAFIS,I)*(Z(NP)-ZFOCUS_$BLMLC(1));
                TEMP2=SURPARA1_$BLMLC(LEAFIS,I+1)*(Z(NP)-ZFOCUS_$BLMLC(1));
                IF (TEMP1<=XYL1 & XYL1 <TEMP2)[
                    NY=I;
                    EXIT;
                ]
            ]
    "So we know NY but are we on the next leaf along?
            IF ((NY = 6) & (LEAFIS < 26)) [
                IF (LEAFTYPE_$BLMLC(LEAFIS)=1) [
                    IF ((NZ=3)|(NZ=7)|(NZ=11)) [
                        IF (XYL1 > (SURPARA1_$BLMLC(LEAFIS+1,1)*(Z(NP)-ZFOCUS_$BLMLC(1)))) [
                            LEAFIS=LEAFIS+1;
                            NY=1; "we can't be further over than ny=1
                        ]
                        ELSE [
                            LEAFIS=0; "but we might be in gap between leaves"
                        ]
                    ]
```



```
                ]
                ELSE [
                    IF ((NZ=5)|(NZ=9)|(NZ=13)) [
                        IF (XYL1 > (SURPARA1_$BLMLC(LEAFIS+1,1)*(Z(NP)-ZFOCUS_$BLMLC(1))))  [
                            LEAFIS=LEAFIS+1;
                            NY=1;
                        ]
                        ELSE [
                            LEAFIS=0; "in gap between leaves"
                        ]
                    ]
                ]
            ]
            ELSEIF ((NY =7) & (LEAFIS <26)) [
                IF (LEAFTYPE_$BLMLC(LEAFIS)=1) [
                    IF ((NZ~=5) & (NZ~=9) & (NZ~=13)) [
                        IF (XYL1 > (SURPARA1_$BLMLC(LEAFIS+1,2)*(Z(NP)-ZFOCUS_$BLMLC(1))))  [
                            LEAFIS=LEAFIS+1; "but we could be in 1 or 2 now
                            DO I=1,7 [
                                TEMP1=SURPARA1_$BLMLC(LEAFIS,I)*(Z(NP)-ZFOCUS_$BLMLC(1));
                                TEMP2=SURPARA1_$BLMLC(LEAFIS,I+1)*(Z(NP)-ZFOCUS_$BLMLC(1));
                                IF (XYL1 >= TEMP1 & XYL1 <TEMP2)[
                                    NY=I;
                                    EXIT;
                                ]
                            ]
                        ]
                        ELSE [
                            LEAFIS=0; "in gap between leaves"
                        ]
                    ]
                ]
                ELSE [
                    IF ((NZ~=3) & (NZ~=7) & (NZ~=11)) [
                        IF (XYL1 > (SURPARA1_$BLMLC(LEAFIS+1,2)*(Z(NP)-ZFOCUS_$BLMLC(1))))  [
                            LEAFIS=LEAFIS+1;
                            DO I=1,7 [
                                TEMP1=SURPARA1_$BLMLC(LEAFIS,I)*(Z(NP)-ZFOCUS_$BLMLC(1));
                                TEMP2=SURPARA1_$BLMLC(LEAFIS,I+1)*(Z(NP)-ZFOCUS_$BLMLC(1));
                                IF (TEMP1<=XYL1 & XYL1 <TEMP2)[
                                    NY=I;
                                    EXIT;
                                ]
                            ]
                        ]
                        ELSE [
                            LEAFIS=0; "in gap between leaves"
                        ]
                    ]
                ]
            ]
        ]
"BELOW IS END OF ELSE DO NOT IGNORE AIR GAPS FOR RANGE REJECTION"
    "]"

"       IF (LEAFIS =0) [
"           OUTPUT NZ,NY,XYL1; ('NZ :',I3,' NY :',I3,' XYL1 :',F10.7);
```



```
"       ]

        IF(LEAFIS~=0) [

"Determine which X region we are in - first calculate leaf pos at zmid"
            TEMP1=SURPARA2_B_$BLMLC(LEAFIS)*(ZMIN_$BLMLC+(ZTHICK_$BLMLC/2));
            TEMP2=SURPARA2_A_$BLMLC(LEAFIS)*(ZMIN_$BLMLC+(ZTHICK_$BLMLC/2));
            HOLE=HOLEPOS_$BLMLC(LEAFIS);
"               TEMP3=LEAFB_$BLMLC(LEAFIS)+HOLE;
"           TEMP4=LEAFA_$BLMLC(LEAFIS)-HOLE;
            TEMP3=TEMP1-HOLE;
            TEMP4=TEMP2-HOLE;
"By now we know which z region we are in so use this to calculate"
"which X region we are in. Also calculate XL and XR for dist calc"
            IF ((NZ>=1) & (NZ<=LEAF_TOP)) ["In top region of leaf"
                Z_LEAF_TOP=ZREG_$BLMLC(LEAFIS,LEAF_TOP);
                TEMP1=TEMP1-((Z_LEAF_TOP-Z(NP))/TAN(THETA_TOP_$BLMLC));
                TEMP2=TEMP2+((Z_LEAF_TOP-Z(NP))/TAN(THETA_TOP_$BLMLC));
                IF ((XYL2>TEMP1 & XYL2<TEMP2) | (XYL2=TEMP1 & UVL2>=0.0) |
                (XYL2=TEMP2 & UVL2<0.0)) [
                    NX=1;
                    XL=ABS(XYL2-TEMP1);
                    XR=ABS(TEMP2-XYL2);
                ]
                ELSEIF ((XYL2<TEMP1 & XYL2>TEMP3) | (XYL2=TEMP1 & UVL2>=0.0) |
                (XYL2=TEMP3 & UVL2>=0.0)) [
                    NX=3;
                    XL=ABS(XYL2-TEMP3);
                    XR=ABS(TEMP1-XYL2);
                ]
                ELSEIF ((XYL2<TEMP3) | (XYL2=TEMP3 & UVL2<0.0))[
                    NX=2;
                    XL=ABS(RMAX_CM(ICM_$BLMLC)-XYL2);
                    XR=ABS(TEMP3-XYL2);
                ]
                ELSEIF((XYL2>TEMP2 & XYL2<TEMP4) | (XYL2=TEMP2 & UVL2>=0.0) |
                (XYL2=TEMP4 & UVL2<0.0)) [
                    NX=4;
                    XL=ABS(XYL2-TEMP2);
                    XR=ABS(TEMP4-XYL2);
                    ]
                ELSEIF((XYL2>TEMP4) | (XYL2=TEMP4 & UVL2>=0.0)) [
                    NX=5;
                    XL=ABS(XYL2-TEMP4);
                    XR=ABS(RMAX_CM(ICM_$BLMLC)-XYL2);
                ]
            ]
            ELSEIF ((NZ>LEAF_TOP) & (NZ<=LEAF_MIDDLE)) [" In middle region of leaf"
                IF ((XYL2>TEMP1 & XYL2<TEMP2) | (XYL2=TEMP1 & UVL2>=0.0) |
                (XYL2=TEMP2 & UVL2<0.0)) [
                    NX=1;
                    XL=ABS(TEMP1-XYL2);
                    XR=ABS(TEMP2-XYL2);
                ]
                ELSEIF ((XYL2<TEMP1 & XYL2>TEMP3) | (XYL2=TEMP1 & UVL2>=0.0) |
                (XYL2=TEMP3 & UVL2>=0.0)) [
                    NX=3;
```

```
                    XL=ABS(TEMP3-XYL2);
                    XR=ABS(XYL2-TEMP1);
                ]
                ELSEIF ((XYL2<TEMP3) | (XYL2=TEMP3 & UVL2<0.0)) [
                    NX=2;
                    XL=ABS(RMAX_CM(ICM_$BLMLC)-XYL2);
                    XR=ABS(XYL2-TEMP3);
                ]
                ELSEIF((XYL2>TEMP2 & XYL2<TEMP4) | (XYL2=TEMP2 & UVL2>=0.0) |
                (XYL2=TEMP4 & UVL2<0.0)) [
                    NX=4;
                    XL=ABS(XYL2-TEMP2);
                    XR=ABS(TEMP4-XYL2);
                ]
                ELSEIF((XYL2>TEMP4) | (XYL2=TEMP4 & UVL2>=0.0)) [
                    NX=5;
                    XL=ABS(XYL2-TEMP4);
                    XR=ABS(RMAX_CM(ICM_$BLMLC)-XYL2);
                ]
            ]
            ELSEIF ((NZ>LEAF_MIDDLE)&(NZ<=LEAF_BOTTOM)) ["In bottom region of leaf"
            Z_LEAF_BOTTOM=ZREG_$BLMLC(LEAFIS,LEAF_MIDDLE);
                TEMP1=TEMP1-((Z(NP)-Z_LEAF_BOTTOM)/TAN(THETA_BOTTOM_$BLMLC));
                TEMP2=TEMP2+((Z(NP)-Z_LEAF_BOTTOM)/TAN(THETA_BOTTOM_$BLMLC));
                    IF ((XYL2>TEMP1 & XYL2<TEMP2) | (XYL2=TEMP1 & UVL2>=0.0) |
                    (XYL2=TEMP2 & UVL2<0.0)) [
                        NX=1;
                        XL=ABS(TEMP1-XYL2);
                        XR=ABS(TEMP2-XYL2);
                    ]
                    ELSEIF ((XYL2<TEMP1 & XYL2>TEMP3) | (XYL2=TEMP1 & UVL2>=0.0) |
                    (XYL2=TEMP3 & UVL2>=0.0)) [
                        NX=3;
                        XL=ABS(TEMP3-XYL2);
                        XR=ABS(XYL2-TEMP1);
                    ]
                    ELSEIF ((XYL2<TEMP3) | (XYL2=TEMP3 & UVL2<0.0)) [
                        NX=2;
                        XL=ABS(RMAX_CM(ICM_$BLMLC)-XYL2);
                        XR=ABS(XYL2-TEMP3);
                    ]
                    ELSEIF((XYL2>TEMP2 & XYL2<TEMP4) | (XYL2=TEMP2 & UVL2>=0.0) |
                    (XYL2=TEMP4 & UVL2<0.0)) [
                        NX=4;
                        XL=ABS(XYL2-TEMP2);
                        XR=ABS(TEMP4-XYL2);
                    ]
                    ELSEIF((XYL2>TEMP4) | (XYL2=TEMP4 & UVL2>=0.0)) [
                        NX=5;
                        XL=ABS(XYL2-TEMP4);
                        XR=ABS(RMAX_CM(ICM_$BLMLC)-XYL2);
                    ]
            ]
            ELSE ["We shouldn't get here"
                NX=1;
                XL=ABS(TEMP1-XYL2);
                XR=ABS(TEMP2-XYL2);
```



```
                OUTPUT NZ;(/'PROBLEM DETERMINING X REGION - NZ:',I5);
            ]

        "Calculates distance to closest boundary in Y and z direction"
            IF(LEAFTYPE_$BLMLC(LEAFIS)=1)[
                IF (NY=1|NY=7) [
                    IF (NZ < 5) [
                        I1=1;
                        I2=5;
                    ]
                    ELSEIF (NZ=5) [
                        I1=5;
                        I2=6;
                    ]
                    ELSEIF (NZ > 5 & NZ < 9) [
                        I1=6;
                        I2=9;
                    ]
                    ELSEIF (NZ =9) [
                        I1=9;
                        I2=10;
                    ]
                    ELSEIF (NZ > 9 & NZ <13) [
                        I1=10;
                        I2=13;
                    ]
                    ELSEIF (NZ=13) [
                        I1=13;
                        I2=14;
                    ]
                    ELSE[
                        I1=14;
                        I2=16;
                    ]
                ]
                ELSEIF (NY=2|NY=6) [
                    IF (NZ=1) [
                        I1=1;
                        I2=2;
                    ]
                    ELSEIF (NZ=2) [
                        I1=2;
                        I2=3;
                    ]
                    ELSEIF (NZ=3) [
                        I1=3;
                        I2=4;
                    ]
                    ELSEIF (NZ=4|NZ=5|NZ=6) [
                        I1=4;
                        I2=7;
                    ]
                    ELSEIF (NZ=7) [
                        I1=7;
                        I2=8;
                    ]
                    ELSEIF (NZ=8|NZ=9|NZ=10) [
```



```
                        I1=8;
                        I2=11;
                    ]
                    ELSEIF (NZ=11) [
                        I1=11;
                        I2=12;
                    ]
                    ELSEIF (NZ=12|NZ=13|NZ=14)[
                        I1=12;
                        I2=15;
                    ]
                    ELSE [
                        I1=15;
                        I2=16;
                    ]
                ]
                ELSEIF (NY=3|NY=5) [
                    IF (NZ=1) [
                        I1=1;
                        I2=2;
                    ]
                    ELSEIF (NZ=15) [
                        I1=15;
                        I2=16;
                    ]
                    ELSE [
                        I1=2;
                        I2=15;
                    ]
                ]
                ELSE [
                    I1=1;
                    I2=16;
                ]
                DIST=MIN(ABS(ZREG_$BLMLC(LEAFIS,I1)-Z(NP)),ABS(ZREG_$BLMLC(LEAFIS,I2)-Z(NP)));
"now for y distance"
                IF (NZ=1|NZ=15) [
                    IF (NY=4) [
                        I1=4;
                        I2=5;
                    ]
                    ELSEIF (NY < 4) [
                        I1=1;
                        I2=4;
                    ]
                    ELSE [
                        I1=5;
                        I2=8;
                    ]
                ]
                ELSEIF (NZ=2|NZ=4|NZ=6|NZ=8|NZ=10|NZ=12|NZ=14) [
                    IF (NY=1) [
                        I1=1;
                        I2=2;
                    ]
                    ELSEIF (NY = 7) [
                        I1=7;
```



```
                        I2=8;
                    ]
                    ELSE [
                        I1=2;
                        I2=7;
                    ]
                ]
                ELSEIF (NZ=3|NZ=7|NZ=11) [
                    IF (NY<3) [
                        I1=1;
                        I2=3;
                    ]
                    ELSEIF (NY=3|NY=4|NY=5) [
                        I1=3;
                        I2=6;
                    ]
                    ELSEIF (NY>5) [
                        I1=6;
                        I2=8;
                    ]
                ]
                ELSEIF (NZ=5|NZ=9|NZ=13) [
                    I1=1;
                    I2=8;
                ]

            TEMP1=SURPARA1_$BLMLC(LEAFIS,I1);
            TEMP2=SURPARA1_$BLMLC(LEAFIS,I2);
            ]
            ELSEIF (LEAFTYPE_$BLMLC(LEAFIS)=2)[
                IF (NY=1|NY=7) [
                    IF (NZ < 3) [
                        I1=1;
                        I2=3;
                    ]
                    ELSEIF (NZ=3) [
                        I1=3;
                        I2=4;
                    ]
                    ELSEIF (NZ > 3 & NZ < 7) [
                        I1=4;
                        I2=7;
                    ]
                    ELSEIF (NZ = 7) [
                        I1=7;
                        I2=8;
                    ]
                    ELSEIF (NZ > 7 & NZ < 11) [
                        I1=8;
                        I2=11;
                    ]
                    ELSEIF (NZ=11) [
                        I1=11;
                        I2=12;
                    ]
                    ELSE[
                        I1=12;
```

```
                        I2=16;
                    ]
                ]
                ELSEIF (NY=2|NY=6) [
                    IF (NZ=1) [
                        I1=1;
                        I2=2;
                    ]
                    ELSEIF (NZ=2|NZ=3|NZ=4) [
                        I1=2;
                        I2=5;
                    ]
                    ELSEIF (NZ=5) [
                        I1=5;
                        I2=6;
                    ]
                    ELSEIF (NZ=6|NZ=7|NZ=8) [
                        I1=6;
                        I2=9;
                    ]
                    ELSEIF (NZ=9) [
                        I1=9;
                        I2=10;
                    ]
                    ELSEIF (NZ=10|NZ=11|NZ=12) [
                        I1=10;
                        I2=13;
                    ]
                    ELSEIF (NZ=13) [
                        I1=13;
                        I2=14;
                    ]
                    ELSEIF (NZ=14)[
                        I1=14;
                        I2=15;
                    ]
                    ELSE [
                        I1=15;
                        I2=16;
                    ]
                ]
                ELSEIF (NY=3|NY=5) [
                    IF (NZ=1) [
                        I1=1;
                        I2=2;
                    ]
                    ELSEIF (NZ=15) [
                        I1=15;
                        I2=16;
                    ]
                    ELSE [
                        I1=2;
                        I2=15;
                    ]
                ]
                ELSE [
                    I1=1;
```



```
                    I2=16;
                ]
                DIST=MIN(ABS(ZREG_$BLMLC(LEAFIS,I1)-Z(NP)),ABS(ZREG_$BLMLC(LEAFIS,I2)-Z(NP)));
"now for y distance"



                TEMP1=SURPARA1_$BLMLC(LEAFIS,LEFT_BORD);
                TEMP2=SURPARA1_$BLMLC(LEAFIS,RIGHT_BORD);
            ]
            ELSE [
                OUTPUT LEAFTYPE_$BLMLC(LEAFIS),LEAFIS; (/'y PROB', I5, ' IN LEAF :',I5);
                TEMP1=SURPARA1_$BLMLC(LEAFIS,1);
                TEMP2=SURPARA1_$BLMLC(LEAFIS,8);
            ]
            TEMP1=ABS((TEMP1*(Z(NP)-ZFOCUS_$BLMLC(1))-XYL1)/
            SQRT(1+TEMP1**2));
            TEMP2=ABS((TEMP2*(Z(NP)-ZFOCUS_$BLMLC(1))-XYL1)/
            SQRT(1+TEMP2**2));

            DIST = MIN(DIST,TEMP1,TEMP2);

"NOW CHECK DISTANCE IN X DIRECTION"
"XL AND XR NOW CALCULATED ABOVE BUT LINES FROM DYNVMLC_CM WILL HAVE TO BE"
"REINSTATED IF ROUNDED LEAVES ARE EVER USED"
"So we now only need this line here now"

            DIST=MIN(DIST,XL,XR);
            IF(DIST<0) [
                OUTPUT LEAFIS,NX,NY,NZ; (/'negative dist: ',4I3);
            ]
            IF (PLT_$BLMLC = 1) [
                WRITE(73,251) XYL2,XYL1,Z(NP),LEAFIS,NX,NY,NZ,
                SUBINDEX_$BLMLC(LEAFIS,NX,NY,NZ);
            ]
]
ELSE[ "beyond outer edges of leaf bank"
"       IF (PLT_$BLMLC = 1) [
"           OUTPUT; ('BY HERE');
"           WRITE(73,252) XYL2,XYL1,Z(NP),LEAFIS,NX,NY,NZ,
"              'X';
"       ]

  IF(XYL1 <= SURPARA1_$BLMLC(1,1)*(Z(NP)-ZFOCUS_$BLMLC(1)))[
      TEMP1=SURPARA1_$BLMLC(1,1);
      TEMP1=ABS((TEMP1*(Z(NP)-ZFOCUS_$BLMLC(1))-XYL1)/
               SQRT(1+TEMP1**2));
    ]
  ELSEIF(XYL1 >= SURPARA1_$BLMLC(TOT_LEAF_$BLMLC,6)*
                   (Z(NP)-ZFOCUS_$BLMLC(1)))[
      TEMP1=SURPARA1_$BLMLC(TOT_LEAF_$BLMLC,8);
      TEMP1=ABS((TEMP1*(Z(NP)-ZFOCUS_$BLMLC(1))-XYL1)/
               SQRT(1+TEMP1**2));
    ]
  DIST=MIN(Z(NP)-ZMIN_$BLMLC,ZMAX_$BLMLC-Z(NP),TEMP1);
 ]
 ]
 ];
```



```
DIST_sngl=SNGL(DIST);
RETURN;
251 FORMAT(F8.3,',',F8.3,',',F8.3,',',I3,',',I3,',',I3,',',I3,',',I3);
252 FORMAT(F8.3,',',F8.3,',',F8.3,',',I3,',',I3,',',I3,',',I3,',',A1);

END; "End of subroutine HOWNEAR_$BLMLC(Rev 1.4)"
"***************************************************************************"

SUBROUTINE MINDISTANCE_$BLMLC(MINDISTANCE,LEAFIS,NX,NY,NZ,ZFL,XYFL,UVL);


;IMPLICIT NONE;
;COMIN/CMs,CM_$BLMLC,EPCONT,STACK,IO_INFO,EGS-IO/;
"T>
"T>**********************************
"T>TYPE DECLARATIONS FOR HOWFAR_$BLMLC
"T>**********************************
"T>
INTEGER
   COUNT,
   IRL,         "T>local region number (absolute), required by HOWNEAR macro
   I, J,         "T>loop control
   REGION_$BLMLC,     "T>region number within CM (relative)
   NEWREGION_$BLMLC,      "T>region number within CM (relative)
   NX,NY,NZ,         "T> Subindices for region
   OUTOFCMFLAG,      "T> Flag to denote particle out of CM
   OUTOFMLCFLAG,     "T> Flag to denote particle out of MLC
   LEAFIS,           "T> Leaf number
   LHS,RHS,      "T> Macro variables to find + and - closest boundary index
   ZLHS,ZRHS,
   YLHS,YRHS,LEAF_CHWITH,LEAF_DE, "for leaf boundary indicees
   IDIR,         "T> direction sign, used in call to where_am_i
   XREG_MIN, XREG_MAX,
   YREG_MIN, YREG_MAX,
   ZREG_MIN, ZREG_MAX,  "Indicees of end boundary regions"
   YREG_STRT,
   LEAF_TOP, LEAF_MIDDLE, LEAF_BOTTOM;



DOUBLE PRECISION
   DIST,       "T>Distance to z boundary along current particle trajectory
   UVL(2),     "T>temporary variable
   TRYY1,TRYY2,
   XoN,XoP,     "T> Negative and Positive leaf centers (rounded leaf)
   Zo,          "T> z position of rounded leaf tip
   XP,XN,YP,YN,ZP,ZN,     "T>+ and - distances in x,y, z directions
   XDIST,YDIST,ZDIST,     "T> x,y, Z distances to nearest boundaries
   DIST1,DIST2,DIST3,     "T> Variables to control particle propagation
   STEP2,                 "T>  "
   TLHS,TRHS,             "T> temporary macro variables like lhs,rhs
   DISCRIMINANT,          "T> Variable for rounded leaf
   TEMP,TEMP1, TEMP2, TEMP3, TEMP4, TEMP5, HOLE,
   STEP_UNIT,
   XYL(2),      "T> rearranged x and y coordinates
   XYFL(2),
   Z_LEAF_BOTTOM,
   Z_LEAF_TOP,
```



```
   XL, XR,
   ZFL,
   MINDISTANCE;

    LEAF_TOP=6;
    LEAF_MIDDLE=10;
    LEAF_BOTTOM=15;

    IF (LEAFIS > 0) [
        IF (LEAFTYPE_$BLMLC(LEAFIS)=1) [
            IF (NY=1) [
                IF ((NZ>=1) & (NZ<5))[
                    ZLHS=1;
                    ZRHS=5;
                ]
                ELSEIF ((NZ>=6) & (NZ<9)) [
                    ZLHS=6;
                    ZRHS=9;
                ]
                ELSEIF ((NZ>=10) & (NZ<13)) [
                    ZLHS=10;
                    ZRHS=13;
                ]
                ELSEIF (NZ>=14) [
                    ZLHS=14;
                    ZRHS=16;
                ]
                ELSE[
                    ZLHS=NZ;
                    ZRHS=NZ+1;
                ]
            ]
            ELSEIF (NY=2) [
                IF ((NZ>=4) & (NZ<7))[
                    ZLHS=1;
                    ZRHS=5;
                ]
                ELSEIF ((NZ >=4) & (NZ<=6)) [
                    ZLHS=4;
                    ZRHS=7;
                ]
                ELSEIF ((NZ>=8) & (NZ<=10))[
                    ZLHS=8;
                    ZRHS=11;
                ]
                ELSEIF ((NZ>=12) & (NZ<=14))[
                    ZLHS=12;
                    ZRHS=15;
                ]
                ELSE [
                    ZLHS=NZ;
                    ZRHS=NZ+1;
                ]
            ]
            ELSEIF (NY=3) [
                IF ((NZ=1)|(NZ=15))[
                    ZLHS=NZ;
```

```
                ZRHS=NZ+1;
            ]
            ELSE[
                ZLHS=2;
                ZRHS=15;
            ]
        ]
        ELSEIF (NY=4)[
            ZLHS=1;
            ZRHS=16;
        ]
        ELSEIF (NY=7) [
            IF ((NZ>=1) & (NZ<5))[
                ZLHS=1;
                ZRHS=5;
            ]
            ELSEIF ((NZ>=6) & (NZ<9)) [
                ZLHS=6;
                ZRHS=9;
            ]
            ELSEIF ((NZ>=10) & (NZ<13)) [
                ZLHS=10;
                ZRHS=13;
            ]
            ELSEIF (NZ>=14) [
                ZLHS=14;
                ZRHS=16;
            ]
            ELSE[
                ZLHS=NZ;
                ZRHS=NZ+1;
            ]
        ]
        ELSEIF (NY=6) [
            IF ((NZ >=4) & (NZ<=6)) [
                ZLHS=4;
                ZRHS=7;
            ]
            ELSEIF ((NZ>=8) & (NZ<=10))[
                ZLHS=8;
                ZRHS=11;
            ]
            ELSEIF ((NZ>=12) & (NZ<=14))[
                ZLHS=12;
                ZRHS=15;
            ]
            ELSE [
                ZLHS=NZ;
                ZRHS=NZ+1;
            ]
        ]
        ELSEIF (NY=5) [
            IF ((NZ=1)|(NZ=15))[
                ZLHS=NZ;
                ZRHS=NZ+1;
            ]
            ELSE[
```



```
                ZLHS=2;
                ZRHS=15;
            ]
        ]
"Now find y boundaries etc"
        IF (NY=1) [
            IF((NZ=1)|(NZ=15))[
                IF (LEAFIS=1)[
                    YLHS=1;
                    LEAF_CHWITH=LEAFIS;
                ]
                ELSE [
                    YLHS=8;
                    LEAF_CHWITH=LEAFIS-1;
                ]
                YRHS=4;
                LEAF_DE=LEAFIS;
            ]
            ELSEIF ((NZ=2)|(NZ=4)|(NZ=6)|(NZ=8)|(NZ=10)|(NZ=12)|(NZ=14))[
                IF (LEAFIS=1)[
                    YLHS=1;
                    LEAF_CHWITH=LEAFIS;
                ]
                ELSE [
                    YLHS=8;
                    LEAF_CHWITH=LEAFIS-1;
                ]
                YRHS=2;
                LEAF_DE=LEAFIS;
            ]
            ELSEIF ((NZ=3)|(NZ=7)|(NZ=11))[
                IF (LEAFIS=1)[
                    YLHS=1;
                    LEAF_CHWITH=LEAFIS;
                ]
                ELSE [
                    YLHS=8;
                    LEAF_CHWITH=LEAFIS-1;
                ]
                YRHS=3;
                LEAF_DE=LEAFIS;
            ]
            ELSEIF((NZ=5)|(NZ=9)|(NZ=13))[
                IF (LEAFIS=1)[
                    YLHS=1;
                    LEAF_CHWITH=LEAFIS;
                ]
                ELSE [
                    YLHS=8;
                    LEAF_CHWITH=LEAFIS-1;
                ]
                YRHS=8;
                LEAF_DE=LEAFIS;
            ]
        ]
        ELSEIF (NY=2)[
            IF ((NZ=1)|NZ=15)[
```



```
                IF (LEAFIS=1)[
                    YLHS=1;
                    LEAF_CHWITH=LEAFIS;
                ]
                ELSE [
                    YLHS=8;
                    LEAF_CHWITH=LEAFIS-1;
                ]
                YRHS=4;
                LEAF_DE=LEAFIS;
            ]
            ELSEIF ((NZ=2)|(NZ=4)|(NZ=6)|(NZ=8)|(NZ=10)|(NZ=12)|(NZ=14))[
                LEAF_CHWITH=LEAFIS;
                YLHS=2;
                YRHS=7;
                LEAF_DE=LEAFIS;
            ]
            ELSEIF ((NZ=3)|(NZ=7)|(NZ=11))[
                IF (LEAFIS=1)[
                    YLHS=1;
                    LEAF_CHWITH=LEAFIS;
                ]
                ELSE [
                    YLHS=8;
                    LEAF_CHWITH=LEAFIS-1;
                ]
                YRHS=3;
                LEAF_DE=LEAFIS;
            ]
            ELSEIF((NZ=5)|(NZ=9)|(NZ=13))[
                IF (LEAFIS=1)[
                    YLHS=1;
                    LEAF_CHWITH=LEAFIS;
                ]
                ELSE [
                    YLHS=8;
                    LEAF_CHWITH=LEAFIS-1;
                ]
                IF (LEAFIS=26)[
                    YRHS=8;
                    LEAF_DE=LEAFIS;
                ]
                ELSE [
                    YRHS=1;
                    LEAF_DE=LEAFIS+1;
                ]
            ]
        ]
        ELSEIF (NY=3)[
            IF ((NZ=1)|NZ=15)[
                IF (LEAFIS=1)[
                    YLHS=1;
                    LEAF_CHWITH=LEAFIS;
                ]
                ELSE [
                    YLHS=8;
                    LEAF_CHWITH=LEAFIS-1;
```



```
                ]
                YRHS=4;
                LEAF_DE=LEAFIS;
            ]
            ELSEIF ((NZ=2)|(NZ=4)|(NZ=6)|(NZ=8)|(NZ=10)|(NZ=12)|(NZ=14))[
                LEAF_CHWITH=LEAFIS;
                YLHS=2;
                YRHS=7;
                LEAF_DE=LEAFIS;
            ]
            ELSEIF ((NZ=3)|(NZ=7)|(NZ=11))[
                LEAF_CHWITH=LEAFIS;
                YLHS=3;
                YRHS=6;
                LEAF_DE=LEAFIS;
            ]
            ELSEIF((NZ=5)|(NZ=9)|(NZ=13))[
                IF (LEAFIS=1)[
                    YLHS=1;
                    LEAF_CHWITH=LEAFIS;
                ]
                ELSE [
                    YLHS=8;
                    LEAF_CHWITH=LEAFIS-1;
                ]
                IF (LEAFIS=26)[
                    YRHS=8;
                    LEAF_DE=LEAFIS;
                ]
                ELSE [
                    YRHS=1;
                    LEAF_DE=LEAFIS+1;
                ]
            ]
        ]
        ELSEIF (NY=4)[
            IF ((NZ=1)|NZ=15)[
                LEAF_CHWITH=LEAFIS;
                YLHS=4;
                YRHS=5;
                LEAF_DE=LEAFIS;
            ]
            ELSEIF ((NZ=2)|(NZ=4)|(NZ=6)|(NZ=8)|(NZ=10)|(NZ=12)|(NZ=14))[
                LEAF_CHWITH=LEAFIS;
                YLHS=2;
                YRHS=7;
                LEAF_DE=LEAFIS;
            ]
            ELSEIF ((NZ=3)|(NZ=7)|(NZ=11))[
                LEAF_CHWITH=LEAFIS;
                YLHS=3;
                YRHS=6;
                LEAF_DE=LEAFIS;
            ]
            ELSEIF((NZ=5)|(NZ=9)|(NZ=13))[
                IF (LEAFIS=1)[
                    YLHS=1;
```

```
                    LEAF_CHWITH=LEAFIS;
                ]
                ELSE [
                    YLHS=8;
                    LEAF_CHWITH=LEAFIS-1;
                ]
                IF (LEAFIS=26)[
                    YRHS=8;
                    LEAF_DE=LEAFIS;
                ]
                ELSE [
                    YRHS=1;
                    LEAF_DE=LEAFIS+1;
                ]
            ]
        ]
        ELSEIF (NY=5)[
            IF ((NZ=1)|NZ=15)[
                LEAF_CHWITH=LEAFIS;
                YLHS=5;
                IF (LEAFIS=26)[
                    YRHS=8;
                    LEAF_DE=LEAFIS;
                ]
                ELSE [
                    YRHS=1;
                    LEAF_DE=LEAFIS+1;
                ]
            ]
            ELSEIF ((NZ=2)|(NZ=4)|(NZ=6)|(NZ=8)|(NZ=10)|(NZ=12)|(NZ=14))[
                LEAF_CHWITH=LEAFIS;
                YLHS=2;
                YRHS=7;
                LEAF_DE=LEAFIS;
            ]
            ELSEIF ((NZ=3)|(NZ=7)|(NZ=11))[
                LEAF_CHWITH=LEAFIS;
                YLHS=3;
                YRHS=6;
                LEAF_DE=LEAFIS;
            ]
            ELSEIF((NZ=5)|(NZ=9)|(NZ=13))[
                IF (LEAFIS=1)[
                    YLHS=1;
                    LEAF_CHWITH=LEAFIS;
                ]
                ELSE [
                    YLHS=8;
                    LEAF_CHWITH=LEAFIS-1;
                ]
                IF (LEAFIS=26)[
                    YRHS=8;
                    LEAF_DE=LEAFIS;
                ]
                ELSE [
                    YRHS=1;
                    LEAF_DE=LEAFIS+1;
```



```
                ]
            ]
        ]
        ELSEIF (NY=6)[
            IF ((NZ=1)|NZ=15)[
                LEAF_CHWITH=LEAFIS;
                YLHS=5;
                IF (LEAFIS=26)[
                    YRHS=8;
                    LEAF_DE=LEAFIS;
                ]
                ELSE [
                    YRHS=1;
                    LEAF_DE=LEAFIS+1;
                ]
            ]
            ELSEIF ((NZ=2)|(NZ=4)|(NZ=6)|(NZ=8)|(NZ=10)|(NZ=12)|(NZ=14))[
                LEAF_CHWITH=LEAFIS;
                YLHS=2;
                YRHS=7;
                LEAF_DE=LEAFIS;
            ]
            ELSEIF ((NZ=3)|(NZ=7)|(NZ=11))[
                LEAF_CHWITH=LEAFIS;
                YLHS=6;
                IF (LEAFIS=26)[
                    YRHS=8;
                    LEAF_DE=LEAFIS;
                ]
                ELSE [
                    YRHS=1;
                    LEAF_DE=LEAFIS+1;
                ]
            ]
            ELSEIF((NZ=5)|(NZ=9)|(NZ=13))[
                IF (LEAFIS=1)[
                    YLHS=1;
                    LEAF_CHWITH=LEAFIS;
                ]
                ELSE [
                    YLHS=8;
                    LEAF_CHWITH=LEAFIS-1;
                ]
                IF (LEAFIS=26)[
                    YRHS=8;
                    LEAF_DE=LEAFIS;
                ]
                ELSE [
                    YRHS=1;
                    LEAF_DE=LEAFIS+1;
                ]
            ]
        ]
        ELSEIF (NY=7)[
            IF ((NZ=1)|NZ=15)[
                LEAF_CHWITH=LEAFIS;
                YLHS=5;
```



```
                IF (LEAFIS=26)[
                    YRHS=8;
                    LEAF_DE=LEAFIS;
                ]
                ELSE [
                    YRHS=1;
                    LEAF_DE=LEAFIS+1;
                ]
            ]
            ELSEIF ((NZ=2)|(NZ=4)|(NZ=6)|(NZ=8)|(NZ=10)|(NZ=12)|(NZ=14))[
                LEAF_CHWITH=LEAFIS;
                YLHS=7;
                IF (LEAFIS=26)[
                    YRHS=8;
                    LEAF_DE=LEAFIS;
                ]
                ELSE [
                    YRHS=1;
                    LEAF_DE=LEAFIS+1;
                ]
            ]
            ELSEIF ((NZ=3)|(NZ=7)|(NZ=11))[
                LEAF_CHWITH=LEAFIS;
                YLHS=6;
                IF (LEAFIS=26)[
                    YRHS=8;
                    LEAF_DE=LEAFIS;
                ]
                ELSE [
                    YRHS=1;
                    LEAF_DE=LEAFIS+1;
                ]
            ]
            ELSEIF((NZ=5)|(NZ=9)|(NZ=13))[
                IF (LEAFIS=1)[
                    YLHS=1;
                    LEAF_CHWITH=LEAFIS;
                ]
                ELSE [
                    YLHS=8;
                    LEAF_CHWITH=LEAFIS-1;
                ]
                IF (LEAFIS=26)[
                    YRHS=8;
                    LEAF_DE=LEAFIS;
                ]
                ELSE [
                    YRHS=1;
                    LEAF_DE=LEAFIS+1;
                ]
            ]
        ]
    ]
    ELSEIF (LEAFTYPE_$BLMLC(LEAFIS)=2) [
        IF (NY=1|NY=7) [
            IF (NZ<=3) [
                ZLHS=1;
```



```
                ZRHS=3;
            ]
            ELSEIF ((NZ>=4) & (NZ<=6)) [
                ZLHS=4;
                ZRHS=7;
            ]
            ELSEIF ((NZ>=8) & (NZ<=10)) [
                ZLHS=8;
                ZRHS=11;
            ]
            ELSEIF (NZ>=12) [
                ZLHS=12;
                ZRHS=16;
            ]
            ELSE[
                ZLHS=NZ;
                ZRHS=NZ+1;
            ]
        ]
        ELSEIF (NY=2|NY=6) [
            IF ((NZ >=2) & (NZ<=4)) [
                ZLHS=2;
                ZRHS=5;
            ]
            ELSEIF ((NZ>=6) & (NZ<=8))[
                ZLHS=6;
                ZRHS=9;
            ]
            ELSEIF ((NZ>=10) & (NZ<=12))[
                ZLHS=10;
                ZRHS=13;
            ]
            ELSE [
                ZLHS=NZ;
                ZRHS=NZ+1;
            ]
        ]
        ELSEIF (NY=3|NY=5) [
            IF ((NZ=1)|(NZ=15))[
                ZLHS=NZ;
                ZRHS=NZ+1;
            ]
            ELSE[
                ZLHS=2;
                ZRHS=15;
            ]
        ]
        ELSEIF (NY=4)[
            ZLHS=1;
            ZRHS=16;
        ]
"Now find y boundaries etc"
        IF (NY=1) [
            IF((NZ=1)|(NZ=15))[
                IF (LEAFIS=1)[
                    YLHS=1;
                    LEAF_CHWITH=LEAFIS;
```

```
                ]
                ELSE [
                    YLHS=8;
                    LEAF_CHWITH=LEAFIS-1;
                ]
                YRHS=4;
                LEAF_DE=LEAFIS;
            ]
            ELSEIF ((NZ=2)|(NZ=4)|(NZ=6)|(NZ=8)|(NZ=10)|(NZ=12)|(NZ=14))[
                IF (LEAFIS=1)[
                    YLHS=1;
                    LEAF_CHWITH=LEAFIS;
                ]
                ELSE [
                    YLHS=8;
                    LEAF_CHWITH=LEAFIS-1;
                ]
                YRHS=2;
                LEAF_DE=LEAFIS;
            ]
            ELSEIF ((NZ=3)|(NZ=7)|(NZ=11))[
                IF (LEAFIS=1)[
                    YLHS=1;
                    LEAF_CHWITH=LEAFIS;
                ]
                ELSE [
                    YLHS=8;
                    LEAF_CHWITH=LEAFIS-1;
                ]
                IF (LEAFIS=26) [
                    YRHS=8;
                    LEAF_DE=LEAFIS;
                ]
                ELSE [
                    YRHS=1;
                    LEAF_DE=LEAFIS+1;
                ]
            ]
            ELSEIF((NZ=5)|(NZ=9)|(NZ=13))[
                IF (LEAFIS=1)[
                    YLHS=1;
                    LEAF_CHWITH=LEAFIS;
                ]
                ELSE [
                    YLHS=8;
                    LEAF_CHWITH=LEAFIS-1;
                ]
                YRHS=3;
                LEAF_DE=LEAFIS;
            ]
        ]
        ELSEIF (NY=2)[
            IF ((NZ=1)|NZ=15)[
                IF (LEAFIS=1)[
                    YLHS=1;
                    LEAF_CHWITH=LEAFIS;
                ]
```



```
                ELSE [
                    YLHS=8;
                    LEAF_CHWITH=LEAFIS-1;
                ]
                YRHS=4;
                LEAF_DE=LEAFIS;
            ]
            ELSEIF ((NZ=2)|(NZ=4)|(NZ=6)|(NZ=8)|(NZ=10)|(NZ=12)|(NZ=14))[
                LEAF_CHWITH=LEAFIS;
                YLHS=2;
                YRHS=7;
                LEAF_DE=LEAFIS;
            ]
            ELSEIF ((NZ=3)|(NZ=7)|(NZ=11))[
                IF (LEAFIS=1)[
                    YLHS=1;
                    LEAF_CHWITH=LEAFIS;
                ]
                ELSE [
                    YLHS=8;
                    LEAF_CHWITH=LEAFIS-1;
                ]
                IF (LEAFIS=26) [
                    YRHS=8;
                    LEAF_DE=LEAFIS;
                ]
                ELSE [
                    YRHS=1;
                    LEAF_DE=LEAFIS+1;
                ]
            ]
            ELSEIF((NZ=5)|(NZ=9)|(NZ=13))[
                IF (LEAFIS=1)[
                    YLHS=1;
                    LEAF_CHWITH=LEAFIS;
                ]
                ELSE [
                    YLHS=8;
                    LEAF_CHWITH=LEAFIS-1;
                ]
                YRHS=3;
                LEAF_DE=LEAFIS;
            ]
        ]
        ELSEIF (NY=3)[
            IF ((NZ=1)|NZ=15)[
                IF (LEAFIS=1)[
                    YLHS=1;
                    LEAF_CHWITH=LEAFIS;
                ]
                ELSE [
                    YLHS=8;
                    LEAF_CHWITH=LEAFIS-1;
                ]
                YRHS=4;
                LEAF_DE=LEAFIS;
            ]
```



```
            ELSEIF ((NZ=2)|(NZ=4)|(NZ=6)|(NZ=8)|(NZ=10)|(NZ=12)|(NZ=14))[
                LEAF_CHWITH=LEAFIS;
                YLHS=2;
                YRHS=7;
                LEAF_DE=LEAFIS;
            ]
            ELSEIF ((NZ=3)|(NZ=7)|(NZ=11))[
                IF (LEAFIS=1)[
                    YLHS=1;
                    LEAF_CHWITH=LEAFIS;
                ]
                ELSE [
                    YLHS=8;
                    LEAF_CHWITH=LEAFIS-1;
                ]
                IF (LEAFIS=26) [
                    YRHS=8;
                    LEAF_DE=LEAFIS;
                ]
                ELSE [
                    YRHS=1;
                    LEAF_DE=LEAFIS+1;
                ]
            ]
            ELSEIF((NZ=5)|(NZ=9)|(NZ=13))[
                YLHS=3;
                LEAF_CHWITH=LEAFIS;
                YRHS=6;
                LEAF_DE=LEAFIS;
            ]
        ]
        ELSEIF (NY=4)[
            IF ((NZ=1)|NZ=15)[
                LEAF_CHWITH=LEAFIS;
                YLHS=4;
                YRHS=5;
                LEAF_DE=LEAFIS;
            ]
            ELSEIF ((NZ=2)|(NZ=4)|(NZ=6)|(NZ=8)|(NZ=10)|(NZ=12)|(NZ=14))[
                LEAF_CHWITH=LEAFIS;
                YLHS=2;
                YRHS=7;
                LEAF_DE=LEAFIS;
            ]
            ELSEIF ((NZ=3)|(NZ=7)|(NZ=11))[
                IF (LEAFIS=1)[
                    YLHS=1;
                    LEAF_CHWITH=LEAFIS;
                ]
                ELSE [
                    YLHS=8;
                    LEAF_CHWITH=LEAFIS-1;
                ]
                IF (LEAFIS=26) [
                    YRHS=8;
                    LEAF_DE=LEAFIS;
                ]
```



```
                ELSE [
                    YRHS=1;
                    LEAF_DE=LEAFIS+1;
                ]
            ]
            ELSEIF((NZ=5)|(NZ=9)|(NZ=13))[
                YLHS=3;
                LEAF_CHWITH=LEAFIS;
                YRHS=6;
                LEAF_DE=LEAFIS;
            ]
        ]
        ELSEIF (NY=5)[
            IF ((NZ=1)|NZ=15)[
                LEAF_CHWITH=LEAFIS;
                YLHS=5;
                IF (LEAFIS=26)[
                    YRHS=8;
                    LEAF_DE=LEAFIS;
                ]
                ELSE [
                    YRHS=1;
                    LEAF_DE=LEAFIS+1;
                ]
            ]
            ELSEIF ((NZ=2)|(NZ=4)|(NZ=6)|(NZ=8)|(NZ=10)|(NZ=12)|(NZ=14))[
                LEAF_CHWITH=LEAFIS;
                YLHS=2;
                YRHS=7;
                LEAF_DE=LEAFIS;
            ]
            ELSEIF ((NZ=3)|(NZ=7)|(NZ=11))[
                IF (LEAFIS=1)[
                    YLHS=1;
                    LEAF_CHWITH=LEAFIS;
                ]
                ELSE [
                    YLHS=8;
                    LEAF_CHWITH=LEAFIS-1;
                ]
                IF (LEAFIS=26) [
                    YRHS=8;
                    LEAF_DE=LEAFIS;
                ]
                ELSE [
                    YRHS=1;
                    LEAF_DE=LEAFIS+1;
                ]
            ]
            ELSEIF((NZ=5)|(NZ=9)|(NZ=13))[
                YLHS=3;
                LEAF_CHWITH=LEAFIS;
                YRHS=6;
                LEAF_DE=LEAFIS;
            ]
        ]
        ELSEIF (NY=6)[
```

```
            IF ((NZ=1)|NZ=15)[
                LEAF_CHWITH=LEAFIS;
                YLHS=5;
                IF (LEAFIS=26)[
                    YRHS=8;
                    LEAF_DE=LEAFIS;
                ]
                ELSE [
                    YRHS=1;
                    LEAF_DE=LEAFIS+1;
                ]
            ]
            ELSEIF ((NZ=2)|(NZ=4)|(NZ=6)|(NZ=8)|(NZ=10)|(NZ=12)|(NZ=14))[
                LEAF_CHWITH=LEAFIS;
                YLHS=2;
                YRHS=7;
                LEAF_DE=LEAFIS;
            ]
            ELSEIF ((NZ=3)|(NZ=7)|(NZ=11))[
                IF (LEAFIS=1)[
                    YLHS=1;
                    LEAF_CHWITH=LEAFIS;
                ]
                ELSE [
                    YLHS=8;
                    LEAF_CHWITH=LEAFIS-1;
                ]
                IF (LEAFIS=26) [
                    YRHS=8;
                    LEAF_DE=LEAFIS;
                ]
                ELSE [
                    YRHS=1;
                    LEAF_DE=LEAFIS+1;
                ]
            ]
            ELSEIF((NZ=5)|(NZ=9)|(NZ=13))[
                YLHS=6;
                LEAF_CHWITH=LEAFIS;
                IF (LEAFIS=26)[
                    YRHS=8;
                    LEAF_DE=LEAFIS;
                ]
                ELSE [
                    YRHS=1;
                    LEAF_DE=LEAFIS+1;
                ]
            ]
        ]
        ELSEIF (NY=7)[
            IF ((NZ=1)|NZ=15)[
                LEAF_CHWITH=LEAFIS;
                YLHS=5;
                IF (LEAFIS=26)[
                    YRHS=8;
                    LEAF_DE=LEAFIS;
                ]
```



```
                ELSE [
                    YRHS=1;
                    LEAF_DE=LEAFIS+1;
                ]
            ]
            ELSEIF ((NZ=2)|(NZ=4)|(NZ=6)|(NZ=8)|(NZ=10)|(NZ=12)|(NZ=14))[
                LEAF_CHWITH=LEAFIS;
                YLHS=7;
                IF (LEAFIS=26)[
                    YRHS=8;
                    LEAF_DE=LEAFIS;
                ]
                ELSE [
                    YRHS=1;
                    LEAF_DE=LEAFIS+1;
                ]
            ]
            ELSEIF ((NZ=3)|(NZ=7)|(NZ=11))[
                IF (LEAFIS=1)[
                    YLHS=1;
                    LEAF_CHWITH=LEAFIS;
                ]
                ELSE [
                    YLHS=8;
                    LEAF_CHWITH=LEAFIS-1;
                ]
                IF (LEAFIS=26) [
                    YRHS=8;
                    LEAF_DE=LEAFIS;
                ]
                ELSE [
                    YRHS=1;
                    LEAF_DE=LEAFIS+1;
                ]
            ]
            ELSEIF((NZ=5)|(NZ=9)|(NZ=13))[
                YLHS=6;
                LEAF_CHWITH=LEAFIS;
                IF (LEAFIS=26)[
                    YRHS=8;
                    LEAF_DE=LEAFIS;
                ]
                ELSE [
                    YRHS=1;
                    LEAF_DE=LEAFIS+1;
                ]
            ]
        ]
    ]
    IF(W(NP)~=0) [
        ZP = (ZREG_$BLMLC(LEAFIS,ZRHS)-ZFL)/W(NP);
        ZN = (ZREG_$BLMLC(LEAFIS,ZLHS)-ZFL)/W(NP);
        IF( (ZP>=0.0) & (ZN>=0.0) ) [
            ZDIST =MIN(ZP, ZN);
        ]
        ELSE [
            ZDIST = MAX(ZP, ZN);
```



```
        ]
    ]
    ELSE [
        ZDIST = 1.0E20;
    ];
    IF((UVL(1)-SURPARA1_$BLMLC(LEAF_DE,YRHS)*W(NP))~= 0 ) [
        YP = (SURPARA1_$BLMLC(LEAF_DE,YRHS)*(ZFL-ZFOCUS_$BLMLC(1))-XYFL(1));
        YP = YP/(UVL(1) - SURPARA1_$BLMLC(LEAF_DE,YRHS)*W(NP));
    ]
    ELSE [
        YP = 1.0E20;
    ]
    IF((UVL(1) - SURPARA1_$BLMLC(LEAF_CHWITH,YLHS)*W(NP))~ = 0 ) [
        YN = (SURPARA1_$BLMLC(LEAF_CHWITH,YLHS)*(ZFL-ZFOCUS_$BLMLC(1))-XYFL(1));
        YN = YN/(UVL(1) - SURPARA1_$BLMLC(LEAF_CHWITH,YLHS)*W(NP));
    ]
    ELSE [
        YN = 1.0E20;
    ]
    IF((YP>=0.0) & (YN>=0.0) ) [
        YDIST =MIN(YP, YN);
    ]
    ELSE [
        YDIST = MAX(YP,YN);
    ] "Left in from dynvmlc but is this correct?"
    IF(ENDTYPE_$BLMLC = 1) [
        TEMP1=SURPARA2_B_$BLMLC(LEAFIS)*(ZMIN_$BLMLC+(ZTHICK_$BLMLC/2));
        TEMP2=SURPARA2_A_$BLMLC(LEAFIS)*(ZMIN_$BLMLC+(ZTHICK_$BLMLC/2));
        HOLE=HOLEPOS_$BLMLC(LEAFIS);
        TEMP3=LEAFB_$BLMLC(LEAFIS)+HOLE;
        TEMP4=LEAFA_$BLMLC(LEAFIS)-HOLE;
        IF ((NZ>=1) & (NZ<=LEAF_TOP)) [
            IF(NX=1) [
                TEMP1=TEMP1-((ZFL-ZMIN_$BLMLC)/TAN(THETA_TOP_$BLMLC));
                TEMP2=TEMP2+((ZFL-ZMIN_$BLMLC)/TAN(THETA_TOP_$BLMLC));
                XL=ABS(XYFL(2)-TEMP1);
                XR=ABS(TEMP2-XYFL(2));
            ]
            ELSEIF (NX=2) [
                XL=ABS(RMAX_CM(ICM_$BLMLC)-XYFL(2));
                XR=ABS(TEMP3-XYFL(2));
            ]
            ELSEIF (NX=3) [
                XL=ABS(XYFL(2)-TEMP3);
                XR=ABS(TEMP1-XYFL(2));
            ]
            ELSEIF (NX=4) [
                XL=ABS(XYFL(2)-TEMP2);
                XR=ABS(TEMP4-XYFL(2));
            ]
            ELSEIF (NX=5) [
                XL=ABS(XYFL(2)-TEMP4);
                XR=ABS(RMAX_CM(ICM_$BLMLC)-XYFL(2));
            ]
        ]
        ELSEIF ((NZ>LEAF_TOP) & (NZ<=LEAF_MIDDLE)) [
            IF (NX=1) [
```



```
                XL=ABS(TEMP1-XYFL(2));
                XR=ABS(TEMP2-XYFL(2));
            ]
            ELSEIF (NX=2) [
                XL=ABS(RMAX_CM(ICM_$BLMLC)-XYFL(2));
                XR=ABS(XYFL(2)-TEMP3);
            ]
            ELSEIF (NX=3) [
                XL=ABS(TEMP3-XYFL(2));
                XR=ABS(XYFL(2)-TEMP1);
            ]
            ELSEIF (NX=4) [
                XL=ABS(XYFL(2)-TEMP2);
                XR=ABS(TEMP4-XYFL(2));
            ]
            ELSEIF (NX=5) [
                XL=ABS(XYFL(2)-TEMP4);
                XR=ABS(RMAX_CM(ICM_$BLMLC)-XYFL(2));
            ]
        ]
        ELSEIF ((NZ>LEAF_MIDDLE)&(NZ<=LEAF_BOTTOM)) [
            Z_LEAF_BOTTOM=ZREG_$BLMLC(LEAFIS,LEAF_MIDDLE);
            TEMP1=TEMP1-((ZFL-Z_LEAF_BOTTOM)/TAN(THETA_BOTTOM_$BLMLC));
            TEMP2=TEMP2-((ZFL-Z_LEAF_BOTTOM)/TAN(THETA_BOTTOM_$BLMLC));
            IF (NX=1) [
                XL=ABS(TEMP1-XYFL(2));
                XR=ABS(TEMP2-XYFL(2));
            ]
            ELSEIF (NX=2) [
                XL=ABS(RMAX_CM(ICM_$BLMLC)-XYFL(2));
                XR=ABS(XYFL(2)-TEMP3);
            ]
            ELSEIF (NX=3) [
                XL=ABS(TEMP3-XYFL(2));
                XR=ABS(XYFL(2)-TEMP1);
            ]
            ELSEIF (NX=4) [
                XL=ABS(XYFL(2)-TEMP2);
                XR=ABS(TEMP4-XYFL(2));
            ]
            ELSEIF (NX=5) [
                XL=ABS(XYFL(2)-TEMP4);
                XR=ABS(RMAX_CM(ICM_$BLMLC)-XYFL(2));
            ]
        ]
    ] "end of focused leaf end"
    XP=XR;
    XN=XL;
    IF( (XP>=0.0) & (XN>=0.0) ) [
        XDIST =MIN(XP, XN);
    ]
    ELSE [
        XDIST = MAX(XP,XN);
    ];
    IF( ZDIST>=0.0) [
        TEMP=ZDIST;
        IF( YDIST>=0.0 ) [
```

```
                TEMP=MIN(TEMP,YDIST);
            ]
            IF( XDIST>=0.0 ) [
                TEMP=MIN(TEMP,XDIST);
            ]
        ]
        ELSEIF ( (YDIST>=0.0) & (XDIST>=0.0) ) [
            TEMP=MIN(XDIST,YDIST);
        ]
        ELSE [
            TEMP=MAX(XDIST,YDIST);
        ]
        IF(TEMP<0) [
        OUTPUT NX,NY,NZ,LEAFIS; "should not happen"
        ('neg dist nx = ',I3,' NY= ',I3,' NZ= ',I3,' LEAF= ',I3);
        OUTPUT XDIST,YDIST,ZDIST;
        ('POS :',F8.3,'  XDIST :',F8.3,' YDIST :',F8.3,'  ZDIST :',F8.3);
        ]
    ]
    ELSE [
        TEMP=1.0E20;
    ]
    MINDISTANCE=TEMP;
    IF ((PLT_$BLMLC = 2) & (LEAFIS < 100) & (LEAFIS > 0)) [
        WRITE(73,251) XYFL(2),XYFL(1),ZFL,LEAFIS,NX,NY,NZ,
        SUBINDEX_$BLMLC(LEAFIS,NX,NY,NZ);
    ]
251 FORMAT(F8.3,',',F8.3,',',F8.3,',',I3,',',I3,',',I3,',',I3,',',I3);
252 FORMAT(F8.3,',',F8.3,',',F8.3,',',I3,',',I3,',',I3,',',I3,',',A1);
RETURN;
END;


"End of BLMLC_cm.mortran (Rev 1.4)"
```

```
%E
/*****************************************************************************
 *
 *  $Id: BLMLC_macros.mortran,v 1.3 2005/11/10 05:19:11 bwalters Exp $
 *
 *****************************************************************************/
"Macros for use in the BLMLC Component Module                          "
"-----------------------------------------------------------------------"
" Files Needed                                                         "
"---------------                                                       "
"1. BLMLC_CM.mortran                                                   "
"2. BLMLC_MACROS.mortran                                               "
"---------------                                                       "
"                                                                      "
" See BLMLC_CM for more details                                        "
"Tony Millin, 2008                                                     "

"-----------------------------------------------------------------------"
"     BLMLC miscellaneous replacement macros                    "
"-----------------------------------------------------------------------"
"                                                                       "
REPLACE {$MAX_N_$BLMLC} WITH {{REDUCE $MAXIMUM_N_$BLMLC}};
"       ==========="

REPLACE {$MAXIMUM_N_$BLMLC} WITH {3};
"       ==================="

" THE MAX # OF the leaves TO BE ALLOWED IN THIS MODULE"
REPLACE {$MAXLEAF} WITH {160}
;
"-----------------------------------------------------------------------"
"     BLMLC component module common                                    "
"-----------------------------------------------------------------------"

"V>COMMON/CM_$BLMLC/
"V>================
"V>ICM_$BLMLC        = index of CM, set as ICM in INPUT_$BLMLC,not reset
"V>IRSTART_$BLMLC    = first region number for this CM
"V>IREND_$BLMLC      = last region number for this CM
"V>N_$BLMLC          = number of regions in CM
"V>TITLE_$BLMLC      = title of CM
"V>ZMIN_$BLMLC       = Front of BLMLC
"V>ZMAX_$BLMLC       = back of BLMLC
"V>ZTHICK_$BLMLC     = Thickness of leaves
"V>ZFRONT_$BLMLC     = Upstream Z boundary of this CM
"V>NGROUP_$BLMLC     = the number of groups of leaves where the leaves
"V>                    in each group have the same width
"V>NUM_LEAF_$BLMLC(I)= the number of leaves in group I
"V>LEAFWIDTH_$BLMLC(I)= the width of each leaf in group I at ZMIN_$BLMLC
"V>                     excluding the tongue
"V>TOT_LEAF_$BLMLC   = the total number of leaves in the MLC
"V>ORIENT_$BLMLC     = the index to indicate the leave direction
"V>                    0: default, leaf orientation in y
"V>                    1:                          in x
"V>START_$BLMLC      = the start position wrt the CAX of the lowermost
"V>                    leaf ie leaf 1 tongue as projected to ZMIN_$BLMLC
"V>HOLEPOS_$BLMLC(I) = distance from leaf tip to start of driving screw hole
```



```
"V>                     for each leaf in group I
"V>LEAFGAP_$BLMLC    = the width of the interleaf air gap at ZMIN_$BLMLC
"V>ENDTYPE_$BLMLC    = the leaf end geomery ( 0 = rounded, 1 = focused )
"V>LEAFRADIUS_$BLMLC = the radius of the leaf end if ENDTYPE_$BLMLC = 0
"V>ZREG_$BLMLC(TOT_LEAF_$BLMLC,8) = the z boundaries of the 7 sub-regions in
"V>                                  z direction
"V>YREG_$BLMLC(TOT_LEAF_$BLMLC,7)
"V>                  = the boundaries along the perpendicular direction
"V>                    to the leaf orientation of sub-regions
"V>SUBINDEX_$BLMLC   = an index number to represent which region the
"V>          belongs in based on sub-dividing each leaf into regions.
"V>ZFOCUS_$BLMLC(2) = the two focus point coordinates: 1. for leave side
"V>                                                    2. for leave end.
"V>SURPARA1_$BLMLC($MAXLEAF,8)  the parameters to describe the leaf side
"V>                              surface i.e. tangent along that side.
"V>LEAFA_$BLMLC(TOT_LEAF_$BLMLC) = coordinates of A side leaves at
"V>                     ZMIN_$BLMLC if ENDTYPE_$BLMLC = 1 or at
"V>                     rounded leaf tip @ ZMIN_$BLMLC+(ZTHICK_$BLMLC)/2
"V>LEAFB_$BLMLC(TOT_LEAF_$BLMLC) = coordinates of B side leaves at
"V>                     ZMIN_$BLMLC if ENDTYPE_$BLMLC = 1 or at
"V>                     rounded leaf tip @ ZMIN_$BLMLC+(ZTHICK_$BLMLC)/2.
"V>SURPARA2_B_$BLMLC($MAXLEAF)the parameters to describe the leaf end
"V>                              surface i.e. tangent along that end.
"V>SURPARA2_A_$BLMLC($MAXLEAF)the parameters to describe the leaf end
"V>                              surface i.e. tangent along that end.
"V>IR_$BLMLC          local region number
"V>LEAFTYPE_$BLMLC(I) Leaf type of leaf I: 1=FULL leaf
"V>                                        2=TARGET leaf
"V>                                        3=ISOCENTER leaf
"V>LEAFWIDTH_$BLMLC(LEAFTYPE) = width of leaf of type LEAFTYPE excl. tongue
"V>WTONGUE_$BLMLC(LEAFTYPE) = width of tongue for LEAFTYPE leaves
"V>WGROOVE_$BLMLC(LEAFTYPE) = width of groove for LEAFTYPE leaves
"V>WTIP_$BLMLC(LEAFTYPE) = width of leaf tip for LEAFTYPE leaves
"V>WRAILTOP_$BLMLC(LEAFTYPE) = width of upper support rail for LEAFTYPE
"V>WRAILBOT_$BLMLC(LEAFTYPE) = width of lower support rail for LEAFTYPE
"V>ZTIP_$BLMLC(LEAFTYPE) = Z where leaf tip starts/ends for LEAFTYPE
"V>ZLEAF_$BLMLC(LEAFTYPE) = Z where leaf starts/ends for LEAFTYPE
"V>ZTONGUE_$BLMLC(LEAFTYPE) = Z where tongue starts/ends for LEAFTYPE
"V>ZGROOVE_$BLMLC(LEAFTYPE) = Z where groove starts/ends for LEAFTYPE
"V>ZHOLETOP_$BLMLC(LEAFTYPE) = Z of top of driving screw hole for LEAFTYPE
"V>ZHOLEBOT_$BLMLC(LEAFTYPE) = Z of bottom of driving screw hole
"V>HOLEPOS_FULL/TAR/ISO_$BLMLC = Distance of hole from leaf tip for leaf
"V>                               type specified.  Later stored in
"V>                               HOLEPOS_$BLMLC(I) for each leaf.
"V>ZRAILTOP_$BLMLC(LEAFTYPE) = Z of upper support rail for LEAFTYPE
"V>ZRAILBOT_$BLMLC(LEAFTYPE) = Z of lower support rail for LEAFTYPE
"V>MIN_PLANE_$BLMLC  min. plane perp. to leaf direction.  For particles
"V>                    in leaves with position < MIN_PLANE_$BLMLC,
"V>                    air gaps and driving screw holes will be ignored when
"V>                    doing range rejection (IGNOREGAPS_$BLMLC=1)
"V>MAX_PLANE_$BLMLC  max. plane perp. to leaf direction.  For particles
"V>                    in leaves with position > MAX_PLANE_$BLMLC,
"V>                    air gaps and driving screw holes will be ignored when
"V>                    doing range rejection (IGNOREGAPS_$BLMLC=1)
"V>IGNOREGAPS_$BLMLC Set to 1 to ignore air gaps and driving screw holes
"I>                    when doing range rejection
"V>                    for particles in the leaves and beyond the most open
```



```
"V>                    leaf.  0 (default) otherwise.
;
REPLACE{;COMIN/CM_$BLMLC/;} WITH {
;COMMON/CM_$BLMLC/EPS,
      ZMIN_$BLMLC,
      ZMAX_$BLMLC,
      ZTHICK_$BLMLC,
      ZFRONT_$BLMLC,
      ZFOCUS_$BLMLC,
      THETA_TOP_$BLMLC,
      THETA_BOTTOM_$BLMLC,
      SURPARA2_B_$BLMLC,
      SURPARA2_A_$BLMLC,
      START_$BLMLC,
      HOLEPOS_$BLMLC,
      LEAFGAP_$BLMLC,
      LEAFRADIUS_$BLMLC,
      LEAFA_$BLMLC,
      LEAFB_$BLMLC,
      SURPARA1_$BLMLC,
      ZREG_$BLMLC,
      YREG_$BLMLC,MIN_PLANE_$BLMLC,MAX_PLANE_$BLMLC,
      LEAFWIDTH_$BLMLC,WTONGUE_$BLMLC,WGROOVE_$BLMLC,
      WTIP_$BLMLC,WRAILTOP_$BLMLC,WRAILBOT_$BLMLC,
      ZTIP_$BLMLC,ZLEAF_$BLMLC,
      ZTONGUE_$BLMLC,ZGROOVE_$BLMLC,ZHOLETOP_$BLMLC,
      ZHOLEBOT_$BLMLC,
      HOLEPOS_FULL_$BLMLC,HOLEPOS_TAR_$BLMLC,HOLEPOS_ISO_$BLMLC,
      ZRAILTOP_$BLMLC,ZRAILBOT_$BLMLC,
      ICM_$BLMLC,IRSTART_$BLMLC,IREND_$BLMLC,N_$BLMLC,N_GAP_$BLMLC,
      IR_$BLMLC,NUM_LEAF_$BLMLC, ORIENT_$BLMLC,ENDTYPE_$BLMLC,
      SUBINDEX_$BLMLC,NGROUP_$BLMLC,TOT_LEAF_$BLMLC,
      LEAFTYPE_$BLMLC,IGNOREGAPS_$BLMLC,
      TITLE_$BLMLC,
      PLT_$BLMLC;
   DOUBLE PRECISION
      EPS,
      ZMIN_$BLMLC,
      ZMAX_$BLMLC,
      ZTHICK_$BLMLC,
      ZFRONT_$BLMLC,
      ZFOCUS_$BLMLC(2),
      THETA_TOP_$BLMLC,
      THETA_BOTTOM_$BLMLC,
      SURPARA2_B_$BLMLC($MAXLEAF),
      SURPARA2_A_$BLMLC($MAXLEAF),
      START_$BLMLC,
      HOLEPOS_$BLMLC($MAXLEAF),
      LEAFGAP_$BLMLC,
      LEAFRADIUS_$BLMLC,
      LEAFA_$BLMLC($MAXLEAF),
      LEAFB_$BLMLC($MAXLEAF),
      SURPARA1_$BLMLC($MAXLEAF,8),
      ZREG_$BLMLC($MAXLEAF,17),
      YREG_$BLMLC($MAXLEAF,8),MIN_PLANE_$BLMLC,MAX_PLANE_$BLMLC;
  $REAL
      LEAFWIDTH_$BLMLC(3),WTONGUE_$BLMLC(3),WGROOVE_$BLMLC(3),
```



```
      WTIP_$BLMLC(3),WRAILTOP_$BLMLC(3),WRAILBOT_$BLMLC(3),
      ZTIP_$BLMLC(3),ZLEAF_$BLMLC(3),
      ZTONGUE_$BLMLC(3),ZGROOVE_$BLMLC(3),ZHOLETOP_$BLMLC(3),
      ZHOLEBOT_$BLMLC(3),
      HOLEPOS_FULL_$BLMLC,HOLEPOS_TAR_$BLMLC,HOLEPOS_ISO_$BLMLC,
      ZRAILTOP_$BLMLC(3),ZRAILBOT_$BLMLC(3);
  INTEGER
      ICM_$BLMLC,IRSTART_$BLMLC,IREND_$BLMLC,N_$BLMLC,N_GAP_$BLMLC,
      IR_$BLMLC,NUM_LEAF_$BLMLC($MAXLEAF), ORIENT_$BLMLC,ENDTYPE_$BLMLC,
      SUBINDEX_$BLMLC($MAXLEAF,5,7,15),NGROUP_$BLMLC,TOT_LEAF_$BLMLC,
      LEAFTYPE_$BLMLC($MAXLEAF),IGNOREGAPS_$BLMLC,PLT_$BLMLC;
  CHARACTER*1 TITLE_$BLMLC(60);

}
 "end of replacement defining common for this CM"
;
" $BLMLC_FIND(REGION, DISTANCE)"
"======================================="
" this macro is used to determine the regon #"
"{p1}: the return region value, local region"
"{p2}: the step dist which is used to calc. the particle final position"
REPLACE {$BLMLC_FIND(#,#);} WITH {;
    XYFL(1)=XYL(1)+{P2}*UVL(1);
    XYFL(2)=XYL(2)+{P2}*UVL(2);
    ZFL=Z(NP)+{P2}*W(NP);
IF((W(NP)>0. & ZFL>=ZMAX_$BLMLC) | (W(NP)<0. & ZFL<=ZFRONT_$BLMLC)) [
        OUTOFCMFLAG=1;
]
"put in = signs to get this to exit stepping loop in HOWFAR"
IF(N_GAP_$BLMLC=1 & ZFL<=ZMIN_$BLMLC & ZFL>=ZFRONT_$BLMLC) [
     {P1}=4;
]
ELSE ["inside leaf bank"
    LEAFIS=0;
    DO I = 1,TOT_LEAF_$BLMLC [ "Determine which leaf we are in"
            TEMP1=SURPARA1_$BLMLC(I,1)*(ZFL-ZFOCUS_$BLMLC(1));
        TEMP2=SURPARA1_$BLMLC(I,8)*(ZFL-ZFOCUS_$BLMLC(1));
        IF((XYFL(1) >= TEMP1) & (XYFL(1) < TEMP2) ) [
                LEAFIS=I;
            EXIT;
        ]
    ]
    TEMP1=SURPARA1_$BLMLC(I,1)*(ZFL-ZFOCUS_$BLMLC(1));
    TEMP2=SURPARA1_$BLMLC(TOT_LEAF_$BLMLC,8)*(ZFL-ZFOCUS_$BLMLC(1));
"   IF(LEAFIS=0) ["
    IF((XYFL(1) < TEMP1) | (XYFL(1) > TEMP2) ) [
        {P1}=1;
        OUTOFMLCFLAG=1;
    ] "assume going into air, set"
          "{P1}=2 for going into solid block"
    ELSE [
            IF(ZFL<ZREG_$BLMLC(LEAFIS,1))[
            NZ=1;
            ]
            ELSE IF(ZFL>ZREG_$BLMLC(LEAFIS,16))[
            NZ=15;
            ]
```

```
            ELSE[
                DO I = 1,15 [ "Determine Z region"
                    IF((ZREG_$BLMLC(LEAFIS,I)<=ZFL) & (ZFL <=ZREG_$BLMLC(LEAFIS,I+1))) [
                        NZ=I;
                    EXIT;
                ]
                ]
            ]
            IF(NZ~=15 & W(NP)>0)[
                DO I=NZ+1,16[
                    IF(I=15 | ZREG_$BLMLC(LEAFIS,I)>ZFL) EXIT;
                NZ=I;
                ]
            ]
            TEMP1=SURPARA1_$BLMLC(LEAFIS,1)*(ZFL-ZFOCUS_$BLMLC(1));
            TEMP2=SURPARA1_$BLMLC(LEAFIS,8)*(ZFL-ZFOCUS_$BLMLC(1));
            IF(XYFL(1)<TEMP1)[
                NY=1;
            ]
            ELSE IF(XYFL(1)>TEMP2)[
                NY=7;
            ]
"Now we know which leaf we are in (leafis) determine ny"
        DO I=1,7 [
            TEMP1=SURPARA1_$BLMLC(LEAFIS,I)*(ZFL-ZFOCUS_$BLMLC(1));
            TEMP2=SURPARA1_$BLMLC(LEAFIS,I+1)*(ZFL-ZFOCUS_$BLMLC(1));
            IF (TEMP1<=XYFL(1) & XYFL(1) <TEMP2)[
                NY=I;
                EXIT;
            ]
        ]
"So we know NY but are we on the next leaf along?"
        IF ((NY = 6) & (LEAFIS < 26)) [
            IF (LEAFTYPE_$BLMLC(LEAFIS)=1) [
                IF ((NZ=3)|(NZ=7)|(NZ=11)) [
                    IF (XYFL(1) > (SURPARA1_$BLMLC(LEAFIS+1,1)*(ZFL-ZFOCUS_$BLMLC(1)))) [
                        LEAFIS=LEAFIS+1;
                        NY=1;
                    ]
                    ELSE [
                        LEAFIS=0; "in gap between leaves"
                        NY=0;
                    ]
                ]
            ]
            ELSE [
                IF ((NZ=5)|(NZ=9)|(NZ=13)) [
                    IF (XYFL(1) > (SURPARA1_$BLMLC(LEAFIS+1,1)*(ZFL-ZFOCUS_$BLMLC(1))))  [
                        LEAFIS=LEAFIS+1;
                        NY=1;
                    ]
                    ELSE [
                        LEAFIS=0; "in gap between leaves"
                        NY=0;
                    ]
                ]
            ]
```



```
        ]
        ELSEIF ((NY =7) & (LEAFIS <26)) [
            IF (LEAFTYPE_$BLMLC(LEAFIS)=1) [
                IF ((NZ~=5) & (NZ~=9) & (NZ~=13)) [
                    IF (XYFL(1) > (SURPARA1_$BLMLC(LEAFIS+1,1)*(ZFL-ZFOCUS_$BLMLC(1))))  [
                        LEAFIS=LEAFIS+1;
                        DO I=1,7 [
                            TEMP1=SURPARA1_$BLMLC(LEAFIS,I)*(ZFL-ZFOCUS_$BLMLC(1));
                            TEMP2=SURPARA1_$BLMLC(LEAFIS,I+1)*(ZFL-ZFOCUS_$BLMLC(1));
                            IF (TEMP1<=XYFL(1) & XYFL(1) <TEMP2)[
                                NY=I;
                                EXIT;
                            ]
                        ]
                    ]
                    ELSE [
                        LEAFIS=0; "in gap between leaves"
                        NY=0;
                    ]
                ]
            ]
            ELSE [
                IF ((NZ~=3) & (NZ~=7) & (NZ~=11)) [
                    IF (XYFL(1) > (SURPARA1_$BLMLC(LEAFIS+1,1)*(ZFL-ZFOCUS_$BLMLC(1))))  [
                        LEAFIS=LEAFIS+1;
                        DO I=1,7 [
                            TEMP1=SURPARA1_$BLMLC(LEAFIS,I)*(ZFL-ZFOCUS_$BLMLC(1));
                            TEMP2=SURPARA1_$BLMLC(LEAFIS,I+1)*(ZFL-ZFOCUS_$BLMLC(1));
                            IF (TEMP1<=XYFL(1) & XYFL(1) <TEMP2)[
                                NY=I;
                                EXIT;
                            ]
                        ]
                    ]
                    ELSE [
                        LEAFIS=0; "in gap between leaves"
                        NY=0;
                    ]
                ]
            ]
        ]
"Now determine X region index"
"Determine which X region we are in - first calculate leaf pos at zmid"
        TEMP1=SURPARA2_B_$BLMLC(LEAFIS)*(ZMIN_$BLMLC+(ZTHICK_$BLMLC/2));
        TEMP2=SURPARA2_A_$BLMLC(LEAFIS)*(ZMIN_$BLMLC+(ZTHICK_$BLMLC/2));
        HOLE=HOLEPOS_$BLMLC(LEAFIS);
"           TEMP3=LEAFB_$BLMLC(LEAFIS)-HOLE;
"       TEMP4=LEAFA_$BLMLC(LEAFIS)+HOLE;
        TEMP3=TEMP1-HOLE;
        TEMP4=TEMP2-HOLE;
"By now we know which z region we are in so use this to calculate"
"which X region we are in. Also calculate XL and XR for dist calc"
        IF ((NZ>=1) & (NZ<=5)) ["In top region of leaf"
            Z_LEAF_TOP=ZREG_$BLMLC(LEAFIS,6);
            TEMP1=TEMP1-((Z_LEAF_TOP-ZFL)/TAN(THETA_TOP_$BLMLC));
            TEMP2=TEMP2+((Z_LEAF_TOP-ZFL)/TAN(THETA_TOP_$BLMLC));
            IF ((XYFL(2)>TEMP1 & XYFL(2)<TEMP2) | (XYFL(2)=TEMP1 & UVL(2)>=0.0) |
```



```
              (XYFL(2)=TEMP2 & UVL(2)<0.0)) [
                NX=1;
            ]
            ELSEIF ((XYFL(2)<TEMP1 & XYFL(2)>TEMP3) | (XYFL(2)=TEMP1 & UVL(2)>=0.0) |
              (XYFL(2)=TEMP3 & UVL(2)>=0.0)) [
                NX=3;
            ]
            ELSEIF ((XYFL(2)<TEMP3) | (XYFL(2)=TEMP3 & UVL(2)<0.0))[
                NX=2;
            ]
            ELSEIF((XYFL(2)>TEMP2 & XYFL(2)<TEMP4) | (XYFL(2)=TEMP2 & UVL(2)>=0.0) |
                   (XYFL(2)=TEMP4 & UVL(2)<0.0)) [
                NX=4;
                ]
                ELSEIF((XYFL(2)>TEMP4) | (XYFL(2)=TEMP4 & UVL(2)>=0.0)) [
                NX=5;
            ]
        ]
        ELSEIF ((NZ>5) & (NZ<=10)) [" In middle region of leaf"
            IF ((XYFL(2)>TEMP1 & XYFL(2)<TEMP2) | (XYFL(2)=TEMP1 & UVL(2)>=0.0) |
               (XYFL(2)=TEMP2 & UVL(2)<0.0)) [
                NX=1;
            ]
            ELSEIF ((XYFL(2)<TEMP1 & XYFL(2)>TEMP3) | (XYFL(2)=TEMP1 & UVL(2)>=0.0) |
            (XYFL(2)=TEMP3 & UVL(2)>=0.0)) [
                NX=3;
            ]
            ELSEIF ((XYFL(2)<TEMP3) | (XYFL(2)=TEMP3 & UVL(2)<0.0)) [
                NX=2;
            ]
            ELSEIF((XYFL(2)>TEMP2 & XYFL(2)<TEMP4) | (XYFL(2)=TEMP2 & UVL(2)>=0.0) |
            (XYFL(2)=TEMP4 & UVL(2)<0.0)) [
                NX=4;
            ]
            ELSEIF((XYFL(2)>TEMP4) | (XYFL(2)=TEMP4 & UVL(2)>=0.0)) [
                NX=5;
            ]
        ]
        ELSEIF ((NZ>10)&(NZ<=15)) ["In bottom region of leaf"
                Z_LEAF_BOTTOM=ZREG_$BLMLC(LEAFIS,16);
            TEMP1=TEMP1-((ZFL-Z_LEAF_BOTTOM)/TAN(THETA_BOTTOM_$BLMLC));
            TEMP2=TEMP2+((ZFL-Z_LEAF_BOTTOM)/TAN(THETA_BOTTOM_$BLMLC));
                IF ((XYFL(2)>TEMP1 & XYFL(2)<TEMP2) | (XYFL(2)=TEMP1 & UVL(2)>=0.0) |
                  (XYFL(2)=TEMP2 & UVL(2)<0.0)) [
                    NX=1;
                ]
                ELSEIF ((XYFL(2)<TEMP1 & XYFL(2)>TEMP3) | (XYFL(2)=TEMP1 & UVL(2)>=0.0) |
                   (XYFL(2)=TEMP3 & UVL(2)>=0.0)) [
                    NX=3;
                ]
                ELSEIF ((XYFL(2)<TEMP3) | (XYFL(2)=TEMP3 & UVL(2)<0.0)) [
                    NX=2;
                ]
                ELSEIF((XYFL(2)>TEMP2 & XYFL(2)<TEMP4) | (XYFL(2)=TEMP2 & UVL(2)>=0.0) |
                   (XYFL(2)=TEMP4 & UVL(2)<0.0)) [
                    NX=4;
                ]
```



```
                ELSEIF((XYFL(2)>TEMP4) | (XYFL(2)=TEMP4 & UVL(2)>=0.0)) [
                    NX=5;
                ]
        ]
        IF (LEAFIS =0) [
            {P1}=1;
        ]
        ELSE [
        {P1}=SUBINDEX_$BLMLC(LEAFIS,NX,NY,NZ);
        ]
    ]
]

;}
;

;
" NEXT COMES HOWNEAR MACRO"
"========================"

REPLACE {$BLMLC_CM_HOWNEAR(#);} WITH {
CALL HOWNEAR_$BLMLC({P1});
}
;
"End of BLMLC_macros.mortran (Rev 1.3)"
```

.